THE ROLE OF GREMLIN-1 IN METABOLIC DYSFUNCTION-ASSOCIATED STEATOTIC LIVER DISEASE

by

Dr. med. Paul Horn, M.Sc.

A thesis submitted to the University of Birmingham for the degree of

DOCTOR OF PHILOSOPHY

NIHR Biomedical Research Centre

Centre for Liver and Gastrointestinal Research

Institute of Immunology and Immunotherapy

University of Birmingham

September 2023

ABSTRACT

Metabolic dysfunction-associated steatotic liver disease (MASLD), formerly known as non-alcoholic fatty liver disease (NAFLD) is an increasing global health problem that is tightly linked to the rising prevalence of obesity and the metabolic syndrome. Hepatocellular lipid accumulation and lipotoxic injury prompt a chronic inflammatory response (metabolic dysfunction-associated steatohepatitis, MASH) that culminates with the activation of hepatic stellate cells (HSCs) and subsequent hepatic fibrogenesis. Liver fibrosis is the most prominent determinant of prognosis in patients with MASH but currently there are no treatments available that target hepatic fibrogenesis directly.

Gremlin-1 has been implicated in liver fibrosis in MASH via inhibition of bone morphogenetic protein (BMP) signalling and has thereby been identified as a potential therapeutic target. Using rat *in vivo* and human *in vitro* and *ex vivo* model systems of MASH fibrosis, we show that while Gremlin-1 was upregulated in human and rat MASH fibrosis, restricted to a small subpopulation of myofibroblasts, neutralisation of Gremlin-1 activity with monoclonal therapeutic antibodies does not reduce liver inflammation or liver fibrosis. Lentiviral overexpression of Gremlin-1 in the hepatic stellate cell line LX-2 and primary HSCs led to changes in BMP-related gene expression, which did not translate into increased fibrogenesis. Furthermore, Gremlin-1 bound to heparin with high affinity, which appeared to prevent Gremlin-1 from entering the systemic circulation, prohibiting Gremlin-1-mediated organ crosstalk. Gremlin-1 also had no effect on hepatic endothelial cell activation and showed no significant expression changes in monocyte-derived macrophages.

Through an integrated analysis of bulk RNA sequencing data sets of human liver fibrosis and *in vitro*-activated hepatic stellate cells, we identified the activin and myostatin antagonist *follistatin-like 3 (FSTL3)* as strongly associated with hepatic fibrogenic responses. *FSTL3* was upregulated in the HSC cell line LX-2 in response to transforming growth factor beta (TGFβ)1 and activin A, and in the hepatocyte cell line HepG2 in response to activin A. Inhibition of FSTL3 by siRNA-mediated knockdown altered fibrogenic gene expression in LX-2 cells and increased lipolytic gene expression in HepG2 cells, which translated into reduced hepatocellular lipid accumulation.

Overall, these findings suggest a redundant role for Gremlin-1 in the pathogenesis of liver fibrosis, which is unamenable to therapeutic targeting. The activin and myostatin inhibitor FSTL3 however seems to be involved in hepatic stellate cell activation and hepatocellular steatosis and warrants further investigation as a therapeutic target in liver fibrosis and MASH in particular.

ACKNOWLEDGEMENT

First I would like to thank Philip Newsome and Chris Weston for their excellent supervision, guidance and teaching provided throughout my project.

I want to thank everyone at the Centre for Liver and Gastrointestinal Research who made my stay abroad such an enjoyable time. Particularly I want to thank everyone directly involved in the project: Marco R. Rink for his help and guidance on the generation and use of lentiviral overexpression vectors, Emma Shepherd and Ellie Northall for all their help throughout the project and in particular their guidance on PCLS, Thin Luu and Celine Hernandez for training me on flow adhesion assays, cell isolation and cell culture techniques, Gary Reynolds for his advice and guidance on Pathology and performing the cryosectioning of PCLS, Scott Davies for his help with fluorescence and high-content microscopy, Daniel A. Patten for providing the HepG2 cells, Trish Lalor for her support and guidance, in particular regarding platelets. I am also very grateful to Vanessa Poon, Kavitha Kirubendran and Alexandra Reeve for the hard work they put into their dissertation projects which partly fed into the work presented here. Many thanks also go to Janine Fear and Graham Caine for their excellent technical and administrative assistance.

Without the help and support from Novo Nordisk this project would not have been possible. I am very grateful for the contribution of everyone in the research team at Novo Nordisk involved in the project, their dedication and the important discussions we had throughout the project. In particular I would like to thank Morten Fog-Tonnesen, Louise Zeuthen and Markus R. Latta for project management at Novo Nordisk and for coordinating our efforts, Morten G. Rasch for developing the therapeutic antibodies, Jenny Norlin for providing data from the rat CDAA-HFD study, Kasper Almholt and Birgitte M. Viuff for *in situ* hybridisation and immunohistochemistry staining on human and rodent liver tissue, Elisabeth D. Galsgaard for providing data from the clinical cohorts, Andreas Hald, Franziska Zosel, Svend Poulsen, Peder L. Norby and Helle Demuth for extensively characterising the antibodies and their heparin-binding properties as well as assay development for Gremlin-1 protein quantification. Thanks also go to Professor Mogens Vyberg at Aalborg University Copenhagen for kindly providing and characterising human liver biopsies and to Lise Lotte Gluud and Mikkel Parsberg Werge at Hvidovre Hospital for providing biosamples and clinical data of the FLINC cohort.

This work largely depended on the availability of human biomaterials for cell isolation. Therefore I would like to thank all patients for their willingness to donate blood or tissue and the clinical staff at the Queen Elizabeth Hospital for blood and tissue collection.

Finally, I am very grateful to the NIHR Birmingham Biomedical Research Centre and to Novo Nordisk for funding the project.

Contents

List of Figures

List of Tables

Abbreviations

α**SMA** α smooth muscle actin

AA arachidonic acid

ADP adenosine-diphosphate

ALK1 activin receptor-like kinase 1

ALK5 TGFβ type I receptor

ALK5i ALK5 inhibitor

ALT alanine aminotransferase

aPS activated platelet supernatant

ArLD alcohol-related liver disease

AST aspartate aminotransferase

AUC area under the curve

BAMBI BMP and activin membrane bound inhibitor

BEC biliary epithelial cell

BMI body mass index

BMP bone morphogenetic protein

BMP2 bone morphogenetic protein 2

BMP4 bone morphogenetic protein 4

BMP7 bone morphogenetic protein 7

BMPER BMP binding endothelial regulator

BMPR2 bone morphogenetic protein receptor 2

BSA	bovine serum albumin
CCL	C-C motif ligand
CCL$_4$	carbon tetrachloride
CCR	C-C chemokine receptor type
CDAA-HFD	choline-deficient, L-amino acid defined, 1% cholesterol, high-fat diet
cDNA	complementary deoxyribonucleic acid
CREB	cAMP response element-binding protein
CTGF	connective tissue growth factor
CXCR	C-X-C chemokine receptor type
DAMP	damage-associated molecular pattern
DEG	differentially expressed gene
DMEM	Dulbecco’s Modified Eagle Medium
ECM	extracellular matrix
EDTA	ethylenediaminetetraacetic acid
eGFP	enhanced green fluorescent protein
ELISA	enzyme-linked immunosorbent assay
EpCAM	epithelial cell adhesion molecule
ER	endoplasmic reticulum
ERK	extracellular signal-regulated kinase
FCS	fetal calf serum
FGFR1	fibroblast growth factor receptor 1
FST	follistatin
FSTL3	follistatin-like 3
FXR	farnesoid X receptor
GFP	green fluorescent protein

GLP-1 glucagon-like peptide 1

GREM1 Gremlin-1

HCC hepatocellular carcinoma

HCV hepatitis C virus

HHSC human hepatic stellate cell

HMGB1 high mobility box 1

HRP horseradish peroxidase

HSC hepatic stellate cell

HSEC hepatic sinusoidal endothelial cell

HUVEC human umbilical vein endothelial cell

ICAM1 intercellular adhesion molecule 1

IFNγ interferon gamma

IL-1β interleukin 1β

IL-4 interleukin 4

ILC Innate lymphoid cell

INHA inhibin α chain

INHBA inhibin β_A chain

INHBB inhibin β_B chain

ISH *in situ* hybridisation

JNK c-Jun N-terminal kinase

LOCI luminescent oxygen channeling immunoassay

LOX lysyl oxidase

LOXL lysyl oxidase-like

LPS lipopolysaccharide

LXR liver X receptor

MAIT cell mucosa-associated invariant T cell

MAPK mitogen-activated protein kinase

MASH metabolic dysfunction-associated steatohepatitis

MASLD metabolic dysfunction-associated steatotic liver disease

MF myofibroblast

MIF monocyte migration inhibitory factor

MMP matrix metalloproteinase

MoMF monocyte-derived macrophages

NAFLD non-alcoholic fatty liver disease

NAS non-alcoholic fatty liver disease activity score

NASH non-alcoholic steatohepatitis

NBL1 neuroblastoma 1, DAN family BMP antagonist

NF-ϰB nuclear factor ϰB

NK cell natural killer cell

NKT cell natural killer T cell

NO nitrogen monoxide

OA oleic acid

PA palmitic acid

PAMP pathogen-associated molecular pattern

PBC primary biliary cholangitis

PBMC peripheral blood mononuclear cells

PBS phosphate-buffered saline

PBSA BSA in PBS

PCLS precision-cut liver slices

PCR polymerase chain reaction

PDGF platelet-derived growth factor

PFA paraformaldehyde

PGI_2 prostaglandin I_2

PPAR peroxisome proliferator-activated receptor

PRR pattern recognition receptor

PSC primary sclerosing cholangitis

PSG Penicillin-Streptomycin-L-Glutamine

RIN RNA integrity number

SCD1 stearoyl-CoA desaturase-1

SGLT2 sodium/glucose cotransporter 2

TG transglutaminase

TGFβ transforming growth factor beta

Thr thrombin

THRβ thyroid hormone receptor beta

TIMP tissue inhibitor of metalloproteinases

TNFα tumor necrosis factor alpha

TREM2 triggering receptor expressed on myeloid cells 2

uPS unstimulated platelet supernatant

VCAM1 vascular cell adhesion molecule 1

VEGF vascular endothelial growth factor

VEGFA vascular endothelial growth factor A

VEGFR2 vascular endothelial growth factor receptor 2

CHAPTER 1

GENERAL INTRODUCTION

Disclaimer: Parts of this introduction have been reproduced from review articles and book chapters written by the author of this thesis [1–3], the latter two not having been published yet.

1.1 The burden of chronic liver disease

The human liver is a remarkable organ that fulfils essential bodily functions, including carbohydrate, lipid and amino acid metabolism, regulation of trace element metabolism (e.g. iron and copper), detoxification, drug metabolism, bile formation and fat digestion, immune surveillance, production of plasma proteins including albumin, lipoproteins and coagulation factors [4]. It is characterised by its huge capacity to regenerate, as it can fully recover even upon severe acute injury or partial organ removal [5]. Repeated or ongoing injury, however, typically causes liver inflammation and deposition of extracellular matrix, a state called liver fibrosis. Eventually, liver fibrosis can progress to cirrhosis, a state of disrupted tissue architecture that can lead to progressive loss of normal hepatic functional capacity. Liver cirrhosis is the most important risk factor for liver-related outcomes, such as chronic and acute-on-chronic liver failure, and hepatocellular carcinoma (HCC) [6]. Across the globe, chronic liver disease is responsible for greater than two million deaths per year, more than 1.3 million caused by cirrhosis and its complications and another million caused by viral hepatitis and HCC [7, 8]. Aetiologies of chronic liver disease include chronic viral hepatitis, alcohol-related liver disease, inherited metabolic disorders such as haemochromatosis or Wilson's disease, as well as autoimmune hepatitis and cholestatic liver diseases. The latter comprises different conditions including primary sclerosing cholangitis (PSC) - a chronic inflammatory autoimmune-like condition closely associated with inflammatory bowel disease leading to sclerosis and destruction of the small and large bile ducts - and primary biliary cholangitis (PBC) - an autoimmune-like inflammation of the microscopic bile ducts mostly affecting women that leads to biliary fibrosis and cirrhosis. In recent decades, the global incidence of chronic liver disease has increased, paralleling the development of obesity, the metabolic syndrome and its complications, and this increase is mainly attributed to metabolic dysfunction-associated steatotic liver disease (MASLD) [8].

1.1.1 Metabolic dysfunction-associated steatotic liver disease

Definition and epidemiology

Obesity, overnutrition and a sedentary lifestyle are increasingly prevalent health problems worldwide, causing several associated diseases, including the metabolic syndrome [9, 10]. Associated with the metabolic syndrome and insulin resistance [11], MASLD (formerly known as NAFLD, non-alcoholic fatty liver disease) is becoming increasingly prevalent, with an estimated 20-30 percent of adults in European countries being affected [12]. MASLD is defined as the excess accumulation of hepatic fat in the presence of at least one cardiometabolic risk factor and in the absence of significant alcohol consumption (i.e. ≥ 30 g/day for men and ≥ 20 g/day for women) or any other secondary cause of hepatic steatosis [13]. While the course of the disease is benign for most patients with simple steatosis (metabolic dysfunction-associated steatotic liver, MASL), about one-fifth of patients develop inflammation of the liver, namely metabolic dysfunction-associated steatohepatitis (MASH, formerly known as NASH - non-alcoholic steatohepatitis). MASH can progress to liver fibrosis and ultimately liver cirrhosis in a further 20 % of patients, and subsequently cause liver failure or hepatocellular carcinoma (Figure 1.1) [12]. Therefore, the increase of MASLD prevalence over the last decades has had a considerable impact on figures for liver transplantation, now being the second-leading cause for liver transplantation in the US [14]. Furthermore, the increasing prevalence of HCC due to MASLD is at least partially responsible for the overall increase in HCC prevalence worldwide [15].

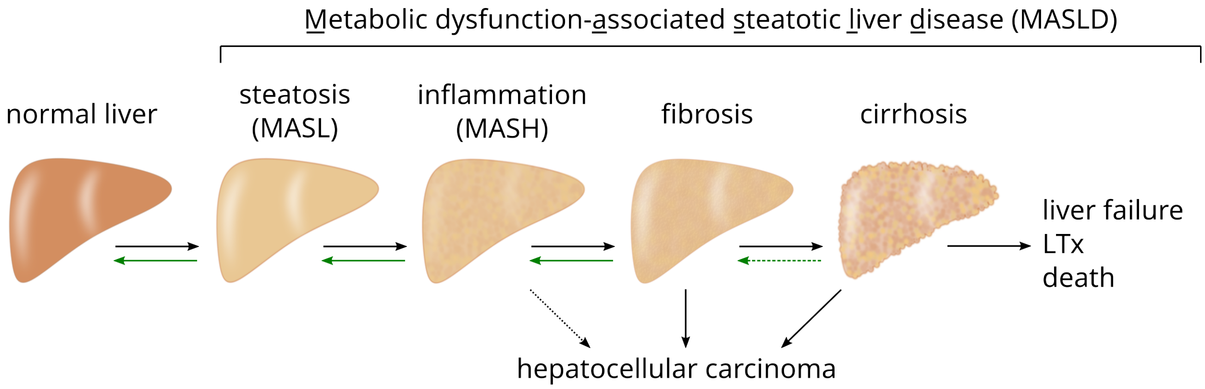

Figure 1.1: The spectrum of metabolic dysfunction-associated steatotic liver disease. MASH - metabolic dysfunction-associated steatohepatitis, LTx - liver transplantation.

Diagnosis and risk stratification

The diagnosis of fatty liver is usually based on the detection of an echo-bright liver on ultrasound in the absence of other causes of liver steatosis. Alternatively, in cases of suspected MASH without detectable steatosis on ultrasound, ultrasound-based controlled attenuated parameter (CAP) or magnetic resonance imaging proton density fat fraction (MRI-PDFF) can be informative [16, 17]. Patients with liver steatosis should undergo a comprehensive workup for suspected MASLD and investigated for alcohol intake, metabolic risk factors and secondary causes of liver steatosis, including viral hepatitis [16]. The diagnosis of steatohepatitis is more challenging though. Normal liver tests do not rule out MASH [18] and thus liver biopsy is required to make a diagnosis of MASH. However, liver biopsy is reserved for patients at increased risk for steatohepatitis or advanced fibrosis or in patients with suspected concomitant secondary liver disease [16, 17].

The stage of fibrosis largely determines strategies for therapeutic management and surveillance of patients with MASLD as it is the major determinant of prognosis in patients with MASH [19, 20]. Current developments in non-invasive testing allow the prediction of risk of fibrosis, and guide clinicians in their decision on which patient needs a liver biopsy. Laboratory scores such as FIB-4 [21] or the MASLD Fibrosis Score (NFS [22]) lack accuracy in detecting fibrosis or differentiating between different stages thereof but their high negative predictive values of 88-92% are useful for ruling out advanced stages of disease [23]. In combination with measurements of liver stiffness and patented serum tests like ELF™, FibroMeter or Fibrotest, such fibrosis scores can guide specialist referral and significantly reduce the need for liver biopsies [24–26]. Novel non-invasive scores like the FAST and NIS-4 are being developed and validated [27, 28], and in the future might provide more accurate assessment of fibrosis.

Ultimately, liver biopsy is the current gold standard for diagnosing MASH and for determining disease activity and the stage of fibrosis. On histopathology, MASLD is characterised by macrovesicular steatosis of more than 5 % of hepatocytes, usually beginning in the centrilobular area (zone 3). The NASH clinical research network (CRN) system is accepted for grading and staging of MASH, and integrates different degrees of steatosis, lobular inflammation and liver cell ballooning as determined by a histopathologist into the non-alcoholic fatty liver disease activity score (NAS) and includes different stages of fibrosis, expanding on the Brunt score (Table 1.1) [29]. Figure 1.2 shows representative images of histopathological features of MASLD, MASH and fibrosis.

Table 1.1: The NASH-CRN scoring system

NAS components		
Item	Score	Extent
Steatosis	0	<5%
	1	5-33%
	2	34-66%
	3	>66%
Lobular inflammation	0	No foci
	1	<2 foci/200x
	2	2-4 foci/200x
	3	>4 foci/200x
Hepatocyte Ballooning	0	None
	1	Few balloon cells
	2	Many cells

Fibrosis Stage		
Item	Score	Extent
Fibrosis	0	None
	1	Perisinusoidal or periportal
	1A	Mild, zone 3, perisinusoidal
	1B	Moderate, zone 3, perisinusoidal
	1C	Portal/periportal
	2	Perisinusoidal and portal/periportal
	3	Bridging fibrosis
	4	Cirrhosis

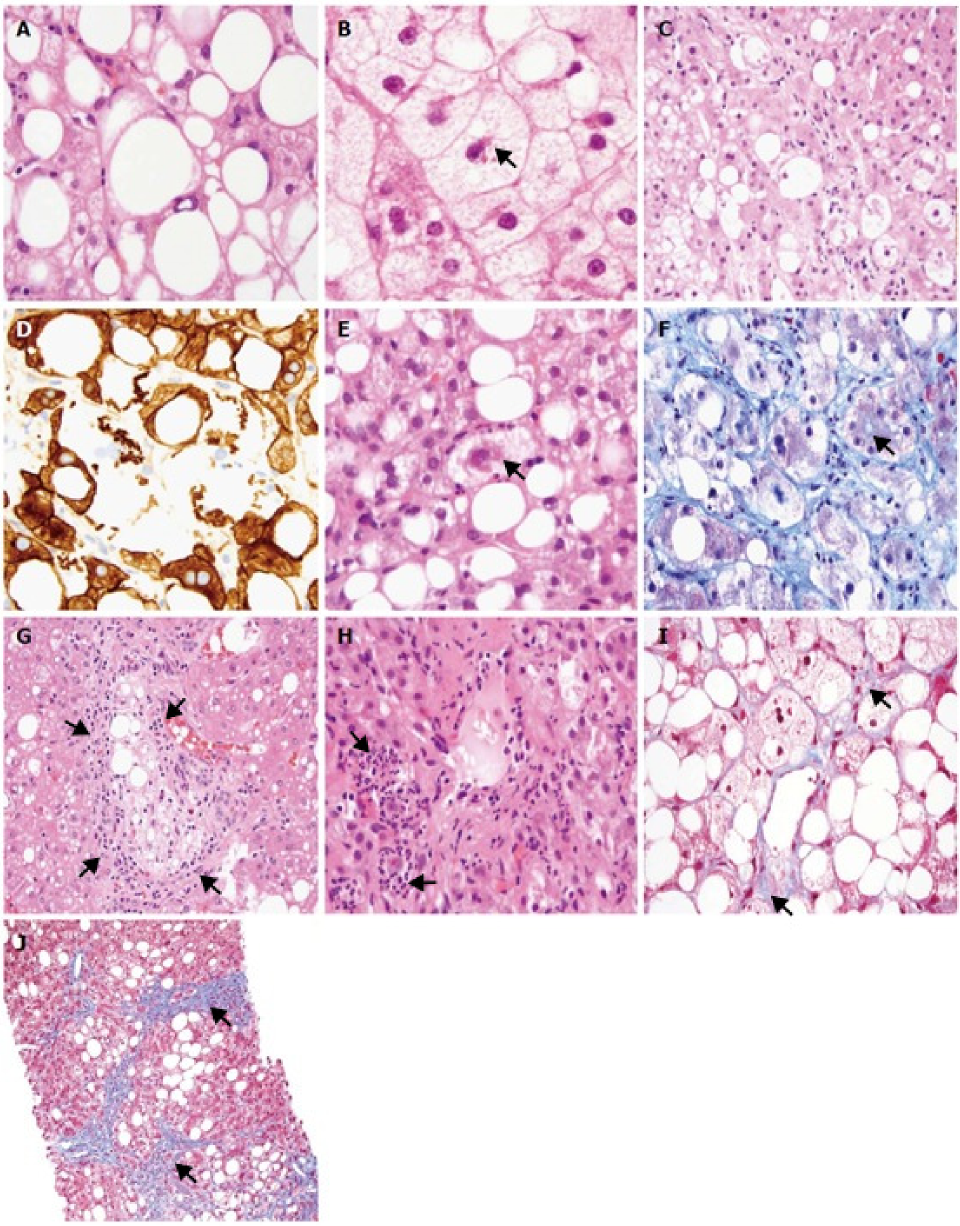

Figure 1.2: *caption see next page*

Figure 1.2 *(previous page)*: Histologic features, grading, and staging of metabolic dysfunction-associated steatotic liver disease. A. Mixed large and small droplet steatosis, single droplet, with nucleus pushed to one side, visible as white ”empty” tissue area H&E stain, 600 ×; **B.** Microvesicular steatosis, nuclei in the centre with foamy cytoplasm, and eosinophilic megamitochondria (arrow), H&E stain, 600 ×; **C.** Ballooned hepatocytes with flocculent cytoplasm (arrow), H&E stain, 600 ×; **D.** Loss of cytoplasmic expression of keratin 8/18 in ballooned hepatocytes, brown DAB staining by immunohistochemistry, 600 ×; **E.** Mallory-Denk body, i.e. eosinophilic agglomerates of cytokeratins and proteins, indicated by arrow, H&E stain, 600 ×; **F.** Mallory-Denk body in blue-green colour and dense perisinusoidal fibrosis, indicated by arrow, Trichrome stain, 600 ×; **G.** Portal lipogranuloma, i.e. inflammatory reaction surrounding steatotic hepatocytes, indicated by arrows, H&E stain, 400 ×; **H.** Mallory-Denk bodies and satellitosis (neutrophils surrounding ballooned hepatocytes, arrow), H&E stain, 600 ×; **I.** Delicate perisinusoidal fibrosis stained in blue (arrow), Trichrome stain, 600 ×; **J.** Bridging fibrosis, i.e. fibrosis connecting the portal fields and central veins, stained in blue (arrows), Trichrome stain, 200 ×.
Figure and caption reproduced with minimal adaptations from Nalbantoglu *et al.* 2014 [30] under the terms of the Creative Commons Attribution-Noncommercial (CC BY-NC 4.0) License.

Current and emerging therapeutic options

The pathophysiology of MASLD is tightly linked to increased body weight and the metabolic syndrome, and therefore the mainstay of intervention is lifestyle change with diet and physical exercise to reduce body weight and improve metabolic function. International guidelines recommend exercise and diet with the aim to achieve a weight loss of 7-10 % in individuals with obesity [16, 17], as this improves inflammation, can halt disease progression and even revert fibrosis [31]. More moderate weight reduction by 3-5 % reduces hepatic fat content and improves metabolic function, but insufficiently reduces disease activity [32]. Patients with severe obesity with a body mass index (BMI) > 40 kg/m^2, or selected cases with a BMI > 35 kg/m^2 might also be eligible for bariatric surgery or endoscopic bariatric interventions, which have also shown high effectiveness on the resolution of steatohepatitis and fibrosis regression

[33–35]. Patients diagnosed with MASLD should also undergo careful cardiovascular risk assessment and management, as they are at increased risk of cardiovascular events and this risk increases with more advanced stages of disease [36].

Currently no licensed drugs are available for the treatment of MASLD, meaning that many patients will progress to liver cirrhosis or HCC and ultimately require liver transplantation. Nevertheless, some compounds licensed for other indications have shown some beneficial effects on liver histology or serum markers of disease severity in clinical trials and their use can therefore be considered for their respective indications in selected patients. For patients with type 2 diabetes mellitus this includes the glucagon-like peptide 1 (GLP-1) analogues liraglutide and semaglutide, which have beneficial effects on resolution of MASH on histology [37, 38], most likely mediated by weight loss and concomitantly improved insulin sensitivity, sodium/glucose cotransporter 2 (SGLT2) inhibitors such as empagliflozin, dapagliflozin and canagliflozin that have shown reductions in liver steatosis [39–41] and the peroxisome proliferator-activated receptor (PPAR) α/γ agonist pioglitazone which has shown beneficial effects on MASH resolution, liver fat content and fibrosis in randomized trials [42–44]. Metformin is the first line treatment option for most individuals with type 2 diabetes mellitus and acts through incompletely understood mechanisms that lead to altered cellular energy sensing, ultimately improving insulin sensitivity and glucose tolerance. Even though metformin does not improve histological MASH or fibrosis, retrospective data point to improved overall survival, reductions in hepatic decompensation and hepatocellular carcinoma incidence in patients with MASLD cirrhosis and type 2 diabetes [45]. Additional compounds that sometimes are used in clinical practice are weight loss-inducing drugs such as the lipase inhibitor orlistat [46–48] or high-dose supplementation with vitamin E, the latter showing consistent effectiveness in reducing serum aminotransferases, histological steatohepatitis and liver fibrosis, likely through anti-oxidant effects reducing hepatocellular lipotoxic stress [49]. Currently, no approved compounds are available for the treatment of inflammation or fibrosis in MASH and a couple of compounds have already failed in late clinical development. However, several promising assets are currently being tested, including the farnesoid X receptor (FXR) agonist obeticholic acid, which is already approved as second-line treatment for patients with PBC, or the stearoyl-CoA desaturase-1 (SCD1) inhibitor aramchol, the pan-PPAR agonist lanifibranor and the thyroid hormone receptor beta (THRβ) agonist resmetirom [50], with resmetirom now having shown efficacy in the phase III MAESTRO-NASH trial [51]. All these compounds have in common that they affect hepatocellular glucose and lipid metabolism, and likely act through reduction of hepatocellular stress. Some compounds, such as PPAR and liver X receptor (LXR) agonists, likely also modify macrophage and hepatic stellate cell (HSC) activation, thereby reducing liver inflammation and fibrosis [116]. This raises hopes that in the near future we will have licensed treatment options available. However, overall low response rates of 26 to 30 % and high placebo response rates still ensure that there is a need to find novel therapeutic targets for drug development.

1.2 Mechanisms of liver fibrosis

Liver fibrosis is the common consequence of chronic liver diseases, independent of their aetiology. It can be understood as a dysregulated inflammatory and wound healing response resulting in the excessive deposition of extracellular matrix [52]. Hepatic fibrogenesis is a complex and dynamic process that involves all hepatic cell populations but also extrahepatic signals such as from the intestine or adipose tissue [53, 54]. Long-lasting liver injury leads to a persistent inflammatory response and to the release of cell damage mediators, causing infiltration of inflammatory leukocytes and activation of matrix-producing cells, HSCs in particular. A plethora of signals are involved, including damage-associated molecular patterns (DAMPs), pathogen-associated molecular patterns (PAMPs), cytokines, growth factors, hypoxia, changes in tissue biomechanics and others [52, 55]. Inflammation and the deposition of fibrous tissue can eventually result in a disruption of the sinusoidal microarchitecture and over the course of years and decades can ultimately progress to liver cirrhosis.

1.2.1 The hepatic microarchitecture

The liver lobule forms the basic functional unit of the liver. Blood flows from the portal branches of the portal vein and the hepatic artery through the hepatic sinusoids into the central vein. Liver sinusoids are lined by specialised fenestrated, permeable endothelial cells [56] and contain the tissue-resident macrophages of the liver, the so-called Kupffer cells [57]. The subendothelial space (space of Disse), is built of loose connective tissue and a basement membrane-like matrix and contains the HSCs, which function as vitamin A storing pericytes of the hepatic sinusoids. These

HSCs produce the fine connective tissue of the Disse space and are instrumental in maintaining microarchitecture and function of the sinusoids [58]. In the space of Disse, the major players of the hepatic inflammatory and fibrotic response are in close proximity, allowing for close intercellular communication (Figure 1.3).

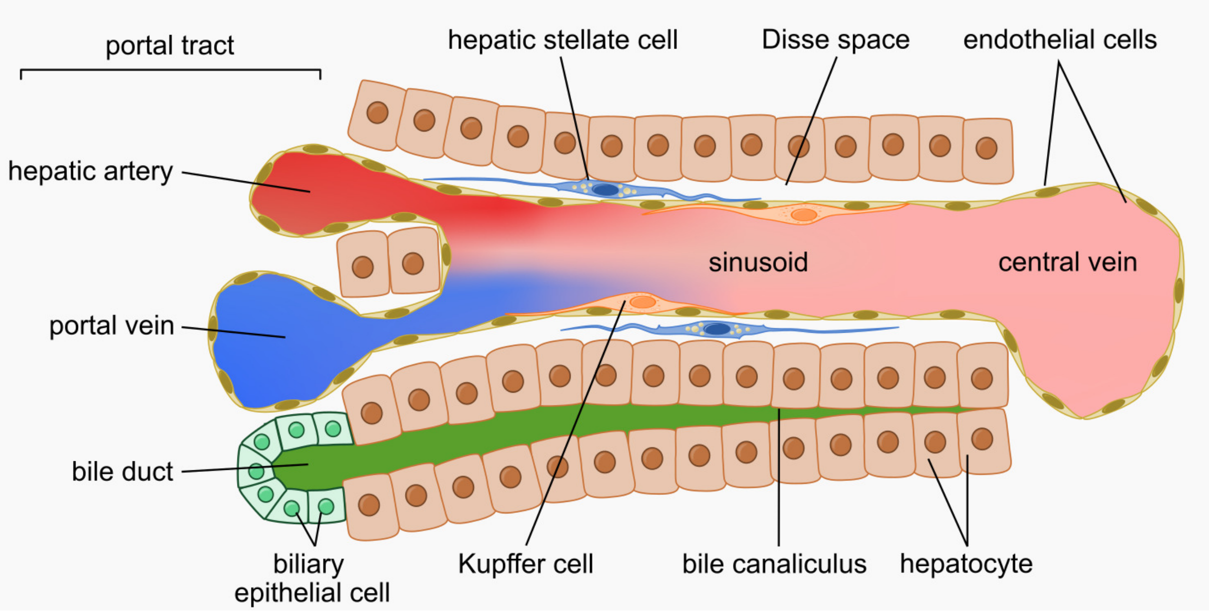

Figure 1.3: Structural organisation of the liver sinusoid. Originally published in Horn & Tacke, “Mechanismen Der Hepatischen Fibrogenese” [2], reproduced with kind permission from Springer.

1.2.2 From liver injury to inflammation

Hepatocellular injury

Injury of hepatic epithelial cells is an essential initiating step in the inflammatory and fibrogenic cascade. Damaged hepatocytes display an altered gene expression profile and secrete fibrogenic factors such as Notch, osteopontin or transforming growth factor beta (TGFβ) [59]. Furthermore, these hepatocytes secrete extracellular vesicles called exosomes which are also directly involved in HSC activation [60]. Apoptotic and necrotic cells also release a number of DAMPs that can trigger inflammatory and fibrotic processes on immune and HSCs [52]. These include nucleotides such as uridine diphosphate or adenosine diphosphate, mitochondrial DNA and the nuclear protein high mobility box 1 (HMGB1) [61–63].

Endothelial cells

In healthy liver, differentiated hepatic sinusoidal endothelial cells (HSECs) maintain the quiescent phenotype of HSCs through their release of nitrogen monoxide (NO). Early in liver injury, endothelial cells start to dedifferentiate, leading to capillarisation, defenestration and reduced NO synthesis with subsequent activation of angiogenic signalling pathways which are tightly linked to the progression of liver fibrosis [64].

The angiocrine cytokine vascular endothelial growth factor (VEGF) plays a dual role in these processes. While maintaining the differentiation of fenestrated HSEC in healthy liver, and thereby exerting anti-fibrotic effects, the release of VEGF is increased in the fibrotic liver. This increase of VEGF promotes capillarisation and defenestration of HSEC through angiogenic processes and is directly involved in stellate cell activation [64]. Interestingly, HSEC are also involved in liver regeneration in acute liver injury, involving activation of the C-X-C chemokine receptor type (CXCR)7-Id1 signalling pathway. In chronic liver injury however, activation of fibroblast growth factor receptor 1 (FGFR1) shifts signalling to a CXCR4 response, which promotes fibrogenic pathways [65].

The role of monocytes and macrophages

Liver macrophages have received increasing attention due to their heterogeneity and diverse functions in liver homeostasis, inflammation and fibrogenesis. The main populations are the tissue-resident Kupffer cells and monocyte-derived macrophages (MoMF) of different functional polarisation [66].

Kupffer cells are the principal hepatic tissue-resident macrophage population and self-renew independent of bone marrow precursors. They play an essential role in maintaining normal tissue homeostasis and immune tolerance, act as sinusoidal sentinels and, due to their high phagocytic capacity, are able to clear cellular detritus and circulating bacteria [67]. In the context of liver injury, Kupffer cells react early to hepatocellular and extrahepatic danger signals, especially PAMPs and DAMPs, and are thus significantly involved in early endothelial activation and pro-inflammatory immune responses [68].

While the stationary Kupffer cells play an important role in the initiation of the inflammatory cascade, infiltration of circulating bone marrow-derived monocytes occurs early in liver injury and drives chronic inflammatory processes. The recruitment of these monocytes to the sinusoidal space is mediated primarily by chemokines, such as C-C motif ligand 2 (CCL2), CCL3, CCL5, CCL9 and CCL10, and their receptors C-C chemokine receptor type 2 (CCR2) and CCR5 [69]. These monocytes eventually differentiate into macrophages and undergo pronounced dynamic phenotypical and functional changes.

Current single cell sequencing data from healthy and fibrotic diseased liver provide a completely new view on the heterogeneity of hepatic macrophage populations. In particular, the classic dichotomous division into classically activated, pro-inflammatory, fibrogenic (”M1-like”), and alternatively activated, anti-inflammatory, regenerative macrophages (”M2-like”) can no longer be maintained [68]. A key finding is the identification of specialised scar-associated/lipid-associated macrophages, characterised by their expression of CD9 and triggering receptor expressed on myeloid cells 2 (TREM2), that are instrumental in shaping the fibrogenic microenvironment in chronic liver injury [70]. These activated macrophages also secrete a number of fibrogenic mediators that are significantly involved in stellate cell activation. In particular, TGFβ, tumor necrosis factor alpha (TNFα), platelet-derived growth factor (PDGF), interleukin 1β (IL-1β) and CCL2 contribute to stellate cell activation through direct binding of their receptors [71]. Macrophages also contribute to liver fibrogenesis through indirect mechanisms. For example, IL-1β produced by MoMF can contribute to hepatocellular fatty degeneration and hepatocellular injury [72], and reactive oxygen species, TNFα and PDGF secreted by Kupffer cells can initiate angiogenic processes in HSEC [73].

Other immune cells in hepatic fibrogenesis

A large number of other immune cells exist in the liver, whose complex interplay has a significant influence on hepatic fibrogenesis. The essential functions of these cells can only be briefly summarised here but are described in detail in recent review articles [52, 74].

Dendritic cells can be divided into conventional and plasmacytoid dendritic cells. The conventional dendritic cells are specialised antigen-presenting cells, and thus play an important mediating role between the innate and acquired immune systems. In the fibrotic liver, dendritic cells expand and take on both pro- and anti-fibrotic properties. The exact role of these cells in liver fibrosis is not yet fully understood [52].

Neutrophil granulocytes contribute to immune cell activation and recruitment via inflammatory cytokines. Furthermore, neutrophil granulocytes can induce a regenerative phenotype and thus regression processes in macrophages [52].

Mast cells represent only a small proportion of hepatic immune cells but expand in the chronically injured liver. Probably via the release of histamine, they drive inflammatory and fibrosis processes [52].

B- and T-lymphocytes play a role as classical effector cells of the adaptive immune response, especially in antigen-mediated diseases such as viral hepatitis or autoimmune liver diseases. However, other types of liver injury can also lead to a non-specific activation of the adaptive immune system, which is then directed against injured hepatocytes [52]. In liver fibrosis, a shift can be observed in the adaptive immune response towards a T_H2 and T_H17 helper cell response. This leads to an increased release of corresponding cytokines, especially IL-4, IL-13, IL-17 and IL-22, which are involved in the activation of HSCs and promote the secretion of extracellular matrix components [52].

Unconventional T cells make up a substantial proportion of the hepatic T lymphocyte population. Best described is the role of natural killer T cells (NKT cells), which are a very heterogeneous cell population that can support but also inhibit fibrotic processes depending on the specific immune environment and cell polarisation (T_H1 *vs* T_H2 response) [52, 74]. The mucosa-associated invariant T cells (MAIT cells), which represent a larger population in the human liver, also most likely play a dual role via the modulation of macrophage function [74].

Innate lymphoid cells (ILCs) are a heterogeneous group of cells composed of natural killer cells (NK cells) and various subpopulations of tissue-derived ILCs. Their exact role in liver fibrosis is still incompletely understood [74]. However, an anti-fibrotic role is usually attributed to them, mediated via the induction of HSC apoptosis and release of interferon gamma (IFNγ) [74].

Platelets

Platelets as the principal haemostatic cell type are amongst the first cells recruited to the liver in acute liver injury [75, 76] and increased numbers and aggregates of platelets have been reported in many different types of acute and chronic liver injury [77]. Aggregates of activated platelets in the liver can initiate the recruitment of leukocytes to the sinusoidal space and activate effector cells, thereby contributing to liver inflammation and tissue damage [78, 79], which has been studied in models of ischaemia-reperfusion, partial hepatectomy, as well as carbon tetrachloride (CCL_4)-induced liver fibrosis [80, 81]. Platelets are also involved in shaping macrophage phenotypes, as antiplatelet treatment modulates macrophage activation *in vitro*, and *in vivo* studies show a shift of Kupffer cell activation towards a more adaptive response and reductions in inflammatory MoMF [79]. Consequently, antiplatelet treatment or depletion of platelets has been shown to be hepatoprotective in models of viral hepatitis, ischaemia-reperfusion and thermal injury as well as models of acute and chronic cholestasis or MASH [79, 81].

1.2.3 Mechanisms of hepatic stellate cell activation and fibrogenesis

Hepatic myofibroblasts and their origins

HSCs are the main matrix-producing cells of the liver [82]. In the quiescent state, HSCs play an important role in the maintenance of tissue homeostasis as vitamin A-storing pericytes of the liver sinusoids [83]. Their activation by different molecules discussed below leads to the upregulation of type I collagens, α smooth muscle actin (αSMA), and tissue inhibitor of metalloproteinases (TIMPs) [71], and activated HSCs also express a number of inflammatory mediators involved in immune cell recruitment and activation [84]. Furthermore, these activated HSCs transdifferentiate into proliferative, migratory, and contractile myofibroblasts that migrate into fibrous tissue and contribute to scar contraction [83].

Recently, single cell sequencing experiments have revealed the heterogeneity of activated HSC populations [85]. While all populations share the expression of extracellular matrix proteins, they differ in their expression profile of inflammatory mediators. Furthermore, HSC show spatial and functional zonation associated with distinct marker expression profiles with central vein-associated *Adamtsl*^{high} HSCs being the main source of activated myofibroblasts in centrilobular hepatic injury [86]. In addition, a population of quiescent HSCs also exists in fibrotic and cirrhotic liver, which tend to have anti-inflammatory and anti-fibrotic roles via the production of growth factors and cytokines [87]. Overall, HSC populations are highly dynamic and can also revert from an activated to a quiescent state [88].

While HSCs are the major source of activated myofibroblasts in the liver, other fibrogenic cell populations are also discussed. Especially in the early phase of biliary fibrogenesis, portal fibroblasts are a major source of myofibroblasts, but tend to play a minor role in hepatotoxic diseases [89]. Another periportal mesenchymal cell population with stem cell properties and high proliferative potential also appears to be involved in the formation of fibrotic septa in various patterns of injury [90]. Controversially discussed in the literature, epithelial- and endothelial-to-mesenchymal transition as well as fibrocytes have been studied as potential sources of hepatic myofibroblasts [91].

Mechanisms of stellate cell activation

TGFβ is the most potent fibrogenic cytokine and is secreted in its latent form by various hepatic cell populations, particularly by migrating immune cells and by damaged hepatocytes [92]. Upon binding to its cellular receptors, TGFβ induces the transcription of type I and III collagens and the transdifferentiation into myofibroblasts via the canonical Smad2/3 pathway [93]. Furthermore, TGFβ participates in HSC activation via mitogen-activated protein kinase (MAPK), extracellular signal-regulated kinase (ERK), and c-Jun N-terminal kinase (JNK) [94]. Activated HSCs also produce TGFβ themselves, maintaining their own activation in a positive feedback loop [95]. PDGF, which is secreted predominantly by endothelial cells, macrophages, and activated HSCs, causes a proliferative and migratory response and thereby is involved in the induction of the myofibroblast phenotype [71]. Other classical HSC activators include the cytokines VEGF and connective tissue growth factor (CTGF), which also contribute to activation, proliferation, and extracellular matrix (ECM) production [96].

A number of other signalling pathways are involved in HSC activation, but will not be discussed in detail here due to space limitations. Of particular note are DAMPs and PAMPs, which act via activation of pattern recognition receptors (PRRs), such as Toll-like receptors [97], and extracellular vesicles released by damaged hepatocytes [98]. Cholesterol also plays an important role, particularly in metabolic liver disease. Free cholesterol leads to inflammasome activation leading to IL-1β release from liver macrophages [99] and also contributes directly to HSC activation [100]. Nuclear receptors, such as FXR, LXR, PPARγ, and PPARδ, are also expressed by HSCs and act as negative regulators of HSC activation [101]. In addition, HSCs interact closely with the extracellular matrix, particularly via integrins, and increased shear stress with increasing endothelial cell capillarisation and fibrosis leads to further fibrogenic activation [55].

Structural changes of the extracellular matrix

In the healthy liver, the Disse space is composed of loose interstitial connective tissue mainly composed of type I, III and V collagens as well as elastin and fibronectin, and a basement membrane-like matrix comprising laminins, type IV collagens, and various proteoglycans [55]. The normal composition and structure of this specialised extracellular matrix is essential for the function of the embedded liver cells. In the context of liver fibrosis, the deposition of fibrillar collagens, especially type I collagen,

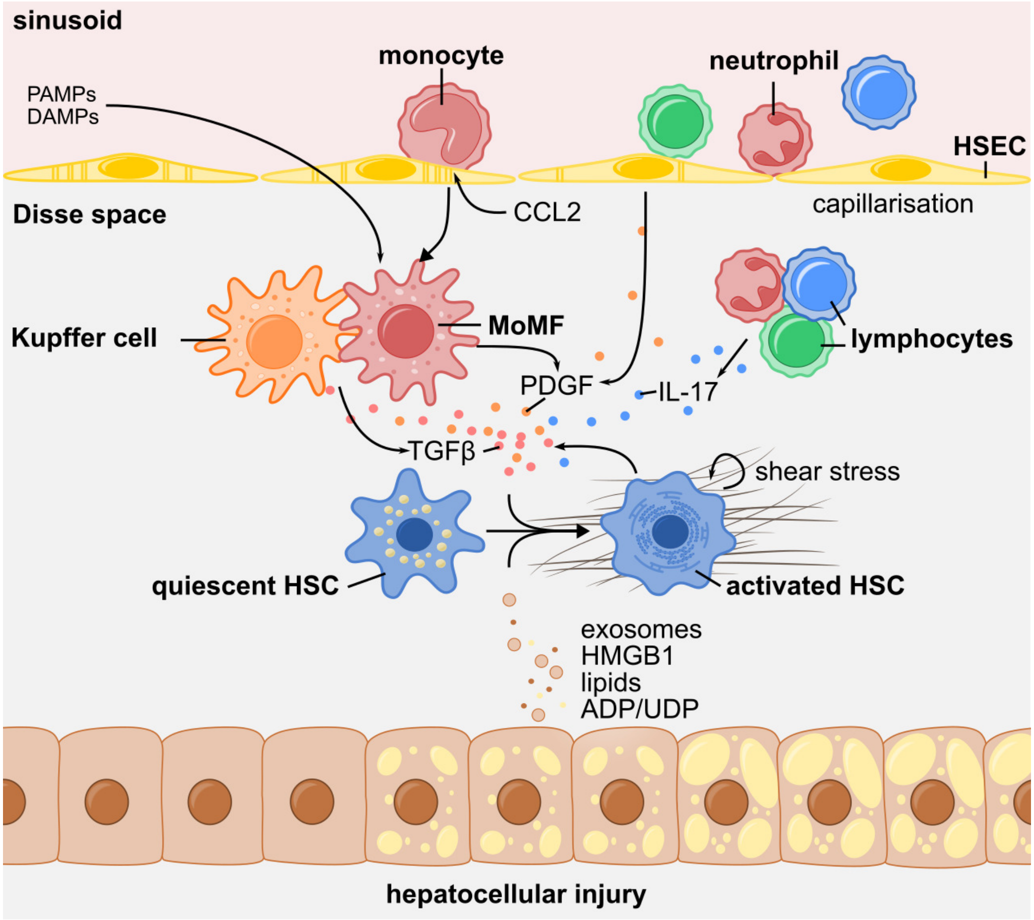

Figure 1.4: General mechanisms of liver fibrosis. HSCs as the principal matrix-producing cells in the liver are activated by a range of hepatic and extrahepatic signals. Injured hepatocytes secrete exosomes, DAMPs and lipid mediators, while infiltrating MoMFs and activated Kupffer cells secrete the fibrogenic mediators TGFβ and PDGF. Other leukocytes also produce fibrogenic cytokines, for example IL-17.
Abbreviations: ADP/UDP - adenosine diphosphate/uridine diphosphate, CCL2 - C-C motif ligand 2, DAMPs - damage-associated molecular patterns, HMGB1 - High-Mobility-Group-Protein B1, HSEC - hepatic sinusoidal endothelial cell, HSC - hepatic stellate cell, IL-17 - interleukin 17, MoMF - monocyte-derived macrophage, PAMPs - pathogen-associated molecular patterns, PDGF - platelet-derived growth factor, TGFβ - transforming growth factor beta
Originally published in Horn & Tacke, “Mechanismen Der Hepatischen Fibrogenese” [2], reproduced with kind permission from Springer.

results in a up to 10-fold increase in the abundance of extracellular matrix proteins [55]. Together with the cross-linking of these collagen fibrils by lysyl oxidases (LOX, LOXLs) and transglutaminase (TG), the density and stiffness of the extracellular matrix increases, which eventually contributes to a partial loss of function of hepatocytes and sinusoidal endothelial cells and to the maintenance of HSC activation [55]. As this process progresses, normal liver microarchitecture is eventually lost, resulting in an abnormal blood flow; a condition referred to as cirrhosis, ultimately leading to portal hypertension and its complications (Figure 1.5).

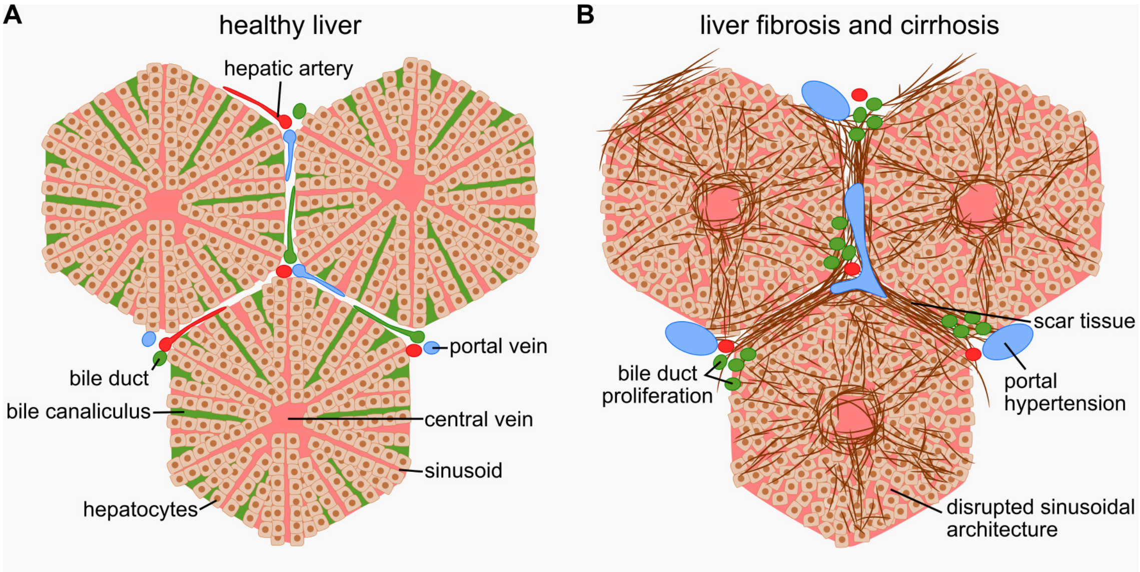

Figure 1.5: Disrupted liver architecture in fibrosis and cirrhosis. A. Healthy liver is characterised by a well-organised sinusoidal organisation of the liver lobule that allows for optimal blood flow and cellular function. **B.** In fibrosis and cirrhosis, deposition of scar tissue disrupts normal sinusoidal architecture, blood and bile flow, leading to loss of hepatocellular function, portal hypertension and proliferation of bile ducts. Originally published in Horn & Tacke, “Mechanismen Der Hepatischen Fibrogenese” [2], reproduced with kind permission from Springer.

1.2.4 General principles of fibrosis regression

The high regenerative potential of the liver has been known since ancient times. Impressively, liver fibrosis even at later stages has the capacity to regress, as observed in patients following successful hepatitis C virus (HCV) therapy or in patients with MASH after severe weight loss [33, 91]. As a result of the cessation of liver injury, the balance between matrix synthesis and degradation is shifted towards increased fibrolysis, resulting in reduced abundance of matix proteins and subsequent fibrosis resolution [102] (Figure 1.6).

Several processes can lead to decreased synthesis of extracellular matrix by hepatic myofibroblasts [91]. CD8$^+$ T cells, NK and NKT cells [103–105] and a reduction in fibrogenic signals including TGFβ and TIMPs [106, 107], induce apoptosis of activated HSCs and another proportion of HSCs inactivate to a quiescent phenotype [88], resulting in a lower abundance of matrix-producing cells. Furthermore, the regenerating liver is characterized by increased senescence of HSCs [108], which describes a state of cell cycle arrest with preserved metabolic activity [109]. Senescent HSCs secrete inflammatory cytokines, but at the same time exhibit decreased fibrogenic activation [110].

In addition to decreased synthesis and secretion of extracellular matrix, active fibrolytic processes are crucial for the regression of fibrosis. These are largely carried out by macrophages, which adopt a more restorative phenotype in the regenerating liver, characterised in part by increased secretion of matrix metalloproteinases (MMPs) [111]. These proteinases actively degrade the extracellular matrix, causing a reduction in scar tissue [112, 113]. This process is aided by the downregulation of MMP-inhibiting TIMPs in HSCs [114]. In addition, these restorative macrophages create an anti-inflammatory milieu, involving the secretion of IL-10, which inhibits inflammatory processes and thereby fibrogenesis [115].

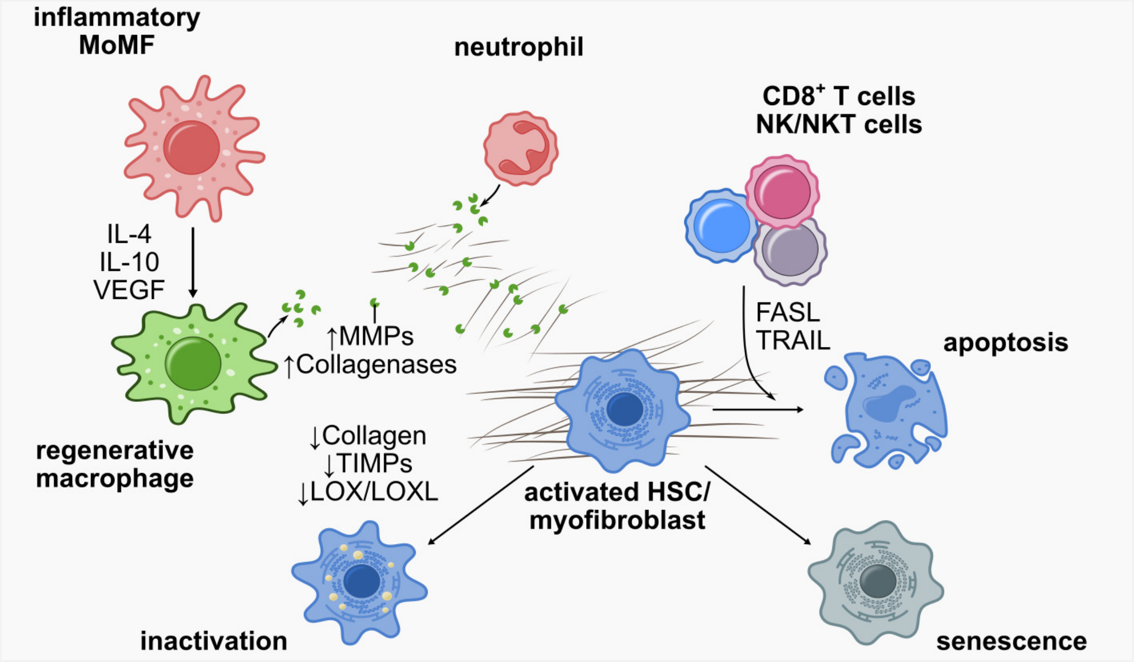

Figure 1.6: General mechanisms of liver fibrosis regression. Apoptosis, senescence and inactivation of activated HSC and myofibroblasts leads to a reduction in the number of matrix-producing cells. This leads to a decreased secretion of ECM components and cross-linking enzymes (LOX, LOXLs) and inhibitors of matrix proteineases (TIMPs). Simultaneously, regenerative macrophages and neutrophil granulocytes secrete matrix-degrading enzymes, including MMPs and collagenases. In sum, this leads to a net reduction in the abundance of extracellular matrix and to a functional regression of fibrosis.
Abbreviations: IL-4 - interleukin 4, IL-10 - interleukin 10, FASL - Fas ligand, HSC - hepatic stellate cell, LOX/LOXL - lysyl oxidase (like), MMP - matrix metalloproteinase, NK/NKT cells - natural killer/natural killer T cells, TIMPs - tissue inhibitors of matrix proteineases, TRAIL - TNF-related apoptosis-inducing ligand, VEGF - vascular endothelial growth factor.
Originally published in Horn & Tacke, "Mechanismen Der Hepatischen Fibrogenese" [2], reproduced with kind permission from Springer.

1.2.5 Therapeutic strategies targeting inflammation and fibrosis

Unfortunately, for many patients with chronic liver disease no sufficiently effective causal therapeutic options are available. Therefore, major efforts are currently underway to develop new therapies that directly target the underlying mechanisms of liver inflammation and fibrosis [116].

Blockade of the chemokine receptors CCR2 and CCR5 can inhibit the infiltration of inflammatory monocytes. While this strategy has been very effective in preclinical models, the phase 3 trial of the CCR2/CCR5 inhibitor cenicriviroc in patients with MASH has unfortunately been negative [117]. Modulation of nuclear receptors, such as FXR or PPAR, is also an interesting approach as it can shift the polarisation of macrophages towards a pro-resolution phenotype [118]. Promising compounds currently in clinical trials include FXR agonists such as obeticholic acid, cilofexor, tropifexor and others, and the pan-PPAR agonist lanifibranor [116]. However, the aforementioned therapeutic approaches have mainly been developed for patients with MASH. Although the basic features of liver inflammation and fibrosis are shared across different aetiologies of chronic liver disease, different mechanisms and cell populations are involved [52]. Therefore, alternative strategies tend to be pursued for other aetiologies where macrophages play a less significant role, such as targeting neutrophils in alcoholic liver disease [119] or T cell-directed therapies in viral and autoimmune hepatitis [120, 121].

Direct inhibition of HSC activation is an obvious therapeutic strategy to prevent fibrosis progression. However, attempts to inhibit TGFβ signalling as the main activator of

HSCs have failed due to the high side effect potential of systemic blockade [122]. Attempts are therefore currently being made to specifically modulate local TGFβ activity by blocking integrins [123]. Furthermore, activators of nuclear receptors in HSCs, such as FXR and PPAR agonists, are expected to have a direct antifibrotic effect [71]. In addition, cell therapies using regenerative differentiated macrophages and mesenchymal stromal cells are being tested in preclinical and early clinical trials and show promising anti-inflammatory and anti-fibrotic signals [124].

1.3 Bone morphogenetic protein signaling in liver fibrosis

1.3.1 The BMP signalling pathway

The TGFβ family of proteins consists of several subfamilies with similar structure and signalling properties, including the TGFβ subfamily, activins and inhibins, bone morphogenetic proteins (BMPs), left-right determination factors and a various group of other family members. Bone morphogenetic proteins are the largest subfamily, comprising more than 15 members in humans [125]. They are constitutively secreted and most members form homodimers although heterodimers have also been described [126]. BMPs were initially discovered as regulators of bone and cartilage formation [127, 128], embryonic development [129] and an array of other cellular functions [130].

BMPs bind to a hetero-tetrameric receptor complex comprised of Type I and Type II receptors, which upon BMP binding form a complex and initiate canonical and non-canonical signalling cascades. The canonical signalling pathway involves the phosphorylation and subsequent activation of the regulatory Smad proteins Smad

1, 5 and 8 which, upon complexing with the co-Smad Smad4, act as transcription factors driving the expression of genes involved in cell differentiation and survival. The activity on gene regulation largely depends on several DNA binding partners acting as co-activators and co-repressors and therefore downstream effects of BMP signalling are largely context-dependent [131]. Interestingly, some BMPs such as BMP2, BMP11 and BMP16 can also bind to TGFβ receptors and thereby signal through the fibrogenic Smad2/3 pathway [132]. Non-canonical signalling pathways involve Rho-, protein kinase C- and PI3K/AKT signalling which can induce various cellular responses depending on cell type and biological context [133].

1.3.2 The role of BMPs in liver health, inflammation and fibrosis

The role of BMPs in liver homeostasis is only incompletely understood. Best described are their roles in iron and glucose metabolism: BMPs 2, 4 and 6 upregulate hepatic hepcidin expression and thereby regulate circulating and hepatic iron levels while BMP9 maintains hepatic insulin sensitivity and glucose tolerance [134]. Furthermore, BMPs are differentially regulated in hepatic organogenesis and likely have a role in cell specification, although specific evidence is largely lacking [134]. Still, recent evidence showed that BMPs have an important role in providing and maintaining specific hepatic cell niches: HSC-derived BMP9/10 maintains normal Kupffer cell differentiation through activin receptor-like kinase 1 (ALK1) signalling, while a similar signalling network exists between endothelial cells and Kupffer cells through BMP2/6, though this has not been validated on a functional level [135]. Similar signalling

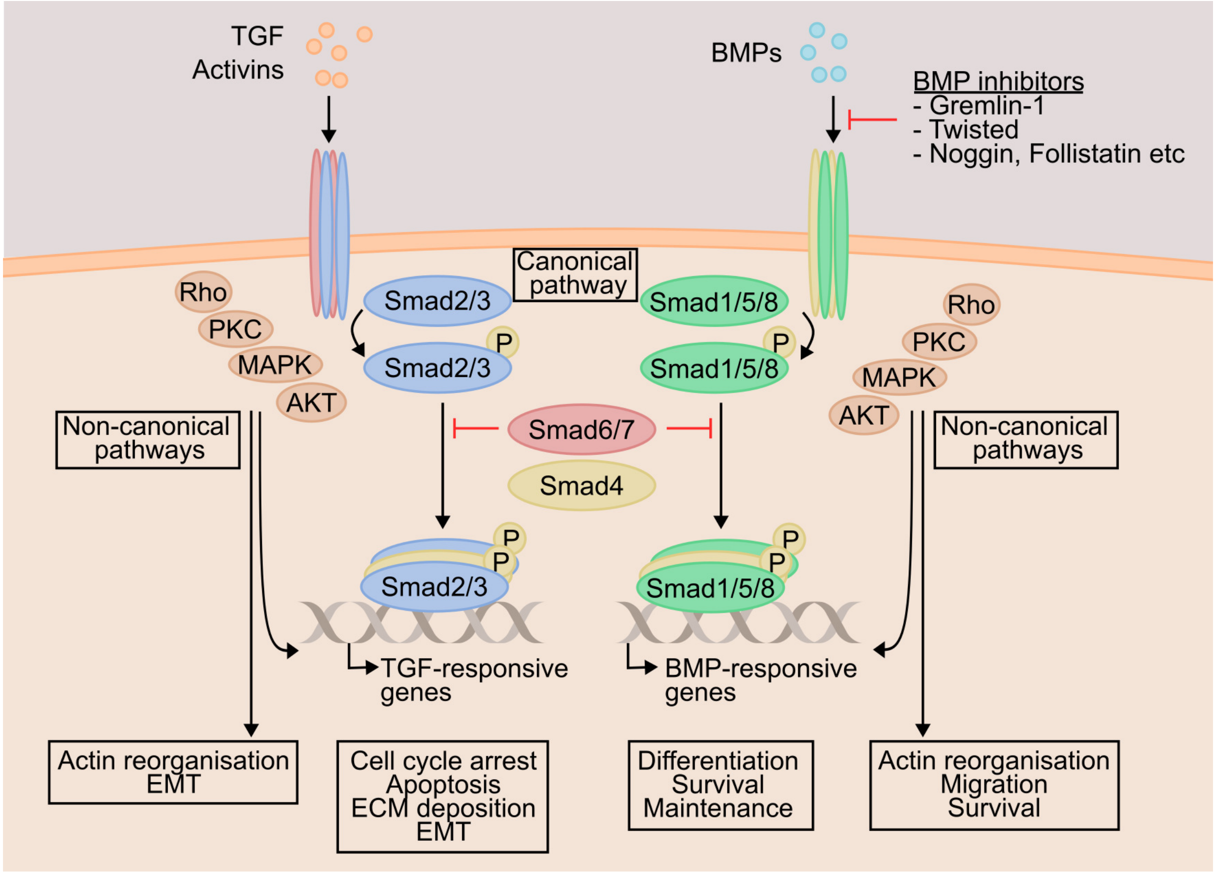

Figure 1.7: The TGFβ and BMP signalling pathway. (see text for details) Abbreviations: AKT - Akt serine/threonine kinase, BMP - bone morphogenetic protein, ECM - extracellular matrix, EMT - epithelial-to-mesenchymal transition, MAPK - mitogen-activated protein kinase, PKC - protein kinase C, TGF - transforming growth factor

networks may be involved in maintaining the quiescent HSC niche as endothelial cell-derived BMPs such as BMP7 are capable of suppressing HSC activation [136].

BMPs have an established role in several diseases, including renal fibrosis, atherosclerosis and pulmonary hypertension [137, 138]. Specific mechanisms, especially regarding fibrosis in chronic liver disease, are poorly understood although experimental evidence suggests a role of BMPs in liver regeneration in both acute and chronic liver injury. Importantly, different BMPs can have various effects on hepatic regenerative capacity: studies suggest that BMP4 and BMP9 reduce liver regeneration [139, 140], recombinant BMP7 can restore liver regeneration after partial hepatectomy [141] and BMP2 is important for hepatocyte differentiation of liver progenitor cells in chronic liver injury and thus may be involved in the regenerative process of the ductular reaction [142].

BMPs may play an essential role in the regulation of HSEC biology, with autocrine BMP2 signalling in HSEC upregulating pro-inflammatory gene expression [143]. This is probably mediated by an upregulation of nuclear factor ϰB (NF-ϰB) signalling which promotes TNFα-induced leukocyte adhesion, resulting in increased intercellular adhesion molecule 1 (ICAM1) and vascular cell adhesion molecule 1 (VCAM1) expression [144]. The pro-inflammatory effect of BMP2 on endothelial cells can be inhibited by BMP inhibitors like Noggin [143] or BMP modulators as BMP binding endothelial regulator (BMPER) [144]. Like BMP2, the structurally similar BMP4 can upregulate NF-ϰB signalling and ICAM1 expression in endothelial cells, thus promoting increased adhesion of monocytes in static adhesion assays [145]. Consequently, endothelial-specific knockout of BMP4 in mice reduces rolling and adhesion of leukocytes in response to TNFα [146]. Endothelial subsets however differ in their susceptibility to BMP2 and BMP4 signalling, as shown for BMP4 on rat carotid and pulmonary endothelial cells [145] and for BMP2 on HSEC and the vascular endothelial cell line HUVEC [143]. Whether BMPs 2 and 4 however regulate leukocyte recruitment in liver disease has not been studied yet. BMP7 and BMP9 might have a more adaptive role in the maintenance of sinusoidal endothelial function. BMP7 inhibits endothelial to mesenchymal transition of murine HSEC [147], which could contribute to the anti-fibrotic effects of BMP7 described below. BMP9 was identified as an important factor for the normal differentiation and maintenance of HSEC biology, with its deletion leading to capillarisation of the sinusoidal endothelium, liver inflammation and fibrosis, whereas treatment of HSEC with BMP9 *in vitro* restores HSEC fenestration in primary murine cell culture [148].

Evidence suggests a role of BMPs in hepatic fibrogenesis. Loss of Smad1/5/8 in mice, one of the central signalling molecules in canonical BMP receptor signaling, leads to severe iron overload and liver fibrosis [149]. Although circulating levels and hepatic gene expression of BMP7 increase with the progression of liver disease, and early findings supported a pro-fibrogenic role for BMP7 [150], more recent experimental data point towards a protective role of BMP7 in liver fibrosis where it represses fibrogenic gene expression in hepatic stellate cells *in vitro* in a Smad-dependent manner [136]. A role for BMP7 is supported by data indicating that the administration of recombinant BMP7 [151, 152] and the adenoviral overexpression of BMP7 [136] attenuate fibrosis in murine models. This might be mediated by direct effects on hepatic stellate cells, as overexpression of BMP7 can inhibit TGFβ-induced activation of HSCs in primary rat HSCs and the human HSC cell line LX-2 [136]. On the other hand, BMP4 exerts fibrogenic effects in a bile duct ligation model, mediated by Smad1 and ERK-MAPK pathways [153]. Similarly, overexpression of BMP9 leads to increased liver fibrosis [140], and paradoxically a complete knockout likewise results in HSC activation and liver fibrosis [148], suggesting the need for a tight regulation of BMPs in liver pathobiology. In murine dietary models of MASH specifically, BMP6 has a protective effect against liver inflammation and fibrosis as shown by knockout of BMP6 [154].

1.3.3 Intra- and extracellular modulators of BMP signalling

The activity of BMPs is regulated by several extracellular soluble BMP inhibitors and antagonists, including the Twisted gastrulation family, Chordin, Noggin, Follistatin and Follistatin-like proteins and the Dan family, including Gremlin-1 [133]. While most of these proteins show clear anti-BMP properties by inhibiting BMP binding to their receptors, interestingly, these modulators can have diverse functions by neutralising, solubilising and transporting BMPs [155]. For example, while Chordin and Twisted gastrulation in complex show anti-BMP behaviour, the latter can promote BMP signalling by preventing BMP proteins from extracellular matrix binding and maintaining them in solution [155]. Extracellular matrix proteins such as Collagens and BMPER can also interact with BMP proteins and modulate their activity [133].

A range of membrane-bound co-receptors and decoy receptors also modulate the activity of BMPs and their receptors. Co-receptors can serve to either increase or repress BMP receptor signalling, with prominent members including the dragon family (potentiating BMPs signalling [156]) or endoglin, which elicits inhibitory effects [157].

Decoy receptors such as BMP and activin membrane bound inhibitor (BAMBI), on the other hand, inhibit BMP signalling by competing with BMP receptors for ligand binding while lacking an intracellular signalling domain [158].

In summary, BMPs are involved in a number of physiological and pathophysiological processes of relevance for the development and progression of chronic liver disease. Therefore, BMPs and their signalling pathways represent potential therapeutic targets.

1.4 Gremlin-1

1.4.1 Structure and function

Gremlin-1 (GREM1) is a secreted protein comprising 184 amino acids, and was discovered in 1998 as a factor regulating embryonic patterning [159]. It belongs to the cystine-knot superfamily of proteins, along with proteins like TGFβ and vascular endothelial growth factor A (VEGFA) [160]. Gremlin-1 is secreted via the constitutive secretory pathway and exists in both glycosylated and non-glycosylated form, and in Western Blot after denaturing gel electrophoresis produces bands at 22 and 26 kDa for the non-glycosylated and glycosylated form, respectively [161]. Furthermore, Gremlin-1 can form homodimers by forming disulfide bonds between cysteine residues at position 141 [162].

Figure 1.8 gives an overview of the cellular sources, biological properties and functions of the Gremlin-1 protein. As a member of the Dan family of proteins, Gremlin-1 binds to BMPs 2, 4 and 7 and thereby inhibits their binding to BMP receptors [161]. The BMP-antagonistic function of Gremlin-1 is responsible for most of the Gremlin-1-

mediated effects described so far, although an increasing number of reports describe important functions mediated by modulating vascular endothelial growth factor receptor 2 (VEGFR2) [163] and antagonising monocyte migration inhibitory factor (MIF) [164]. The interaction of Gremlin-1 with VEGFR2 mediates pro-angiogenic responses [163], and is dependent on dimerisation of Gremlin-1 and its binding to heparin or heparan sulfate [162, 165], although the latter is not necessary for the interaction with BMPs [166–168]. Interestingly, recent studies also found that Gremlin-1 can bind to and neutralise TGFβ1 and thereby dampen fibrotic processes [169–171].

Under healthy conditions in humans and rodents, Gremlin-1 gene expression is high in the gastrointestinal tract, omental adipose tissue, lymph nodes and in the brain but low in liver [172]. Its important role in kidney development and bone formation is demonstrated by renal agenesis and deformed limbs caused by complete knockout of *Grem1* in mice, which is neonatally lethal [173]. Furthermore, knockdown in adult mice leads to intestinal and bone marrow failure, indicating a role for epithelial and stem cell regeneration [174]. Mainly mediated by its effect on VEGFR2, and probably independent of BMP signalling, dimeric Gremlin-1 mediates pro-angiogenic responses with implications for atherosclerosis and cancer development [163, 165, 175–177]. Importantly, Gremlin-1 is also involved in adipogenesis and mediates adipocyte dysfunction in hypertrophic adipose tissue by inhibiting BMP4 [172, 178, 179]. This likely plays a role in the development of diabetes mellitus type 2, where increased levels of Gremlin-1 have been observed [172, 180]. Not least, Gremlin-1 expression has been discovered in platelets, which store the protein in alpha-granules

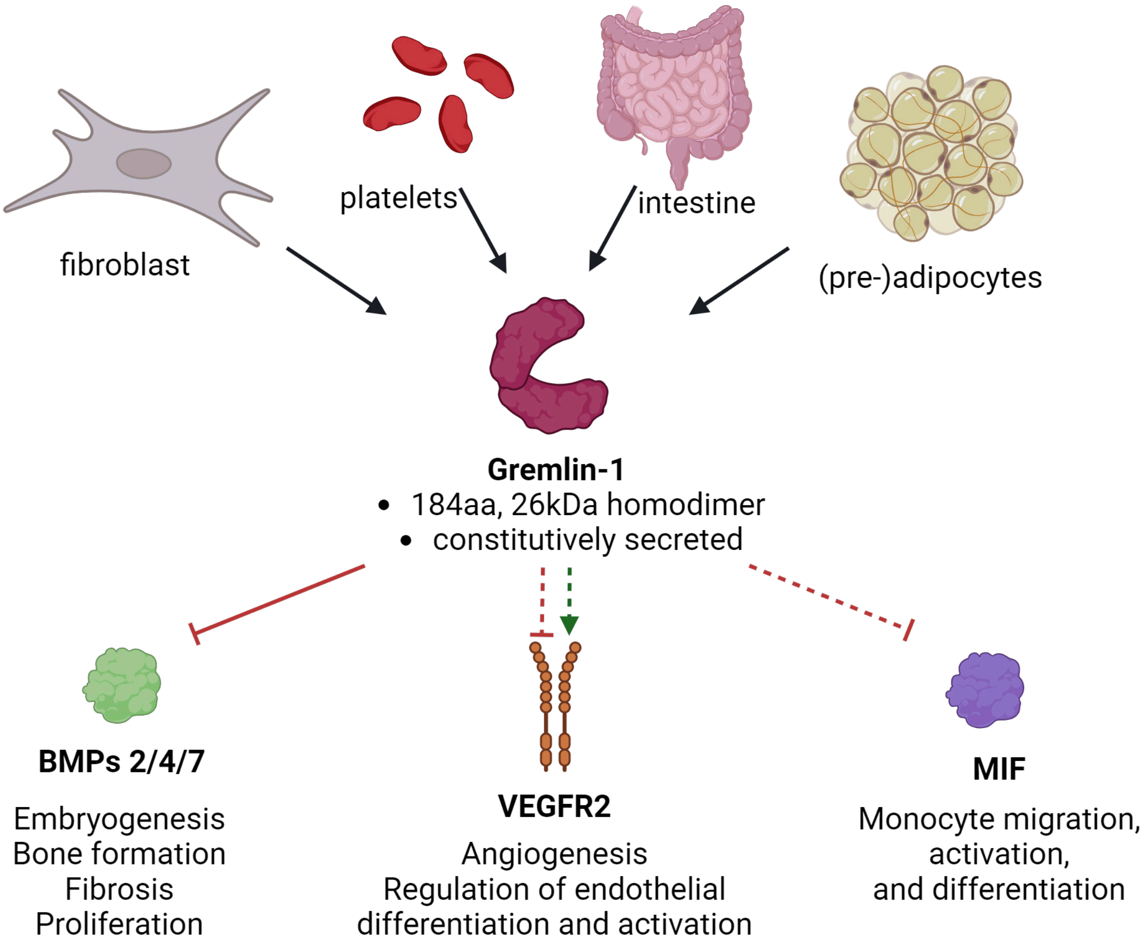

Figure 1.8: Overview of Gremlin-1 sources and putative biological functions. (see text for details)
Abbreviations: BMP - bone morphogenetic protein, MIF - macrophage migration inhibitory factor, VEGFR2 - vascular endothelial growth factor receptor 2.
Figure was created with BioRender.com.

and release Gremlin-1 upon activation [181], potentially mediating monocyte-mediated inflammation and macrophage activation in atherosclerotic plaques [164, 181–183].

1.4.2 Gremlin-1 in liver inflammation and fibrosis

Fibrosis is now accepted as the major determinant of prognosis in patients with chronic liver disease and MASLD in particular [16]. Indeed, although Gremlin-1 in the liver has not been studied in great detail yet, preliminary evidence supports a potential role for Gremlin-1 in liver fibrosis. BMPs and BMP antagonists like Gremlin-1 are believed to play a role in the induction of fibrogenic responses in fibroblasts and were therefore proposed as regulatory factors in organ fibrosis. While BMPs 2 and 4 can induce inflammatory processes as described above, BMP2/4 and 7 are thought to exert mainly anti-fibrotic functions in the liver by interfering with the TGFβ signalling pathway, while their inhibition by BMP antagonists like Gremlin 1 consequently would lead to a shift of the balance towards a pro-fibrotic state [133]. Indeed, Gremlin-1 is highly expressed in fibroblasts in different organs, including skin, lung, kidney and pancreas, and expression in those organs increases with the presence and progression of fibrosis [173, 184, 185]. In intestinal fibrosis, Gremlin-1 promotes fibroblast proliferation and activation through increased fatty acid oxidation mediated by VEGFR2/MAPK signalling [186] and has thereby been identified as a promising therapeutic target.

Despite Gremlin-1 being expressed at very low or undetectable levels under healthy conditions in human (GSE3526, [172]) and rodent liver [187], mRNA expression has been described to increase in fibrotic liver, as seen in *Mdr2*$^{-/-}$ mice (a model of cholestatic liver disease) fed a cholate containing diet [187] and porcine serum-induced murine liver fibrosis [188]. This increase in hepatic Gremlin-1 expression is thought to be mainly attributable to activation of HSCs, with human HSC-derived myofibroblasts showing increased Gremlin-1 expression compared to quiescent and early activated HSC [187, 189]. Similarly in mice, Gremlin-1 expression is much higher in portal fibroblasts than in activated HSCs in both bile duct ligation and CCL_4 models of liver fibrosis [89]. This increase of Gremlin-1 expression with progression of fibrosis at both the cellular and organ level implies a potential role for Gremlin-1 in hepatic fibrogenesis, and indeed, there is some evidence that Gremlin-1 promotes liver fibrosis. This has been shown by decreased TGFβ signalling and liver fibrosis markers upon down-regulation of hepatic Gremlin-1 following lentiviral transfection of animals with Gremlin-1 siRNA in a rat CCL_4 model [190]. Similarly *in vitro*, Gremlin-1 overexpression in HSC cell culture models promotes the expression of pro-fibrogenic marker genes, whilst siRNA-mediated down-regulation of Gremlin-1 leads to decreased expression of these activation markers [188, 190]. Recent clinical data show that Gremlin-1 gene expression is associated with liver fibrosis in subjects with diabetes and MASLD, further supporting a role for Gremlin-1 in liver fibrosis in this disease [180]. The same group found that Gremlin-1 promotes hepatocellular senescence, which could promote liver fibrosis through the YAP/TAZ pathway [191]. On the other hand, Gremlin-1 can bind and inactivate TGFβ1, which has been shown to inhibit fibrotic processes in the heart [169] and connective tissue [170]. The exact role of Gremlin-1 in liver fibrosis and its suitability as a therapeutic target remains undefined.

1.5 Follistatin-like 3

1.5.1 Structure, regulation and function

Follistatin-like 3 (FSTL3) is a 263 amino acid protein with a molecular weight of 27.6 kDa and belongs to the group of follistatin-like proteins, which are secreted proteins characterised by cysteine-rich follistatin domains [192]. It was first described as a gene overexpressed in certain kinds of B-cell leukemia and is expressed in various adult tissues with tight regulation during embryogenesis [193].

FSTL3 shares high sequence similarities with Follistatin and as such avidly binds and inactivates activins, myostatin [194], and to a lesser degree some BMPs including BMP2 [195]. FSTL3 plays an important role in whole body energy metabolism, as demonstrated by knockdown studies on FSTL3, which leads to increased insulin production, glucose tolerance and a reduction in visceral adipose tissue mass and insulin sensitivity [196]. Additional physiological functions include bone formation and bone strengthening, mainly mediated by anti-resorptive effects on osteoclasts through ADAM12 [197] and repression of the BMP antagonists SOST, which inhibits bone formation through inhibiting Wnt signalling [198], as well as regulation of haematopoiesis, stem cell differentation and placenta development [192].

Mainly mediated through its inhibitory effects on activin A, FSTL3 is thought to promote cardiac hypertrophy [199] and cardiomyocyte-produced FSTL3 can induce fibroblast activation and production of extracellular matrix [200] which is attenuated by FSTL3 knockout [199]. FSTL3 also shapes macrophage function, as shown for atherosclerosis, where it promotes foam cell formation through increased lipid uptake and inflammatory gene expression [201]. Furthermore, FSTL3 has been implicated in a range of malignant tumours and plays a role in tumour cell proliferation and metastasis [192].

1.5.2 Follistatin-like 3 in liver inflammation and fibrosis

Evidence for a role of FSTL3 in liver inflammation and fibrosis is lacking. FSTL3 expression is increased in human MASLD and MASH livers but shows no correlation with the stage of fibrosis [202]. Knockout of FSTL3 leads to liver steatosis in mice, probably mediated by increased insulin sensitivity and upregulation of *de novo* lipogenic genes [196, 203]. Furthermore, overexpression of FSTL3 leads to reduced hepatocellular lipid accumulation [204], which further supports a role in hepatic steatosis. Therefore, by reducing hepatocellular steatosis, FSTL3 could potentially attenuate MASLD/MASH disease progression.

On the other hand, little evidence exists on FSTL3 and processes of liver inflammation and fibrosis. The structurally related FSTL1 has been implicated in HSC activation, liver inflammation and fibrosis in several murine models of liver disease [205, 206] and some indirect evidence suggests a role for FSTL3 in hepatic fibrogenesis: the FSTL3 target myostatin promotes fibrotic responses in the HSC cell line LX-2, and activin A, the main target of FSTL3, promotes HSC activation through SMAD2/3 signalling on stellate cells directly and through induction of an inflammatory phenotype on macrophages [207–209]. The aforementioned fibrogenic effects of FSTL3 on cardiac fibroblasts however would support a pro-fibrotic role of FSTL3 in chronic liver disease [200]. Therefore, while the literature suggests an involvement of FSTL3 in liver fibrosis, be it pro- or anti-fibrotic, its exact role still needs to be defined.

1.6 Hypothesis and Aims

Chronic liver diseases - and liver fibrosis as the main prognostic determinant - pose increasing global health care challenges. Currently, no licenced pharmacological treatment options are available to directly target hepatic inflammation or fibrogenesis. Evidence suggests that Gremlin-1 might be involved in hepatic stellate cell activation and thereby promote the progression of chronic liver disease. However, the therapeutic potential of blocking Gremlin-1 has not been studied yet.

Therefore, we hypothesised that Gremlin-1 is upregulated in MASH fibrosis and promotes hepatic fibrogenic pathways in chronic liver disease. Furthermore, we hypothesise that blocking Gremlin-1 ameliorates the inflammatory and fibrotic response in humans and animal models of liver fibrosis.

The aims of this project were as follows:

1. To assess the expression profile of Gremlin-1 across different aetiologies of liver disease and stages of disease.
2. To identify the main hepatic cell types expressing Gremlin-1.
3. To characterise the effects of Gremlin-1 and anti-Gremlin-1 treatment on hepatic stellate cell activation *in vitro* and hepatic inflammatory and fibrotic processes *in vivo* and *ex vivo*.

4. To characterise the role of Gremlin-1 on hepatic sinusoidal endothelial cell activation, leukocyte recruitment and the differentiation of monocyte-derived macrophages.

5. To identify common transcriptional signatures in activated hepatic stellate cells and human liver fibrosis in order to identify and validate potential novel therapeutic targets.

CHAPTER 2

MATERIALS AND METHODS

2.1 Ethics

All work on human tissue and blood conformed with the Human Tissue Act and studies were approved by the local ethics review board (Immune regulation, 06/Q2702/61 and 04/Q2708/41; Inflammation, 18-WA-0214; Fibrosis, 19-WA-0139). Tissue samples were taken from explanted diseased livers of patients undergoing liver transplantation for end-stage liver disease of different aetiology (metabolic dysfunction-associated steatotic liver disease (MASLD)/metabolic dysfunction-associated steatohepatitis (MASH), alcohol-related liver disease (ArLD), primary biliary cholangitis (PBC), primary sclerosing cholangitis (PSC)) or donor livers from organ donors that were not deemed suitable for transplantation after organ retrieval. Blood samples for cell isolation were taken from patients with hereditary hemochromatosis undergoing venesection for iron overload or healthy volunteers. Human tissue and blood samples for detection of Gremlin-1 mRNA by *in situ* hybridisation or circulating Gremlin-1 protein by luminescent oxygen channelling immunoassay (LOCI) were collected as part of the Fatty Liver Disease in Nordic Countries (FLINC) study (Clinicaltrials.gov, NCT04340817). All patients or their legal representatives gave informed written consent prior to all procedures.

2.2 Cell culture

2.2.1 Hepatic biliary epithelial cells, hepatic sinusoidal endothelial cells and hepatic myofibroblasts

Biliary epithelial cells (BECs), hepatic sinusoidal endothelial cells (HSECs) and hepatic myofibroblasts (MFs) were isolated as established in our research group, based on previous work from the institute [210]. A slice of liver of approximately five to ten millimetre thickness was taken from explanted diseased liver or donor liver not suitable for transplantation (Ethics see 2.1). The liver slice was processed after a maximum storage time of 24 hours in Dulbecco's Modified Eagle Medium (DMEM) (11500416, Gibco) at 4 °C. After mincing the tissue, 20 mL of phosphate-buffered saline (PBS) (137 mM NaCl, 2.7 mM KCl, 8.1 mM $Na_2HPO_4 \cdot 2H_2O$, 1.47 mM KH_2PO_4 , pH=7.4) and a 5 mL aliquot of collagenase (10 mg/mL, C9891-500mg, Sigma-Aldrich) were added to the tissue homogenate and incubated at 37 °C for 25 to 45 minutes, depending on the texture of the liver tissue. The resulting digest was then filtered through a fine mesh and the volume topped up to 200 mL with sterile PBS, followed by three washing steps with PBS and centrifugation at 900xg at room temperature for 5 minutes. Subsequently, the cells underwent gradient centrifugation at 900xg for 25 minutes at room temperature without brake over a 77 %-33 % Percoll (GE17-0891-01, Sigma-Aldrich) gradient in 15 mL conical tubes (Corning). The cells at the interface were collected and washed two times in PBS at 900xg for 5 minutes at room temperature.

These centrifugation and washing steps were followed by a stepwise positive magnetic bead selection to isolate BEC and HSEC. For isolation of BEC, the pellet was incubated with 50 µL of anti-epithelial cell adhesion molecule (EpCAM) mouse monoclonal antibody (10 µg/mL, clone HEA125, 61004, Progen) in 500 µL PBS at 37 °C for 30 minutes under constant agitation. Subsequently, cells were washed and incubated with 10 µL cold anti-mouse-IgG-coupled magnetic beads (11041, Invitrogen) in 500 µL PBS for 30 minutes at 4 °C under constant agitation. Following the addition of 6 mL of ice-cold PBS, the tube was placed in a magnet and the supernatant removed and transferred into a new 15 mL conical tube. The procedure was repeated once again and the EpCAM$^+$ cells were resuspended in BEC media (Table 2.1) and seeded onto collagen-coated tissue culture flasks. BEC were not used in this thesis and given to other researchers at the institute.

The conical tube containing supernatant from BEC isolation was then placed in a magnet to remove residual beads and cells were spun-down at 900xg for 5 minutes at room temperature. The supernatant was removed and cells were resuspended in 500 µL cold PBS containing 10 µL anti-CD31-conjugated magnetic beads (11155D, Invitrogen), followed by a 30 minutes incubation at 4 °C with constant agitation. The positive selection of CD31$^+$ cells was performed as for BEC isolation and the HEA125$^-$CD31$^-$ supernatant was collected for MF culture. CD31$^+$ HSEC were recovered from the magnet and resuspended in HSEC medium (Table 2.1) and plated on a collagen-coated tissue culture flask. Finally, the supernatant from HSEC isolation was placed in a magnet to remove residual beads and cells were spun down at 900xg for 5 minutes at room temperature. The pellet was then resuspended in fibroblast culture medium (Table 2.1) and the cells seeded on a uncoated plastic tissue culture flask.

HSEC were grown in full HSEC medium (Table 2.1) on collagen-coated polystyrene culture flasks until 90% confluent and subcultured at a 1:4 ratio using Gibco TrypLE Express Enzyme (12605010, Fisher Scientific) for cell dissociation. MFs were grown in full fibroblast medium (Table 2.1) on uncoated polystyrene culture flasks until 90% confluent and subcultured at a 1:3 ratio using Gibco TrypLE Express Enzyme for cell dissociation. Both HSEC and MF were used up to passage 5.

Table 2.1: Composition of culture media

BEC	HSEC	Fibroblast
DMEM/F12	Human endothelial SFM	DMEM
10 % HS	10 % HS	16 % FCS
100 U/mL PS	100 U/mL PSG	100 U/mL PSG
2 mM L-Glutamine	10 ng/mL HGF	
10 ng/mL EGF	10 ng/mL VEGF	
2 mg/mL Hydrocortisone		
10 ng/mL Choleratoxin		
2 nM Triiodo-thyronine		
0.124 U/mL Insulin		
5 ng/mL HGF		
10 ng/mL VEGF		

Abbreviations: DMEM - Dulbecco's Modified Eagle Medium, EGF - epidermal growth factor, FCS - fetal calf serum, HGF - hepatocyte growth factor, HS - human serum, PS(G) - penicillin-streptomycin(-glutamine), SFM - serum-free medium, VEGF - vascular endothelial growth factor

2.2.2 LX-2 cells, primary human hepatic stellate cells and HepG2

LX-2 cells were purchased from Merck (SCC064, Merck KGaA, Germany), reconstituted and cultured according to the distributor's instructions. Cells were subcultured at a 1:3 to 1:6 ratio using Gibco TrypLE Express Enzyme for cell dissociation. Only LX-2 cells up to a passage number of 15 were used for experiments. For cell culture experiments, LX-2 cells were seeded at a density of $25x10^3$ cells/cm^2 in 2% fetal calf serum (FCS), 1% Penicillin-Streptomycin-L-Glutamine (PSG) (10378016, FisherScientific Ltd) in Gibco DMEM (high-glucose, containing pyruvate, 10313021, FisherScientific Ltd) on uncoated polystyrene cell culture multiwell plates. Cells were grown to adhere over 24 hours and serum-starved in 0.2% FCS medium (containing PSG) for another 24 hours before changing medium to treatment conditions in 0.2% FCS medium.

Primary human hepatic stellate cell (HHSC) isolated from adult healthy donors were purchased from Caltag Medsystems Ltd (IXC-10HU-210, Lot numbers: 300075-7, 300079-1, 300080-1). Cells were grown in 10% FCS, 1% PSG (10378016, FisherScientific Ltd) in DMEM (high-glucose, containing pyruvate, 10313021, FisherScientific) and subcultured in a 1:4 ratio using Gibco TrypLE Express Enzyme (12605010, Fisher Scientific) for cell dissociation. HHSC were used up to a passage number of 3 (parent cells) or 4 (lentivirally transduced cells). For cell culture experiments, HHSC were seeded at a density of $7.5x10^3$ cells/cm^2 in 10% FCS, 1% PSG in Gibco DMEM (high-glucose, containing pyruvate, 10313021, FisherScientific) on uncoated polystyrene cell culture multiwell plates. Cells were grown to adhere over 24 hours and serum-starved in 2% FCS medium (containing PSG) for another 24 hours before changing medium to treatment conditions in 2% FCS medium.

HepG2 cells are a human hepatoma cell line and were purchased from ECACC (#85011430). Cells were grown in 10% FCS and 1% PSG in DMEM on uncoated polystyrene cell culture flasks and subcultured in a 1:6 ratio using Gibco TrypLE Express Enzyme. For experiments, cells were seeded at a density of $25x10^3$ cells/cm^2 in full culture medium on uncoated polystyrene cell culture plates. All cell culture experiments on HepG2 cells were performed in full culture medium without serum starvation.

All cells were grown and maintained in cell culture incubators at 37°C in a 5% CO_2 atmosphere.

2.2.3 Peripheral blood mononuclear cells

Peripheral blood mononuclear cells (PBMC) were isolated from venesection blood from patients with haemochromatosis or from healthy volunteers, i.e. healthy researchers in the institute who consented to give blood for research (Ethics see 2.1) using an established protocol [211]. Blood was anticoagulated with ethylenediaminetetraacetic acid (EDTA) and processed immediately. Lymphoprep^{TM} (Stemcell technologies) was used as density gradient medium and 15 mL were aliquoted in each 50 mL conical tube. After diluting blood 1:1 in 0.1% BSA in PBS (PBSA), 30 mL of diluted blood was carefully layered on top of Lymphoprep^{TM} and centrifuged at 800xg for 20 minutes at room temperature without brake. The top layer containing plasma was carefully removed and the band of cells, consisting of PBMC, at the interface collected into new 50 mL conical tubes. To remove residual plasma, medium and contaminating platelets, PBMCs were washed three times in 0.1% PBSA at 150xg for 10 minutes at room temperature. Cells were then counted using a Neubauer haemocytometer and resuspended in medium at a density depending on subsequent procedures.

2.2.4 Monocyte-derived macrophages

For monocyte-derived macrophage experiments, PBMCs were isolated as described above (2.2.3). Cell density was adjusted to $5\text{x}10^6$ cells per mL of culture medium (Table 2.2) and 2 mL of cell suspension (=10 million cells) were seeded into each well of a 6-well plate. PBMCs were then incubated on plastic for 2 hours at 37°C and 5 % CO_2 to allow for monocytes to adhere. The plate was then vigorously swirled and washed three times with 2 mL sterile PBS to remove non-adherent non-monocytic cells. After this step, all remaining cells were assumed to be monocytes.

Differentiation into macrophages was achieved by adding 2 mL of macrophage activation medium (Table 2.2) per well and subsequent incubation at 37°C and 5 % CO_2 for five days. On day five, medium was replaced with macrophage stimulation medium (Table 2.2) containing different additives, depending on the specific experiment, and incubated for another two days before harvesting cells and supernatants for analysis.

Table 2.2: Composition of monocyte and macrophage culture media

monocyte medium	macrophage activation	macrophage stimulation
RPMI	RPMI	RPMI
10 % FCS	10 % FCS	10 % FCS
1 % PSG	1 % PSG	1 % PSG
	5 ng/mL M-CSF	25 ng/mL M-CSF
		additives (e.g. LPS, IFNy, IL-4)

Abbreviations: FCS - fetal calf serum, IFNγ - interferon gamma, IL-4 - interleukin 4, LPS - lipopolysaccharide, M-CSF - macrophage colony-stimulating factor, PSG - penicillin-streptomycin-glutamine, RPMI - Roswell Park Memorial Institute Medium

2.2.5 Washed human platelets

Platelets were isolated from human blood with a protocol modified from Cazenave *et al* [212]. The blood was obtained from patients with haemochromatosis undergoing venesection for iron overload (Ethics see 2.1). Blood was anticoagulated with a citrate-dextrose solution (C3821, Sigma-Aldrich) in a ratio of 1:9, i.e. 50 mL for one blood bag. After collection, blood was transferred into 50 mL conical bottom tubes (Corning) and centrifuged at 250xg at room temperature and without brake for 16 minutes. Only the upper two thirds of the platelet-rich plasma on top of the resulting layers were taken and transferred into a new 50 mL conical bottom tube (Corning). After adding 0.5 µL/mL prostaglandin I_2 (PGI_2) (1 mM, P6188, Sigma-Aldrich) to avoid platelet activation, the blood was incubated at 37°C for 10 minutes. Before centrifugation of the platelet-rich plasma at 2,200xg at room temperature for 16 minutes, a further 0.5 µL/mL PGI_2 were added. The resulting supernatant was decanted, making sure no visible traces of plasma remained. The pellet was gently resuspended in modified Tyrode's albumin solution (NaCl 136.5 mM, KCl 2.7 mM, $NaHCO_3$ 11.9 mM, NaH_2PO_4 0.43 mM, HEPES

5 mM, Glucose 5.5 mM, bovine serum albumin (BSA) 0.35 %), followed by the addition of 2 µL/mL heparin (5000 U/mL, H3149-25KU, Sigma-Aldrich) and 0.5 µL/mL PGI_2, then washing in Tyrode's albumin solution and 0.5 µM PGI_2 two times at 1,900xg for 8 minutes at room temperature. Prior to the final centrifugation step, platelets were counted using a Neubauer haemocytometer and the resulting pellet was resuspended in DMEM with the platelet count adjusted to 300×10^6/mL. Platelet lysates were obtained by repeated freeze-thaw cycles and sonication.

2.3 Stimulation of platelets and flow cytometry

Washed platelets were stimulated with different known platelet activators in order to generate activated platelet supernatant (aPS) for treatment of cells in subsequent studies. Platelets at a concentration of 300×10^6 cells/mL were dispensed in seven sterile 15 mL conical tubes and treated with either thrombin (BML-SE363-1000, Enzo Life Sciences, Inc.), adenosine-diphosphate (ADP) (HB-5502-FG, Hart Biologicals Limited) or arachidonic acid (AA) (HB-5506-FG, Hart Biologicals Limited) at different concentrations or without any activating compound (buffer, unstimulated platelet supernatant (uPS)) and incubated for up to 30 minutes with intermittent agitation. After 5, 15 and 30 minutes, samples were taken for subsequent analyses. In order to create uPS and aPS, 1 mL of platelet suspension of each tube was decanted after 5, 15 and 30 minutes and transferred into 1.5 mL microtubes. Subsequently, platelet suspensions were pelleted at 13,000xg for 20 minutes at 4 °C and aliquoted in new 1.5 mL microtubes for subsequent analyses and assays. For flow cytometry, 100 µL of stimulated platelet suspension were fixed in 1% paraformaldehyde (PFA) in PBS for 30 to 60 minutes at room temperature and washed two times with 2% FCS in PBS to remove fixative. Platelets were then stained with PE-conjugated anti-CD41 antibody (303705, BioLegend), FITC-conjugated anti-CD62P antibody (4293603, BDBiosciences) or the respective isotype control antibodies PE mouse IgG1$_\kappa$ (400111, Biolegend) and FITC rat IgG1$_\lambda$ (4293603, BDBiosciences), at 1:50 dilution for 30 minutes at room temperature in the dark. Subsequently, platelets were washed two times with 2 mL 2% FCS in PBS and resuspended in a final volume of 1 mL 2% FCS in PBS before finally being analysed on a CyAN^{TM} ADP Analyser (Beckman-Coulter).

2.4 Precision-cut liver slices

To study the effects of interventions targeted at Gremlin-1 in a human *ex vivo* liver model, we used the method of precision-cut liver slices (PCLS) as described previously [213]. Cylinders of liver tissue were prepared by taking biopsies from resection or explant livers using a disposable 8 mm skin biopsy punch blade (ACCU-Punch, EMS). These cylinders were subsequently embedded in 3 % low-melt Agarose (A9414, Sigma) in phenol-free Hank's Buffered Salt Solution (HBSS, 14175095, Gibco) and cut into 250 µm sections using a vibratome (VT1200S, Leica biosystems). Next, the slices were equilibrated in pre-warmed full PCLS culture medium (Table 2.3) at 37°C for one hour, and meanwhile, treatment conditions were prepared in PCLS culture medium. Treatment solutions were then added at 1.5 mL per well into a 12-well plate containing 3 µm transwell inserts (GD665631, SLS). Finally, one piece of PCLS was transferred into the insert in each respective well and the plates were incubated for 24 hours on a rocker at 37°C in a humidified atmosphere containing 5 % CO_2, shaking at a frequency of 20/min.

Table 2.3: Composition of PCLS culture medium

Williams E medium
2 % FCS
100 U/mL PS
2 mM L-Glutamine
1X Insulin-Transferrin-Selenium (ITS-G)
100 nM dexamethasone

Abbreviations: FCS - fetal calf serum, PS - penicillin-streptomycin

2.5 Animal experiments

All animal experiments were performed by Novo Nordisk, Maalov, Denmark and were approved by The Danish Animal Experiments Inspectorate using permission 2017-15-0201-01215. Male, 8-10 weeks old Sprague Dawley rats (n=130, Janvier Labs, France) were fed a choline-deficient, L-amino acid defined, 1% cholesterol, high-fat diet (CDAA-HFD) (A16092003, Research Diets Inc, New Brunswick, New Jersey) for the duration of 12 weeks, with weekly subcutaneous administration of 25, 2.5, 1 or 0.25 mg/kg of NNC0502-2021 heparin-displacing or 25, 2.5, or 1 mg/kg NNC0502-0361 non heparin-displacing antibody during weeks 6 to 12. The first dose was administered as a double dose to increase time spent at steady state drug exposure. In the isotype control group, isotype human IgG1.1 antibody was administered at a dose of 25 mg/kg. A separate group of animals was fed control chow diet (n=5, chow, Altromin 1324, Brogaarden, Lynge, Denmark) for the duration of the study without any antibody treatment. After 6 weeks of dosing, animals were sacrificed in a fed state 6 days post last dose, and plasma and tissue were collected for analysis. Plasma was collected by sublingual sampling two days before drug administration for the first two weeks, as well as two days after drug administration throughout duration of the study. Liver enzymes alanine aminotransferase (ALT) and aspartate aminotransferase (AST) in plasma were quantified according to manufacturer's instructions on the Cobas C501 machine (Roche Diagnostics, Basel, Switzerland).

2.6 Lentiviral overexpression of GREM1

2.6.1 Construction of the lentiviral vector for GREM1 overexpression

Lentiviral transduction is a suitable and well-established model for stable overexpression of transcripts and proteins in both cell lines and primary cells [214]. We used a replication-deficient recombinant second generation lentivirus and cloned the coding sequence for Gremlin-1 (Origene, Cat-No RC210835) into the plasmid pWPI (kindly provided by Roy Bicknell at University of Birmingham), also containing the coding sequence for the enhanced green fluorescent protein (eGFP). In the following, this plasmid will be referred to as Gremlin-1 (GREM1)-pWPI. The pWPI plasmid including the sequence for eGFP but lacking the GREM1 insert (green fluorescent protein (GFP)-pWPI) was used to generate an empty vector control in subsequent experiments (GFP-control). Figure 2.1 gives an overview of the cloning steps for production of the GREM1-pWPI plasmid.

GFP-only control and GREM1 lentiviruses were produced by transfecting HEK293T cells with Lipofectamine 3000 (L3000001, Invitrogen) in OptiMEM (31985070, Gibco)

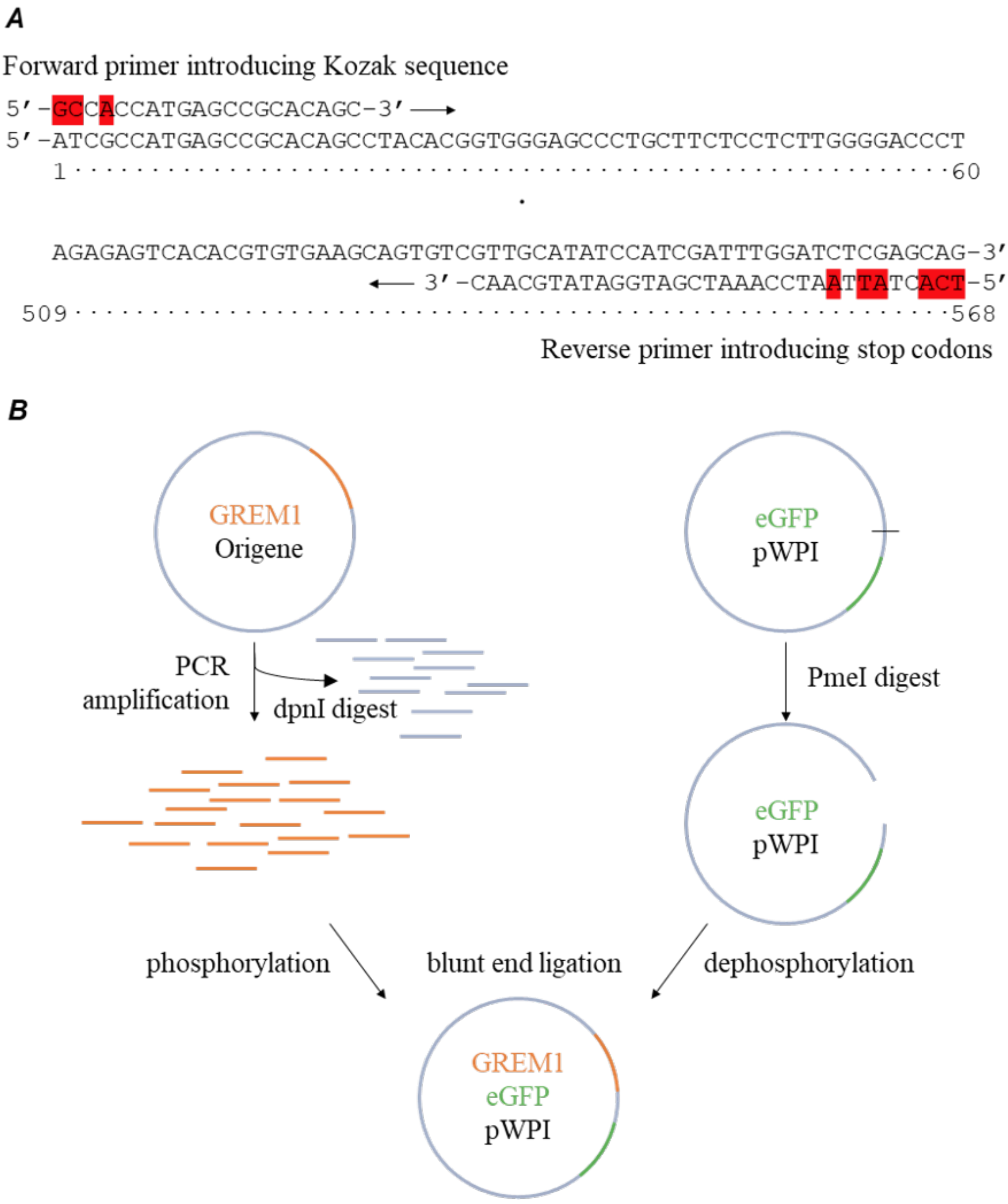

Figure 2.1: Cloning of the GREM1-pWPI plasmid. A The Gremlin-1 sequence was modified by using mismatching primers to introduce a more efficient Kozak sequence for optimal overexpression and introducing stop codons. Mismatched primer bases are highlighted in red. **B** Simplified schematic for cloning of the GREM1-pWPI plasmid. First, the modified GREM1 sequence was amplified by polymerase chain reaction (PCR) using the aforementioned primers followed by digesting the remaining plasmids with the restriction enzyme DpnI and 5'phosphorylation of the amplified inserts. To prepare the plasmid pWPI for insertion of the GREM1 encoding fragment the plasmid was digested with PmeI, followed by de-phosphorylation to prevent backbone re-ligation in subsequent steps. Finally, the GREM1 inserts were co-incubated with the PmeI-digested pWPI plasmids in the presence of DNA ligase before transforming competent E. coli and Sanger sequencing (Source Bioscience) to confirm correct orientation of the insert and the fidelity of the polymerase reaction (not shown).

containing 14.4 µg GFP-pWPI or GREM1-pWPI, 8.33 µg psPAX2 - providing the lentiviral replication function - and 2.63 µg pMD2.G - for pseudotyping with the VSV-G, enabling cell entry of the virus into mammalian cells. Supernatants were collected on the two days following transfection and concentrated by density gradient centrifugation on 10% sucrose. The concentrated pseudovirus particles were aliquoted and stored at -80°C. Human cell lines and primary cells were transduced by incubation with 5 µL of the GREM1 or GFP-control virus per 100,000 cells in full growth media. Lentivirally transduced LX-2 cells were sub-cultured until confluent before being sorted on the BD FACSAria^{TM} (BD Biosciences) to obtain cells with top 10 % highest eGFP expression. No sorting was performed on lentivirally transduced primary cells due to limitations in cell numbers and long-term culture.

2.6.2 DNA gel electrophoresis

Agarose gel electrophoresis was performed to verify the correct size of oligonucleotides and linearised plasmid during cloning procedures. 2 g of agarose were added to 100 mL of Bionic^{TM} Buffer (Sigma) and brought to the boil in a microwave. The 2 % agarose solution was then cooled on ice before adding 10 µL of 10,000X SYBR Safe (S33102, Invitrogen) and mixing well. The gel was then poured onto the gel chamber and a comb was inserted. After leaving the gel to solidify, 5 µL of 100bp or 1kb DNA ladder (N0551S and N3232L, New England Biolabs) and samples diluted 1:5 in Gel Loading Dye (B7021S, New England Biolabs) were pipetted into the wells. The gel was then run on 100 V for two hours before being imaged imaging on a ChemiDoc Imaging station (ChemiDoc MP, BioRad, UK).

2.6.3 Validation of GREM1 overexpression

A combination of different methods was used to verify transduction and GREM1 overexpression. Transduction with both the GFP-control and GREM1 lentivirus should lead to production of eGFP by the cells, which can be detected by fluorescent microscopy and flow cytometry. Cells were visually checked for successful transduction by inspection under an inverted fluorescent microscope. For flow cytometry, cells were detached and suspended in FACS buffer (PBS + 2 % FCS + 1 mM EDTA) and filtered through a 70 µm sterile nylon mesh before being analysed on a flow cytometer (CyAn^{TM} ADP Analyzer, Beckman Coulter or BD FACSAria^{TM}). Cells with a fluorescence intensity higher than that of non-transduced cells were identified as expressing eGFP and the percentage of positive cells was calculated. In addition, quantitative polymerase chain reaction (PCR) was performed to check for overexpression of the GREM1 insert (see section 2.10.2b).

2.7 Functional assays

2.7.1 Flow-based adhesion assays

Flow-based adhesion assays are a standard method in our group for the *in vitro* study of the interaction between HSEC and leukocytes under conditions of laminar flow and were performed according to established standard protocols [215]. HSEC were seeded at a density of 60,000 cells per channel in 6 channel µ-slides with a growth area of 0.6 cm^2 per channel (µ-Slide VI 0.4, IbidiTreat, Ibidi), pre-coated with rat-tail collagen type I (C3867, Sigma). Complete HSEC medium was used for growing cells in slides for 24 to 48 hours. When monolayers reached 90 % confluency, medium was changed to serum-free medium, i.e. complete HSEC medium without serum, with or without additional treatment conditions and incubated for additional 24 hours with a medium change after 20 hours with the addition of 10 ng/mL tumor necrosis factor alpha (TNFα, 300-01A, Peprotech) or vehicle control.

The setup for flow-based adhesion assays is shown in figure 2.2 and consisted of a thermostatically controlled transparent chamber with an inverted microscope, an electronic solenoid valve, silicone tubing and a syringe driver holding a 50 mL glass syringe. Prior to the assay, the chamber was pre-heated to 37°C and the tubing system including the valve was flushed with sterile distilled water making sure no air bubbles were remaining in the system. A 50 mL glass syringe was then pre-filled with 10 mL distilled water, connected to 25 cm tubing and inserted into the syringe driver set to re-fill with a rate of 0.28 mL/min to generate physiological shear-stress of 0.05 Pa. Next, 2.5 mL and 5 mL syringes with the plunger removed were connected to the inflow valves to flow either cells or wash buffer, respectively. A length (12 cm) of silicone tubing was connected to the outflow valve to connect to the Ibidi slides.

The silicone tubing of both the outflow and syringe tubing were connected to the ports of the channel on the Ibidi slide to be analysed making sure no air bubbles were in the system. The channel was then washed with washing buffer to remove debris while checking integrity of the monolayer under the microscope. Next, PBMCs were pipetted into the 2.5 mL syringe and the solenoid valve switched to flowing cells for 5 minutes before switching back to washing buffer. After washing the channel for 3 minutes with washing buffer, videos were recorded for ten fields of view for ten seconds each. In order to prevent recording cells more than once, the microscope objective was moved against the direction of flow for all assays [215].

Counting of cells was performed in Fiji ImageJ with the plugin CellCounter (Kurt De Vos, University of Sheffield, GNU General Public License) after taking snapshots of the recorded videos. Videos were viewed in parallel to distinguish flowing and rolling cells from adherent cells. Cells were identified as either rolling or firmly adherent, with the latter being divided in round adherent, activated shape-changed and transmigrated cells. Figure 2.2 gives an example of different stages of cell adhesion and transmigration. Light and dark shape-changed cells were both summarised as shape-changed cells.

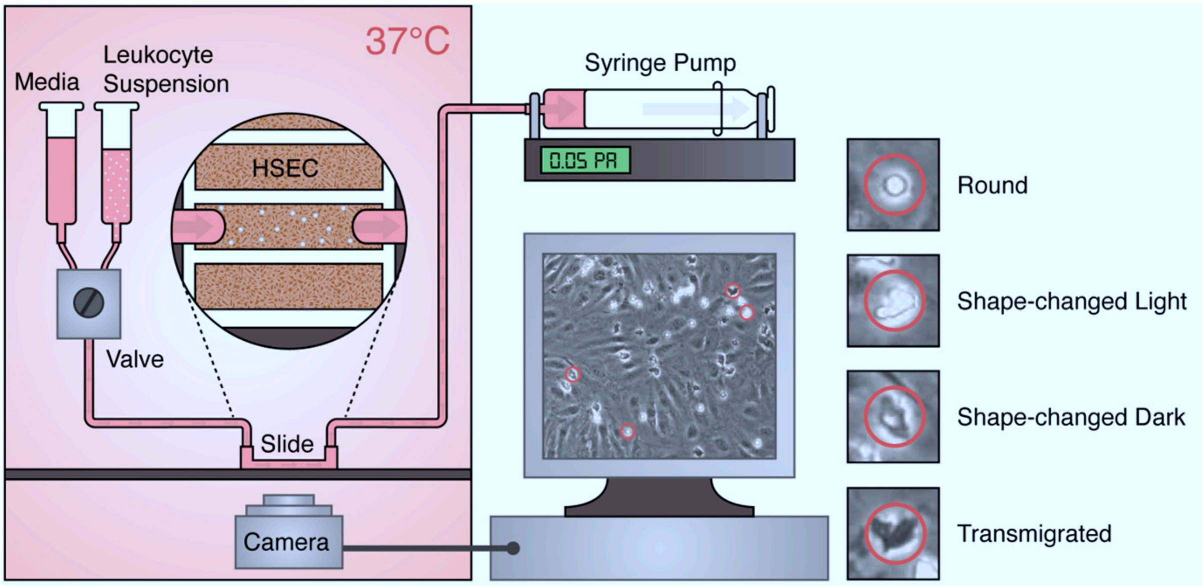

Figure 2.2: Technical set-up for flow-based adhesion assays (courtesy of Joseph Tickle [216])

2.7.2 Collagen contraction assays

Later in the process of activation, hepatic stellate cells transdifferentiate into myofibroblast-like cells, which are characterised by a contractile and extracellular matrix (ECM)-producing phenotype. Cellular contraction and remodelling of the ECM can be assessed using collagen contraction assays, by quantifying the size reduction of a collagen cushion over time [217].

LX-2 cells were detached with TripLE and resuspended in serum-free growth medium at a concentration of $3x10^5$ cells/mL. Bovine collagen (A1064401, Thermo Fisher) was diluted to a concentration of 3 mg/mL in ice-cold sterile PBS, and 200 µL of this solution were added for every 400 µL of cell suspension. Due to its acidity, which is required to keep collagen in solution, a yellow discolouration of the culture medium could be observed. To adjust the pH to physiologic levels, 6 µL of 1 M NaOH solution were added immediately and mixed well, being careful to avoid the formation of bubbles. Correct pH was confirmed using pH indicator paper. Next, 500 µL per well of the resulting cell-collagen-suspension were added to a 24 well plate and kept in a 37 °C incubator for a minimum of 20 minutes to allow the collagen to solidify. During incubation, treatment conditions were prepared in culture medium with increased serum content (e.g. 4 % FCS in DMEM for LX-2), and after the collagen cushions were released with the help of a 10 µL pipette tip, 500 µL of treatment solution were added per well. Finally, the plates were imaged every 24 hours for up to five days using the ChemiDoc Imaging station (ChemiDoc MP, BioRad, UK).

2.7.3 Scratch wound assays

Hepatic stellate cells acquire a migratory phenotype upon activation, which enables cells to migrate into tissue sites of injury. Scratch wound assays are an easy and often-used method to assess cell migration *in vitro* [218].

Cells were seeded into wells of a 24-well plate and grown until confluent. To prevent cell proliferation from influencing the results, assays were performed in reduced serum conditions (0.5 % FCS for LX-2 and 2 % FCS for myofibroblasts), unless specified otherwise. Optionally, cells were pretreated as specified in the results section, before applying a vertical scratch wound using a 200 µm pipette tip. To prevent cells from re-attaching to the wound area, wells were washed twice in PBS before replacing media with treatment conditions.

Subsequently, cells were imaged using the CelliQ Live Cell Imager for up to 72 hours and the width of the scratch wound was quantified using a custom-made ImageJ plugin modified from Suarez-Arnedo et al [219] (for the code see Appendix A.4). In brief, images were pre-processed by applying a Gaussian blur filter, enhancing contrast and filtering on the variance of intensity values before binarising the image. Based on the binarised image, the wound width was measured as the sum of the largest two cell-free areas, if the second-largest cell-free area was at least 30 % the size of the largest one.

Next, a 4-parametric Gompertz curve was fitted to the change in wound width over time and the first derivative of this function yielded the wound closure rate.

2.7.4 Lipid uptake assay

Preparation of fatty acid treatment complexes

Treating cells with fatty acids requires the fatty acids to be solubilised in the aqueous cell culture media. In human blood plasma, free fatty acids are mainly bound to albumin, facilitating fatty acid transport despite their hydrophobicity. To mimic physiologic conditions, free fatty acid-BSA complexes were prepared in a 5:1 molar ratio. Firstly, 100 mM solutions of palmitic acid (PA) and oleic acid (OA) were prepared by incubating the required amount of fatty acid solid in 1 mL of a 0.1 M NaOH solution at 70°C on a heating block until fatty acids were completely dissolved. 0.89 mL of fatty acid solution was then - while still at 70°C - quickly added to a 14.4 % solution of fatty acid-free BSA (A8806-5G, Sigma) in PBS. To prepare a vehicle control solution without fatty acids, 0.89 mL of saline were added instead of the fatty acid solution. Subsequently, the 10 mM fatty acid-BSA complex solutions were incubated for 30 min at 37°C with constant agitation. The PA solution partially precipitated, resulting in a cloudy appearance and thus was additionally sonicated for 15 min in a sonicator water bath, bringing the PA back into solution and binding to BSA. This procedure resulted in 10 mM stock solutions of PA or OA in 13.3 % BSA in PBS. Stock solutions were aliquoted and stored at -20°C.

Cell culture and siRNA knockdown

HepG2 cells were trypsinised using TrypLE (12605010, Gibco) and reconstituted at a concentration of 1×10^5 cells/mL in full culture medium. Meanwhile siRNA mixes of follistatin-like 3 (FSTL3) siRNA (FlexiTube GeneSolution for FSTL3, SI03019247, Quiagen) or negative control siRNA (1027310, Quiagen) were prepared in serum-free OptiMEM (31985070, Gibco) and HiPerfect transfection reagent (301705, Quiagen) at a concentration of 30 nM, vortexed for 10 seconds and incubated for 10 minutes at room temperature. 20 µL of this mix were pipetted into each well of an imaging 96-well microplate, followed by addition of 1×10^4 cells in 100 µL. Plates were then swirled to evenly mix transfection complexes and cells. After incubation for 24 h at 37°C in a humidified 5 % CO_2 atmosphere, cells were treated with 100 ng/mL Activin A (130-115-013, Miltenyi Biotec) or PBS vehicle control in full culture medium. On the next day, positive control wells were treated with PA:OA 0.2:0.4 mM solution or BSA vehicle control in full culture medium and incubated for 24 h to allow lipid accumulation. Next, Cells were treated with PA:OA 0.2:0.4 mM solution or BSA with 1X LipidTox Deep Red neutral lipid stain (H34477, Invitrogen) in full culture medium and plates were imaged on a ZEISS Celldiscoverer 7 automated live cell imager using a 20X objective. Deep red fluorescence was acquired using an Ex/Em 625 nm/660:760 nm filter set and phase gradient images were taken for gaussian curvature analysis.

Quantification of lipid uptake

For quantification of lipid uptake in HepG2 cells, we programmed ImageJ scripts for measuring fluorescence positive area and lipid area based on Gaussian curvature analysis. The full scripts can be found in the appendix (Appendix A.5 and A.6).

Figure 2.3 gives an outline of the principal image analysis pipeline for the quantification of lipid uptake. We used two separate methods: firstly, quantification based on the Gaussian curvature and secondly based on the fluorescent signal from LipidTox DeepRed stain.

Both methods had in common that the cell area was defined by applying a variance filter on the phase gradient image (Figure 2.3A and B) followed by thresholding to obtained a binarised image (Figure 2.3C) which was used as a mask for calculating cell-positive areas with the fluorescence and Gaussian method. The Gaussian curvature is the product of the principal curvature, which can be calculated as the eigenvalues of the Hessian matrix. The Hessian matrix was obtained from the phase gradient images and multiplying the smallest (Figure 2.3D) and largest (Figure 2.3E) Hessian eigenvalues (i.e. the principal curvature), resulted in the Gaussian curvature matrix (Figure 2.3F). By thresholding on this image we defined the Gaussian curvature-positive area. For quantification of lipid content based on fluorescence (Figure 2.3G) we first removed the background (Figure 2.3H), before applying a threshold to define the fluorescence-positive area (Figure 2.3I).

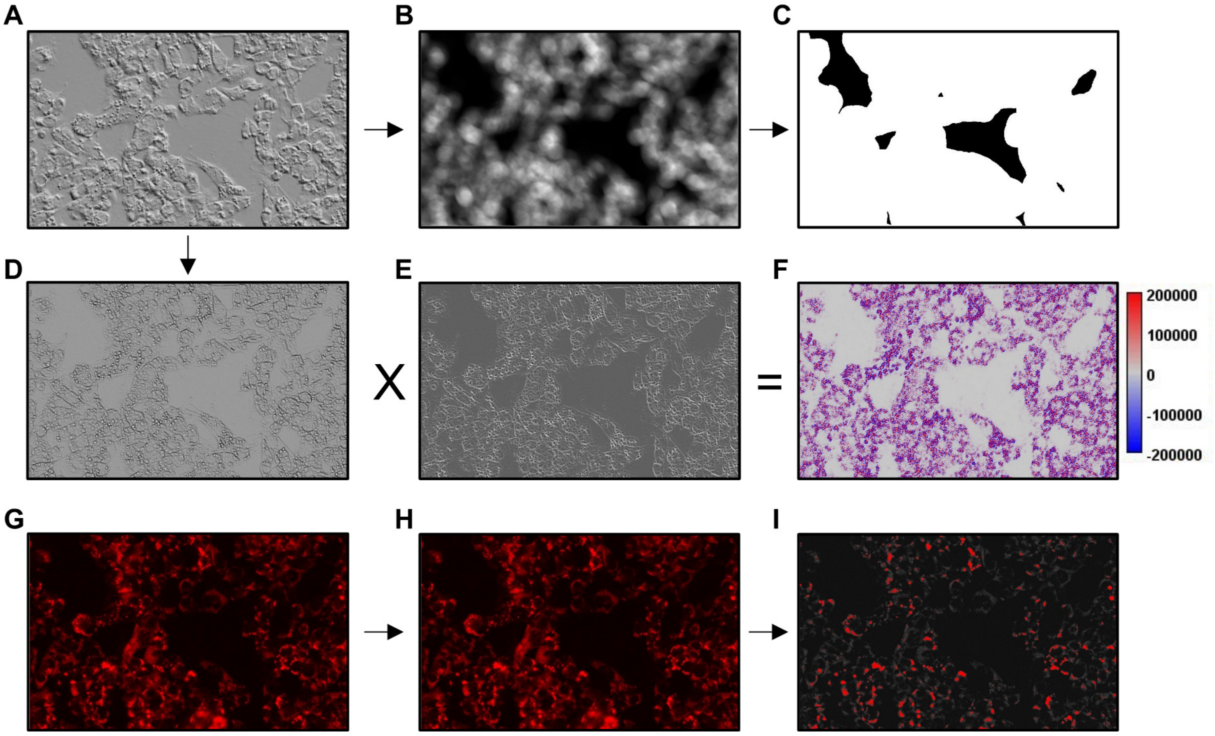

Figure 2.3: Workflow of lipid uptake quantification. Phase gradient images **(A.)** underwent a variance filter **(B.)** and thresholding based on the variance of intensity values resulted in a binarised image defining the cell-positive area **(C.)**. For identification of small ellipsoid structures in the phase gradient image, representing lipid droplets, we calculated the Hessian eigenvalues from the curvature of intensity values. By multiplying the smallest **(D.)** and the largest **(E.)** eigenvalues for each point, we obtained a matrix of Gaussian curvature **(F.)**, which here is colour-coded in blue and red. Highly positive values (red) indicate the presence of ellipsoid structures, while highly negative values (blue) indicate hyperbolic structures. Gaussian curvature-positive area was defined by thresholding. For identification of fluorescence-positive area, we used LipidTox DeepRed **(G.)**, and after background removal **(H.)** applied a threshold to obtain the positive area **(I.)**.

2.8 Generation and characterisation of anti-Gremlin-1 antibodies

All data for characterisation of the anti-Gremlin-1 antibodies and respective protein biophysics data were derived from Novo Nordisk, including SMAD1 phosphorylation in LX-2 cells, C2C12/BRE-Luc reporter gene assay, heparin fluorescence polarisation assay, size-exclusion chromatography and Gremlin-1 cell association assay. All these methods as well as the methodology for generation of the therapeutic anti-Gremlin-1 antibodies are described in detail in the respective publication [220].

2.9 Protein quantification

2.9.1 Enzyme-linked immunosorbent assays

The Human GREM1 enzyme-linked immunosorbent assay (ELISA) Kit (EKH4238, Nordic Biosite), Human Albumin ELISA Kit (E88-129, Bethyl Laboratories) and Human CXCL4/PF4 Quantikine ELISA Kit (DPF40, R&D systems) were used to measure concentrations of Gremlin-1, albumin or CXCL4 proteins in human biosamples according to manufacturer's instructions and all samples were measured in duplicate. Absorbance readings were acquired at 450 nm and 570 nm using a plate reader (Synergy HT, BioTek). The specific absorbance values at 450 nm were corrected for optical impurities by subtracting absorbance values at 570 nm. A standard curve was created by fitting the corrected absorbance values to a four-parametric log-logistic curve using the R package `drc`[221] (for an example see fig. 2.4).

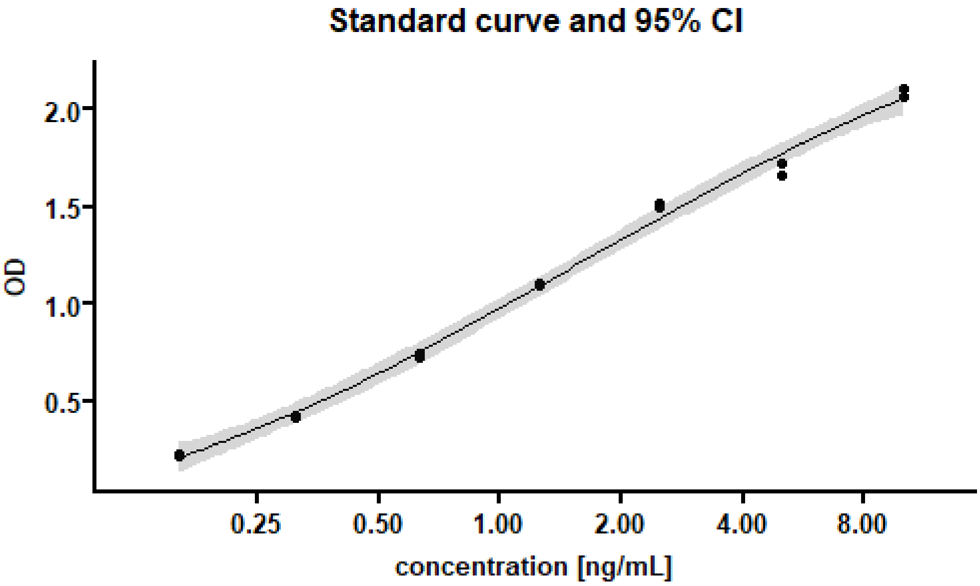

Figure 2.4: Example for an ELISA standard curve. Dots show the raw data points and the line the fitted four-parameter log-logistic curve. The grey area represents the 95 % confidence interval.

2.9.2 Luminescent oxygen channelling immunoassay

Luminescent oxygen channeling immunoassay (LOCI) were performed by our collaboration partner Novo Nordisk and based on anti-gremlin monoclonal antibody pairs generated at Novo Nordisk A/S, Denmark. Acceptor beads were directly coupled to antibodies while streptavidin coated donor beads were used in combination with biotinylated antibodies. Recombinant human gremlin-1 protein, Novo Nordisk A/S, China, was used as calibrator material and positive control. Briefly, a mixture of the conjugated acceptor beads and the biotinylated antibodies were produced to a final concentration of 33.3 µg/mL and 0.75 µg/mL, respectively. In a 384 well assay plate, 15 µL of the mixture were added to 5 µL of plasma sample and incubated for 1 hour at room temperature (RT) in the dark. Next, 30 µL of donor beads (67 µg/mL) were added to each sample and the plate was incubated for 30 min at RT. Addition of donor beads was performed in a green-light room to avoid bleaching. The samples were analysed on a PerkinElmer Envision instrument. All samples were measured in duplicates.

2.9.3 Cell-based ELISA

Cell-based ELISA provide a means for measuring protein abundance in cultured cells. The general principle is that cells are cultured in cell culture multiwell plates and after undergoing different treatment conditions are fixed and stained with antibodies against proteins of interest. Similar to a standard sandwich ELISA, the primary antibody is then detected using a secondary horseradish peroxidase (HRP)-conjugated antibody and subsequent chromogenic detection on a plate reader. The following gives a more detailed account of the assay performed for this thesis:

First, 96-well plates were coated with rat tail collagen, followed by seeding of primary HSEC at a density of 10,000 cells/well in a volume of 100 µL standard HSEC medium (see Table 2.1) using a multichannel pipette and a sterile reservoir. Cells were then incubated for 24 hours, when cells reached approximately 90 % confluence. Subsequently cells were dosed in duplicate with different concentrations of TNFα, recombinant human Gremlin-1 (not published, Novo Nordisk A/S) or vehicle control in full HSEC medium and incubated for 24 hours. After treatment, wells were washed with 100 µL/well sterile PBS and subsequently fixed in 100 µL/well ice-cold methanol for 10 minutes, before washing three times again with PBS. Fixed and washed plates were kept sterile and stored at 4°C until further processing.

On the day of the analysis, PBS was removed from each well and plates were washed two times with 50 µL/well of washing buffer (0.1 % BSA in PBS). Then, 50 µL/well of blocking buffer (2 % goat serum in PBS) were added and incubated for 45 minutes at room temperature on a plate shaker at low speed. Plates were washed three times with 50 µL/well of PBS before adding 50 µL/well of primary antibody raised against intercellular adhesion molecule 1 (ICAM1) (BBA3, R&Dsystems), vascular cell adhesion molecule 1 (VCAM1) (BBA5, R&Dsystems), CD31 (JC70A, Dako) or mouse IgG1 isotype control (MAB002, R&Dsystems) antibody at a final concentration of 2 µg/mL in PBS. After incubation at room temperature for 45 minutes on a plate shaker at low speed, the plate was washed with PBS and 50 µL/well of goat anti-mouse IgG-HRP (P0447, Dako) secondary antibody solution at a concentration of 0.8 µg/mL in PBS were added and the plate incubated for 45 minutes at room temperature on a plate shaker at low speed. During incubation, substrate buffer was prepared by adding 2 OPD tablets (Dako) to 6 mL sterile distilled water using a plastic forceps and vortexing to allow tablets to completely dissolve. Next, the plate was washed again three times with PBS and 2.5 µL of 30 % H_2O_2 were added to the substrate buffer. The substrate buffer was added to each well at 50 µL/well and incubated at room temperature for up to 10 minutes protected from light. Here, the development of yellow colour denoted a positive result. Finally, the reaction was stopped by adding 50 µL/well of 0.5 M H_2SO_4, resulting in a colour change, and the results read on a multiwell plate reader at a wavelength of 490 nm.

2.9.4 AST activity assay

Aspartate aminotransferase (AST) activity was measured in supernatants from human PCLS by colorimetric activity assay (701640, Cayman Chemical) according to manufacturer's instructions on a absorbance micro-well plate reader (Synergy HT, BioTek).

2.10 Gene expression analysis

2.10.1 RNA isolation and Reverse Transcription

For isolation of RNA from cells, cells were washed twice with ice-cold PBS before being lysed in 350-700 µL Buffer RLT (79216, QIAgen, Germany) containing 1 % β-mercaptoethanol. Subsequently, RNA was extracted with the RNeasy Mini Kit or RNeasy Micro Kit (74104 and 74004, respectively, QIAgen, Germany), following manufacturer's instructions, including on-column DNA digestion (RNase-Free DNase Set, 79254, QIAGEN). RNA concentrations were then determined on a spectrophotometer (NanoPhotometer Classic, Implen) and the RNA transcribed to complementary deoxyribonucleic acid (cDNA) with the High-capacity cDNA Reverse Transcription Kit (4368813, Applied Biosystems™) according to manufacturer's instructions and finally, the cDNA concentration was adjusted to 10 ng/mL by diluting with nuclease-free water for downstream quantitative Real-Time PCR.

2.10.2 Quantitative real-time PCR

Gene expression was quantified with either TaqMan™ assays or - for quantification of lentivirally transduced inserts - custom-made primers using the SYBR™ Green method. TaqMan™ assay IDs and custom-made primer sequences are given in tables A.1 and A.2 of the appendix, respectively.

Reaction mixes were prepared in white 96- or 384 LightCycler™ 480 Multiwell PCR plates (Roche Diagnostics) as specified in table 2.4 and PCR reactions were run on the LightCycler® 480 II (Roche Diagnostics) with cycling conditions as given in table 2.5.

Table 2.4: Composition of reaction mixes for TaqMan® and SYBR® Green qRT-PCR

	Reagent	**Volume (µL)**	**Source**
TaqMan®	PerfeCTa FastMix II (2x)	5	Quantabio
	TaqMan® assay (20x)	0.5	ThermoFisher Scientific
	Nuclease-free water	2	QIAGEN
	cDNA (10 ng/µL)	2.5	-
SYBR® Green	PowerUp™ SYBR® Green Master Mix	10	Applied Biosystems™
	Primer Mix 2µM	5	Sigma
	cDNA (10 ng/µL)	5	-

Cycle threshold (Ct) values were obtained using the second derivative method in the LightCycler 480 software (version 1.5.1.62) and gene expression was quantified using a modification of the ΔΔCt method [222] as follows:

$$-\Delta\Delta Ct = \Delta Ct\ (sample) - mean(\Delta Ct\ )(control\ group)$$

Table 2.5: Cycling conditions for TaqMan® and SYBR® Green qRT-PCR

Type	Step	Temperature	Time	Cycles
TaqMan®	Initial Denaturation	95 °C	3 min	
	Denaturation	95 °C	15 s	40x
	Annealing/Extension/ Acquisition	60 °C	1 min	
SYBR® Green	Activation	50 °C	2 min	
	Initial Denaturation	95 °C	2 min	
	Denaturation	95 °C	15 s	40x
	Annealing	60 °C	15 s	
	Extension/Acquisition	72 °C	1 min	
	Melting Curve	72 °C - 95 °C	-	

where ΔCt is the difference between the Ct values of the gene of interest and the reference gene. For human liver samples, reference genes were selected based on reference gene analysis using the `Normfinder` function [223] in the R package `generefer` and the mean of Ct values for all chosen reference genes, corresponding to the geometric mean of gene expression, was taken as the reference Ct value for calculating the ΔCt, as described in the literature [224]. Calculating the -$\Delta\Delta$Ct relative to the mean ΔCt of all controls served to preserve the variance in the control group.

2.10.3 Lexogen QuantSeq 3’ mRNA sequencing

RNA was isolated as described above (Section 2.10.1) and quality checked on a spectrophotometer. RNA was then submitted to Genomics Birmingham at the University of Birmingham for quality control, library preparation and sequencing. Quality control was performed using Qubit High Sensitivity RNA assay (Q32852, Invitrogen$^{\text{TM}}$) on a Qubit 2.0 fluorometer (Invitrogen) and RNA ScreenTape (5067-

5576, Agilent) on the Agilent TapeStation 4200. Single-end 75 base-pair libraries were generated using the QuantSeq 3' mRNA-Seq Library Prep Kit FWD for Illumina (015.96, Lexogen) with an RNA input of 100 ng. Quality of libraries was then checked using the Agilent TapeStation D1000 ScreenTape (5067-5582, Agilent) and Qubit dsDNA High Sensitivity kit (Q32851, Invitrogen). Finally, pooled libraries at 1.6 pM were sequenced on the NextSeq 500 sequencing platform (Illumina) on a NextSeq Mid 150 flowcell.

2.11 Histological methods

All the histological staining methods outlined below were performed by our collaboration partner Novo Nordisk, Maalov, Denmark.

2.11.1 Immunohistochemistry

Rat liver samples (full-thickness slabs of right medial and left lateral lobes) were fixed for three to five days in neutral-buffered formalin (NBF), then paraffin-embedded and sectioned (4 μm nominal thickness). Sections were stained manually with Picrosirius Red (PSR), and in the Ventana Autostainer with anti-CD45 at 2 μg/mL (Abcam ab10558, Cambridge, UK), anti-alpha-smooth muscle actin (α-SMA) at 0.04 μg/mL (clone EPR5368, Abcam ab124964), anti-CD68 at 1.5 μg/mL (clone E3O7V, Cell Signaling 97778, Danvers, MA), anti-CD11b at 0.5 μg/mL (clone EPR1344, Abcam ab133357), or anti-type I collagen at 4 μg/mL (Southern Biotech 1310-01, Birmingham, AL) using heat-induced epitope retrieval at basic pH, HRP-coupled detection polymers, and the Purple chromogen. All primary antibodies were of rabbit or goat origin to avoid background from the mouse anti-gremlin therapeutic antibody. Stained liver sections were scanned as 8-bit RGB colour images (pixel size: 442 nm) using a NanoZoomer S60 digital slide scanner (Hamamatsu Photonics K.K., Hamamatsu City, Japan). Quantitative image analysis was applied to the entire liver sections using Visiopharm Integrator System software (VIS ver. 8.4; Visiopharm, Hørsholm, Denmark). The fractional area (%) of PSR, CD45, α-SMA, CD68, CD11b, and Col1a1 stains was expressed relative to total sectional area. The lipid area fraction was determined based on PSR-stained sections.

2.11.2 In situ hybridisation

Twenty-five human diagnostic, formalin-fixed, paraffin-embedded (FFPE) histological liver needle biopsies were retrieved from the archives at Department of Pathology at Aalborg University Hospital, Denmark. The biopsies were diagnosed as normal, n=5, MASH with mild fibrosis, n=7, MASH with moderate/severe fibrosis, n=6, and MASH with cirrhosis, n=7. RNAscope duplex in situ hybridization (ISH) was performed on the Leica Biosystems BOND RX platform. RNAscope probes (Advanced Cell Diagnostics (ACD) Newark, California) directed against rat or human GREM1 and human THY1 or COL3A1 were hybridized for 2 h at 42°C using RNAscope 2.5 LS Duplex Reagent Kit (ACD) followed by RNAscope amplification. Fast red chromogenic detection of GREM1 was followed by green chromogenic detection (ACD) of THY1 or COL3A1. Sections were counterstained with haematoxylin.

2.12 Computational biology

2.12.1 Analysis of publicly available bulk RNAseq experiments

Publicly available datasets from liver tissue transcriptome experiments were retrieved from the Gene Expression Omnibus (GEO), the European Nucleotide Archive and ArrayExpress [225–227].

Raw sequencing data were transferred to the public Galaxy server usegalaxy.org to pre-process the data [228]. Data were transformed to standard FASTQ format using the `fasterq-dump` function. Quality control, quality and adapter trimming were performed with fastp and default settings [229]. The trimmed sequencing files were then aligned to the human Gencode reference transcriptome (version 36, available from https://www.gencodegenes.org/human) using `salmon quant` from the pseudoalignment tool salmon with `--validate Mappings`, `--seqBias` and `--gcBias` turned on with default settings [230]. For downstream analyses, gene or transcript counts were imported into R using the `tximport` pipeline for salmon output [231]. Differential gene expression was performed with the DESEq2 package using the likelihood ratio test or the Wald test as appropriate [232]. Variance stabilised expression values, obtained using the `vst` function in DESeq2, were used for visualisation of gene expression and for correlation and regression analyses. For public microarray datasets we used the deposited normalised expression values for downstream statistical analyses.

2.12.2 Lexogen QuantSeq 3’ mRNA sequencing

Raw sequencing files were obtained from Genomics Birmingham at the University of Birmingham. Adapter and quality trimming were performed using `fastp` using the adapter sequence GATCGGAAGAGCACACGTCTGAACTCCAGTCAC and settings

```
--trim_poly_g --trim_poly_x
--cut_tail --cut_window_size=4 --cut_mean_quality=20
--disable_quality_filtering
--low_complexity_filter --complexity_threshold=30
--length_required 36.
```

After quality control with `fastqc`, gene abundance was quantified using a decoy-aware transcriptome index (transcriptome gencode version 29, genome GRCh38) and `salmon 1.5.9` with default settings. Downstream data import into R and differential gene expression analysis were performed as described for publicly available RNAseq data using the `tximport` and `DESeq2` packages.

2.12.3 Analysis of single-cell RNAseq data

Raw count matrices for liver single-cell RNA sequencing datasets were obtained from the GEO server (GSE136103) and the Liver Cell Atlas website ([233], GSE192742).

Low quality cells were removed if the number of detected features was below 300 or the percentage of mitochondrial genes per cell was higher than 30 percent. Following quality filtering, gene expression was normalised by cluster-based log-normalisation using the `igraph` method in the `quickCluster` function from the `scran` package [234].

Variable features were identified using the fitted mean-variance calculated with the `modelGeneVar` function with default settings. Doublet contamination was removed using the default method of the `doubletFinder v3` package [235].

Following quality control and cleaning of both datasets separately, both datasets were integrated based on their common genes and using the reciprocal principal component analysis (RPCA) method implemented in the `Seurat v4` package [236]. Based on the integrated gene expression matrix, data scaling, principal component analysis and nearest neighbour graph-based clustering were performed using the standard Seurat workflow. Cell types were manually annotated by marker gene expression obtained from the `FindConservedMarkers` function in `Seurat v4` and based on the annotation provided by the Guilliams lab [135].

2.13 Statistical analyses

All statistical analyses were performed R version 4.2 and using the `rstatix` and `PMCMRplus` package. Graphs were drawn using `ggplot2`, `ggubr` and `ggprism` packages.

Data are shown as means ± SD, if not stated otherwise. Normal distribution was tested by inspecting QQ plots and by Shapiro-Wilks test. To test for homogeneity of variance we used Levene procedure. Depending on data distribution, we used the following statistical procedures: One-way analysis of variance (ANOVA), Two-way ANOVA, Welch's test or Kruskall-Wallis test with post-hoc Bonferroni-Holm, Dunnett or Dunn-Holm correction and for testing of ordinal or nominal data the χ^2-test. Four parameter log-logistic regression analysis for dose-response experiments was performed using the `drc` package and `LL.4` starter function in R. An alternative hypothesis was accepted if two-sided $p < 0.05$.

CHAPTER 3

GREMLIN-1 EXPRESSION IN HUMAN AND RODENT LIVER FIBROSIS

3.1 Introduction

Under healthy conditions, Gremlin-1 is expressed in a range of organs and has important roles in organ development, bone formation and regeneration of bone marrow and intestinal epithelial cells [173, 174]. It is also thought to play a role in a range of diseases, including atherosclerosis, cancer development and obesity-induced adipose tissue dysfunction [181, 237, 238]. Gremlin-1 is expressed mainly in fibroblasts and stem cells and plays a role in organ fibrosis in a range of different organs, including the kidney, lung, pancreas, skin and the intestine [173, 184–186, 239].

Data on hepatic fibrosis are less clear, however. Overall, hepatic expression of Gremlin-1 is considered to be low [172] and - similar to expression in fibroblasts in other organs - mainly restricted to activated hepatic stellate cell (HSC) and hepatic myofibroblast (MF) [89, 189]. Consistent with these findings, Gremlin-1 is increased in rodent models of liver fibrosis [89, 187, 188] and in human metabolic dysfunction-associated steatohepatitis (MASH) and MASH fibrosis [180]. Evidence on the cellular localisation of Gremlin-1, however, is mostly based on gene expression from isolated cells focusing on fibrogenic cell populations and from *in vitro* cell culture data. No spatial expression data are currently available and systematic exploration of expression changes or cellular localisation of Gremlin-1 in healthy and fibrotic human and rodent livers have not been described.

Therefore, in this chapter we aimed to characterize the expression of Gremlin-1 in healthy and fibrotic human and rodent liver, and to identify the specific cell types responsible for Gremlin-1 expression. Furthermore, we wanted to select animal models that show adequate liver injury and upregulation of Gremlin-1, suitable for testing of potential therapeutic compounds, and confirm that we could recapitulate human disease in an animal model. For this purpose, we applied RNAscope *in situ* hybridisation (ISH) and quantitative PCR to human and rodent biosamples, analysed publicly available bulk and single-cell transcriptome data sets of human liver or primary human hepatic cells, and measured circulating Gremlin-1 and its heparin-binding properties by luminescent oxygen channeling immunoassay (LOCI) and size-exclusion chromatography, respectively.

3.2 Results

3.2.1 Upregulated hepatic *GREM1* in human and rat MASH

We first wanted to establish how Gremlin-1 expression changes in MASH and the identity of the main cell types expressing Gremlin-1. Our collaboration partners at Novo

Nordisk performed RNAscope *in situ* hybridisation on human liver and were unable to detect *GREM1* in the pathologically normal state. However, staining significantly increased with MASH fibrosis and localized to the fibrotic septa in the periportal region (Figure 3.1A). *GREM1* expression co-localized with *THY1* and *COL3A1* positive cells (Figure 3.1B), indicating myofibroblasts in the portal fibrotic area as the major Gremlin-1-expressing cell type in human MASH. However, only a small proportion of *THY1/COL3A1*$^+$ cells expressed *GREM1*, and the expression was highly variable between and within each specimen (Figure 3.1A and B).

Next, we wanted to establish whether rodent MASH models adequately reflect the changes in hepatic *GREM1* expression we observed in human MASH, helping to decide on a suitable model for *in vivo* studies. We found no evidence of consistent *Grem1* expression in healthy and fibrotic mouse liver tissues (including CCl_4, *Mdr2* knockout, Western Diet, images not shown). Conversely, *Grem1* ISH staining was consistently increased in livers of rats fed a choline-deficient, L-amino acid-defined high-fat diet (CDAA-HFD) for twelve weeks. Similar to our observations in human MASH liver tissue, *Grem1* expression in rat livers mainly localised to periportal and fibrotic areas (Figure 3.1C).

3.2.2 Pinning down the cellular localisation of *GREM1* expression

To confirm the identity of cell types expressing Gremlin-1 in human liver, we integrated two large publicly available human single-cell RNA sequencing data sets (GSE136103[70] and GSE192742[135]). The resulting integrated data set comprised all major parenchymal and non-parenchymal cell populations and showed no major

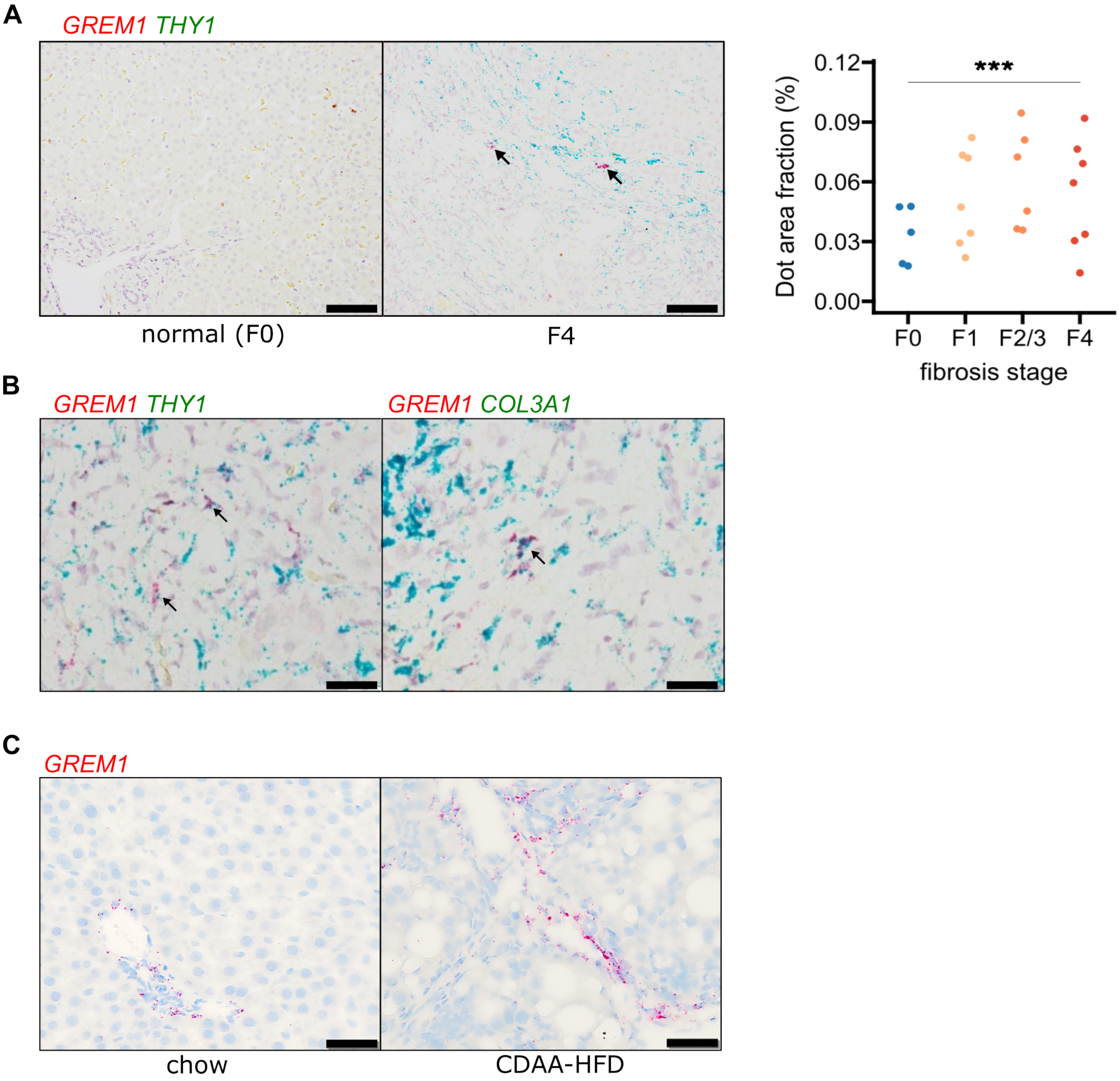

Figure 3.1: Validation of *GREM1* expression in human and rat MASH liver fibrosis. **A.** Left panel shows representative RNAscope in situ hybridisation (ISH) images for co-staining of *GREM1* (red) and *CD45* (green) in normal human liver and MASH fibrosis. The right panel shows scoring of ISH staining intensity across different stages of liver fibrosis. Significance was assessed by two-sided Jonckheere-Terpstra test (***$p = 1.3x10^{-09}$). Scale bar = 200 μM. **B.** Representative histological images of RNAscope in situ hybridisation (ISH) for co-staining of *GREM1* (red) and *THY1* or *COL3A1* (green). Representative double positive cells are indicated by arrows. Scale bar = 50 μM. **C.** Representative RNAscope in situ hybridisation (ISH) images for GREM1 (red) in rats fed a standard chow or CDAA-HFD for 12 weeks. Scale bar = 50 μM.
Abbreviations: CDA-HFD - choline-deficient, L-amino acid defined, 1% cholesterol, high-fat diet, COL3A1 - Collagen Type III Alpha 1 Chain, GREM1 - Gremlin-1, THY1 - Thy-1 antigen Images and data produced by Novo Nordisk

batch effects across data sets (Figure 3.2A and B, respectively). However, *GREM1* expression was very low and - on the global scale - could not easily be assigned to a specific cell population (Figure 3.2C). As the literature and our ISH results suggested that *GREM1* expression was mainly restricted to the stromal niche, we focused on the mesenchymal compartment of the integrated scRNA-seq data set and identified four distinct clusters, based on marker gene expression (Table 3.1) corresponding to vascular smooth-muscle cells (VSMC), quiescent HSC (qHSC), activated HSC and MF and portal fibroblasts (PF) (Figure 3.2D-F). Again, *GREM1* expression was low and found mainly on smooth muscle cells and portal fibroblast populations, the latter coexpressing *THY1* and *COL3A1* (Figure 3.2F). Concordantly, when performing quantitative PCR on cultured human cell lines and primary hepatic cells, *GREM1* mRNA expression was highest in LX-2 cells, primary human HSC HHSC and MF when compared to biliary epithelial cell (BEC) and hepatic sinusoidal endothelial cell (HSEC) (Figure 3.3).

Therefore, we hypothesised that Gremlin-1 is involved in hepatic fibrogenesis and that its expression should correlate with the stage of fibrosis in MASH, in concordance with our RNAscope ISH results (see above). As the performance of RTqPCR is dependent on the adequate choice of reference genes, we first performed reference gene analysis on a first subset of livers using the *Normfinder* algorithm [223]. Figure 3.4 shows the stability values for a range of reference genes and combinations thereof, based on which we have chosen the combination of *ERCC3*, *SRSF4* and *HPRT1* as reference genes for all subsequent experiments on human liver tissue. Indeed, RTqPCR on human explant livers of different aetiologies (all fibrosis stage F4) showed 4.8 to

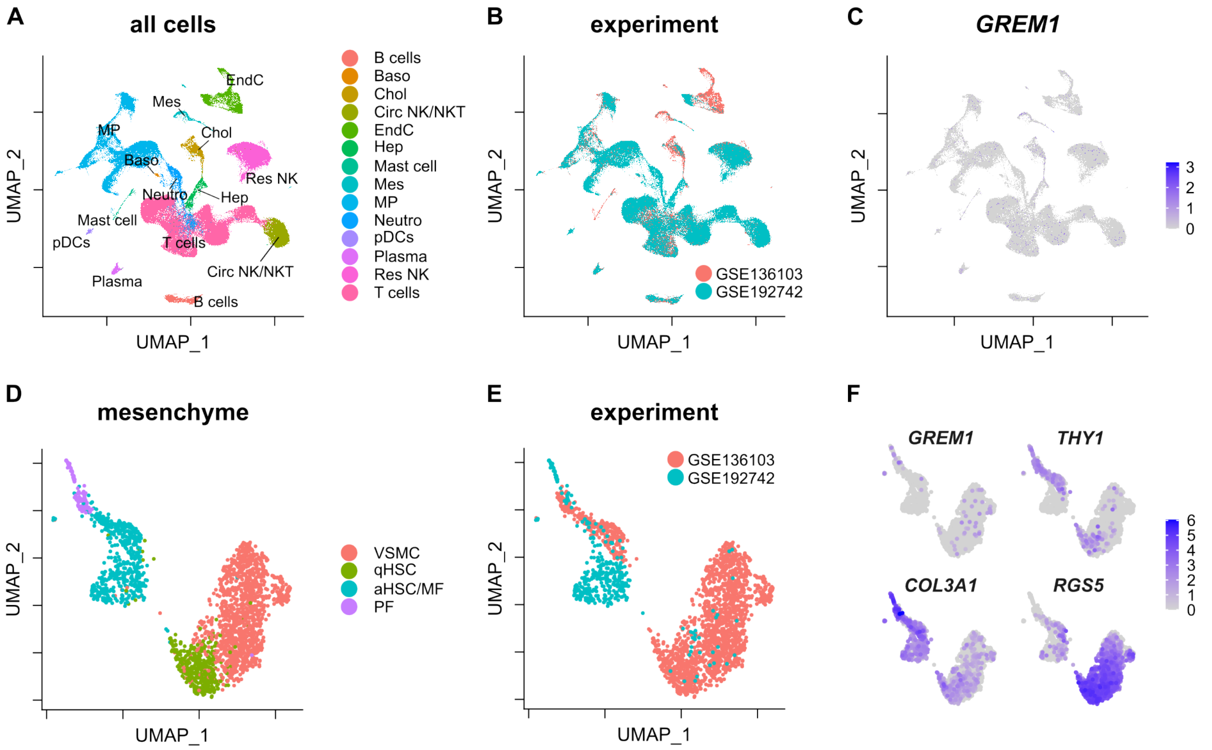

Figure 3.2: *GREM1* expression in publicly available human scRNA-seq data. A. UMAP representation of all cells in GSE136103 and GSE192742 scRNA-sequencing data sets. Cells are coloured by cell type identity. **B.** UMAP representation of all cells in GSE136103 and GSE192742 scRNA-sequencing data sets. Cells are coloured by experiment. **C.** Log2-normalised *GREM1* gene expression in all cells. **D.** UMAP representation of mesenchymal cells in GSE136103 and GSE192742 scRNA-sequencing data sets. Cells are coloured by cell cluster identity. **E.** UMAP representation of mesenchymal cells in GSE136103 and GSE192742 scRNA-sequencing data sets. Cells are coloured by experiment. **F.** Log2-normalised gene expression of *GREM1*, *THY1*, *COL3A1* and *RGS5* in mesenchymal cells.
Abbreviations: a/qHSC - activated/quiescent hepatic stellate cell, Baso - basophil granulocyte, Chol - cholangiocyte, Circ NK/NKT - circulating natural killer/natural killer T cells, COL3A1 - Collagen Type III Alpha 1 Chain, EndC - endothelial cell, GREM1 - Gremlin-1, Hep - hepatocytes, Mes - mesenchymal cells, MF - myofibroblast, MP - mononuclear phagoytes, Res NK - resident natural killer cell, pDC - plasmocytoid dendritic cell, PF - portal fibroblast, RGS5 - Regulator Of G Protein Signalling 5, THY1 - Thy-1 antigen, VSMC - vascular smooth muscle cells.

Table 3.1: Top 5 % marker genes for mesenchymal scRNA-seq clusters

VSMC	**qHSC**	**aHSC/MF**	**PF**
MYH11	*RGS5*	*GGT5*	*SFRP2*
DSTN	*HIGD1B*	*CFH*	*STEAP1*
MYL9	*COLEC11*	*IGFBP3*	*WT1*
TPM2	*FABP5*	*ADAMTSL2*	*RARRES1*
TAGLN	*FABP4*	*ITGBL1*	*FBLN1*
ADIRF		*FBLN5*	*C3*
RERGL		*C7*	*VCAN*
MYL6		*CXCL12*	*MMP2*
ACTA2		*MEG3*	*LOX*
PHLDA2			*LXN*
PLN			*CPXM1*
BCAM			*GPRC5A*
TPM1			*FBLN2*
CRIP1			*DPT*
			PTGFRN
			COL8A1
			MEDAG
			PDPN
			MFAP2
			EFEMP1
			PRRX1
			CTHRC1
			SPOCK1

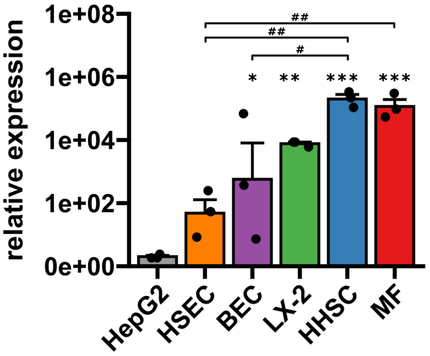

Figure 3.3: RTqPCR results for *GREM1* on primary hepatic cells and selected cell lines. Data are given as individual data points (each representing a different sample measured in duplicate) and mean ± SD for expression values relative to the mean of HepG2 cells and normalised to to expression of *SRSF4*. *$p < 0.05$, **$p < 0.01$, ***$p < 0.001$ compared to HepG2, #$p < 0.05$, ##$p < 0.01$ in indicated comparisons. Statistical group comparisons were performed using One-way ANOVA and post-hoc Tukey-HSD test.
Abbreviations: BEC - biliary epithelial cell, HepG2 - hepatoma cell line HepG2, HHSC - human hepatic stellate cell, HSEC - hepatic sinusoidal endothelial cell, LX-2 - hepatic stellate cell line LX-2, MF - myofibroblast.

9.8-fold increased *GREM1* mRNA expression in MASH, alcohol-related liver disease (ArLD), primary biliary cholangitis (PBC) and primary sclerosing cholangitis (PSC) liver tissues when compared to donor livers without fibrosis (all $p < 0.05$, Figure 3.5). However, when analysing publicly available bulk RNA sequencing from a total of 352 patients with metabolic dysfunction-associated steatotic liver disease (MASLD) (n = 58 E-MTAB-9815, n = 78 GSE130970, n = 216 GSE135251), capturing the whole spectrum of MASLD and MASH, we found no correlation of *GREM1* expression with the histological stage of fibrosis (Figure 3.6).

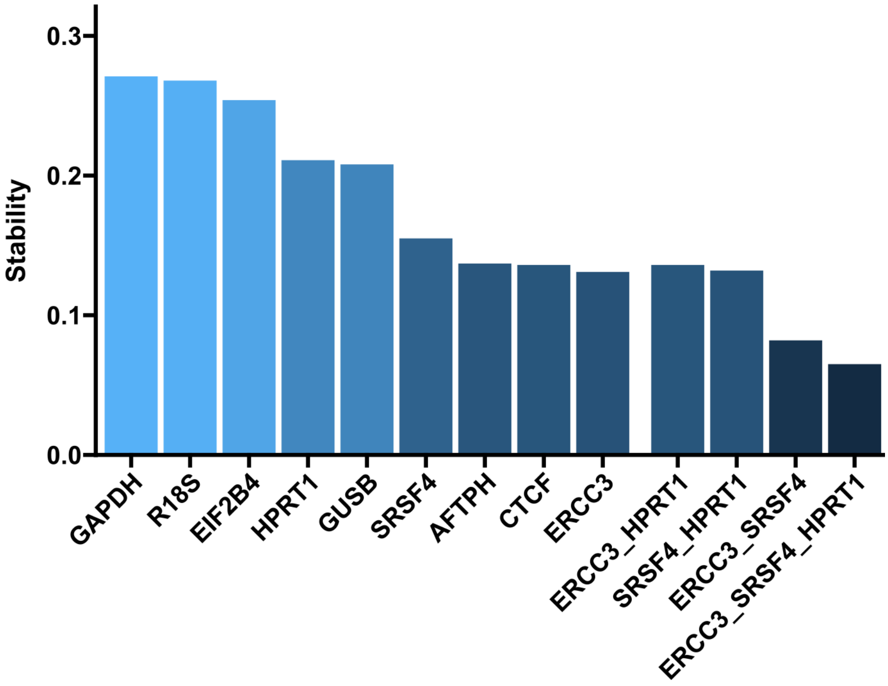

Figure 3.4: Reference gene analysis for human liver RTqPCR. RTqPCR was performed on the first subset of n = 5 livers per disease (donor, ArLD, MASH, PSC and PBC) in order to identify suitable reference genes for subsequent RTqPCR experiments. The bar diagram shows the stability values obtained through *Normfinder* for a set of potential reference genes and combinations thereof. Lower stability values indicate more stable expression with lower inter-group and intra-group variability. Bars are coloured by stability value for emphasis. The combination of *ERCC3*, *SRSF4* and *HPRT1* was chosen for all subsequent RTqPCR experiments on human liver tissue.
Abbreviations: AFTPH - Aftiphilin, ArLD - alcohol-related liver disease, CTCF - CCCTC-Binding Factor, EIF2B4 - Eukaryotic Translation Initiation Factor 2B Subunit Delta, ERCC3 - Excision Repair Cross-Complementing Rodent Repair Deficiency Gene, GAPDH - Glyceraldehyde-3-Phosphate Dehydrogenase, GUSB - Glucuronidase Beta, HPRT1 - Hypoxanthine Phosphoribosyltransferase 1, MASH - metabolic dysfunction-associated steatohepatitis, PBC - primary biliary cholangitis, PSC - primary sclerosing cholangitis, SRSF4 - Serine And Arginine Rich Splicing Factor 4.

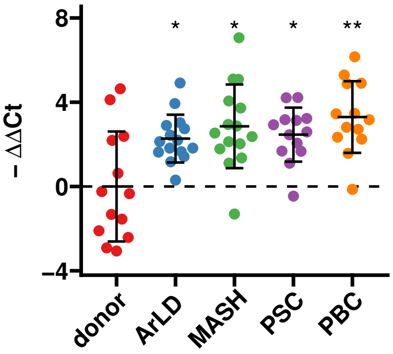

Figure 3.5: Quantification of human *GREM1* qPCR across chronic liver diseases of different aetiology. Data are given as individual data points (each representing a different patient sample measured in duplicate) and mean -ΔΔCt ± SD, relative to donor liver and normalised to the expression of *SRSF4*, *HPRT1*, and *ERCC3*. ArLD ($p = 0.014$), MASH ($p = 0.012$), PBC ($p = 0.014$) and PSC ($p = 0.004$).
n = 13 - 15 per group. *$p < 0.05$, **$p < 0.01$ compared to donor using Welch One-Way ANOVA with post-hoc multiple Welch t-tests compared to donor as reference group and Bonferroni-Holm correction.
Abbreviations: ArLD - alcohol-related liver disease, MASH - metabolic dysfunction-associated steatohepatitis, PBC - primary biliary cholangitis, PSC - primary sclerosing cholangitis.

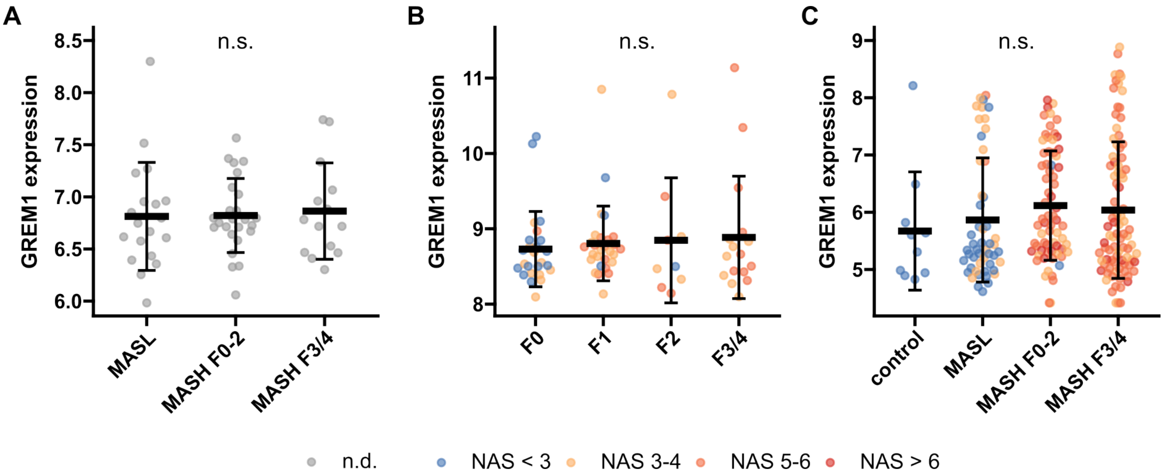

Figure 3.6: *GREM1* gene expression in publicly available bulk RNAseq from MASLD liver. A. E-MTAB-9815 (n = 58), **B.** GSE130970 (n = 78), **C.** GSE135251 (n = 216). All data are given as individual data points (each representing a different patient sample) and mean±SD of variance stabilised expression as obtained from the `vst` function in `DESeq2`.
n.s. - not significant, statistical significance was tested using likelihood ratio test and Benjamini Hochberg correction in DESeq2.
Abbreviations: GREM1 - Gremlin-1, MASH - metabolic dysfunction-associated steatohepatitis, MASL - metabolic dysfunction-associated liver steatosis.

3.2.3 *GREM1* expression upon hepatic fibrogenic cell activation

Bulk RNA sequencing, however, might mask the responses of a small number of fibroblasts and Gremlin-1 is known to be upregulated in HSC in response to transforming growth factor beta (TGFβ)1. Therefore, we analysed publicly available RNA sequencing data sets derived from primary HSC treated with TGFβ1 for 24, 48 or 72 hours. As can be seen in Figure 3.7, *GREM1* was consistently upregulated upon TGFβ1 treatment at all time points with highest $\log_2$-fold changes at 24 hours after treatment.

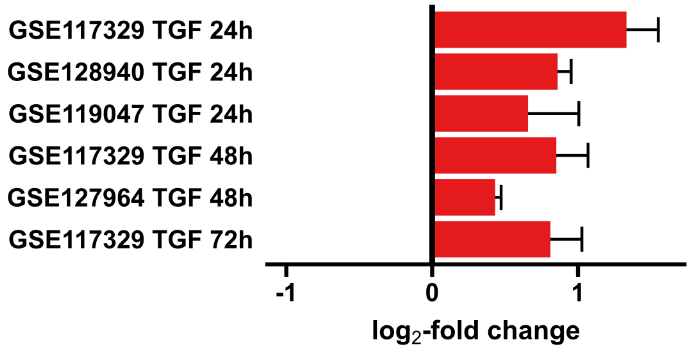

Figure 3.7: *GREM1* expression changes in primary HSC upon TGFβ treatment. The graph shows mean±SD $\log_2$-fold change gene expression changes from publicly available bulk RNA sequencing data sets, calculated with the `DESeq2` pipeline. The GEO accession numbers and length of TGFβ-treatment are given on the left hand side. Abbreviations: GREM1 - Gremlin-1, HSC - hepatic stellate cell, TGF - transforming growth factor.

To verify expression changes of *GREM1* mRNA in fibrogenic cells *in vitro*, we treated LX-2 cells, primary MF and HHSC with 50 U/mL TGFβ1 for 24 hours and performed RTqPCR. TGFβ1 treatment led to a significant upregulation of *GREM1* expression in LX-2 and MF ($p = 0.016$ and $p = 0.036$, respectively, Figure 3.8). In primary HHSC however, although TGFβ1 treatment upregulated *GREM1* expression this change did not reach statistical significance ($p = 0.129$, Figure 3.8)

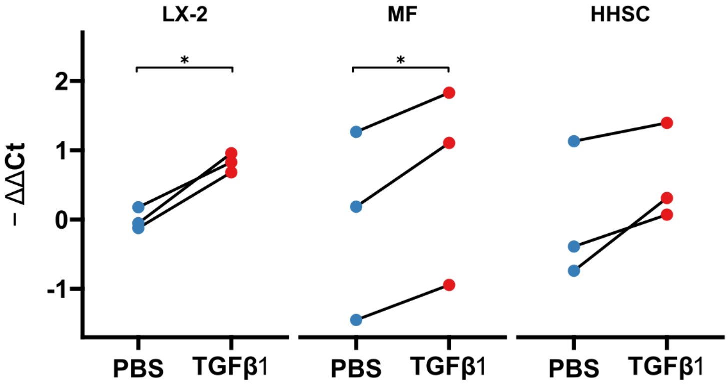

Figure 3.8: RTqPCR results of *GREM1* expression in fibrogenic cells in response to TGFβ1. LX-2 cells, MF and HHSC were treated with TGFβ1 or phosphate-buffered saline (PBS) for 24 h. Data are given as single data points (each representing an independent experiment measured in duplicate) of -ΔΔCt, relative to PBS control and normalised to the expression of *SRSF4*. Connecting lines indicate differences between paired samples.
*$p < 0.05$ using two-sided paired t-test.
Abbreviations: GREM1 - Gremlin-1, HHSC - human hepatic stellate cell, LX-2 - HSC cell line LX-2, MF - myofibroblast, PBS - phosphate-buffered saline, TGFβ - transforming growth factor beta, SRSF4 - Serine And Arginine Rich Splicing Factor 4.

3.2.4 Circulating Gremlin-1 and heparin-binding properties

Increased circulating Gremlin-1 protein has been described in patients with type 2 diabetes and in MASH and has been linked to higher MASH disease severity [180]. Therefore, we wanted to verify these findings and investigate whether circulating Gremlin-1 protein also correlates with the stage of fibrosis. Measurements of circulating Gremlin-1 protein were performed by our collaboration partner Novo Nordisk using an in-house developed luminescent oxygen channelling immunoassay (LOCI, alphaLISA) using different combinations of yet unpublished human recombinant anti-Gremlin-1 antibodies. However, despite high sensitivity, Gremlin-1 protein was undetectable in plasma or serum in two independent patient cohorts (Figure 3.9A and B). Using size exclusion chromatography, also performed by Novo Nordisk, we observed that dimeric Gremlin-1 forms dimers and trimers in complex with heparin (Figure 3.9C), suggesting that Gremlin-1 might be retained on cell surfaces and extracellular matrix and thus not enter systemic circulation.

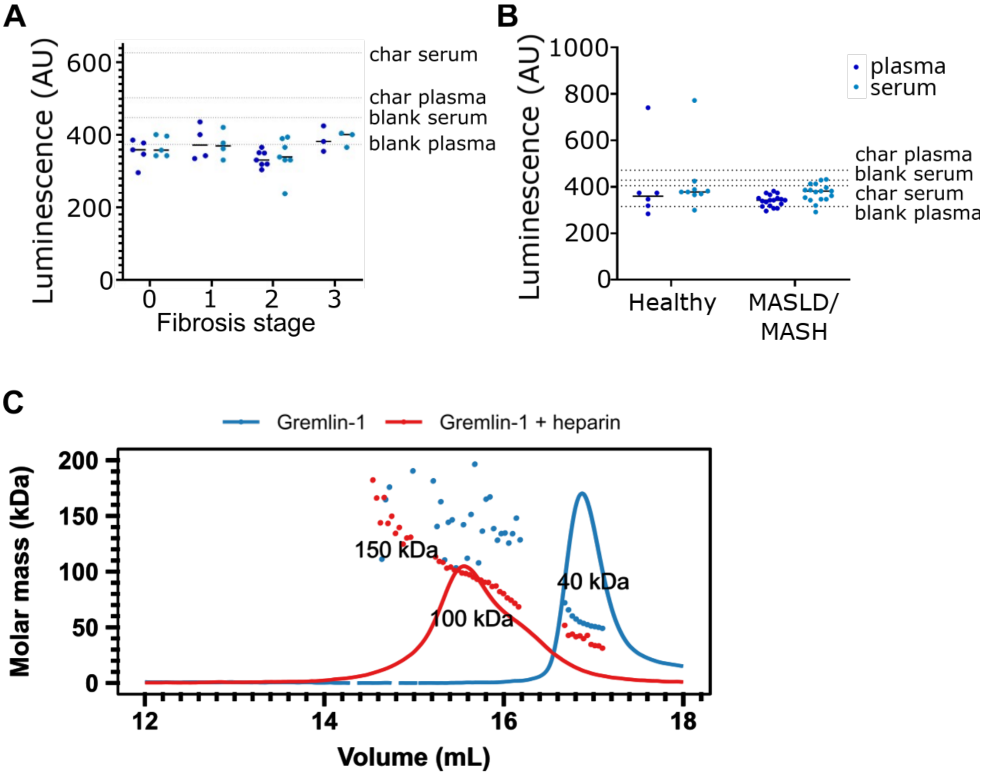

Figure 3.9: Circulating Gremlin-1 protein and evidence for heparin-binding properties. A. Signal for Gremlin-1 protein in the LOCI assay in serum or plasma of MASH patients at different stages of fibrosis. **B.** Signal for Gremlin-1 protein in the LOCI assay in serum or plasma of healthy controls and MASLD/MASH. Data in A and B are given as single data points and median of luminescence signal. Dotted horizontal lines correspond to signal measured in control matrices, as given in text annotations. **C.** Size exclusion chromatography for Gremlin-1 and heparin. Either Gremlin-1 or Gremlin-1 + heparan sulfate were run on a size exclusion chromatography column. The graph shows UV signal (continuous line) and estimated molar mass (points) on the y-axis depending on the eluting volume on the x-axis. Text annotations give the estimated molar mass corresponding to each peak. char serum/plasma: charcoal-treated serum/plasma.
Abbreviations: MASLD - metabolic dysfunction-associated steatotic liver disease, MASH - metabolic dysfunction-associated steatohepatitis.
Data generated by Novo Nordisk.

3.3 Discussion

Gremlin-1 has been identified as a potential driver of tissue fibrosis across different organs including the liver [240]. Expression in other organs is mainly limited to fibroblasts and other fibrogenic cells such as pancreatic stellate cells [185, 240], but has also been described for preadipocytes [172]. However, data on the regulation of Gremlin-1 in liver fibrosis and its exact cellular localisation are scarce. Therefore, we aimed to characterise the expression pattern of Gremlin-1 in human and rodent liver fibrosis and sought to assess changes in circulating Gremlin-1 and its correlation with disease phenotype.

Gremlin-1 is mainly expressed in adipose tissue, the intestine and the kidneys, while hepatic expression is considered low in healthy human [172] and rodent tissue [187]. In healthy mouse liver, Gremlin-1 expression was undetectable (data not shown), but others have previously found increased mRNA expression in murine fibrotic liver in *Mdr2*$^{-/-}$ mice fed a cholate-containing diet [187] and porcine serum-induced murine liver fibrosis [188]. Similarly, in patients with type 2 diabetes and MASH, Hedjazifar *et al* have found increased Gremlin-1 expression and a positive correlation with liver steatosis, inflammation, ballooning and the stage of fibrosis [180]. Our findings of increased RNAscope ISH signal in human and rat MASH fibrosis largely corroborate existing evidence, although our secondary analyses from existing bulk RNA-sequencing data sets were conflicting. Furthermore, our RNAscope studies on human livers highlight the heterogeneity of Gremlin-1 expression between and within individual livers, resulting in a high risk of sampling bias. Not least, by RTqPCR we showed increased hepatic Gremlin-1 expression across different aetiologies of end-stage chronic liver disease, pointing towards a role that is not limited to metabolic liver disease.

The exact cellular localisation of hepatic Gremlin-1 is under continuous investigation. Using RNAscope ISH, we found that Gremlin-1 mRNA expression localised to *COL3A1* and *THY1* positive cells in the periportal and fibrotic area. In the liver, THY1 is expressed on periportal cells, mainly including the mesenchymal stem cell niche [241, 242] and portal fibroblasts [243, 244]. THY1$^+$ cells are abundant in fetal liver [245] but rare in healthy adult liver [241]. Still, a recent report highlighted that a population of THY1$^+$ portal fibroblasts with mesenchymal stem cell features and high proliferative capacity contributes to the formation of fibrotic septa in liver fibrosis of different aetiologies [90]. While CD45$^+$ THY1$^+$ lymphocyte populations have also been described [243], their role in liver biology is unclear and screening publicly available single-cell RNA sequencing cell atlases [70, 135, 233] suggests that their numbers are low. The gene *COL3A1* codes for the fibrillar type III collagen pro-alpha1 chain, which is associated with type I collagen in the hepatic extracellular matrix [55]. *COL3A1* expression is mostly restricted to fibrogenic cells but can be found at lower levels in cholangiocytes and hepatic endothelial cells [246], and therefore we are confident that *GREM1*$^+$ *THY1*$^+$ *COL3A1*$^+$ cells indeed represent a subset of portal fibroblasts.

Some authors previously found increased Gremlin-1 expression in human HSC-derived myofibroblasts when compared to quiescent and early activated HSC [187, 189]. However, later studies found evidence that Gremlin-1 expression is most abundant in portal fibroblasts when compared to HSC in murine bile duct ligation and

CCl_4 models of fibrosis [89], suggesting that portal fibroblast-derived myofibroblasts, rather than HSC-derived myofibroblasts, are the predominant Gremlin-1 expressing cells of the liver. Still, as mentioned above, hepatic Gremlin-1 expression seems to be very low, evidenced by available liver scRNA-seq data [70, 135]. In our integrated analysis of both data sets, *GREM1* was barely detectable but showed considerable expression in smooth muscle cell subsets and a subset of cells also expressing *COL3A1* and *THY1*, the latter corresponding to the scar-associated mesenchymal cell population 3B identified by Ramachandran *et al*, which is characterised by the expression of portal fibroblast markers [70]. In line with an expression of Gremlin-1 in fibrogenic cell populations, we found highest expression by RTqPCR in primary myofibroblasts and activated HSC, followed by LX-2 cells with considerably lower expression in BEC, HSEC and the hepatocyte cell line HepG2. Taken together, our data confirm periportal myofibroblasts as the predominant hepatic cell population expressing Gremlin-1.

The discrepancy between results obtained through ISH and RTqPCR on the one hand and RNA sequencing results on the other hand warrants further discussion. The most likely reason for this difference is that liver explants from patients with end-stage liver disease represent a very distinct clinical entity, quite different from the presented MASH samples analysed using ISH and RNA sequencing approaches, that may present with excessive organ fibrosis, a sustained inflammatory state and ductular reaction [247–249]. Additional investigations into end stage liver disease tissue and material from biliary fibrosis, e.g. using *in situ* hybridization for *GREM1*, may have helped to confirm this association. Nevertheless, technical problems with transcript quantification may have contributed to our observations: While both RTqPCR and RNA scope detect transcripts by using specific oligonucleotide probes and primers that generate a signal upon binding to their target sequence and therefore only cover a small part of the transcript [250, 251], RNA sequencing, at least using standard protocols and chemistry used in the presented data sets, covers the whole transcript sequence [252]. However, sensitivity of RNA sequencing highly depends on the read depth of the protocol used [253] and therefore the RNA data sets analysed here, with a read depth of only a couple of million reads per sample, lack sensitivity for detecting lowly abundant transcripts. This problem is accentuated in single-cell sequencing, where transcriptome libraries are generated from single cells, and naturally the number of detected transcripts per cell is currently about a magnitude lower than in bulk RNA sequencing experiments [254]. Furthermore, data normalisation poses a risk of quantification bias, too. In RTqPCR, normalisation is usually based on the use of reference transcripts and relative changes in target gene abundance are calculated relative to the expression of reference transcripts [250]. Consequently, the quality of data normalisation in RTqPCR is highly dependent on the choice of reference genes and therefore others have suggested to combine reference genes, especially for complex experimental scenarios with expected heterogeneity across samples [224]. Therefore, we performed a comprehensive reference gene analysis using the `Normfinder` algorithm [223] and identified the combination of *ERCC3*, *SRFS4* and *HPRT1* as highly stably expressed between and within different conditions, which allowed confident relative comparisons between aetiologies of chronic liver disease. By contrast, normalisation of RNA sequencing data is based on overall data distribution and is not dependent on the use of reference genes for quantification, but results will differ based on the strategy of read alignment, transcript quantification, normalisation and differential gene expression analysis [255]. Finally, the number of healthy control subjects in the largest RNA sequencing data set GSE135251 was quite low, which might have masked potential differences in expression. Overall, data distribution seems to align between ISH and RNA sequencing cohorts, although this was not statistically significant in the latter. Therefore, differences in the biology between F4 fibrosis and end-stage liver disease - and not technical reasons - are the most likely reason why RTqPCR results were so different. However, this will need substantiation with additional data in the future.

TGFβ1 is one of the main and best studied regulators of HSC activation and triggers a shift in the HSC transcriptome, pushing the upregulation of fibrotic genes and transdifferentiation to a myofibroblast-like phenotype [71]. Importantly, based on the literature and our findings discussed above, the regulation of *GREM1* expression following TGFβ1 stimulation needs to be seen in the context that HSC are not a relevant source of Gremlin-1 in the liver. Still, we found that Gremlin-1 was regulated across existing bulk RNA sequencing data sets of TGFβ1-induced HHSC activation and by RTqPCR in TGFβ1-stimulated LX-2, primary MF and - at least numerically - in HHSC. The specific conditions of cell culture may have contributed to this regulation of *GREM1*, as cultured HSC are usually activated when grown on plastic, a hard surface with high shear stress. Growing cells in monoculture further adds to an altered phenotype that is distinct from primary fibrogenic cells *in vivo*. Therefore, the high expression of *GREM1* in cultured LX-2 and HHSC and its increase with TGFβ1 stimulation, that in the literature are often used as a surrogate for the relevance of Gremlin-1 in hepatic stellate cells, appear to be artefacts of *in vitro* culture. Furthermore, hepatic fibroblasts and HSC represent heterogeneous cell populations that may also differ between aetiologies of liver disease. While we assume that the primary MFs were mainly derived from activated HSC, we did not ascertain their lineage origin, e.g. by studying specific marker expression. Similarly, we did not specifically verify the HSC origin and potential heterogeneity of the commercially sourced HHSC. Still, in the following chapter we will use LX-2 cells, primary MF and HHSC as cell culture models to study the effects of modifying Gremlin-1 activity on hepatic fibrogenic cells, complemented by rat *in vivo* and human *ex vivo* models of MASH liver fibrosis.

Other groups have reported increased levels of Gremlin-1 protein in the blood of patients with MASLD/MASH and cardiovascular disease and even found correlations with parameters of hepatic disease activity and insulin resistance [180]. To our surprise, using highly sensitive and specific luminescent channelling assays, we found no evidence of circulating Gremlin-1 protein. The absence of Gremlin-1 protein from circulation was confirmed by Novo Nordisk using alternative assays, including ELISA and chromatography with data not shown in this work (personal communication Novo Nordisk). Still, we did not confirm our findings in individuals with end-stage liver disease, the population that showed highest gene expression in qPCR. Therefore, while we cannot finally rule out presence of Gremlin-1 protein in the blood, previous findings relating to correlations of circulating Gremlin-1 need to be interpreted with caution. In the next chapter, we will further explore the potential reasons why Gremlin-1 protein cannot be detected in circulation.

Overall, we provide compelling evidence for an upregulation of hepatic Gremlin-1 in MASH fibrosis and particularly in end-stage liver disease of different aetiologies, although this did not translate into detectable circulating levels. In agreement with existing evidence, *GREM1* seems to be mainly expressed in a small subset of *THY*$^+$ *COL3A1*$^+$ periportal myofibroblast. Therefore, we feel that this warrants further validation of Gremlin-1 as a marker for portal fibroblasts and investigations into its role in end-stage liver disease, cholestatic liver conditions and ductular reaction.

CHAPTER 4

GREMLIN-1 AS A THERAPEUTIC TARGET IN LIVER FIBROSIS

4.1 Introduction

Gremlin-1 is involved in tissue fibrosis in a range of different organs [256]. In the previous chapter we showed that *GREM1* mRNA expression correlates with increased fibrosis in human metabolic dysfunction-associated steatohepatitis (MASH) fibrosis and the rat choline-deficient, L-amino acid defined, 1% cholesterol, high-fat diet (CDAA-HFD) model of MASH. We also found, in line with existing literature, that *GREM1* localises to *THY1*$^{+}$ *COL3A1*$^{+}$ cells in the fibrotic scar and that it is upregulated in hepatic matrix-producing cells in response to transforming growth factor beta (TGFβ).

Evidence from the literature suggests that Gremlin-1 is not only upregulated in hepatic fibrogenic cells but plays an active role in the activation of hepatic stellate cells (HSCs) and maintenance of their matrix-producing myofibroblast phenotype. Overexpression of *GREM1* in HSC-T6 cells induces gene and protein expression of Col1a1, α smooth muscle actin (αSMA) and TGFβ1 [188, 190] while conversely, siRNA mediated knockdown results in the downregulation of fibrogenic signals [190]. The latter also translated into reduced fibrosis area in CCl_4-treated rats upon *GREM1* siRNA-mediated knockdown *in vivo* [190]. Furthermore, a recent report using immortalised human hepatocytes highlighted that Gremlin-1 can induce hepatocellular senescence, and thereby may be involved in driving disease progression in MASH [191].

However, to date the effects of therapeutic inhibition of Gremlin-1 in human liver fibrosis, and MASH in particular, have not been studied. In this chapter, we aimed to further characterize the effects of Gremlin-1 on human fibrogenic cells and evaluate the therapeutic efficacy of an anti-Gremlin-1-directed antibody treatment in rodent and human *in vivo* and *ex vivo* models of MASH fibrosis.

4.2 Results

4.2.1 GREM1 overexpression in LX-2 and primary human hepatic stellate cells

Generation of the GREM1-GFP-pWPI lentivirus

A detailed description of the methodology used for generation of lentiviral vectors is given in the methods chapter (Section 2.6.1, page 51). The GREM1 insert, containing the coding sequence for Gremlin-1 and a modified Kozak sequence, was cloned from the plasmid by PCR and correct size of the PCR product was confirmed by DNA gel electrophoresis (Figure 4.1A). The vector pWPI (encoding *GFP* from a separate locus) was linearized by PmeI digest and dephosphorylation (Figure 4.1B), and the *GREM1* insert blunt end ligated prior to transformation of NEB stable competent E. coli followed by Sanger sequencing of the resultant colonies at Source BioScience to confirm correct assembly of the *GREM1*-pWPI plasmid. pWPI plasmids without the coding

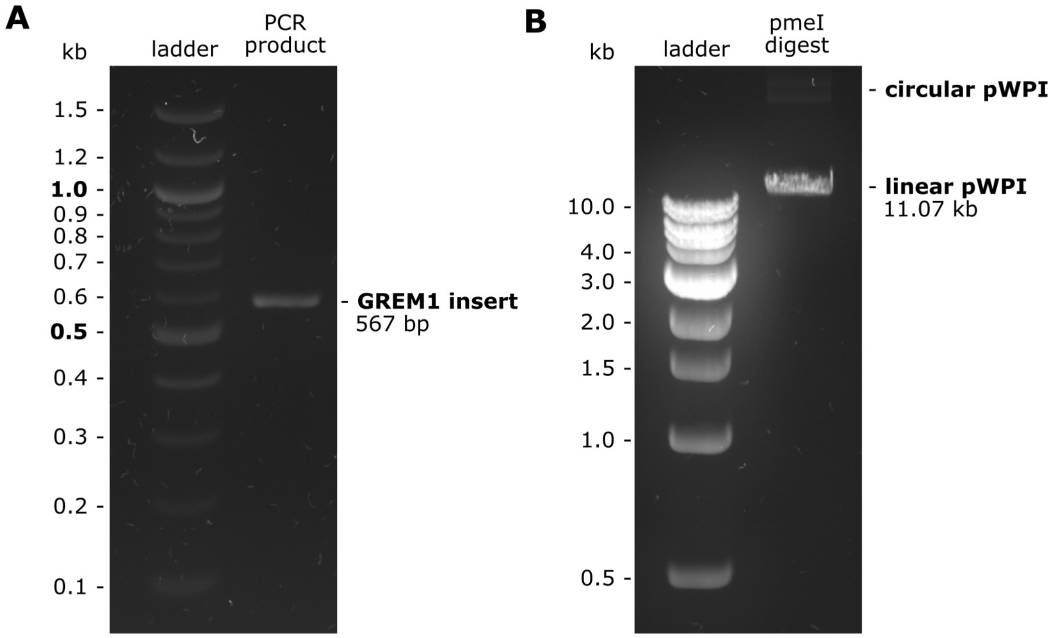

Figure 4.1: Confirmation of PCR reaction and pmeI digest by DNA gel electrophoresis. A. DNA gel electrophoresis of *GREM1* insert after cloning PCR. The predicted size was 567 bp. **B.** DNA gel electrophoresis of the linearised pWPI plasmid after pmeI digest and dephosphorylation. The predicted molecular size was 11.07 kbp. The molecular sizes of the DNA size ladder are given on the left hand side of each gel image.

sequence for *GREM1*, obtained through backbone re-ligation, were used as negative lentiviral controls. Finally, lentivirus was generated by transfection of HEK293T cells and gradient centrifugation of the resulting supernatants as described in the methods (Section 2.6.1, page 51).

Validation of GREM1 overexpression

After incubation of LX-2 or primary human hepatic stellate cell (HHSC) with lentivirus, transduction of cells was first confirmed visually by fluorescent microscopy (Figure 4.2), verifying integration and translation of the GFP coding sequence. In order to assess the percentage of transduced cells, we performed flow cytometry, using non-transduced cells as negative control. Figure 4.3 shows the gating strategy, which was also used for flow sorting of lentivirally transduced LX-2 cells based on GFP fluorescence.

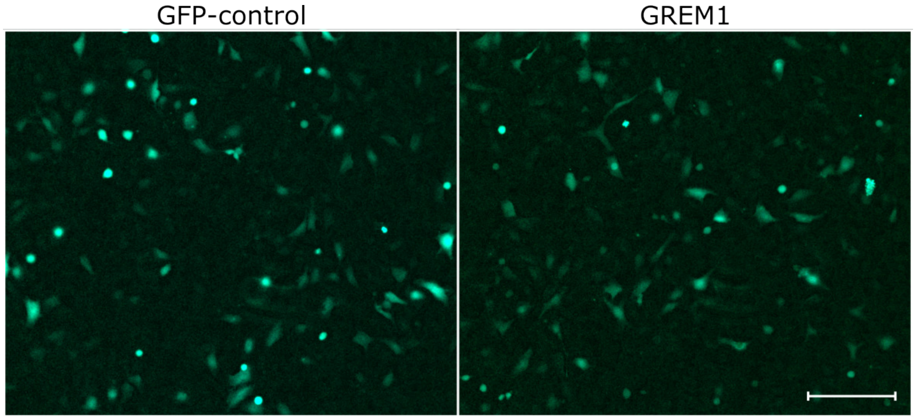

Figure 4.2: Representative images of GFP fluorescence in lentivirally transduced LX-2 cells. Cells were transduced with either *GFP*-control pWPI (left) or *GREM1* pWPI (right) lentivirus and imaged on a fluorescent microscope. Scale bar = 100μM. The images shown underwent background subtraction, Gaussian filtering, contrast and brightness adjustment.

In LX-2 cells, transduction with the GFP-control lentivirus led to a numerically higher percentage of GFP-positive cells than the GREM1 virus, resuting in 80 compared to 60 % GFP positivity (Figure 4.4A). In order to align expression levels of both GFP-control and GREM1 transduced cells, LX-2 cells were flow-sorted based on GFP positivity. After sorting, *GFP* mRNA expression was equal between both cell lines, while *GREM1* mRNA was 177-fold higher in *GREM1*-transduced cells compared to GFP-control ($p < 0.001$, Figure 4.4B). In HHSC, however, *GREM1* transduction was more efficient with 60% GFP$^+$ cells compared to only 30% in GFP alone controls ($p = 0.029$, Figure 4.4C). Because of the fragility and overall low numbers of primary HHSC available, we omitted flow sorting and consequently, both *GFP* and *GREM1* mRNA expression were significantly higher in *GREM1*-transduced cells

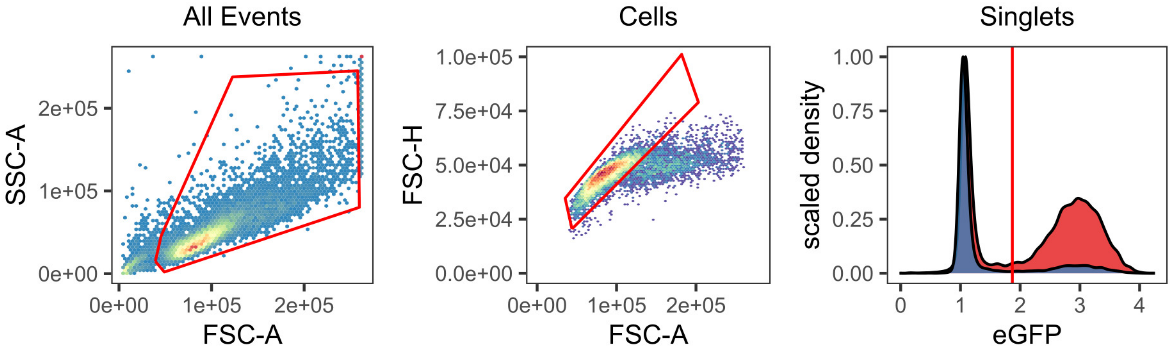

Figure 4.3: Gating strategy for flow sorting of lentivirally transduced cells. First, cells were selected (left panel) before gating on singlets (middle panel). Cells were then gated based on the 99 percent percentile of non-transduced cells to identify cells positive for GFP (right panel). Red polygons in the first two panels show gates used to select cells and the red vertical line in the right panel shows the cut-off for GFP positivity. Right hand panel: blue histogram - GFP-control pWPI, red histogram - GREM1 pWPI.

compared to *GFP* controls ($p = 0.004$ and $p = 0.020$, respectively, Figure 4.4D). Notably, *GREM1* expression was higher in HHSC compared to LX-2 cells ($C_t = 18$ vs $C_t = 21.5$, respectively, in GFP-control cells).

Effects on gene expression

Next, we wanted to test whether lentiviral overexpression of GREM1 in primary human hepatic stellate cells (HHSC) and LX-2 cells affects fibrogenic gene expression. To that end, GFP-control and GFP:GREM1 cells were seeded to about 80% confluence and subsequently serum-starved in reduced serum-conditions for 24 hours (2 % FBS in DMEM for HHSC, 0.5 % FBS in DMEM for LX-2). Next, cells were treated with 50 U/mL TGFβ1 or an equivalent volume of 0.1 % BSA in PBS (PBSA) as vehicle control.

For HHSC, TGFβ1 treatment of control GFP cells significantly upregulated the expression of *COL1A1* and *TIMP1* ($p = 0.002$, and $p = 0.024$, respectively) while the expression of *ACTA2* was numerically upregulated but did not reach statistical

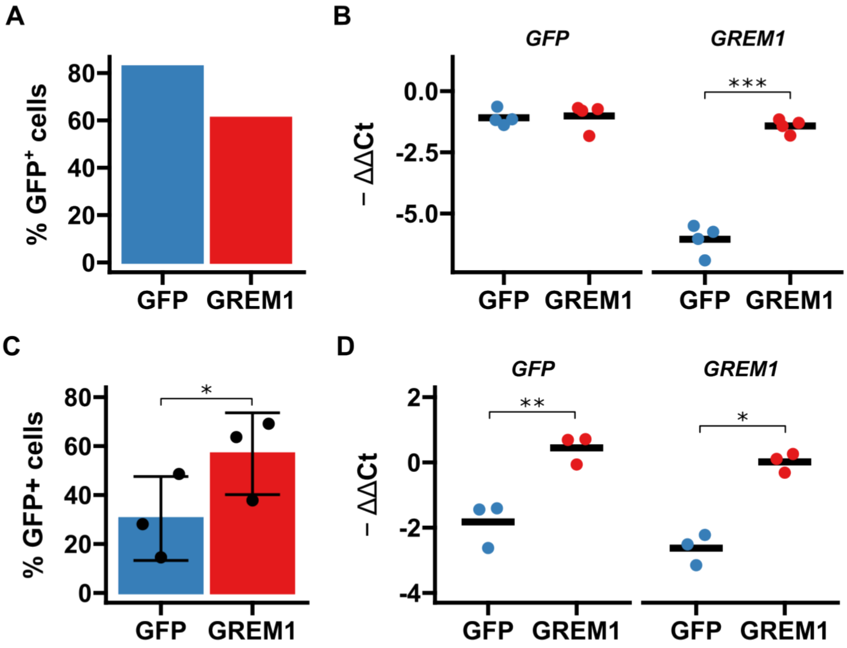

Figure 4.4: Validation of *GREM1* overexpression in LX-2 and HHSC by flow cytometry and RTqPCR. A. Bar graph showing percentage of GFP-positive cells in *GREM1* or *GFP*-control lentivirally transduced LX-2, n = 1. **B.** SybrGreen RTqPCR results for *GFP* and *GREM1* mRNA in lentivirally transduced LX-2, n = 4. **C.** Bar graph showing percentage of GFP-positive cells in *GREM1* or *GFP*-control lentivirally transduced HHSC, n = 3. **D.** SybrGreen RTqPCR results for *GFP* and *GREM1* mRNA in lentivirally transduced HHSC, n = 3.

Data in **A** and **C** are given as individual data points and mean ± SD; data in **B** and **D** are given as individual data points (each representing a different sample measured in duplicate) and mean. $^{*}p < 0.05$, $^{**}p < 0.01$ and $^{***}p < 0.001$ using paired two-sided t-test.

Abbreviations: GFP - green fluorescent protein, GREM1 - Gremlin-1.

significance and exhibited a much greater variance ($p = 0.239$, Figure 4.5A). *GREM1* overexpression led to a slight but non-significant down-regulation of *ACTA2* ($p = 0.113$) while *COL1A1* and *TIMP1* were unaffected ($p = 0.567$, and $p = 0.710$, respectively, Figure 4.5A), and there was no impact on the response of the cells to TGFβs1 stimulation.

Likewise in LX-2 cells, treatment of control cells with TGFβ1 significantly increased the expression of *COL1A1*, *ACTA2*, *TIMP1*, *CCL2* and *LOX* ($p = 4.3\text{x}10^{-7}$, $p = 0.032$, $p = 1.3\text{x}10^{-4}$, $p = 3.9\text{x}10^{-5}$ and $p = 0.005$, respectively, Figure 4.5B). Again, *GREM1* overexpression did not affect either *COL1A1*, *ACTA2* or *TIMP1* expression (all $p > 0.05$). However, in the absence of TGFβ1 treatment, GREM1 overexpression led to a significant, albeit weak, upregulation of *LOX* ($p = 0.02$, Figure 4.5B) and a weak and non-significant increase in *CCL2* and *LOXL1* mRNA expression ($p = 0.11$ and $p = 0.15$, respectively, Figure 4.5B). Similar to that observed for HHSCs, there was no impact of *GREM1s* expression on the response of the cells to TGFβs1 stimulation.

In LX-2 cells, we additionally measured the expression of genes involved in BMP signalling pathways. TGFβ1 treatment significantly reduced the expression of *BMP4*, *SMAD3*, *SMAD6* and *SMAD9* ($p = 0.00013$, $p = 0.003$, $p = 0.038$ and $p = 0.035$, respectively), and significantly increased the expression of *BMPR1B*, *BMPR2*, *ID1*, *INHBA*, *SMAD1* and *SMAD7* ($p = 0.0002$, $p = 0.0002$, $p = 0.002$ and $p = 0.0004$ and $p = 1.2\text{x}10^{-6}$ respectively, Figure 4.5C). *ID2* was also numerically increased, but did not reach statistical significance ($p = 0.056$). *GREM1* overexpression led to a slight but significant reduction of *BMP4*, *SMAD6* and *SMAD7* in vehicle-control treated cells ($p = 0.016$, $p = 0.013$ and $p = 0.032$, respectively) and significantly reduced *INHBB* expression independently of TGFβ1 treatment ($p = 2.4 \times 10^{-5}$). *BMP7* and *SMAD1* were overall upregulated in response to *GREM1* overexpression ($p = 0.008$ and $p = 0.007$, Figure 4.5C), while *SMAD6* was downregulated ($p = 0.01$, Figure 4.5C).

In light of these qPCR results, we decided to screen for overall transcriptional changes in response to the overexpression of GREM1 in LX-2 and HHSC, enabling us to study potential effects on pathways further downstream from GREM1 signalling. For this purpose, we performed Lexogen QuantSeq 3'-RNA sequencing on lentivirally transduced cells without TGFβ1 treatment. Unfortunately, two samples, LX2_3_GREM1 and HHSC_1_GREM1, were severe outliers in principal component analysis (Figure 4.6). Going back to the quality control metrics, we found that for these two outlier samples, DNA yield in the library preparation was much lower compared to other samples (6.98 nM and 29.3 nM, compared to about 65 to 105 nM in other samples, table 4.1). Therefore, we concluded that technical reasons were responsible for these anomalies, and removed these samples and their paired counterparts from subsequent analyses.

Volcano plots and heatmaps visualising results of differentially expressed gene (DEG) analysis in LX-2 and HHSC are shown in Figures 4.7 and 4.8, respectively. The results of the DEG analysis for the top 100 (LX-2) or top 50 (HHSC) genes are given in the Appendix A.2 in tables A.3 and A.4, respectively. In summary, overexpression of *GREM1* only changed the expression of a few genes with no apparent connection to distinct pathways or cellular functions, both in gene set over-representation tests and gene set enrichment analysis. There also was no overlap between significantly regulated genes in LX-2 or HHSC.

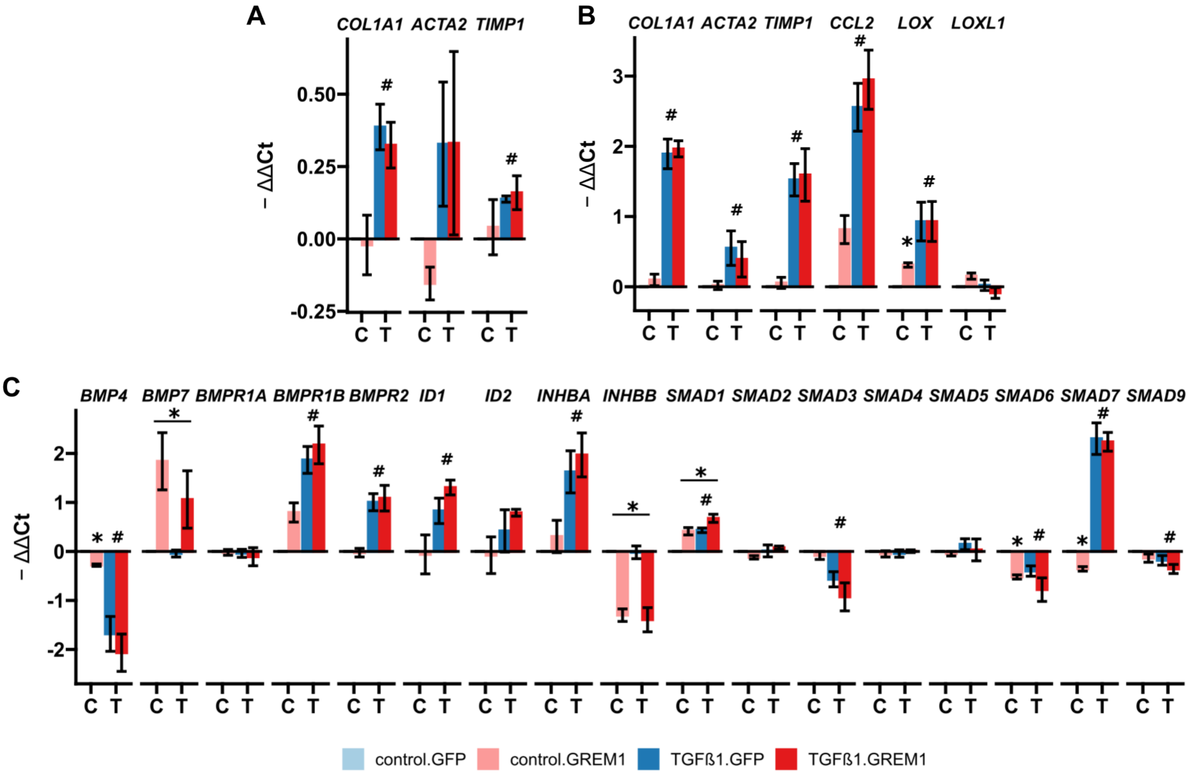

Figure 4.5: RTqPCR on lentivirally transduced, *GREM1* or *GFP*-control overexpressing primary HHSC (A.) and LX-2 (B. and C.). **A.** Fibrogenic gene expression in lentivirally transduced HHSC. **B.** Fibrogenic gene expression in lentivirally transduced LX-2. **C.** BMP signalling-related gene expression in lentivirally transduced LX-2.

All data are given as mean ± SEM of -ΔΔ Ct relative to GFP and vehicle control and normalised to the expression of SRSF4. $^*p < 0.05$ in GREM1 vs GFP-control, # $p < 0.05$ in TGFβ1 vs vehicle control using repeated measures Two-way ANOVA and post-hoc paired t-test (HHSC) or unpaired Welch t-test (LX-2) for pre-selected comparisons and Bonferroni-Holm adjustment. C - control-treated, T - 50 U/mL TGFβ1-treated.

Abbreviations: ACTA2 - alpha smooth muscle actin, BMP - bone morphogenetic protein, BMPR1A/B - BMP receptor 1A/B, BMPR2 - BMP receptor 2, COL1A1 - collagen type I alpha 1, ID1/2 - inhibitor of DNA binding 1/2, INHBA - inhibin beta A, INHBB - inhibin beta B, LOX - lysyl oxidase, LOXL1 - lysyl oxidase homolog 1, TIMP1 - tissue inhibitor of metalloproteinases 1.

Table 4.1: Main quality metrics for QuantSeq 3' mRNA sequencing of lentivirally transduced LX-2 and primary HHSC.

sample	A260/A280	A260/A230	RIN	reads		mapping rate
				before filtering	after filtering	
LX2_1_GFP	2.008	2.174	9.2	15.20M	14.60M	80.46%
LX2_1_GREM1	2.000	2.217	9.5	19.17M	18.18M	79.96%
LX2_2_GFP	2.070	2.565	9.9	20.90M	20.08M	81.32%
LX2_2_GREM1	2.061	1.578	9.9	18.43M	17.71M	82.25%
LX2_3_GFP	2.057	3.130	10	14.34M	13.78M	85.01%
LX2_3_GREM1	2.028	3.460	10	11.32M	10.15M	68.51%
HHSC_1_GFP	1.976	2.187	9.9	15.11M	14.56M	88.66%
HHSC_1_GREM1	1.954	2.000	10	13.38M	11.92M	75.08%
HHSC_2_GFP	1.941	1.980	10	13.07M	12.60M	86.52%
HHSC_2_GREM1	2.000	1.660	10	17.81M	17.22M	88.94%
HHSC_3_GFP	2.000	1.800	9.9	15.04M	14.32M	87.89%
HHSC_3_GREM1	2.000	1.778	9.8	14.72M	14.08M	88.56%

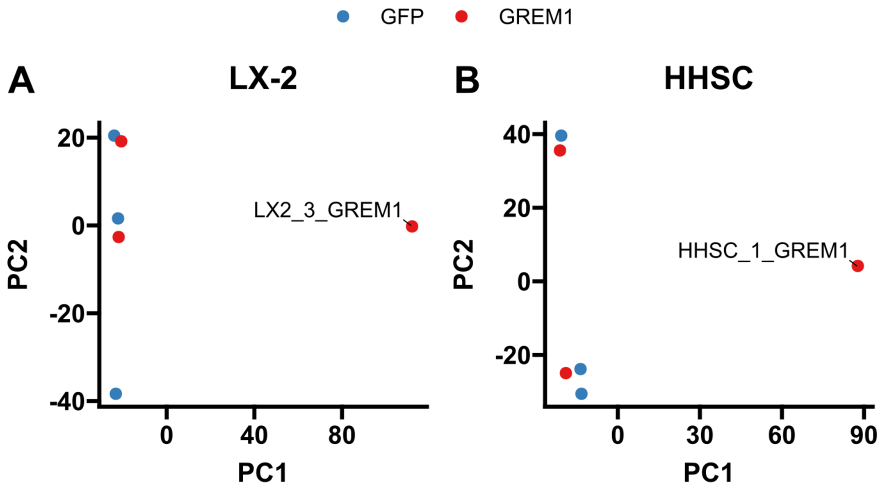

Figure 4.6: PCA analysis for *GREM1* overexpressing LX-2 and HHSC. Scatter plots of the first two principal components (PC) **A.** in LX-2 **B.** and HHSC lentiviral transduced cells. The outliers in each PCA plot are indicated and named.

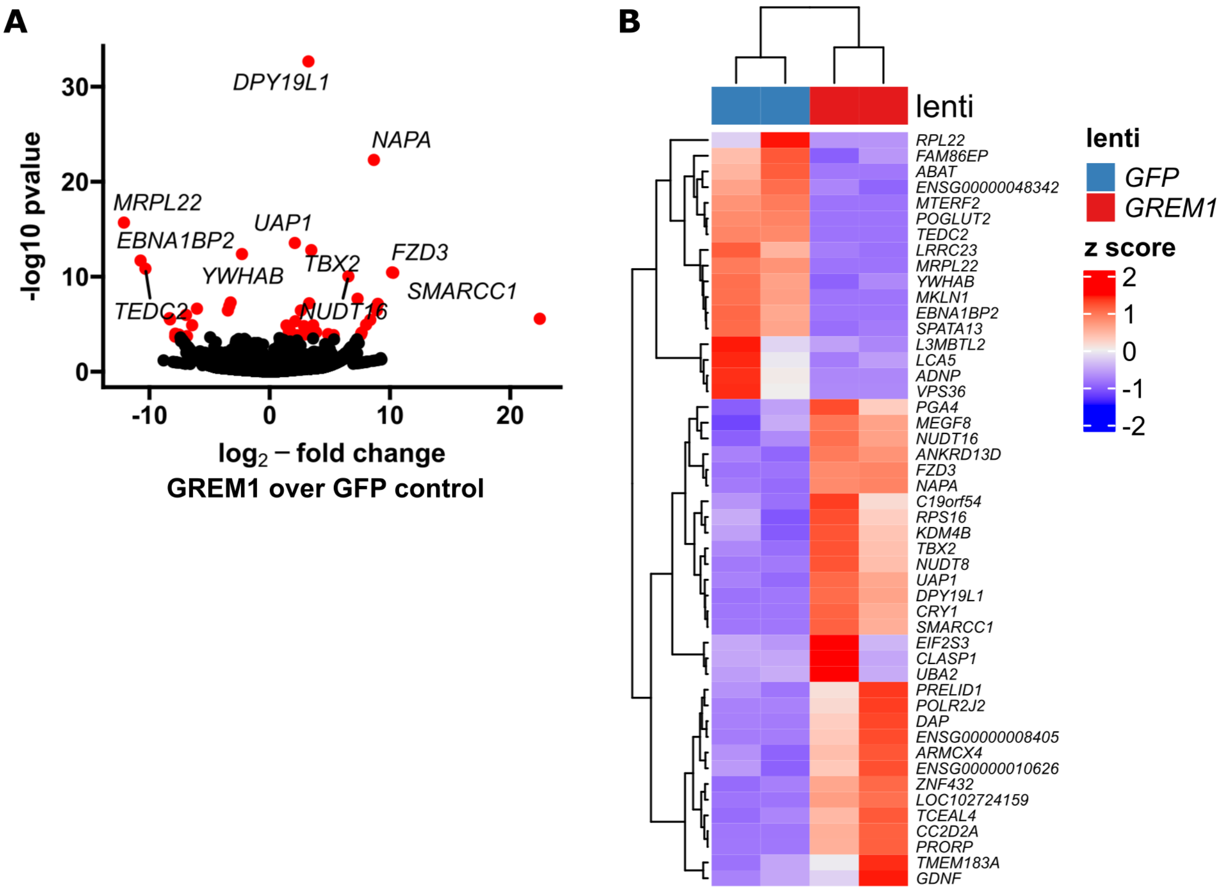

Figure 4.7: RNA sequencing results for *GREM1* overexpressing LX-2 A. Volcano plot showing $\log_2$-fold changes and the negative decadic logarithm of unadjusted p-values for all expressed genes. Significantly regulated genes (i.e. adj. p-value < 0.05) are labelled and marked in red. **B.** Heatmap showing centred and scaled gene expression for significantly regulated genes with rows representing genes and columns representing individual experiments.

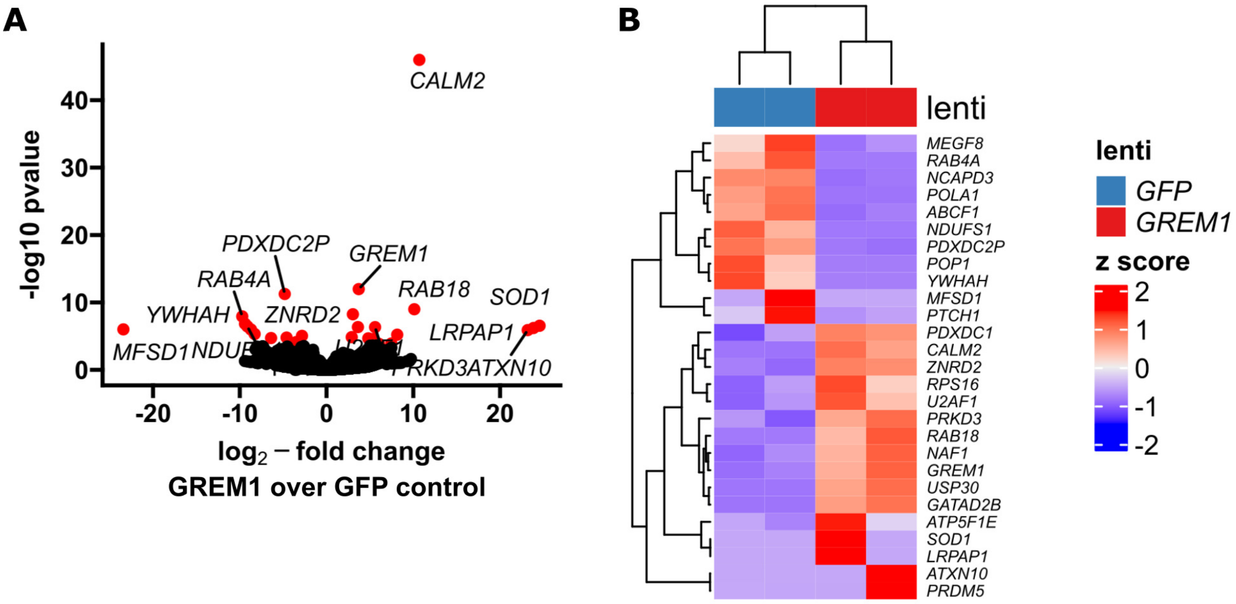

Figure 4.8: RNA sequencing results for GREM1 overexpressing primary HHSC **A.** Volcano plot showing $\log_2$-fold changes and the negative decadic logarithm of unadjusted p-values for all expressed genes. Significantly regulated genes (i.e. adj. p-value < 0.05) are labelled and marked in red. **B.** Heatmap showing centred and scaled gene expression for significantly regulated genes with rows representing genes and columns representing individual experiments.

Contraction assays

Cell contractility is an important hallmark in the transdifferentation of quiescent hepatic stellate cells into myofibroblast-like cells. Collagen contraction assays are a commonly used tool for the investigation of cultured cells' ability to modify and contract their surrounding extracellular matrix.

In order to investigate the effect of GREM1 overexpression on the contractility of LX-2 cells, we seeded these cells in a collagen cushion and after proper setting of the collagen matrix, the collagen cushion was released from the well plate and the cells were treated with either vehicle control, 10 ng/mL platelet-derived growth factor (PDGF), 5 U/mL or 50 U/mL TGFβ1. After 24 hours incubation, culture plates were imaged on a

ChemiDoc MP imaging station and subsequently measured using Fiji (ImageJ). For a detailed protocol please see section 2.7.2 on page 57.

As shown in Figure 4.9, *GREM1* overexpression led to an overall decrease in contractility of LX-2 cells, independent of the treatment condition (all $p < 0.05$). TGFβ1 at a concentration of 50 U/mL increased contractility compared to vehicle control, but only in *GFP*-control cells ($p = 0.028$).

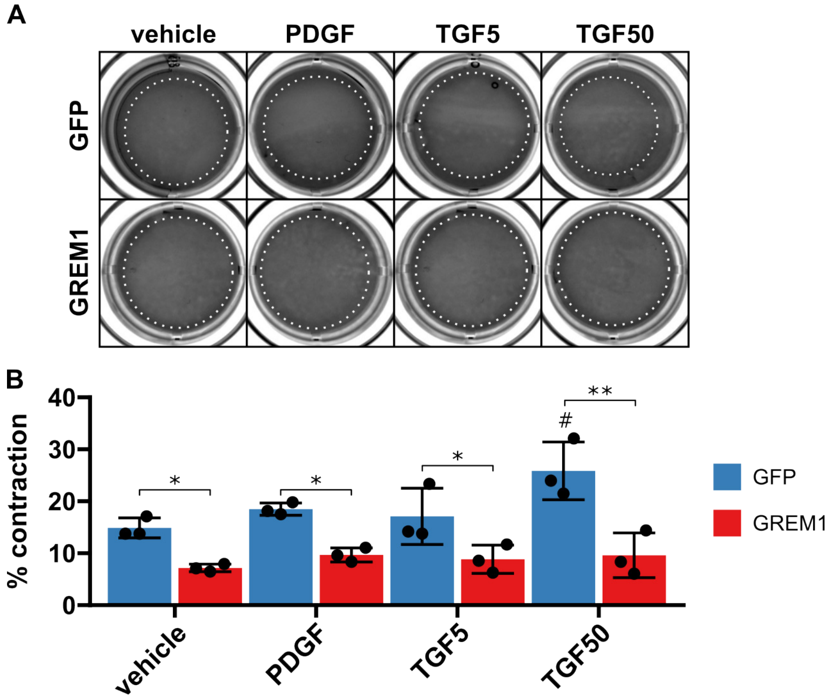

Figure 4.9: Contraction assay in lentivirally transduced LX-2 cells. A. Representative images of collagen cushions 24 hours after stimulation. Wells are arranged by overexpression vector (rows) and treatment condition (columns). Dashed white line indicates collagen cushion area. **B.** Column diagram representing the quantified relative contraction measured as the percent reduction in collagen surface area, for each condition. Data are given as mean ± SD and single data points (each representing an individual experiments performed in technical duplicate). $^*p < 0.05$, $^{**}p < 0.01$ for indicated comparison and $\#p < 0.05$ compared to vehicle control using Two-Way ANOVA with post-hoc Bonferroni-Holm adjustment.
Abbreviations: GFP - green fluorescent protein, GREM1 - Gremlin-1, PDGF - platelet derived growth factor, TGF5/50 - transforming growth factor 5/50 U/mL.

Scratch wound assays

Another important feature of activated hepatic stellate cells is increased motility, which enables cells to migrate to sites of tissue injury. Different assays have been used in the literature to assess cell migration. Among these are scratch-wound assays, which are robust, easy to set up and therefore good tools for screening purposes.

The detailed protocol can be found in the methods section (2.7.3) on page 58. Briefly, *GFP*-control and *GREM1*-overexpressing LX-2 cells were seeded on 24-well plates and grown until confluent. Using a 100 µL pipette tip, a vertical scratch was then applied to the monolayer and closure of the wound was imaged on the CelliQ live-cell imager for up to 72 hours. The wound width was then measured using a custom-made ImageJ plugin (see A.4, page 226).

Figure 4.10A shows representative images of a wound closure in untreated LX-2 cells over the course of 72 hours. Wound closure was then analysed using non-linear regression analysis. The time course of the wound width followed a Gompertz function (Figure 4.10B), which is a sigmoid curve characterised by an asymmetric growth rate, where the asymptote is reached more gradually on the right side of the curve. The wound closure rate for each time point was calculated as the first derivative function of the wound width over time (Figure 4.10C).

Overall, we did not observe any consistent effect of GREM1-overexpression on the wound closure dynamics in LX-2 cells. Maximum wound closure rates were similar between *GFP*-control and *GREM1* overexpressors, both in untreated and PDGF-

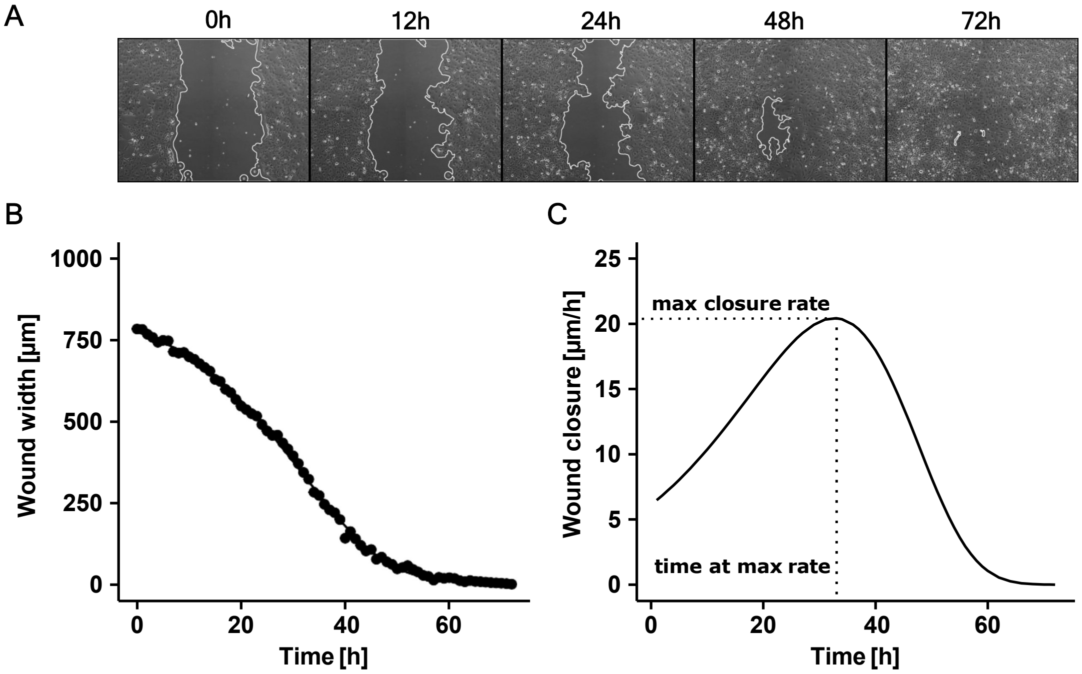

Figure 4.10: Methodology of scratch-wound assay analysis. A. Representative images of wound closure in untreated LX-2 cells over the course of 72 hours. **B.** Wound width over time in a representative experiment, where each dot represents a single data point. A Gompertz curve was fitted to the graph (continuous line). **C.** The first derivative of the wound width over time was used to calculate the wound closure rate for each time point. The continuous line gives the first derivative function, with the maximum closure rate and time needed to reach the maximum rate indicated.

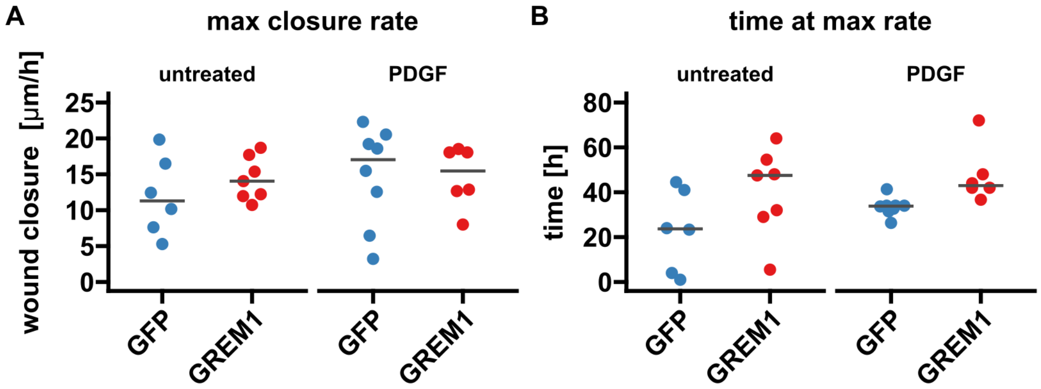

Figure 4.11: Scratch wound healing assay on lentivirally transduced LX-2 cells. **A.** Maximum wound closure rate in µm/h. **B.** Time passed until maximum wound closure rate was reached in hours.
Data are given as individual data points (each representing an indipendent experiment performed in technical duplicate) and median. Differences were not statistically significant using Kruskal-Wallis-test and post-hoc Dunn correction.
Abbreviations: GFP - green fluorescent protein, GREM1 - Gremlin-1, PDGF - platelet derived growth factor.

stimulated cells ($p > 0.05$, Figure 4.11A). Likewise, the time needed until the maximum wound closure rate was reached, was not significantly affected although numerically longer in GREM1 overexpressing cells ($p > 0.05$, Figure 4.11B).

4.2.2 Characterisation of therapeutic anti-Gremlin-1 antibodies

Given the potential role of Gremlin-1 in hepatic fibrogenesis in MASH, our collaboration partners at Novo Nordisk developed therapeutic anti-Gremlin-1 antibodies to test whether neutralisation of Gremlin-1 can reduce fibrosis in models of MASH. All data on characterisation of the therapeutic antibodies in the following was generated by Novo Nordisk and is given here for the sake of completeness and context. The antibodies are named according to the Novo Nordisk internal numbering with suffixes added to indicated heparin-binding properties. As described earlier, Gremlin-1 contains a heparin-binding domain and shows avid binding to glycosaminoglycans such as heparan-sulfate. HD indicates heparin-displacing, meaning that the antibody removes Gremlin-1 from its heparin binding, and ND non-displacing properties of the respective antibody.

The generated antibodies were highly effective in blocking recombinant human Gremlin-1 from binding to BMP4 in a Gremlin-1/BMP4 inhibition ELISA (IC50 = 2.7 - 3.1×10^{-9} M, Figure 4.12A) and in a BRE-Luc BMP reporter gene assay (EC50 = 1.3 - 1.4×10^{-8} M, Figure 4.12B). Treatment of LX-2 cells with BMP4 increased SMAD1 phosphorylation, which was prevented by the addition of recombinant Gremlin-1, and anti-Gremlin-1 antibodies but not isotype control effectively restored SMAD1 phosphorylation in the presence of Gremlin-1 in a dose-dependent manner (KD = 2.0 - 4.0 nM, Figure 4.12C). Antibodies differed in their binding stochastics, as determined by size exclusion chromatography. The 0032:ND/0568:ND antibodies formed complexes with Gremlin-1 dimers in a 2:2 ratio, while the 0030:HD compound bound Gremlin-1 dimers in a 1:1 ratio (Figure 4.12D).

Anti-Gremlin-1 antibodies had different effects with regards to heparin binding. Using a fluorescence polarization assay we found that Gremlin-1 immobilised heparin with high affinity ($KD_{[Grem1\ alone]}$ = 10.20 nM, Figure 4.12E), confirming previous chromatography findings (see Figure 3.9). While the 0568:ND (parent antibody of 0032:ND) compound did not affect heparin binding of Gremlin-1, the 0030:HD antibody reduced the affinity ($KD_{[Grem1]}$ = 13.54 nM, $KD_{[0568:ND]}$ = 19.56 nM vs $KD_{[0030:HD]}$ = 118.65 nM, Figure 4.12E). In line with these results, Atto-532-conjugated Gremlin-1 bound to the cell surface of LX-2 cells, which was prevented by the 0030:HD antibody but not 0032:ND or

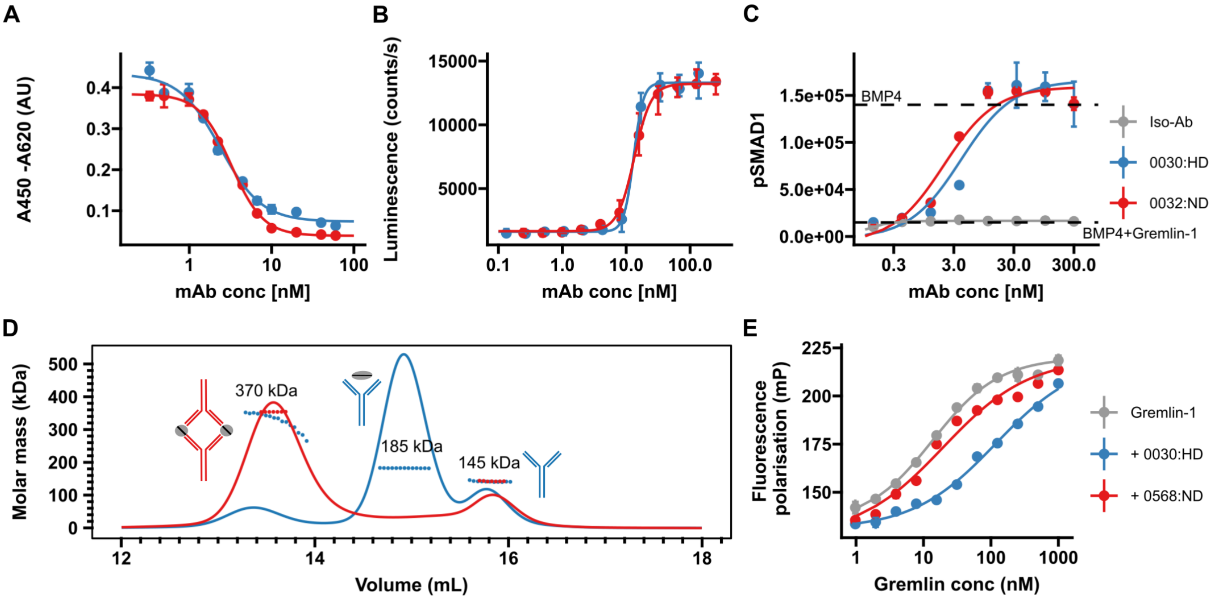

Figure 4.12: Characterisation of heparin- (0030:HD) and non-heparin-displacing (0032:ND/0568:ND) therapeutic anti-Gremlin-1 antibodies. **A.** Gremlin-1/BMP4 inhibition ELISA. BMP4-coated microplates were incubated with mixes of biotinylated Gremlin-1 and anti-Gremlin-1 antibody and BMP4-bound Gremlin-1 detected using streptavidin-HRP complex. **B.** C2C12 BMP responsive element-Luc reporter gene assay. BMP reporter C2C12 cells were treated with serial dilutions of anti-Gremlin-1 antibody with recombinant human Gremlin-1 and BMP4. Increased luminescence indicates higher BMP4 activity. **C.** SMAD1 phosphorylation assay on LX-2 cells. LX-2 cells were treated with BMP4, Gremlin-1 and serially diluted anti-Gremlin-1 antibody, and phosphorylated SMAD1 (pSMAD1) was measured by alphaLISA. **D.** Size-exclusion chromatography for Gremlin-1 in combination with heparin-displacing (0030:HD) or non-heparin-displacing (0032:ND) anti-Gremlin-1 antibody. The graph shows UV signal (continuous line) and estimated molar mass (points) on the y-axis depending on the eluting volume on the x-axis. Text annotations give the estimated molar mass corresponding to each peak. **E.** Fluorescence polarisation heparin-binding assay. Serial dilutions of Gremlin-1 were incubated with fixed amounts of fluorescein-heparan sulfate and 1.5-fold molar excess anti-Gremlin-1 antibody.
A.-C. and E: Data are given as mean ± SD and were fitted to a 4-parameter log-logistic curve. Iso-Ab, Isotype control
Data generated by Novo Nordisk.

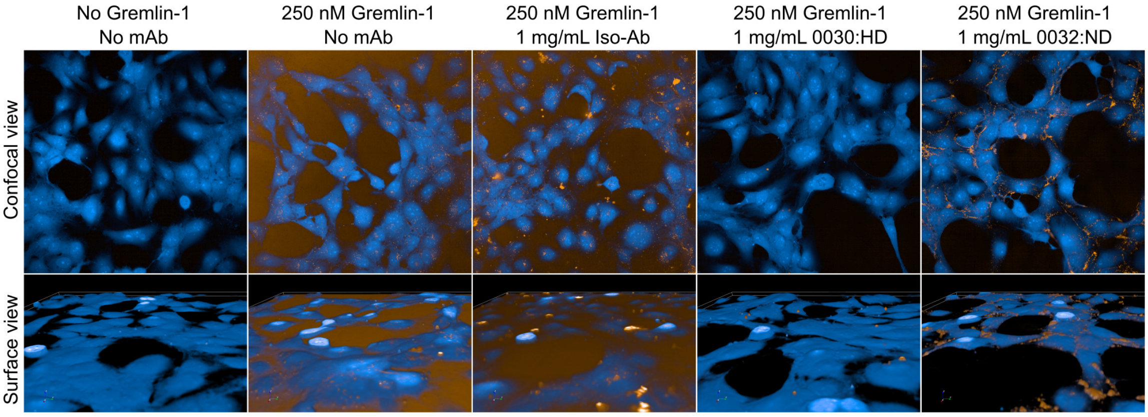

Figure 4.13: Gremlin-1 cell association assay. The upper panel shows the cell surface view and the lower panel the three-dimensional confocal view for Atto-532-labelled Gremlin-1 (yellow-gold) on LX-2 cells (labelled with CellMask Blue). Representative images for different combinations of 250 nM Gremlin-1 and isotype or heparin-displacing and non-displacing anti-Gremlin-1 antibodies are given. Iso-Ab, Isotype control
Images and data generated by Novo Nordisk.

isotype control (Figure 4.13). Size exclusion chromatography on mixes of Gremlin-1, heparin and anti-Gremlin-1 antibodies revealed that the 0030:D antibody formed 1:1 complexes with free Gremlin-1 not involving heparin, while the 0032:ND antibody captured heparin-bound Gremlin-1, leading to the formation of higher-order complexes that were insoluble and precipitated (Figure 4.14).

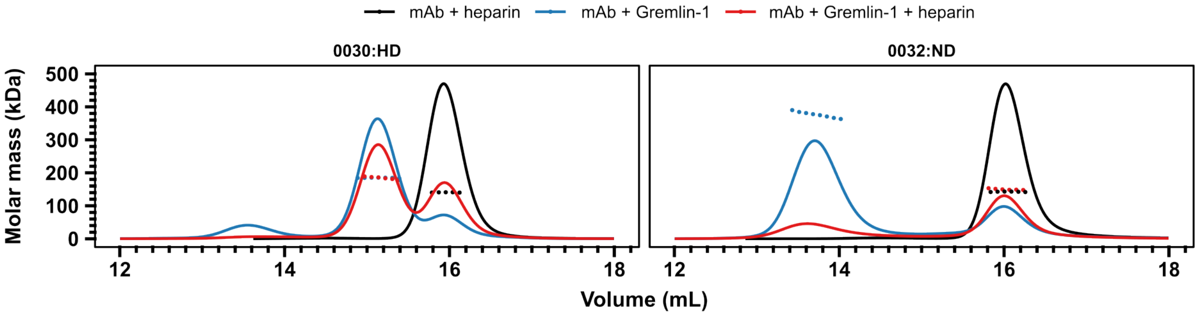

Figure 4.14: Size-exclusion chromatography for Gremlin-1-anti-Gremlin-1-heparin complexes. Different combinations of heparin-displacing (0030:HD, **left**) or non-displacing (0032:ND, **right**) therapeutic anti-Gremlin-1 antibodies with heparin alone, Gremlin-1 alone or Gremlin-1 and heparin were run on a size exclusion chromatography column. The graph shows UV signal (continuous lines) and estimated molar mass (points) on the y-axis depending on the eluting volume on the x-axis.
Data generated by Novo Nordisk.

4.2.3 Effect of anti-Gremlin-1 treatment on fibrotic cells *in vitro*

After validating the therapeutic antibodies, we first wanted to verify their therapeutic applicability using primary human fibrogenic liver cells, namely primary human hepatic stellate cells (HHSC) and primary hepatic myofibroblasts (MF). While overexpression of GREM1 elicited no response, there potentially already is sufficient Gremlin-1 present in untreated cells and therefore we wanted to investigate the effects of inhibiting Gremlin-1. For this purpose we used the human heparin-displacing antibody (0030:HD) only and compared its effects to recombinant human IgG1.1 as isotype control.

Fibrogenic gene expression

We first performed RTqPCR on lysates from primary HHSC and MF treated with anti-Gremlin-1 or isotype control antibodies at 100 nM concentration, with or without TGFβ1 treatment. Inhibition of TGFβ type I receptor (ALK5) using a small molecular ALK5 inhibitor (ALK5i) served as a positive control.

In HHSC, ALK5i significantly reduced the expression of *COL1A1* ($p = 0.0361$), while *ACTA2* and *TIMP1* were unaffected ($p = 0.692$ and $p = 0.931$, respectively, Figure 4.15). Anti-Gremlin-1 treatment did not affect the expression of *COL1A1*, *ACTA2* or *TIMP1* expression, neither with nor without TGFβ1 treatment (all $p > 0.05$, Figure 4.15).

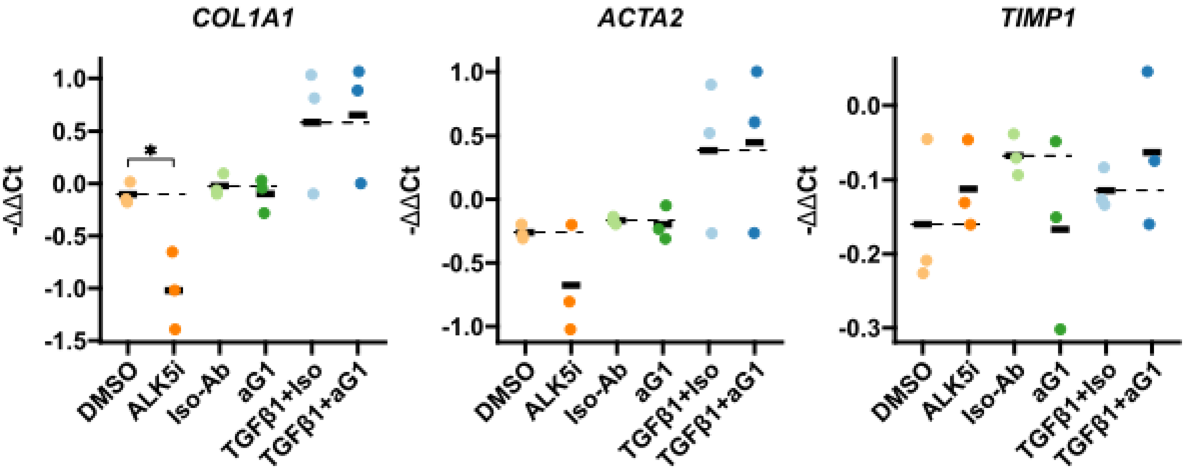

Figure 4.15: RTqPCR results for fibrogenic marker genes in primary human hepatic stellate cells treated with anti-Gremlin-1 (0030:HD) or isotype control antibodies. Data are given as individual data points (each representing a different experiment using an individual cell donor and measured in duplicate) and mean for -ΔΔCt relative to untreated control and normalised to the expression of SRSF4. *$p < 0.05$ using One-Way ANOVA and post-hoc paired t-tests for pre-defined comparisons with Bonferroni-Holm adjustment.
Abbreviations: ACTA2 - alpha smooth muslce actin, aG1 - anti-Gremlin-1, ALK5i - ALK5 inhibitor, COL1A1 - collagen type 1 alpha 1, DMSO - dimethyl sulfoxide, Iso - Isotype control, TGFβ1 - transforming growth factor beta 1, TIMP1 - tissue inhibitor of metalloproteinases 1.

Similarly in primary MF, ALK5i led to a numerical but non-significant reduction of *COL1A1* and *TIMP1*, while *ACTA2* was not affected ($p = 0.123$, $p = 0.056$ and $p = 0.968$, respectively, Figure 4.16). Again, independent of stimulation with TGFβ1, anti-Gremlin-1 treatment had no effect on *COL1A1*, *ACTA2* and *TIMP1* expression (all $p > 0.762$, Figure 4.16).

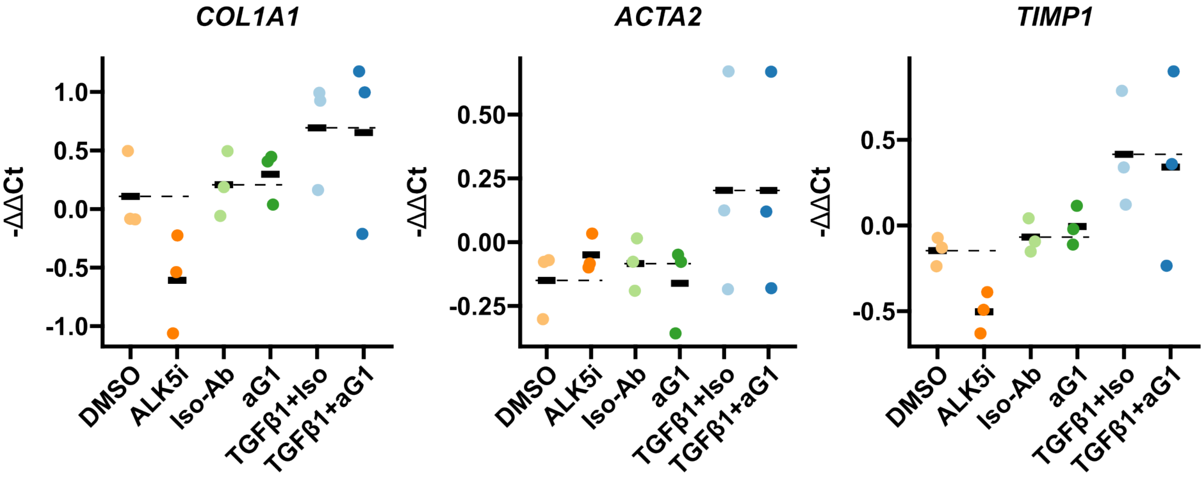

Figure 4.16: RTqPCR results for fibrogenic marker genes in primary human hepatic myofibroblasts treated with anti-Gremlin-1 (0030:HD) or isotype control antibodies. Data are given as individual data points (each representing a different experiment using an individual cell donor measured in duplicate) and mean for -ΔΔ Ct relative to untreated control and normalised to the expression of SRSF4. Statistical testing was done using One-Way ANOVA and post-hoc paired t-tests for pre-defined comparisons with Bonferroni-Holm adjustment. aG1, anti-Gremlin-1; Iso, Isotype control

Abbreviations: ACTA2 - alpha smooth muslce actin, aG1 - anti-Gremlin-1, ALK5i - ALK5 inhibitor, COL1A1 - collagen type 1 alpha 1, DMSO - dimethyl sulfoxide, Iso-Ab - Isotype control, TGFβ1 - transforming growth factor beta 1, TIMP1 - tissue inhibitor of metalloproteinases 1.

Contraction assays

We also performed collagen matrix contraction assays on parent LX-2 cells to investigate the effects of recombinant human Gremlin-1 and the therapeutic anti-Gremlin-1 antibody on the contractile myofibroblast phenotype. As can be seen in Figure 4.17, while 50/mL TGFβ1 led to increased LX-2 contractility, neither recombinant Gremlin-1 nor anti-Gremlin-1 antibody had any effect on matrix contraction.

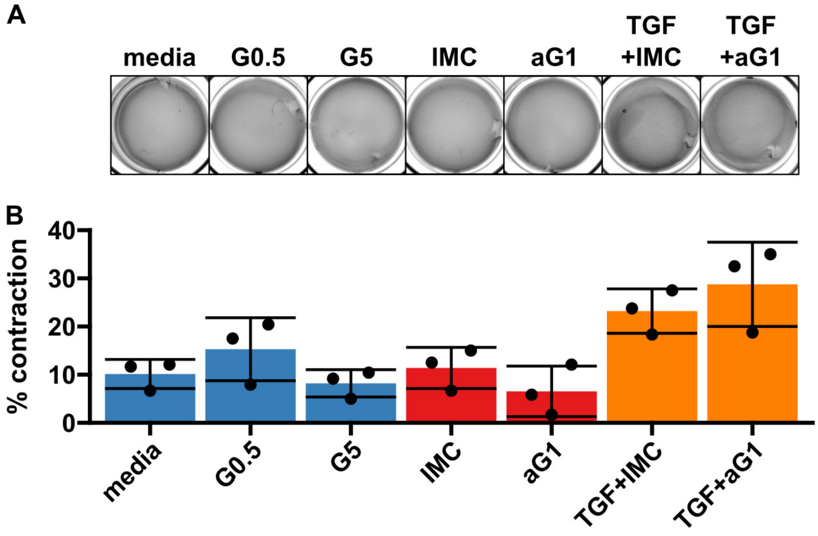

Figure 4.17: Contraction assay in LX-2 cells upon gremlin-1 or anti-gremlin-1 treatment. A. Representative images of collagen cushions 24 hours after stimulation. Treatment conditions are given on the top. **B.** Column diagram representing the quantified relative contraction measured as the percent reduction in collagen surface area, for each condition. Data are given as mean ± SD and single data points for each experiment. Each experiment was run in technical duplicates.
Abbreviations: ACTA2 - alpha smooth muslce actin, aG1 - anti-Gremlin-1, ALK5i - ALK5 inhibitor, COL1A1 - collagen type 1 alpha 1, DMSO - dimethyl sulfoxide, G0.5 - 0.5 µg/mL Gremlin-1, G5 - 5 µg/mL Gremlin-1, IMC - isotype matched control, TGFβ1 - transforming growth factor beta 1, TIMP1 - tissue inhibitor of metalloproteinases 1.
The heparin-displacing anti-Gremlin-1 antibody 0030:HD was used at a concentration of 100 nM for this experiment.

Scratch wound assays

Testing the effects of anti-Gremlin-1-treatment on LX-2 cell migration, we performed scratch wound assays on cells treated with anti-Gremlin-1, isotype control or vehicle control in the absence or presence of PDGF co-treatment. Similar to results for lentivirally transduced LX-2 cells, anti-Gremlin-1 treatment did not have any significant effect on maximum closure rate or time until the maximum closure rate was achieved ($p > 0.05$, Figure 4.18A and B). However, anti-Gremlin-1 treatment led to a numerical, albeit non-significant, reduction in the time to maximum wound closure rate ($p = 0.87$, Figure 4.18B).

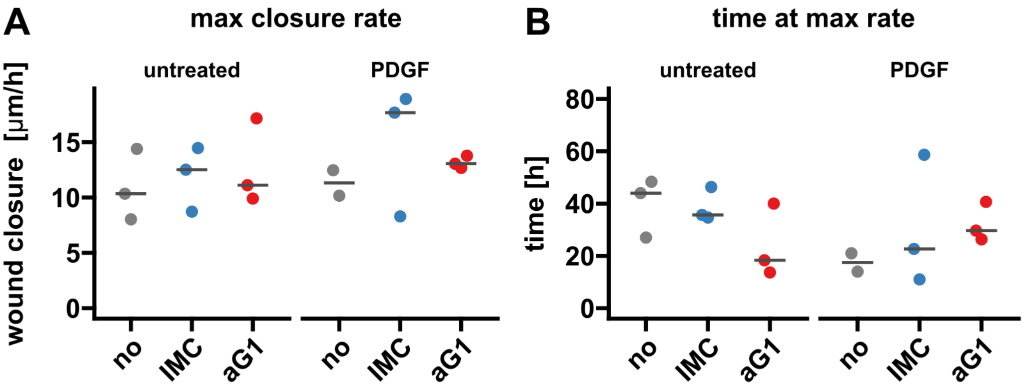

Figure 4.18: Scratch wound healing assay on parent LX-2 cells. A. Maximum wound closure rate in µm/h. **B.** Time passed until maximum wound closure rate was reached in hours.
Data are given as individual data points (each representing a separate experiment run in technical duplicate) and median. Differences were not significantly different using Kruskal-Wallis-test and post-hoc Dunn correction.
Abbreviations: aG1 - anti-Gremlin-1, IMC - Isotype matched control, PDGF - platelet-derived growth factor.
The heparin-displacing anti-Gremlin-1 antibody 0030:HD was used at a concentration of 100 nM for this experiment.

4.2.4 Effect of anti-Gremlin-1 treatment on MASH fibrosis in rats

Our experiments to this point were performed on monolayer cell culture, which are not representative of whole body systems and published data still suggests that Gremlin-1 has a role in the fibrotic response. Therefore, we used a rat model of MASH to test the effects of targeting Gremlin-1 on liver inflammation and fibrosis *in vivo*. The antibodies used in the rat model were derived from the human antibodies described above by grafting the variable regions of the heavy and light chains onto a murine IgG1 scaffold. All animal experiments were performed by our collaboration partner Novo Nordisk and the results are presented here for the sake of completeness and context. Male Sprague Dawley rats were fed a CDAA-HFD for 12 weeks. In the latter 6 weeks, therapeutic ”murinised” antibodies (heparin-displacing 2021:HD or non-displacing 0361:ND) or isotype control murine IgG1 were injected subcutaneously once every week. Blood and tissue were then analysed for markers of hepatic injury and liver fibrosis (Figure 4.19A). Figures 4.19, 4.20 and 4.22 give the results for the highest antibody concentrations used, only. Extended data for all antibody concentrations used in this experiment can be found in Appendix A.3.

As expected, animals on the CDAA-HFD developed reduced body weight ($p = 1.12 \times 10^{-8}$) and displayed a MASH phenotype with increased levels of alanine aminotransferase (ALT) ($p = 2.07 \times 10^{-4}$), increased liver weight ($p = 1.87 \times 10^{-10}$), steatosis ($p = 3.35 \times 10^{-15}$), picrosirius red (PSR) positive fibrosis area ($p = 4.69 \times 10^{-8}$) and CD45$^+$ immune cell infiltrates ($p = 4.55 \times 10^{-5}$) (Figure 4.19B-H).

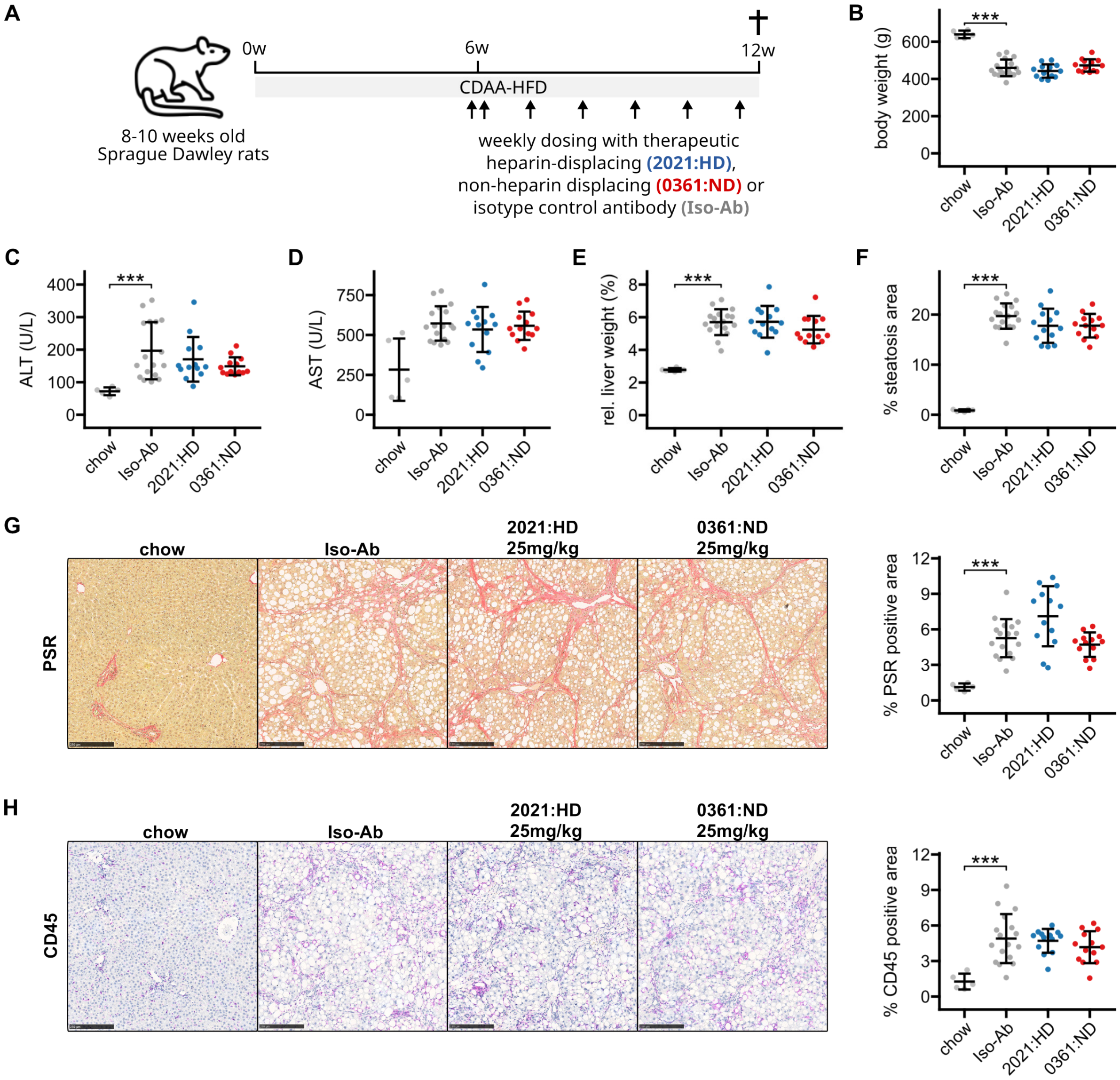

Figure 4.19: Results for anti-Gremlin-1 antibody treatment on CDAA-HFD induced MASH and fibrosis in rats. **A.** Schematic showing the study design for the animal experiment. **B.** Quantification of body weight in grams at the end of the study. **C.** Quantification of plasma ALT in U/L. **D.** Quantification of plasma aspartate aminotransferase (AST) in U/L. **E.** Quantification of relative liver weight as the percentage of total body weight. **F.** Quantification of histological liver steatosis area in percent. **G.** Left panel shows representative histological images for picrosirius red staining for different treatment conditions. Scale bars represent 250 µm. Right panel shows quantification of picrosirius red staining (PSR) in percent of total area. **H.** Left panel shows representative histological images for CD45 IHC for different treatment conditions. Scale bars represent 250 µm. Right panel shows quantification of CD45 IHC in percent of total area.
Data are given as individual data points (each representing a different animal sample measured in duplicate) mean ± SD for n=5 (chow), n=17 (Iso-Ab) and n=13 (2021:HD & 0361:ND) animals per group. Significance was determined by multiple two-sided paired Welch t-tests against Iso-Ab, followed by Bonferroni-Holm adjustment (***$p < 0.001$). Images and data generated by Novo Nordisk.

We also assessed gene expression changes in the CDAA-HFD model in response to therapeutic antibody. In line with immunohistochemistry results, the CDAA-HFD led to a significantly increased expression of *Grem1*, fibrosis marker genes *Col1a1*, *Col3a1*, *Timp1* and *Tgfb1*, as well as *Tnf* as a marker of the inflammatory response (all $p < 0.001$, Figure 4.21). However, neither heparin-displacing nor non-displacing antibody had any effect on gene expression (all $p > 0.05$, Figure 4.21). Results for all antibody concentrations are given in the appendix (Table A.6).

To assess target engagement, circulating concentrations of Gremlin-1 were measured using a Novo Nordisk in-house developed alpha-LISA. Circulating Gremlin-1 was undetectable in all animals, except for those treated with the highest dose of heparin-displacing antibody (Figure 4.22 and Figure A.1). Still, despite target engagement in the high-dose displacing antibody group, neither the heparin-displacing nor the non-displacing therapeutic anti-Gremlin-1 antibody had any significant impact on markers of liver injury, inflammation or fibrosis (Figure 4.19B-H and Figure 4.20, $p > 0.05$).

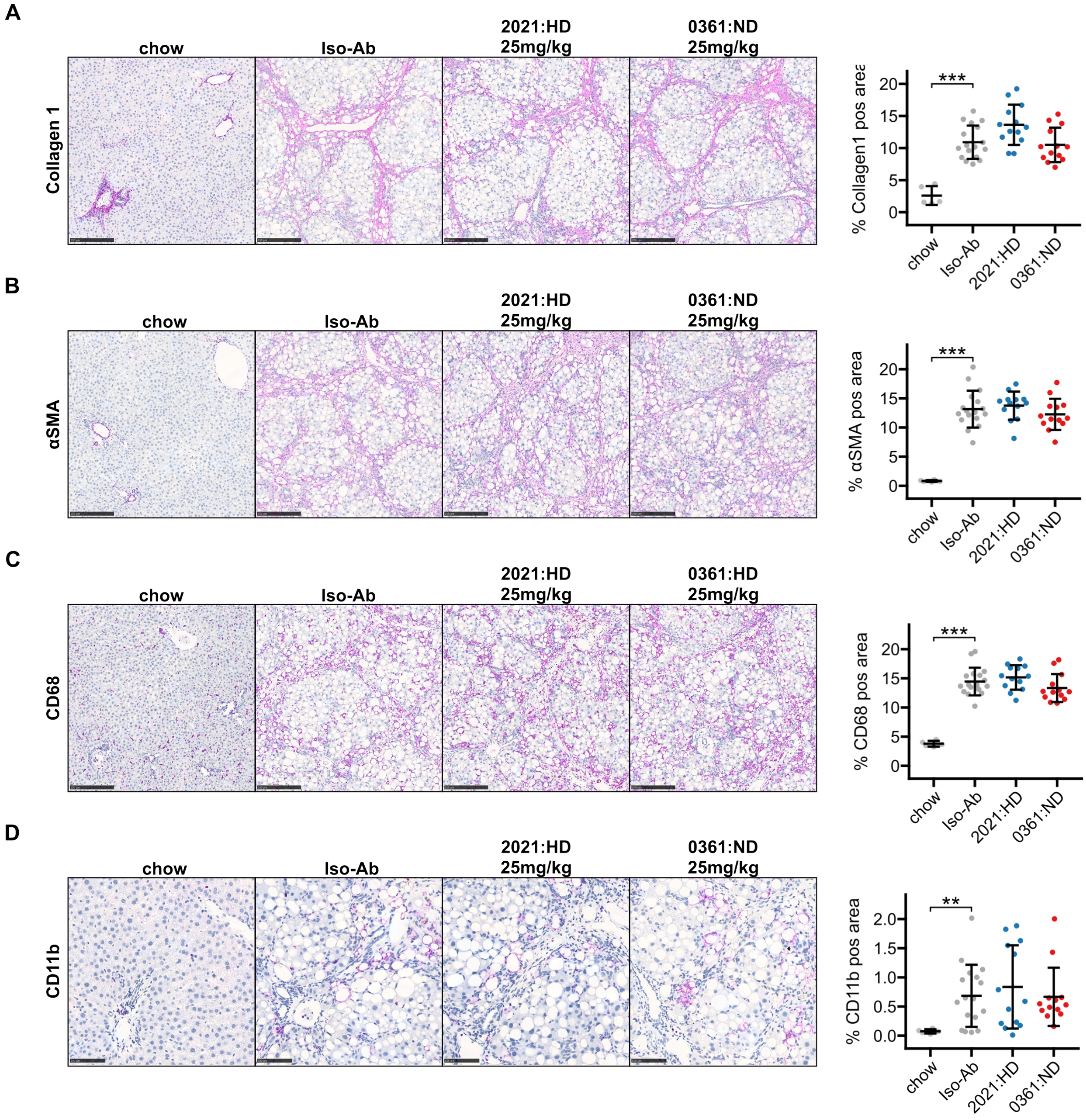

Figure 4.20: Additional IHC data from rat CDAA-HFD study. Left panels show representative IHC images for different treatment conditions. Scale bars represent 250 µm. Right panels show staining quantification in percent of total area. **A.** Collagen 1,

B. Alpha smooth muscle actin (αSMA), **C.** CD68, **D.** CD11b.

Data are given as individual data points (each representing a different animal sample) and mean ± SD for n = 5 (chow), n = 17 (Iso-Ab) and n = 13 (2021:HD & 0361:ND) animals per group. Significance was determined by multiple two-sided paired Welch t-tests against Iso-Ab, followed by Bonferroni-Holm adjustment (**$p < 0.01$, ***$p < 0.001$). Images and data generated by Novo Nordisk.

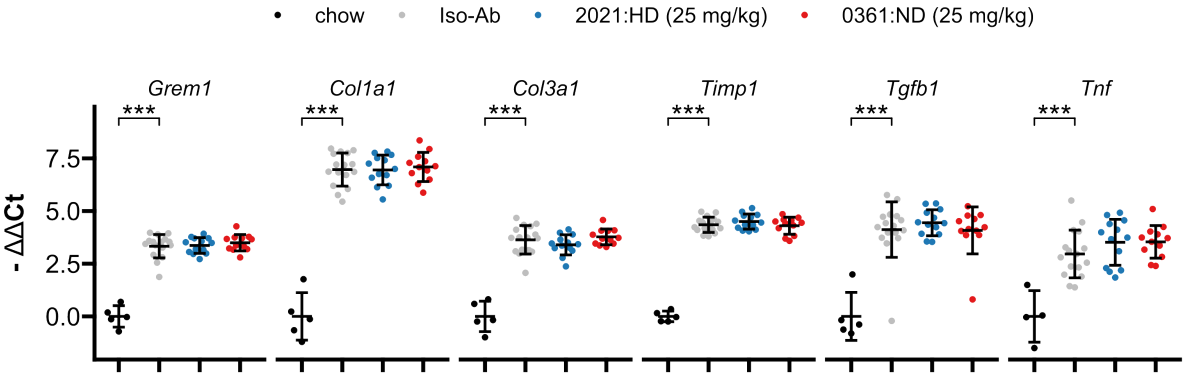

Figure 4.21: RTqPCR results for anti-Gremlin-1 antibody treatment on CDAA-HFD induced MASH and fibrosis in rats. Data are given as single data points (each representing a different animal sample measured in duplicate) and mean ± SEM for -ΔΔCt relative to chow control and normalised to B2m expression. ***$p < 0.001$ using One-Way ANOVA and post-hoc Dunnett test compared to Iso-Ab treated animals. Abbreviations: Col1a1 - collagen type 1 alpha 1, Col3a1 - collagen type 3 alpha 1, Grem1 - Gremlin-1, Tgfb1 - transforming growth factor beta 1, Timp1 - tissue inhibitor of metalloproteinases 1, Tnf - tumour necrosis factor alpha.
Data generated by Novo Nordisk.

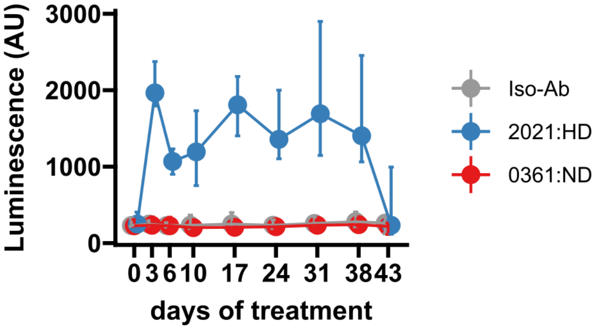

Figure 4.22: Target engagement in rat CDAA-HFD study. Peripheral blood was taken throughout the treatment with isotype control, heparin-displacing (2021:HD) or non-heparin-displacing (0361:ND) anti-Gremlin-1 antibody. Gremlin-1 concentration was measured using Novo Nordisk in-house alphaLISA. Data are given as median and 25 - 75 % interquartile range of fluorescent signal. Due to overall low signal, no confident absolute quantification of Gremlin-1 concentrations was possible.
Data generated by Novo Nordisk.

4.2.5 Effect of anti-Gremlin-1 treatment on human cirrhotic PCLS

We next aimed to assess whether anti-Gremlin-1 directed treatment, in the absence of an effect on rats *in vivo*, still has an anti-fibrotic effect on human liver disease. For this purpose, we prepared 250 µm thick precision-cut liver slices (PCLS) from human cirrhotic MASH and alcohol-related liver disease (ArLD) livers and treated these for 24 hours with 50 U/mL TGFβ1, 1 µM ALK5i, 100 nM heparin-displacing anti-Gremlin-1 therapeutic antibody (0030:HD) or their respective vehicle and isotype controls.

To test for toxic effects of any treatment condition, we measured Albumin concentrations and aspartate aminotransferase (AST) activity in the supernatants of cultured PCLS. Albumin is secreted by functional hepatocytes and its concentration should therefore reflect hepatocellular secretory function, whereas AST is a mitochondrial protein that is released from hepatocytes upon severe cell damage. Neither Albumin concentration nor AST activity were different between treatment conditions ($p = 0.358$ and $p = 0.112$, respectively, Figure 4.23). However, both Albumin concentration and AST activity were highly variable across the different livers used for PCLS preparation ($p = 3.39 \times 10^{-8}$ and $p = 6.62 \times 10^{-10}$, respectively, Figure 4.23).

Similar to target engagement studies in CDAA-HFD-fed rats undergoing anti-Gremlin-1 treatment, we wanted to assess release of Gremlin-1 from extracellular matrix binding by measuring Gremlin-1 concentrations in the supernatants of cultured PCLS. To that end, Gremlin-1 protein quantification was performed by our collaboration partner Novo Nordisk using the alpha-LISA described above. As shown in Figure 4.24A, the signal

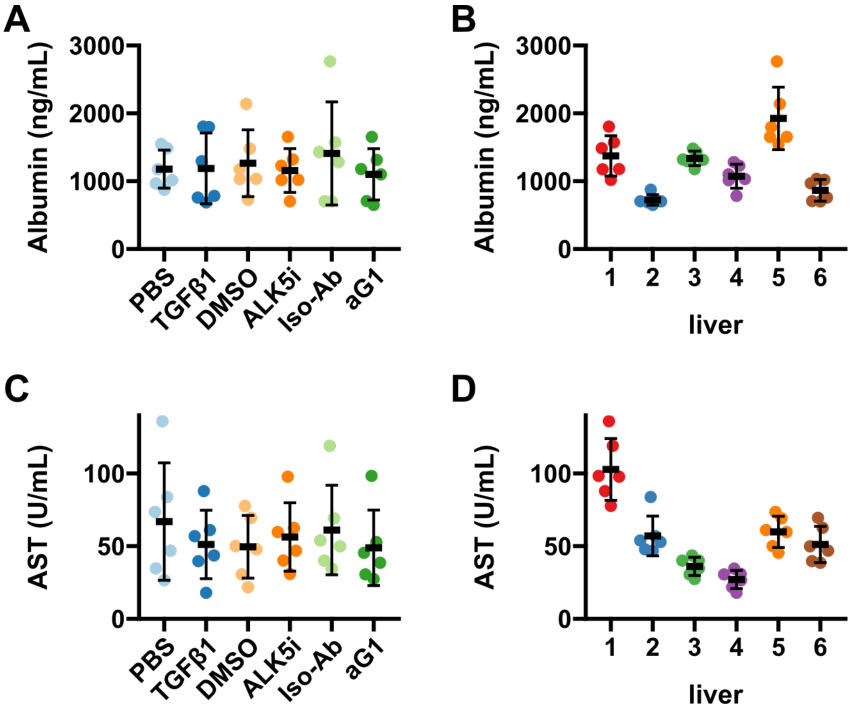

Figure 4.23: Biochemical responses of human PCLS exposed to heparin displacing anti-Gremlin-1 antibody. **A.** and **B.** Albumin concentration and **C.** and **D.** AST activity in supernatants of cirrhotic PCLS, grouped by treatment condition (**A.** and **C.**) or liver identity (**B.** and **D.**).

All data are given as individual data points (each representing an individual PCLS experiment measured in duplicate) and mean ± SD. The heparin-displacing anti-Gremlin-1 antibody 0030:HD was used for this experiment.

Abbreviations: aG1 - anti-Gremlin-1, ALK5i - ALK5 inhibitor, DMSO - dimethyl sulfoxide, Iso-Ab - Isotype matched control, PCLS - precision-cut liver slices, TGFβ1 - transforming growth factor beta 1.

Liver disease aetiologies: MASH (PCLS 1-3,5), MetALD (PCLS 4), ArLD (PCLS 6) for Gremlin-1 protein was below the lower limit of detection in all supernatants tested and therefore quantification was not possible.

Delivery of antibody-based therapeutics to fibrotic areas is always a concern [257] and therefore we wanted to determine whether our method of delivery enabled the therapeutic antibody to reach the fibrotic septa in PCLS and potentially elicit a response. For this purpose, PCLS were treated with non-heparin displacing AlexaFluor488 (AF488)-conjugated anti-Gremlin-1 or isotype control antibodies. Fluorescence was visualised by confocal microscopy. In addition, we performed DAPI staining to identify cell nuclei, and red fluorescence was detected on the AF594 channel to capture hepatocyte-derived red autofluorescence. Figure 4.24B shows representative confocal microscopy images and H&E staining. Fluorescence in the AF488 channel was low in PBS and Iso-Ab-treated PCLS and co-localised with red autofluorescence in the AF594 channel. In aG1-treated PCLS however, AF488 fluorescent signal was stronger and localised to fibrotic septa, and this signal was distinct from the AF594 autofluorescence.

Next, we performed RTqPCR for fibrogenic targets *COL1A1*, *ACTA2* and *TIMP1* to study the effects of each treatment on human cirrhotic PCLS. TGFβ1 significantly increased the expression of *COL1A1* and *TIMP1* ($p = 0.033$ and $p = 0.047$, respectively) and led to a non-significant increase in *ACTA2* expression ($p = 0.095$, Figure 4.25). Concordantly, inhibition of TGFβ1 signalling by pharmacologic ALK5 inhibition significantly reduced the expression of *COL1A1*, *ACTA2* and *TIMP1* ($p = 9.9 \times 10^{-4}$, $p = 0.040$ and $p = 0.003$, respectively, Figure 4.25). Anti-Gremlin-1 treatment, however, had no effect on target gene expression ($p > 0.283$, Figure 4.25).

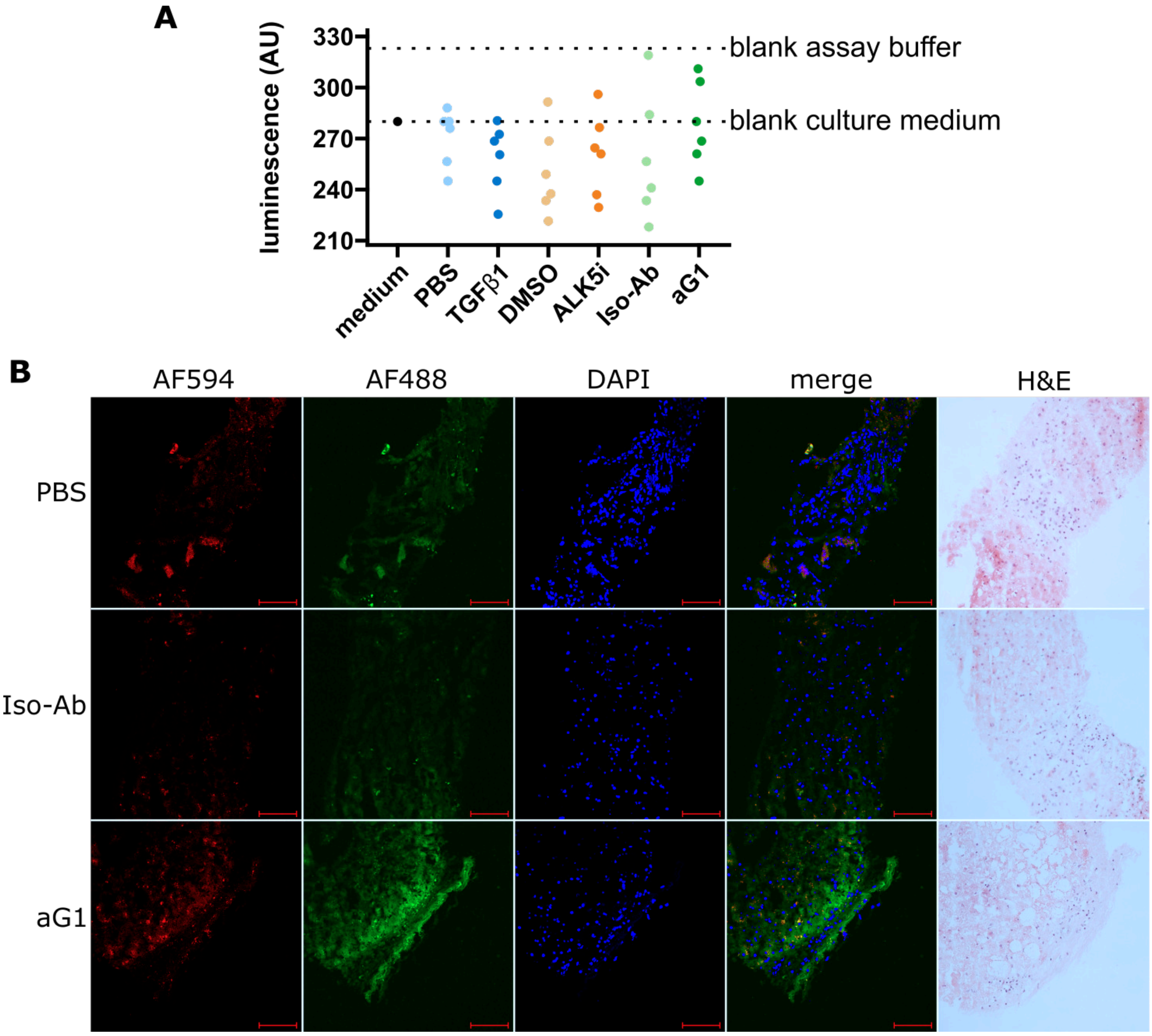

Figure 4.24: Target engagement studies in PCLS. A. Results of alphaLISA for Gremlin-1 protein in supernatants of treated cirrhotic PCLS. Data are given as individual data points (each representing an individual PCLS experiment measured in duplicate) for fluorescent signal intensity and dotted lines indicate the signal intensities obtained using blank culture medium or blank assay buffer. **B.** One set of cirrhotic PCLS was treated with either PBS or AF488-conjugated non-heparin displacing isotype control or anti-Gremlin-1 antibody for 24 h. Unfixed frozen sections were imaged after autofluorescence quenching and staining with DAPI. Red autofluorescence was detected using the AF594 channel. Scale bar represents 100 µm.

Abbreviations: aG1 - anti-Gremlin-1, DMSO - dimethyl sulfoxide, Iso-Ab - isotype control antibody, PBS - phosphate-buffered saline, TGFβ1 - transforming growth factor beta 1.

The heparin-displacing anti-Gremlin-1 antibody 0030:HD was used for this experiment.

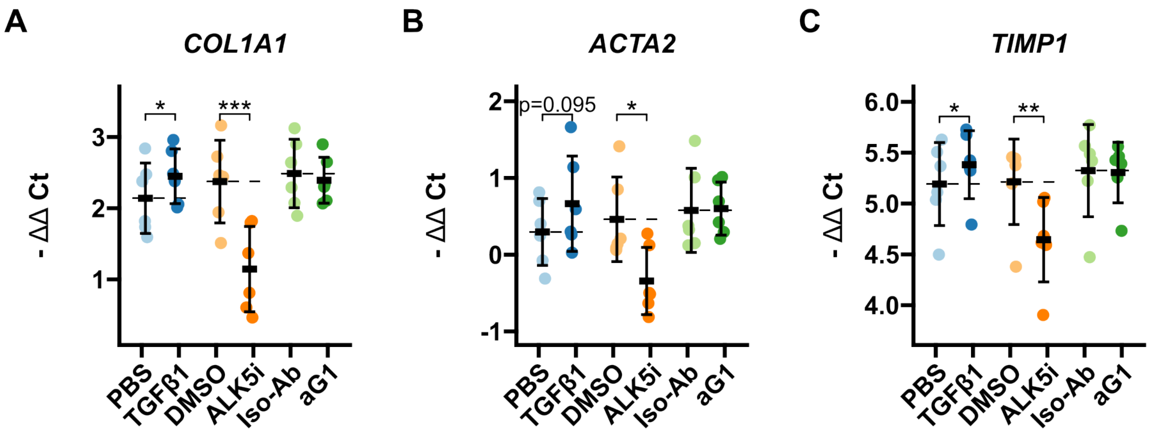

Figure 4.25: RTqPCR results for fibrogenic marker genes in cirrhotic PCLS. Data are given as individual data points (each representing an individual PCLS experiment measured in duplicate) and mean ± SD for -ΔΔ Ct relative to untreated control and normalised to the geometric mean of *SRSF4*, *HPRT1*, *CTCF* and *ERCC* expression. **p* < 0.05, ***p* < 0.01, ****p* < 0.001 using One-Way ANOVA and post-hoc paired t-tests for pre-defined comparisons with Bonferroni-Holm adjustment.
Abbreviations: ACTA2 - alpha smooth muslce actin, aG1 - anti-Gremlin-1, ALK5i - ALK5 inhibitor, COL1A1 - collagen type 1 alpha 1, DMSO - dimethyl sulfoxide, Iso - Isotype control, TGFβ1 - transforming growth factor beta 1, TIMP1 - tissue inhibitor of metalloproteinases 1.
The heparin-displacing anti-Gremlin-1 antibody 0030:HD was used for this experiment.

We then measured soluble pro-collagen 1 in PCLS tissue culture supernatants to assess the effect of anti-Gremlin-1 treatment on the protein level. In five samples, the ELISA returned negative values and therefore, these samples were removed from subsequent analysis. As shown in Figure 4.26, TGFβ1-treatment had no significant effect on pro-collagen 1 concentrations ($p = 0.35$), while ALK5i treatment led to a slight but significant reduction in pro-collagen 1 levels ($p = 0.047$). However, anti-gremlin-1 antibody treatment had no effect on pro-collagen 1 levels ($p = 0.177$).

While we found no changes in typical fibrogenic marker genes or pro-collagen 1 protein levels upon treatment with anti-Gremlin-1 antibody, we also wanted to check for changes in gene expression not directly related to organ fibrosis as the functions of Gremlin-1 have not been determined exhaustively. For this purpose, we performed

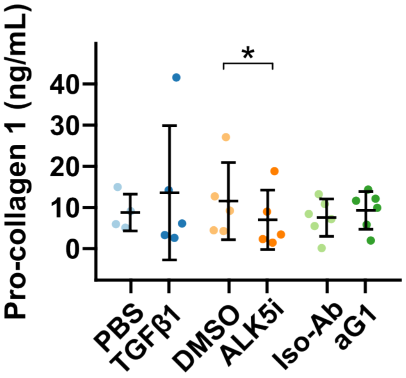

Figure 4.26: Pro-collagen 1 protein levels as determined by ELISA in PCLS culture supernatants. Data are given as individual data points (each representing a different PCLS sample measured in duplicate) and mean±SD. **p* < 0.05 using One-Way ANOVA and post-hoc paired t-tests for pre-defined comparisons with Bonferroni-Holm adjustment.
Abbreviations: aG1 - anti-Gremlin-1, ALK5i - ALK5 inhibitor, DMSO - dimethyl sulfoxide, Iso - Isotype control, TGFβ1 - transforming growth factor beta 1.
The heparin-displacing anti-Gremlin-1 antibody 0030:HD was used for this experiment.

3'-mRNA sequencing, which was carried out by the Genomic Services at the University of Birmingham. Table 4.2 provides the main quality read-outs for all samples. Most samples had a A230/A260 ratio of more than 1.800 and RNA integrity numbers (RINs) of more than 6, with the exception of 3 samples, respectively. However, lower A230/A260 ratios and RIN values did not correlate with the number of sequenced reads or the mapping rate, the latter consistently being around 75 %, while the number of reads greatly varied between 1.82 and 23.58 million.

We then performed differential gene expression analysis. Figure 4.27A shows the volcano plot for differential gene expression analysis and Figure 4.27B gives a heatmap for the differentially expressed genes. Only four genes were significantly regulated, one that was up- and three that were downregulated. Table 4.3 gives the $\log_2$-fold changes and unadjusted and adjusted p-values for the top 10 regulated genes. Gene

Table 4.2: Main quality metrics for QuantSeq 3' mRNA sequencing of PCLS.

sample	A260/A280	A260/A230	RIN	reads: before filtering	reads: after filtering	mapping rate
1-1_IMC	2.006	2.421	6.1	19.57M	19.27M	75.50%
1-2_aG1	2.013	2.508	6.8	5.92M	5.82M	74.92%
2-1_IMC	2.020	2.345	6.7	6.15M	5.97M	73.38%
2-2_aG1	2.029	2.724	5	11.30M	11.02M	73.69%
3-1_IMC	2.045	2.544	7.2	1.82M	1.78M	75.41%
3-2_aG1	2.033	2.480	5.9	8.91M	8.75M	76.31%
4-1_IMC	1.973	1.460	6.1	22.19M	21.94M	76.20%
4-2_aG1	1.974	1.833	6.5	23.58M	23.42M	74.20%
5-1_IMC	1.971	2.202	5.1	14.71M	14.39M	76.10%
5-2_aG1	1.992	2.213	4.9	9.13M	8.97M	77.55%
6-1_IMC	1.982	1.413	6.8	12.67M	12.42M	75.49%
6-2_aG1	1.983	1.671	6.9	14.92M	14.72M	76.60%

Abbreviations: RIN - RNA integrity number

set enrichment and over-representation analyses did not return any significantly enriched pathways (FDR > 0.05).

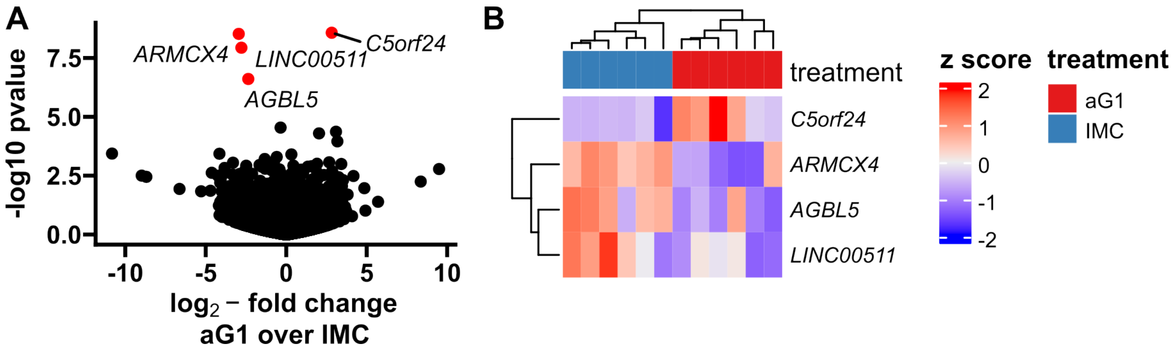

Figure 4.27: Results of RNA sequencing from human cirrhotic PCLS. A. Volcano plot showing $\log_2$-fold changes and the negative decadic logarithm of unadjusted p-values for all expressed genes. Significantly regulated genes (i.e. adj. p-value < 0.05) are labelled and marked in red. **B.** Heatmap showing centred and scaled gene expression for significantly regulated genes.
The heparin-displacing anti-Gremlin-1 antibody 0030:HD was used for this experiment

Table 4.3: Top 10 differentially expressed genes in PCLS aG1 vs Iso-Ab

log2FoldChange	p-value	padj	gene symbol
2.83	2.67E-09	4.05E-05	*C5orf24*
-2.95	2.99E-09	4.05E-05	*ARMCX4*
-2.79	1.16E-08	1.05E-04	*LINC00511*
-2.36	2.47E-07	1.67E-03	*AGBL5*
-0.35	2.87E-05	1.55E-01	*LRRC41*
3.09	4.30E-05	1.94E-01	*LGALS1*
2.04	5.05E-05	1.96E-01	*NPLOC4*
3.18	1.10E-04	3.74E-01	*TMEM176A*
-4.15	3.70E-04	9.74E-01	*RAB6B*
-10.82	3.65E-04	9.74E-01	*PRKAA2*

4.3 Discussion

In recent years, Gremlin-1 has been recognised as a potential therapeutic target for treating patients with MASH, and MASH fibrosis, in particular. Baboota *et al* recently suggested that anti-Gremlin-1-based therapies may be capable of halting or even reversing MASH progression through inhibition of hepatocellular senescence [191]. In this chapter, we aimed to develop and evaluate anti-Gremlin-1 neutralising antibodies as therapeutic assets for the treatment of MASH fibrosis.

In the previous chapter, we found increased levels of GREM1 expression in MASH fibrosis and localisation of GREM1 to hepatic fibroblasts. In this chapter however, we observed no therapeutic effect of antibody-mediated neutralisation of Gremlin-1 protein, neither in a CDAA-HFD rat *in vivo* model nor in human *ex vivo* or *in vitro* culture models of MASH fibrosis. We extensively tested and characterised our therapeutic antibodies and were able to show high-affinity binding to Gremlin-1 and functional inhibition of its BMP4-inhibitory activity. Furthermore, treating rats with the heparin-displacing anti-Gremlin-1 antibody *in vivo* led to a significant increase in circulating Gremlin-1 protein, evidencing reliable target engagement. However, the small subset of COL3A1^{+}/THY1^{+} periportal fibroblasts unlikely represents the major fibrogenic cell population in MASH. While periportal myofibroblasts play an important role in biliary fibrosis [243, 258], in most chronic liver diseases such as MASH and alcohol-related liver disease, HSC-derived myofibroblasts represent the predominant fibrogenic cell population [82, 259]. Moreover, hepatic Gremlin-1 expression is quite low when compared to organs such as the intestine or visceral adipose tissue [172]. Others suggested that Gremlin-1 plays an important role in visceral adipose tissue biology by driving adipocyte hypertrophy and adipose tissue dysfunction [238]. Given the important role of visceral adipose tissue dysfunction in metabolic dysfunction-associated steatotic liver disease (MASLD)/MASH development [260], Gremlin-1 could drive the development and progression of MASH by modulating local adipose tissue function. Some authors have hypothesised that visceral adipose tissue Gremlin-1 may act directly on the liver via delivery through the blood stream [180], but this seems unlikely considering the high affinity binding of Gremlin-1 to glycosaminoglycans such as heparin, which likely prevents Gremlin-1 from entering the blood stream. Furthermore it has been suggested that Gremlin-1 could act through induction of hepatocellular senescence [191]. While we did not measure senescence markers in our study, *in situ* hybridisation (ISH) data from our previous chapter suggest that GREM1 expressing cells are quite distant to hepatocytes. Given the local retention of Gremlin-1 due to its heparin-binding capacity, we feel it is unlikely that Gremlin-1 has any considerable effects on hepatocytes *in vivo*.

We carefully selected the CDAA-HFD rat model of MASH fibrosis for our *in vivo* studies as this was the only animal model tested that showed convincing and reliable hepatic upregulation of Gremlin-1 upon liver injury. While the CDAA-HFD model reliably reproduces the histological hallmarks of hepatic disease in MASH, such as liver steatosis, inflammation and fibrosis [118], it does not incorporate extrahepatic factors such as obesity and adipose tissue dysfunction as drivers of disease. On the contrary, the CDAA-HFD leads to reduced weight gain and reduced visceral adiposity compared to control diet [118]. Data on adipose tissue biology in response to CDAA-HFD are scarce, but the expression and release of the obesogenic cytokine leptin, which is considered a hallmark of severe obesity and the metabolic syndrome [261], is actually reduced in CDAA-fed mice [262]. Likewise, although we have not specifically tested for adipose tissue Gremlin-1 expression in this model, obesity-induced changes in adipose tissue Gremlin-1 expression and biology are likely not adequately reflected in the CDAA-HFD model. Taken together with the role of Gremlin-1 in adipose tissue dysfunction [172], we feel that blocking Gremlin-1 may well have an effect in other models of MASH fibrosis, e.g. the Western Diet model or high-fat, high-fructose diets more adequately reflecting the metabolic phenotype.

PCLS are now a well-established method that allows the study of hepatic signalling pathways *ex vivo*, and unlike monolayer cell culture models reflect cell-cell interactions in the liver [213]. We used liver specimens from patients undergoing liver transplantation, which enabled the study of effects of anti-Gremlin-1 treatment on clinically relevant, chronically diseased liver. However, patients already suffered from end-stage liver disease which is usually not amenable to pharmacological interventions aimed at reversing disease. We were also limited to studying samples after a maximum of 24 hours of treatment, because in previous experiments we observed tissue and RNA degradation when keeping cirrhotic PCLS in culture for longer. While others incubated cirrhotic PCLS for up to 48 hours, they still observed significant changes in gene expression as early as 24 hours after dosing [263], and we also found a clear anti-fibrotic response upon ALK5 inhibition, indicating functionality of our experimental setup. Still, the high variability of Albumin and AST levels in PCLS supernatants across different explant livers highlights the heterogeneity in PCLS composition and quality. Furthermore, the effects of blocking Gremlin-1 may take longer than 24 hours and potential effects of Gremlin-1 on infiltrating immune cells and extrahepatic signals, e.g. from the gut or adipose tissue, are not reflected in PCLS and limit generalisability of our observations.

Our negative findings from rat *in vivo* and human *ex vivo* models were largely corroborated by our results obtained through *in vitro* cell culture of fibrogenic liver cells. Anti-Gremlin-1 treatment was ineffective in reducing pro-fibrogenic gene expression in both LX-2 and primary HHSC, although the low number of biological replicates in these experiments might have masked any potential effects. This was in line with findings that lentiviral overexpression of GREM1 in both cell culture models did not alter the expression of fibrogenic genes in response to TGFβ1. Interestingly, overexpression numerically increased the expression of *CCL2*, a proinflammatory cytokine upregulated in early stellate cell activation [259] and significantly increased *LOX* expression, which plays an important role in collagen-crosslinking and is typically upregulated later in the HSC activation cascade [259, 264] and has also been found to be upregulated in human ocular trabecular meshwork cells in response to Gremlin-1 [265]. *GREM1* overexpression also modulated the expression of BMP-signalling-related genes, summarised in Figure 4.28, including *BMP7*, some SMADs and *INHBB*. BMP7 is a typical target of Gremlin-1 and has been described as an anti-fibrotic modulator of HSC activation [136]. The upregulation of *BMP7* mRNA, as well as *SMAD1*, a canonical SMAD protein in the BMP signalling pathway [266], suggests that GREM1 overexpression may have induced counter-regulatory responses which could have dampened any potential pro-fibrogenic effect. The downregulation of inhibitory *SMADs 6* and *7* in response to *GREM1* overexpression could be seen in the same light, as reduced inhibitory SMAD abundance could dis-inhibit BMP signalling [267], although dis-inhibition of TGFβ signalling is possible as well [268]. The gene *INHBB* coding for the inhibin β_B chain was also prominently downregulated in cells overexpressing *GREM1*. Importantly, the biological function of *INHBB* is dependent on the expression of *inhibin* α *chain (INHA)*, which associates with inhibin β chain proteins to form heterodimers called inhibins [269]. In the absence of the inhibin α chain, inhibin β_B chain forms Activin B, a homodimer composed of inhibin β_B chain protein [269]. Older publications found no evidence of *INHA* mRNA in human and rodent liver [270, 271], findings that were corroborated by more recent immunohistochemistry data which found a lack of evidence for inhibin α protein in non-tumorous human liver [272]. Therefore, the decreased expression of *INHBB* in response to GREM1 overexpression likely translates into reduced abundance of the fibrogenic Activin B protein. Similar to limitations outlined in the previous chapter, we did not ascertain the phenotype and origin of primary cell cultures, and heterogeneity of primary cell isolates (e.g. composition of fibroblast origins in HHSC cultures) may have impacted our results. Notably, we did not find a consistent transcriptional regulation when applying RNA sequencing to the lentiviral overexpressors and low-abundance transcripts relating to BMP signalling were not recovered using this approach. Furthermore, some very high $\log_2$-fold changes reported for RNA sequencing may be false high estimates owing to small sample sizes and known limitations of variance-based approaches for deriving fold-change estimates in differential gene expression analysis [273]. Taken together, our findings suggest that overexpression of *GREM1* in LX-2 cells may induce counter-regulatory programs that override any net fibrogenic effects of Gremlin-1.

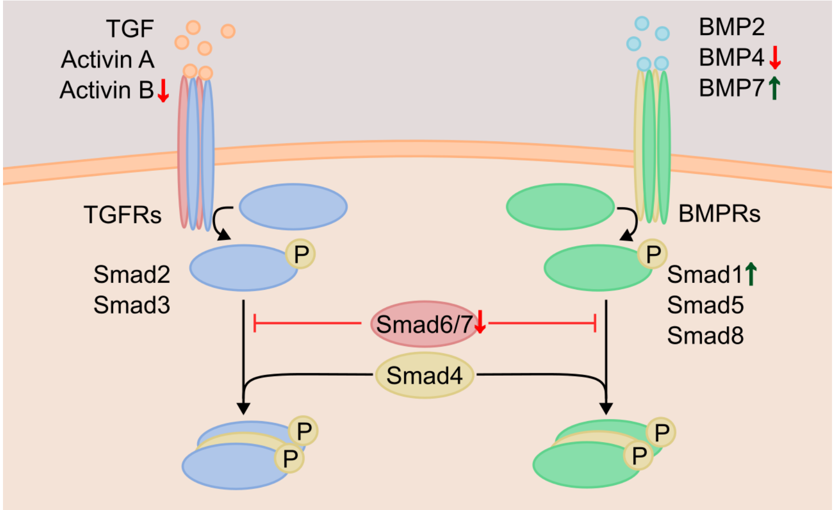

Figure 4.28: Overview of GREM1 overexpression effects on the BMP signalling pathway. Increased gene expression is indicated by upwards pointing arrows in green and decreased gene expression by downwards pointing arrows in red.
Abbreviations: BMP - bone morphogenetic protein, BMPRs - BMP receptors, TGF - transforming growth factor, TGFRs - TGF receptors.

Similarly, we did not observe any consistent effect of lentiviral overexpression or anti-Gremlin-1 treatment on the contractile phenotype or wound healing response in collagen contraction and scratch-wound assays. As an exception, we found a consistent lack of contractility in the GREM1 overexpressing LX-2 cells, although we did not ascertain that the cells remained viable under these low shear stress conditions. In addition, in scratch-wound assays we did not observe any consistent response of LX-2 cells to PDGF stimulation and we therefore have to conclude that the assay did not work as expected and we cannot draw any conclusions regarding changes in the wound healing response. Finally, most of the experiments were underpowered due to the use of only three biological replicates, and therefore, any potential effect of modulating Gremlin-1 activity may have been missed.

Overall, considering the minor role of periportal fibroblasts, the main cell population expressing Gremlin-1, in MASH fibrosis and the lack of an effect upon neutralisation of Gremlin-1, the role of hepatic Gremlin-1 in liver fibrosis seems questionable. While some authors described *in vivo* effects of siRNA knockdown of Gremlin-1 on liver fibrosis in a carbon tetrachloride (CCL_4) model of liver fibrosis in rats [190], others did not find any effect of adenoviral overexpression or intraperitoneal injection of recombinant Gremlin-1 protein on steatosis, inflammation and fibrosis in high-fat diet-fed mice [274]. Furthermore, recent studies suggest that Gremlin-1 might not be a solely pro-fibrotic protein acting through inhibition of BMPs. Studies on myocardial fibrosis, urinary carcinoma and intervertebral disc degeneration found that Gremlin-1 can also directly antagonise TGFβ1 [169–171], thereby potentially exerting anti-fibrotic effects. In summary, the specific role of Gremlin-1 in organ fibrosis seems to depend on the context, including the local balance of BMPs and TGFβ proteins.

Heparin-binding properties of target proteins pose potential challenges to the development of therapeutic antibodies. As shown in the previous chapter, Gremlin-1 protein binds to heparin with high affinity. Similarly, antibodies can differ in their binding properties towards protein-heparin complexes. In the presence of heparin, non-displacing antibodies led to the formation of insoluble complexes, which *in vivo* could cause the formation of immune complexes and subsequently cause local inflammatory reactions. In the presented study, the heparin-binding properties of Gremlin-1 offered an opportunity for target engagement studies. In response to heparin-displacing antibody treatment in rats, the signal for circulating Gremlin-1 increased, evidencing removal from its local heparin binding. Picking up these changes not only made us confident that the antibody engaged its target but also that the LOCI assay presented in the previous chapter was indeed working as intended.

Unfortunately, we did not observe an increase in soluble Gremlin-1 in PCLS treated with anti-Gremlin-1 antibody. While it is possible that the antibody was not binding to its target, we showed positive fluorescent staining of the fibrotic scar by fluorescence-labelled non-displacing anti-Gremlin-1 antibody. This suggests that the antibody was able to penetrate PCLS scar tissue and bind to Gremlin-1. However, given the low abundance of GREM1 ISH staining in human liver fibrosis (see Chapter 3, page 79), soluble Gremlin-1 concentrations might have been too low to produce any meaningful signal. Our results stress the importance of heparin-binding properties for therapeutic antibody development. Interactions between antibodies, target protein and heparin should always be taken into account when developing novel therapeutic strategies.

In addition, our findings regarding the heparin-binding properties of Gremlin-1 shed light on its biological function and its potential use as a biomarker. Heparin-binding is a hallmark of TGFβ superfamily proteins [275], including Gremlin-1 belonging to the Dan family. Therefore it does not come as a surprise that Gremlin-1 also possesses high-affinity binding properties towards glycosaminoglycans such as heparin sulphate [165]. Our findings of absent Gremlin-1 protein in the blood in lieu with detectable levels upon treatment with heparin-displacing anti-Gremlin-1 antibody in the rat *in vivo* study indicates that heparin-binding may retain Gremlin-1 protein in close proximity to its functional niche. This could preclude the release of Gremlin-1 protein into systemic circulation and at the same time amplify local activity in the spatial niche surrounding Gremlin-1-expressing cells. Still, extracellular vesicles [276] and platelets can contain Gremlin-1 [181], which may still enable inter-organ communication through Gremlin-1. Taken together, the implications of Gremlin-1 heparin-binding properties and its absence from systemic circulation, at least in our assays, clearly need to be considered when studying its function, therapeutic application and suitability as a biomarker.

In summary, our data provide compelling evidence that hepatic Gremlin-1 is not a suitable target for antifibrotic therapies in MASH-induced liver fibrosis. However, this does not preclude a role for Gremlin-1 in other liver diseases, and biliary fibrosis in particular. Furthermore, mounting evidence suggests that Gremlin-1 has a role in carcinogenesis and future studies will have to define its role in HCC development. Not least, the role of Gremlin-1 in adipose tissue is well established and targeting visceral adipose rather than hepatic Gremlin-1 might be a more promising target in MASH. More research is needed though, to confirm a link between adipose Gremlin-1, hepatic inflammation and fibrosis.

CHAPTER 5

GREMLIN-1 IN HEPATIC SINUSOIDAL ENDOTHELIAL CELLS AND MONOCYTE-DERIVED MACROPHAGES

5.1 Introduction

In the previous two chapters we explored the expression pattern of Gremlin-1 in liver fibrosis and the impact of increased Gremlin-1 or antibody-mediated neutralisation of the protein on the activation of hepatic matrix-producing cells *in vitro* and on liver fibrosis *in vivo* and *ex vivo*. While chronic liver injury and inflammation are the culmination of the activation of hepatic stellate cells driving liver fibrosis, this process is preceded by the activation of endothelial cells, leukocyte recruitment and activation of inflammatory cells, such as proinflammatory monocytes which drive liver pathology.

Gremlin-1 has been described as an angiogenic factor acting through agonism of vascular endothelial growth factor receptor 2 (VEGFR2) on endothelial cells [163, 165], a process dependent on the heparin-binding properties of Gremlin-1 [165]. One study also found that Gremlin-1 can directly induce endothelial cell activation and leukocyte extravasation through VEGFR2-induced cAMP response element-binding protein (CREB) signalling [277]. Bone morphogenetic proteins (BMPs) are also involved in the activation of endothelial cells and can directly upregulate adhesion molecules such as intercellular adhesion molecule 1 (ICAM1) and vascular cell adhesion molecule 1 (VCAM1) [144]. While Gremlin-1 is upregulated in endothelial cells under control of the transcription factor CREB, it was expressed at very low levels in primary human hepatic sinusoidal endothelial cell (HSEC) according to our own findings (see Chapter 3). Platelets, which play an important role in inflammatory processes in atherosclerosis, contain Gremlin-1 and release their cargo upon degranulation [181]. Platelets also accumulate in the injured liver and are implicated in the progression of MASLD [78, 79] and therefore could serve as a source of Gremlin-1 protein in liver endothelial cell activation.

Platelet-derived Gremlin-1 has also been found to promote monocyte migration, adhesion and survival and differentiation to macrophages by inhibiting monocyte migration inhibitory factor (MIF) [181]. Evidence is contradictory though, as previously the same group found that, also by acting through inhibition of MIF, Gremlin-1 can suppress adhesion and induce apoptosis of monocytes [278]. Gremlin-1 is also highly expressed in macrophages localised to the atherosclerotic plaque, and in this context has been identified as a negative modulator of macrophage differentiation and plaque formation [279].

The direct role of Gremlin-1 in liver endothelial cell and monocyte-derived macrophages (MoMF) activation has not been studied to date and Figure 5.1 illustrates the proposed role of Gremlin-1 in inflammatory cell recruitment and differentiation. In this chapter, we aimed to explore the impact of Gremlin-1 on endothelial cell activation and the expression of *GREM1* in MoMF in order to assess whether - in the absence of a direct effect on liver fibrosis - Gremlin-1 might be involved in earlier inflammatory processes. For this purpose we performed RTqPCR and cell-based ELISA for *ICAM1* and *VCAM1*, flow-based adhesion assays on primary human HSEC treated with recombinant human Gremlin-1 or platelet-derived supernatants. We also screened public RNA sequencing databases of MoMF of different differentiation for changes in Gremlin-1 expression and sought to validate these findings using RTqPCR on *in vitro* differentiated MoMF.

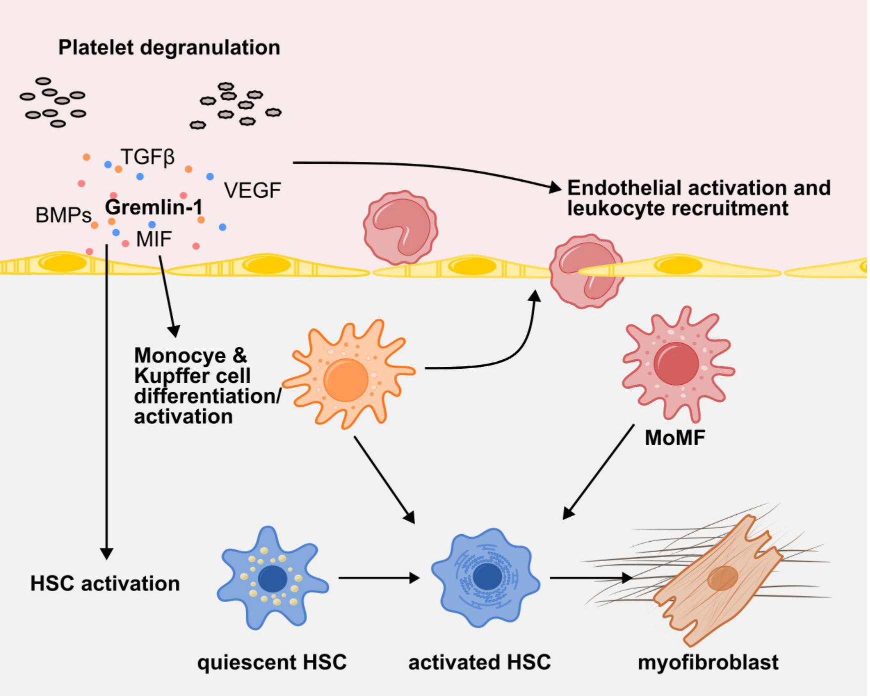

Figure 5.1: Proposed role of Gremlin-1 in inflammatory cell interaction. Gremlin-1 can be released from activated platelets, along other proteins such as BMPs, TGFβ MIF or VEGF. We proposed that Gremlin-1 derived from platelets, inflammatory cells or activated HSCs is involved in endothelial cell activation, leukocyte recruitment and inflammatory macrophage differentiation.
Abbreviations: BMP - bone morphogenetic protein, HSC - hepatic stellate cell, MIF - monocyte migration inhibitory factor, MoMF - monocyte-derived macrophages, TGFβ - transforming growth factor beta, VEGF - vascular endothelial growth factor.

5.2 Results

5.2.1 Endothelial cell activation

Flow-based adhesion assays

Endothelial activation is an important step in the fibrotic cascade in chronic liver disease. Activated endothelial cells upregulate adhesion molecules, such as ICAM1 and VCAM1, which play an important role in transendothelial migration of infiltrating leukocytes. To study the effects of Gremlin-1 on leukocyte adhesion and transmigration on endothelial cells, we employed flow-based adhesion assays. HSEC were seeded in 6-well Ibidi slides and were pre-treated with recombinant human Gremlin-1 before stimulation with tumor necrosis factor alpha (TNFα). TNFα treatment strongly and significantly increased the total number of adherent, activated and migrated cells while Gremlin-1 was without effect ($p = 4.4\text{x}10^{-4}$ and $p = 0.99$, respectively, Figure 5.2A). TNFα also led to a shift in the cell state of recorded peripheral blood mononuclear cells (PBMC) with an increase in the proportion of rolling and adherent cells, while the proportion of activated cells was decreased (Figure 5.2B). Figure 5.3 illustrates cell number differences and different types of adhesion in flow-adhesion assays.

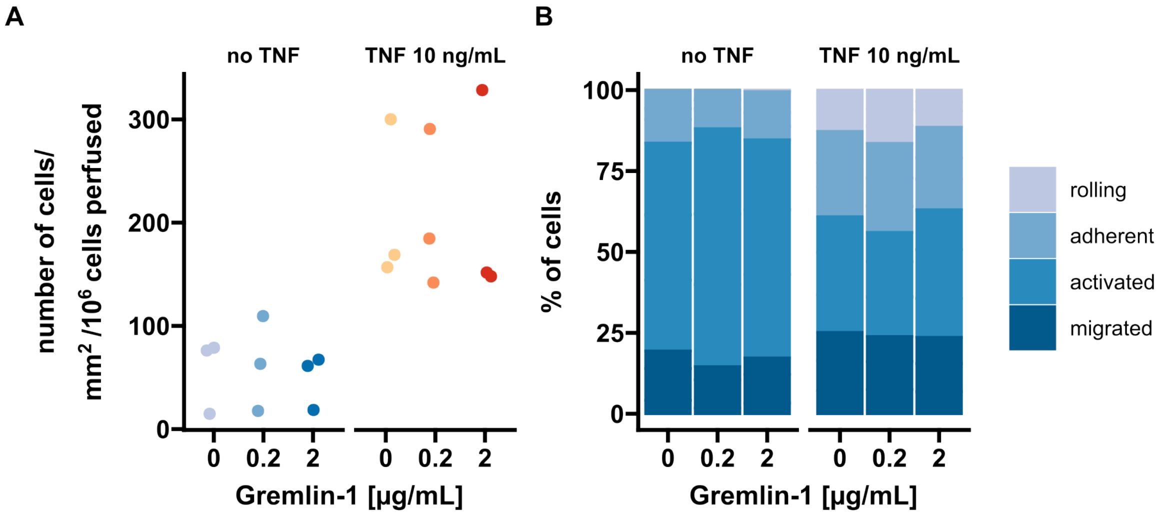

Figure 5.2: Flow-based adhesion assay on HSEC in response to rhGremlin-1. HSEC were seeded in 6-well Ibidi slides and grown until 80% confluent. Cells were then treated with 0, 0.2 or 2 µg/mL rhGremlin-1 and incubated for 24 hours before running the flow-based adhesion assay with PBMC. **A.** Total number of cells that adhered to the HSEC monolayer, following treatment with Gremlin-1 alone or co-treatment with TNFα for the final 6 hours. Data are given as single data points (each representing an individual HSEC experiment with ten fields of view recorded). **B.** Percentage of cells classified by type of adhesion.
Abbreviations: TNF - tumour necrosis factor.

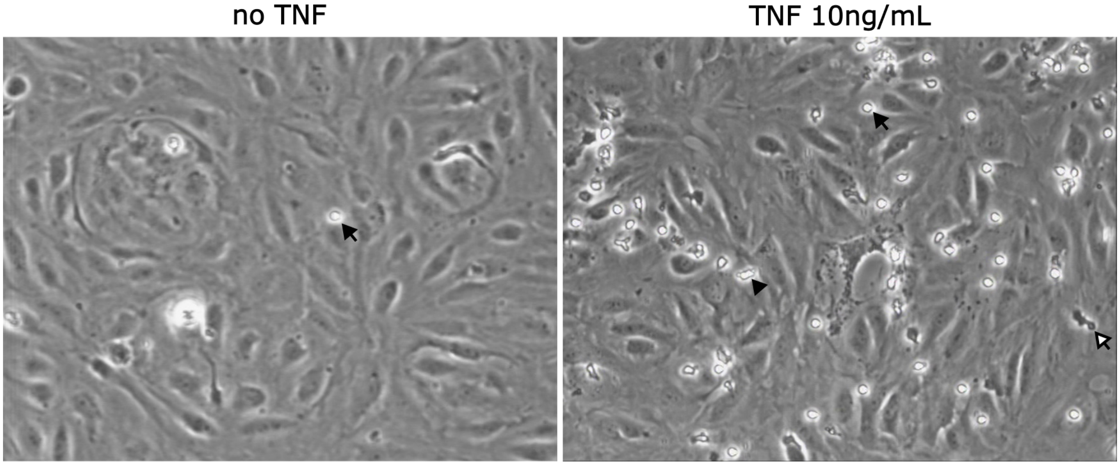

Figure 5.3: Representative images from flow-based adhesion assays on untreated (left) and treated (right) HSEC. Arrows indicate types of leukocyte adhesion: ⬉ - adherent, ▶ - activated, ⇖ - migrated.
Abbreviations: TNF - tumour necrosis factor.

Expression of adhesion molecules

As treatment with recombinant human Gremlin-1 had no effect on leukocyte adhesion in flow-based adhesion assays, we used lentiviral overexpression of *GREM1* to check for an effect on endothelial adhesion molecule expression, using the same methods as shown in Section 4.2.1.

On the protein level, *GREM1* overexpression had no significant effect on the expression of either ICAM1 or VCAM1 in cell-based enzyme-linked immunosorbent assay (ELISA) ($p = 0.293$ and $p = 0.713$, respectively, Figure 5.4). Similarly on the mRNA level, *GREM1* overexpression was without effect on *ICAM1* and *VCAM1* expression ($p = 0.358$ and $p = 0.723$, respectively), while TNFα significantly upregulated both *ICAM1* and *VCAM1* ($p = 0.028$ and $p = 0.016$, respectively, Figure 5.5).

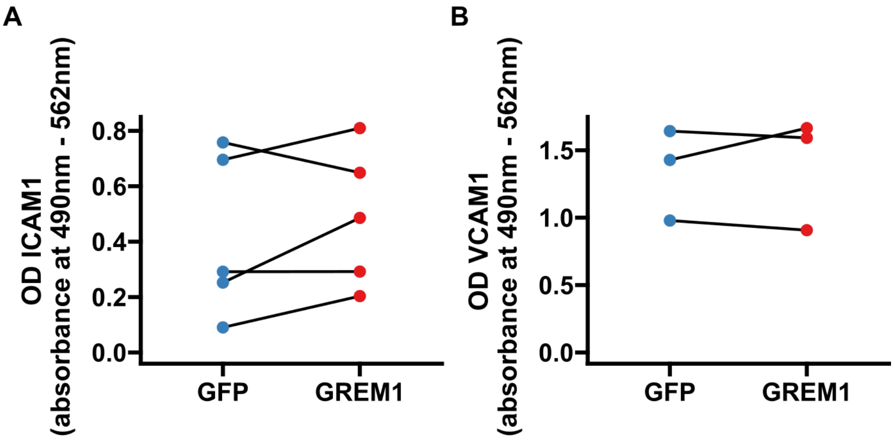

Figure 5.4: Cell-based ELISA for **A.** ICAM1 and **B.** VCAM1 on TNFα-stimulated primary HSEC upon lentiviral transduction. ICAM1 and VCAM1 were not detectable on HSEC without TNFα stimulation and corresponding data therefore not shown. Data are given as individual data points (each representing an individual HSEC sample measured in duplicate). Lines connect datapoints from paired data, i.e. samples from the same donor. Differences were not significant using paired two-sided Student's t-test.
Abbreviations: GFP - green fluorescent protein, GREM1 - Gremlin-1, ICAM1 - intercellular adhesion molecule 1, VCAM1 - vascular cell adhesion molecule 1.

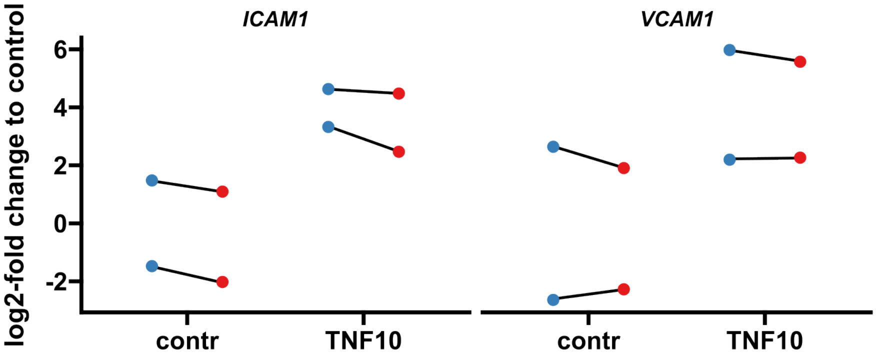

Figure 5.5: RTqPCR for *ICAM1* and *VCAM1* on primary HSEC upon lentiviral transduction. Data are given as individual data points (each representing an independent HSEC experiment measured in duplicate). Lines connect datapoints from paired data, i.e. samples from the same donor. Statistical testing between *GREM1* (red) and *GFP* (blue) overexpressors was omitted due to small sample size of n=2.
Abbreviations: Contr - vehicle control, ICAM1 - intercellular adhesion molecule 1, TNF10 - TNFα stimulation (10 ng/mL), VCAM1 - vascular cell adhesion molecule 1

5.2.2 Platelet-derived Gremlin-1 and its effect on endothelial cell activation

We did not find evidence that recombinant Gremlin-1 or lentiviral overexpression of GREM1 had any considerable effect on HSEC activation, measured by flow-based adhesion assays and mRNA and protein expression of adhesion molecules ICAM1 and VCAM1. As the effects of Gremlin-1 depend on the presence of other soluble factors, in particular BMPs, we sought to study a more complex system that provides Gremlin-1 in addition to BMPs. Previously, it has been shown that platelets are involved in MASH pathophysiology [79] and carry Gremlin-1, TGFβ1 and BMPs, which can be released upon platelet activation [181, 280, 281]. Therefore, in the following study, we established a protocol to generate Gremlin-1-containing supernatants from activated platelets for stimulating HSEC in flow-based adhesion assays. To this end, we used platelets isolated from patient blood and stimulated these with well known activators of platelet adhesion and granule secretion - namely thrombin (Thr), adenosine-diphosphate (ADP) and arachidonic acid (AA). Platelet activation leads to degranulation with release of alpha granule content, including Gremlin-1, BMPs and platelet factor 4 (PF4, CXCL4). Furthermore, platelet degranulation also leads to the surface exposure of the alpha granule protein P-selectin (CD62P), which therefore can be used as a marker for platelet activation in flow cytometry [282].

Platelet activation and Gremlin-1 release

First, we isolated platelets from citrate-anticoagulated patient blood using selective centrifugation (see Section 2.2.5, page 47). Subsequently, to find the optimum condition for platelet activation and Gremlin-1 release, platelet suspensions were treated with Thr, ADP or AA at different concentrations for 5, 15 or 30 minutes. After stimulation platelets were sampled, fixed in paraformaldehyde (PFA) and underwent flow cytometry for the general platelet marker CD41 and the platelet activation marker CD62P. Platelet suspensions were also centrifuged at 4°C and supernatants stored at -80°C for subsequent analysis of soluble factors. Figure 5.6 shows the gating strategy for measuring the mean fluorescence intensity (MFI) for CD62P of all CD41-positive platelets.

Figure 5.7 shows the platelet activation response to different stimulation conditions. As can be seen in Figure 5.7A, Thr and AA but not ADP at low and high concentrations led to a significant increase in surface expression of the platelet activation marker CD62P (Thr 1 U/mL: $p = 8.2 \times 10^{-13}$, Thr 5 U/mL: $p = 8.2 \times 10^{-13}$, ADP 3 µM and 10 µM: $p = 1.0$, AA 100 µM: $p = 4.8 \times 10^{-4}$ and AA 500 µM: $p = 8.3 \times 10^{-13}$). This translated into an increased

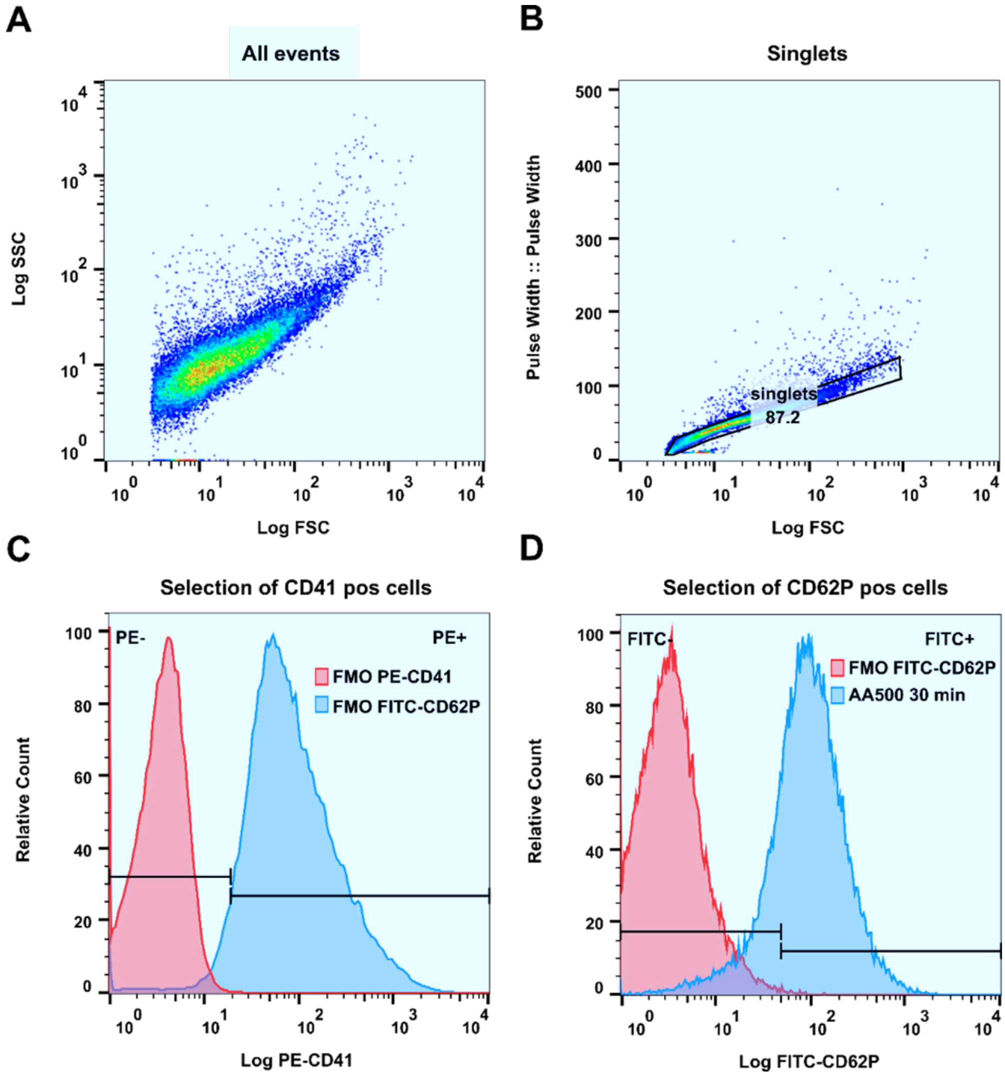

Figure 5.6: Gating strategy for platelet flow cytometry. **A** All events were recorded and **B** singlets selected based on Forward Scatter (FSC)-Pulse Width Plots. Fluorescence-minus-one (FMO) controls were used to set gates on **C** CD41$^+$ and **D** CD62P$^+$ events. CD62$^+$ platelets were gated on CD41$^+$ cells only

abundance of the protein CXCL4/platelet factor 4 in supernatants in thrombin-treated platelets only (Thr 1 U/mL: $p = 5.1\text{x}10^{-4}$, Thr 5 U/mL: $p = 3.2\text{x}10^{-3}$, all other $p > 0.89$, Figure 5.7). For both CD62P and CXCL4, there was no significant effect of the duration of stimulation in Two-Way ANOVA.

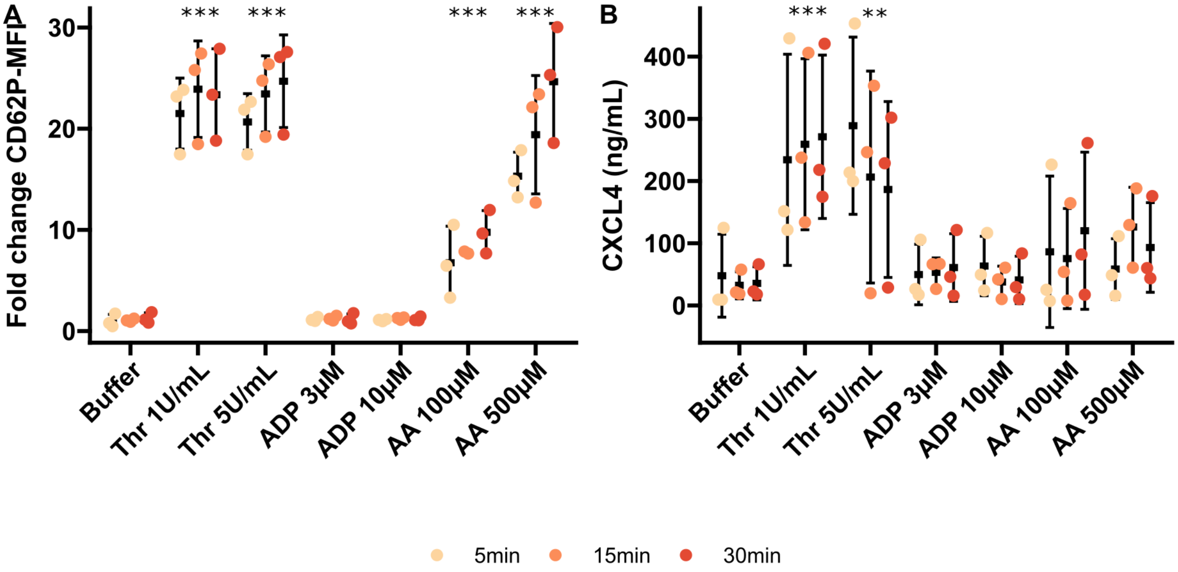

Figure 5.7: Platelet activation markers after stimulation of platelets. Platelets were stimulated with either buffer, Thrombin (Thr), ADP or arachidonic acid (AA) for 5, 10 or 15 minutes. **A.** Fold change of mean fluorescence intensity for CD62P staining in flow cytometry. **B.** CXCL4 protein concentration in platelet supernatants as measured by ELISA. Data are given as mean ± SD and single data points for n=3 biological replicates measured in duplicate.
Abbreviations: AA - arachidonic acid, ADP - adenosine-diphosphate, CXCL4 - C-X-C motif ligand 4, Thr - thrombin.
**$p < 0.01$, ***$p < 0.001$ compared to Buffer using Two-Way ANOVA and post-hoc Tukey HSD.

Gremlin-1 can be released from α-granules upon platelet activation. Figure 5.8 shows results of Gremlin-1 concentrations in platelet supernatants as measured by commercially available ELISA. In line with the increased release of CXCL4 in response to thrombin, thrombin at low and high concentrations led to a significant increase in Gremlin-1 concentration (Thr 1 U/mL: $p = 0.0018$, Thr 5 U/mL: $p = 0.0015$). While AA led to numerical increase in Gremlin-1 concentration, this did not reach statistical significance (AA 100 µM: $p = 0.31$, AA 500 µM: $p = 0.46$). We observed no effect of ADP on Gremlin-1 release from platelets (both $p = 1.0$). As for CXCL4 release, the duration of stimulation had no effect on Gremlin-1 release in Two-Way ANOVA.

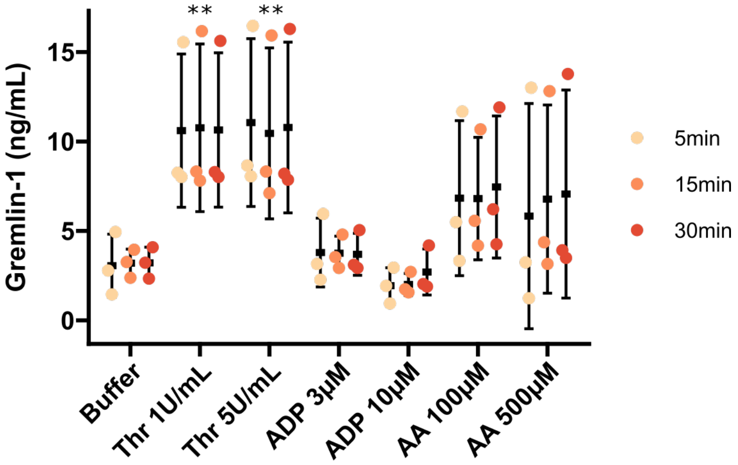

Figure 5.8: Gremlin-1 concentration in platelet supernatants after stimulation with buffer, Thrombin (Thr), ADP or arachidonic acid (AA) for 5, 10 or 15 minutes. Gremlin-1 concentrations were determined by ELISA. Data are given as mean ± SD and single data points for n=3 biological replicates measured in duplicate.
Abbreviations: AA - arachidonic acid, ADP - adenosine-diphosphate, Thr - thrombin.
**$p < 0.01$, ***$p < 0.001$ compared to Buffer using Two-Way ANOVA and post-hoc Tukey HSD.

Effect of platelet-derived Gremlin-1 on flow-based adhesion

Based on the results on platelet activation and Gremlin-1 release, we selected activated platelet supernatant (aPS) from thrombin 1 U/mL stimulated platelets for subsequent flow-based adhesion assays and used buffer-stimulated supernatants (unstimulated platelet supernatant, uPS) as a control. Flow-based adhesion assays were performed as described above, treating HSEC for 24 hours with aPS or uPS 1:1 diluted in serum- and VEGF-free HSEC culture medium supplemented with 0.1 % bovine serum albumin

(BSA). Figure 5.9 shows the results for two independent experiments using PBMCs from two different donors (experiment 1 and 2) and three independently generated aPS/uPS. Stimulation with aPS led to a slight, but non-significant increase in the number of adherent and transmigrating cells ($p = 0.077$, Figure 5.9A). This did not translate into any apparent shift in the proportion of rolling, adherent, activated or migrated cells (Figure 5.9B).

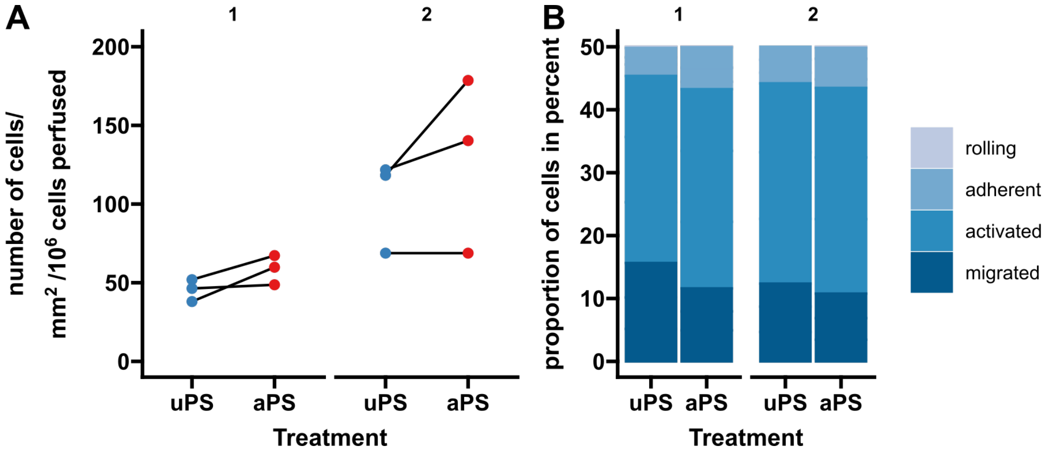

Figure 5.9: Flow-based adhesion assay on HSEC in response to activated platelet supernatant.
HSEC were seeded in 6-well Ibidi slides and grown until 80 % confluent. Cells were then treated with unstimulated platelet supernatant (uPS) or activated platelet supernatant (aPS) and incubated for 24 hours before running the flow-based adhesion assay with PBMC. The graphs represent two independent experiments (1 and 2) using PBMCs from different healthy volunteer donors. Each experiment was done using uPS and aPS generated from three independent donors. **A.** Total number of cells that adhered to the HSEC monolayer, depending on treatment with uPS or aPS. Data are given as single data points (each representing a different PBMC sample with ten fields of view recorded) and lines connecting paired data. **B.** Percentage of cells by type of adhesion.

5.2.3 Monocyte-derived macrophages

Next, we wanted to explore changes of *GREM1* expression in macrophages, which play an important role in liver fibrogenesis. Macrophages have previously been described to express Gremlin-1 and we hypothesised that Gremlin-1 might be able to shape macrophage phenotype and function. All work on public macrophage RNA sequencing datasets was performed as part of the Bachelor dissertation project of Vanessa Poon, who was jointly supervised by Dr Chris Weston and the author. Searching public data repositories, we identified seven datasets on monocyte-derived macrophages, that were stimulated with a range of cytokines, reflecting different macrophage phenotypes. Table 5.1 gives an overview of all datasets, the method of macrophage generation and stimulations used for cell differentiation.

The datasets were quite heterogeneous in that they used different methods for monocyte isolation, macrophage differentiation and experimental setup as well as sequencing platforms. Some authors used magnetic bead selection based on CD14 surface expression, either using MACS sorting or the commercial clinical-grade CliniMACS LP-14 Mo-DC system. Others used simple adhesion of PBMCs to plastic to select for adhering monocytes while one study did not disclose at all the exact method used for monocyte generation. All studies but one used M-CSF-substituted medium over two to seven days for macrophage differentiation, while the other study used human serum instead. Treatment conditions included lipopolysaccharide (LPS), LPS+interferon gamma (IFNγ) and interleukin 4 (IL-4). Notably, timing of differentiation treatment differed substantially between studies. While some authors added treatment conditions from the start of macrophage differentiation, others did so only at the end of macrophage stimulation.

In order to get an overview of the similarity of different datasets, we performed correlation analyses between the expression matrices, which are displayed in Figure 5.10. As expected, datasets from LPS, IFNγ and LPS+IFNγ-treated

Table 5.1: Overview of macrophage transcriptome datasets

Accession	cell source	differentation	treatments	platform
GSE98368 [283]	CD14 MACS	M-CSF 2d	IFNy 2d*	Illumina HiSeq 2000
GSE100382 [284]	CD14 MACS	M-CSF#	LPS 3h	Illumina HiSeq 2000
GSE123603 [285]	not described	human serum 7d	IL4 24h	Illumina NextSeq 500
GSE135753 [286]	PBMC adhesion	M-CSF#	LPS 6h	Illumina NextSeq 500
GSE132732 [287]	PBMC adhesion	M-CSF 2d	IL4 48h*	Illumina NextSeq 500
GSE146028 [288]	LP14 process	M-CSF 7d	IFNy+LPS, IL4 24h*	Illumina HiSeq 4000
GSE163165 [289]	CD14 MACS	M-CSF 7d	LPS 24h	Illumina HiSeq 2500

Abbreviations: IL4 - interleukin 4, IFNγ - interferon gamma, LPS - lipopolysaccharide, M-CSF - macrophage colony-stimulating factor
* treatment simultaneous with M-CSF stimulation, # no differentiation time given

macrophages were similar to each other and clustered together, while datasets from IL-4-treated MoMF clustered separately.

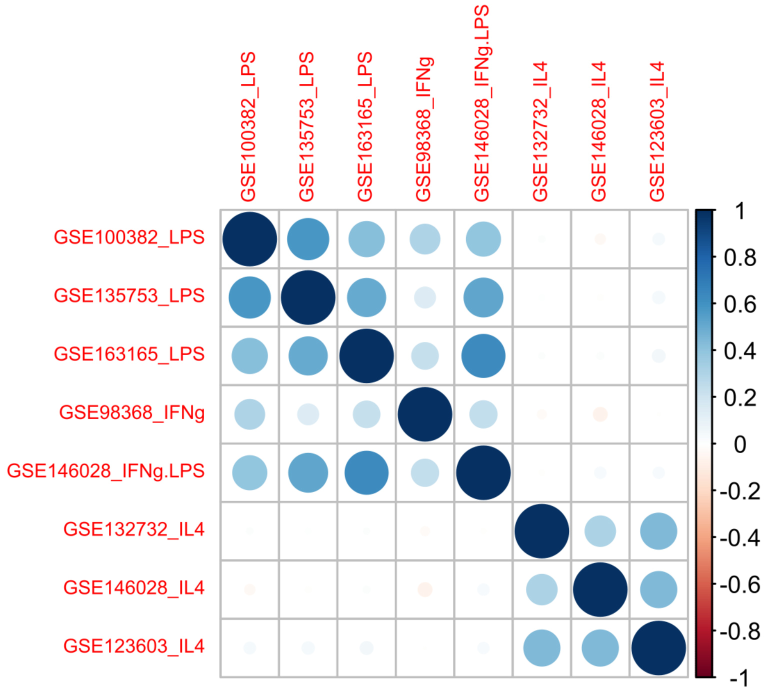

Figure 5.10: Correlation plot of public monocyte-derived macrophage RNAseq datasets. Pearson's correlation coefficients comparing different RNA sequencing datasets are indicated by circle size and colour and datasets are clustered by correlation coefficients based on complete hierarchical clustering.
Abbreviations: IFNγ - interferon gamma, IL4 - interleukin 4, LPS - lipopolysaccharide.

Next, we identified the top 2000 differentially regulated genes (DEGs) across all datasets, based on adjusted p-values obtained through the *DESeq2* pipeline. These genes were then clustered based on their $\log_2$-fold changes across datasets and gene set over-representation tests were performed for each cluster separately. The $\log_2$-fold changes and high-level function annotations for each cluster are given in Figure 5.11. LPS and IFNγ-treated cells showed gene expression changes enriched for pro-inflammatory pathways, in particular complement activation, IFNγ / LPS signalling and general macrophage activation, while genes relating to autophagy, metabolic regulation, leukocyte differentiation, extracellular matrix organisation and ERK1/2 signalling were downregulated. In contrast, IL4 stimulation led to only very small changes in gene expression that did not seem to correspond to any of the above mentioned pathways.

As we were mainly interested in gene expression changes relating to BMP signalling, we selected BMP-related genes and their $\log_2$-fold changes are shown in Figure 5.12. In addition to differential gene expression analysis for single data sets, results from LPS and IL-4-treated cells were summarised in a meta-analysis using the Fisher method and inverse normal method of p-value combination. Results of the meta-analysis are given on the right-hand side next to the heatmap in Figure 5.12. Only a few genes were consistently regulated with either LPS or IL-4 treatment. In LPS-treated cells, the activin gene INHBA was most strongly upregulated, followed by GREM1, which interestingly was downregulated upon LPS+IFNγ combination treatment. Additional upregulated genes included *BMP2*, the BMP-antagonist *neuroblastoma 1, DAN family BMP antagonist (NBL1)*, bone morphogenetic protein receptor 2 (*BMPR2*) and the *SMADs 4* and *7*. Only two genes were consistently upregulated with IL-4 treatment: *SMAD7* and the activin and BMP antagonist follistatin (*FST*).

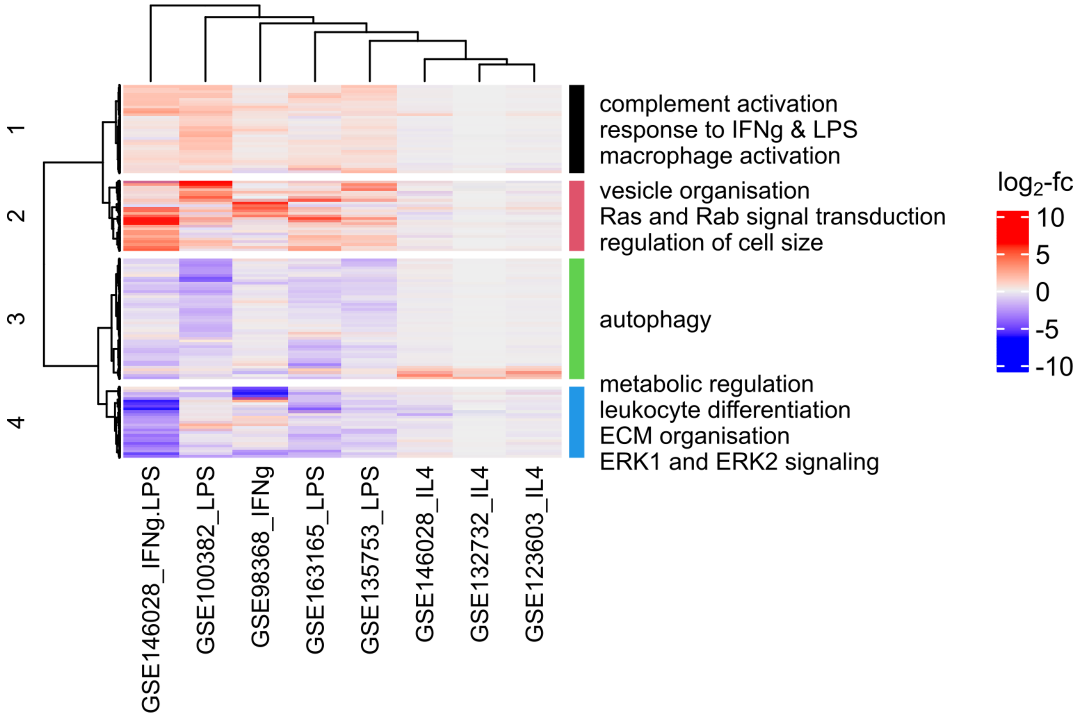

Figure 5.11: Top 2000 differentially expressed genes (DEGs) in macrophage RNAseq - Heatmap and over-representation analysis. Based on adjusted p-values we identified the top 2000 DEGs across all datasets. Genes are displayed in a heatmap with colours indicating $\log_2$-fold changes. Genes were clustered using Ward D hierarchical clustering (clusters indicated on the left) and gene set over-representation analysis (ORA) was performed on each cluster separately. The top enriched terms from ORA are annotated on the right hand side.
Abbreviations: ECM - extracellular matrix, ERK - extracellular signal-regulated kinase, IFNγ - interferon gamma, IL4 - interleukin 4, LPS - lipopolysaccharide.

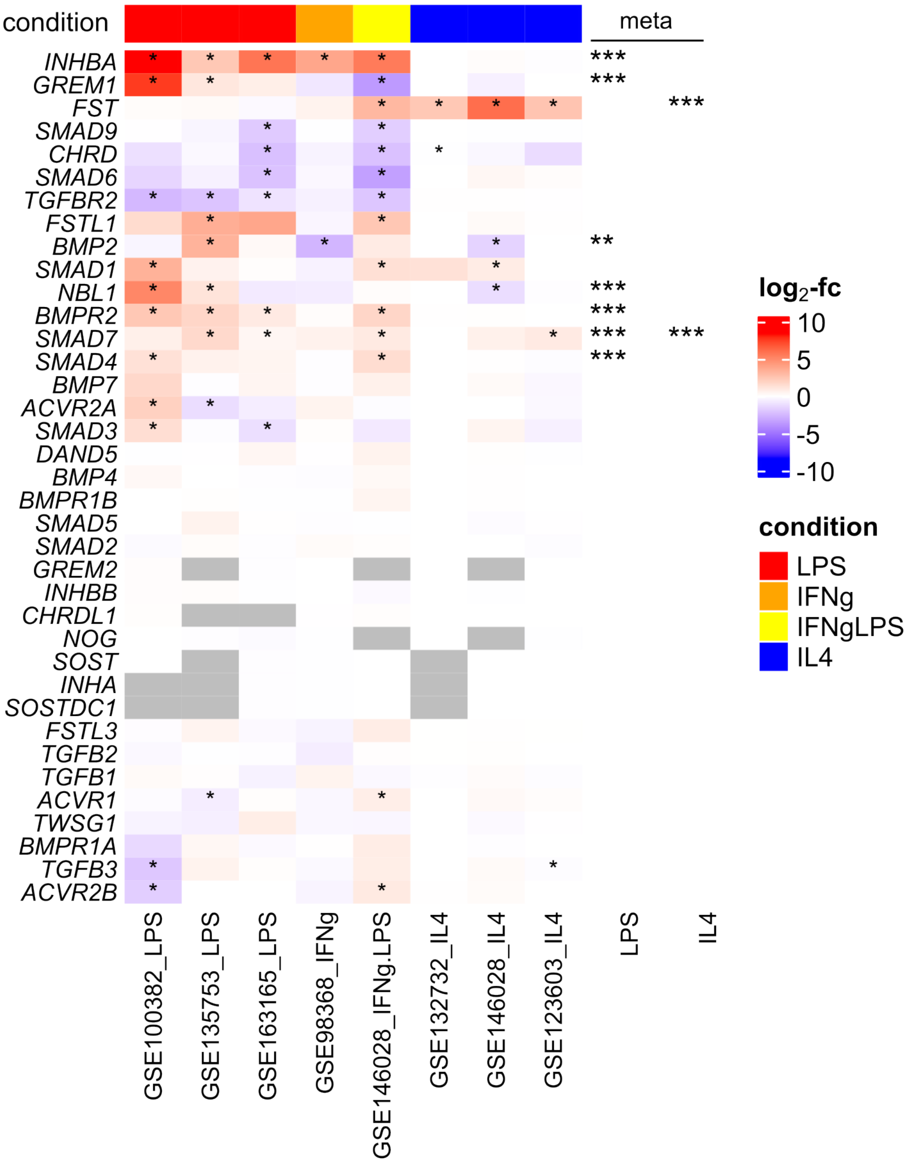

Figure 5.12: Heatmap of BMP-related genes in monocyte-derived macrophages. Log_2-fold changes of BMP-related genes are colour-coded and significance in *DESeq2* differential gene expression analysis indicated with asterisks. The two columns on the right indicate significance levels in differential gene expression meta-analysis obtained from p-value combination using the Fisher and inverse normal method in the *metaRNAseq* package.
Abbreviations: IFNγ - interferon gamma, IL4 - interleukin 4, LPS - lipopolysaccharide. *$p < 0.05$, **$p < 0.01$, ***$p < 0.001$ using Wald test in `DESeq2`

In order to validate increased expression in monocyte-derived macrophages upon pro-inflammatory stimulation with LPS and decreased expression upon combination treatment with LPS+IFNγ, we isolated PBMC-derived monocytes. Monocytes were differentiated into macrophages by stimulation with M-CSF for five days and were subsequently treated with LPS, LPS+IFNγ or IL-4 in the presence of M-CSF for an additional 48 hours. RTqPCR results of pro- and anti-inflammatory marker genes and for *GREM1* are given in Figure 5.13. Pro-inflammatory marker genes *CXCL10* and *IRF1* were consistently upregulated with LPS treatment, while the anti-inflammatory marker gene *CD163* was downregulated with both LPS+IFNγ and IL-4 stimulation. *MRC1*, another anti-inflammatory marker gene slightly decreased with LPS and fell more distinctly with LPS+IFNγ treatment. *MRC1* was however not regulated with IL-4 stimulation. *GREM1* was not regulated with any of the treatment condition. As we did not see any changes of *GREM1* in the first two sets of experiments we omitted statistical testing and any additional experiments on monocyte-derived macrophages.

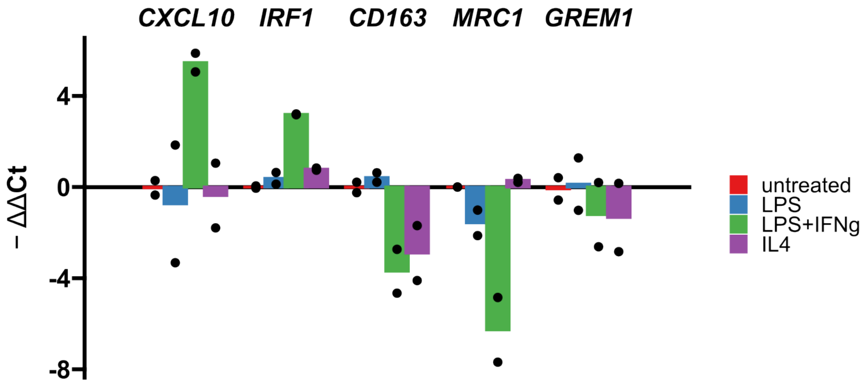

Figure 5.13: RTqPCR for macrophage phenotype markers on primary PBMC-derived macrophages. PBMC-derived monocytes, obtained through adhesion to plastic culture plates, were differentiated into macrophages by stimulating with 5 ng/mL M-CSF over five days, and subsequently were stimulated with either LPS, IFNγ, IL-4 or vehicle control for 48 hours. Data are given as individual data points of n = 2 primary MoMF measured in duplicate and colour-coded bars represent the mean for each treatment condition.
Abbreviations: CXCL10 - C-X-C motif ligand 10, IRF1 - interferon regulatory factor 1, IFNγ - interferon gamma, IL4 - interleukin 4, MRC1 - mannose receptor C-type 1, GREM1 - gremlin-1, LPS - lipopolysaccharide.
Statistical testing was omitted due to small sample size of n = 2.

5.3 Discussion

Endothelial cell activation and infiltration of inflammatory monocytes and their differentiation to monocyte-derived macrophages are important steps in the inflammation cascade in chronic liver diseases and are linked to the progression of liver fibrosis [290]. So far, research on hepatic Gremlin-1 was mainly limited to studies on the effects on HSC activation as discussed in previous chapters, and its role on hepatic sinusoidal endothelium or in hepatic MoMF (monocyte-derived macrophages) has not been investigated yet. In this chapter, we show that recombinant human Gremlin-1 had no effect on leukocyte adhesion to HSEC or on adhesion molecule expression. Furthermore we confirmed the release of low quantities of Gremlin-1 from activated platelets but found no considerable effects of platelet supernatants on flow-based adhesion assays. Analyses from publicly available MoMF RNA sequencing datasets suggested a differential regulation of Gremlin-1 by LPS and IFNγ which were not reproducible in our own *in vitro* assays.

Although there is no literature available on Gremlin-1 effects on hepatic endothelium, previous research on BMP-signalling in the liver and on Gremlin-1 and BMPs on extrahepatic endothelial cells suggested an involvement in endothelial cell activation. Gremlin-1 can be upregulated in stressed endothelial cells. This has been shown in pulmonary artery endothelial cells, where hypoxia leads to the upregulation of Gremlin-1 expression mediated by the transcription factor CREB [291]. Gremlin-1 can act directly on endothelial cells by activating VEGFR2, which induces angiogenic responses [163, 165]. This process seems to be dependent on the dimerisation of Gremlin-1, as VEGFR2 antagonistic effects have been described for monomeric forms of Gremlin-1 [162]. By activating the VEGFR2-CREB axis, Gremlin-1 can directly promote the inflammatory activation of endothelial cells *in vitro*, resulting in the production of inflammatory chemokines and upregulation of adhesion molecules ICAM1 and VCAM1 [277]. Studies on kidney inflammation further support an involvement of Gremlin-1 in inflammatory processes through endothelial cell activation: Gremlin-1 elicits inflammatory responses in the kidney, including infiltration of leukocytes and expression of inflammatory cytokines, which are abrogated by VEGFR2 kinase inhibition or blockade of the Notch pathway [292].

Furthermore, Gremlin-1 is best known as a BMP antagonist and existing evidence suggests a role of BMPs in endothelial activation. BMP2 is a driver of angiogenesis in hepatocellular carcinoma [293] and can act as an activator of HSEC [143]. In extrahepatic vascular endothelium, BMP2 promotes leukocyte adhesion *in vivo*, which was inhibited by the synthetic BMP antagonist dorsomorphin [144]. Also, siRNA-mediated knockdown of the BMP-regulator BMP binding endothelial regulator (*BMPER*) led to an upregulation of VCAM1 and ICAM1 in human umbilical vein endothelial cells (HUVECs) and increased leukocyte adhesion *in vitro* and *in vivo*, effects that were abrogated by adding the BMP antagonist Noggin [144]. Not least, vascular smooth muscle cell-derived BMP2 and 4 can drive monocyte chemotaxis through the activation of the BMP receptor BMPR2 [294]. Despite this wealth of evidence suggesting a role for Gremlin-1 in immune cell recruitment we found no effect of recombinant human Gremlin-1 on HSEC activation or leukocyte adhesion *in vitro*. While we did not further investigate the reasons for the lack of an effect in light of negative data on liver inflammation presented in the previous chapter, we can speculate on a number of reasons for these unexpected results. As discussed above, Gremlin-1 can have different effects on endothelial cells, depending on the pathways involved: mostly pro-inflammatory by activating VEGFR2 or potentially anti-inflammatory by blocking the endothelial cell-activating effects of BMPs. Therefore, on HSEC these could cancel out, leading to a net absence of an effect or a minimal effect that our assays are not sufficiently sensitive to detect. Furthermore, the micro milieu in monolayer cell culture is not representative of the hepatic inflammatory microenvironment, meaning that specific factors necessary for a Gremlin-1 effect, such as BMP might be insufficiently provided, or the use of allogeneic blood and endothelium masks any effect. In addition, the anti-CD31 antibody used for isolation of primary HSEC is not specific to sinusoidal endothelium. Therefore, our HSEC culture likely represents a mix of vascular and sinusoidal endothelial cells and while we did not specifically test for the heterogeneity of primary cultures the composition may well have biased our results. Not least, the effect on VEGFR2 is still under ongoing debate and a recent report found no effect of recombinant Gremlin-1 on VEGFR2 signalling activity [295].

Platelets are a relevant contributor to liver inflammation and disease progression [81], and recent literature in particular found protective effects of anti-platelet treatments against steatohepatitis and hepato-carcinogenesis in MASLD [79]. Gremlin-1 can be released from platelets and seems to be functionally active on monocytes by modulating their proliferation, differentiation and function [181]. Platelets can be easily activated upon handling in the laboratory and we therefore used an established protocol for the isolation and clean-up of platelets using heparin and prostaglandin I_2 (PGI_2) for preventing their premature activation [212]. This provided us with clean and inactive platelet suspensions, which easily activated and degranulated upon treatment with thrombin or high doses of arachidonic acid, known platelet activators [296]. This was evidenced by increased P-selectin (CD62P) surface expression and release of CXCL4 into the supernatant, which are hallmark marker proteins of platelet α-granules [282]. Surprisingly though, we were not able to induce platelet degranulation with ADP at 2 or 10 µM concentrations. ADP is considered a weak platelet activator, whose main role is in co-activation of other signals, including thrombin and arachidonic acid [297]. Therefore, it would be plausible that ADP at the concentrations used here and without co-stimulation did not result in α-granule release. Still, with thrombin and arachidonic acid we found two stimulants that resulted in adequate α-granule degranulation for generating supernatants from activated platelets.

Platelets contain three different types of granules: α-granules, which contain coagulation factors, cytokines, chemokines, growth factors, including TGFβ1, PDGF and BMPs, dense granules containing nucleotides, biogenic amines such as catecholamines and serotonin, and lysosomes which mainly contain lytic enzymes [280, 298]. Therefore, they should contain a mixture of different proteins related to BMP-signalling, including Gremlin-1. Using commercially available ELISA, we found that stimulation with thrombin at low and high concentrations led to a potent release of Gremlin-1 into the culture medium, whereas this was not significant for stimulation with arachidonic acid. Therefore, we used thrombin-stimulated platelet supernatants for the subsequent flow-based adhesion experiments. Treatment with aPS led only to a slight and non-significant increase in leukocyte adherence. For several reasons we omitted further follow up on this angle of research into Gremlin-1: The concentration of Gremlin-1 detected in aPS was very low and as reported in the literature, platelet BMP content can differ substantially between donors [280]. Although we did not check for abundance of BMP proteins in aPS, we feel that any potential effect of Gremlin-1 and BMPs would only partially account for the increase in leukocyte adherence and thus the number of replicates would be too large to be feasible when using primary human cells. Notably though, evidence generated by our group showed that treating HSEC with intact platelets results in increased recruitment of leukocytes in flow-based adhesion assays [78], which suggests that platelets provide additional signals not related to their vesicle content that might be important for endothelial cell activation. Therefore, using intact platelets instead of their supernatants might have yielded different results.

Although evidence is scarce, literature points towards a role of Gremlin-1 in monocyte differentiation and macrophage polarisation. An as yet non peer-review published meeting abstract suggests that Gremlin-1 can be upregulated in response to hypoxia in alveolar macrophages [299] and another report indicated that Gremlin-1 is secreted by macrophages in atherosclerotic plaques [278]. Gremlin-1 has been described as a regulator of monocyte survival and macrophage differentiation mainly via modulation of MIF [278]. Levels of Gremlin-1 correlate with the severity of coronary disease [182] and through inhibition of MIF reduces macrophage differentiation in atherosclerotic plaques in ApoE$^{-/-}$ mice [278]. In addition, BMPs 4 and 7 have been shown to drive anti-inflammatory M2-like differentiation of macrophages [300, 301], and thus by inhibition of BMP-signalling Gremlin-1 could potentially promote an inflammatory M1-like phenotype. In line with these published results of upregulated Gremlin-1 in activated macrophages, we found increased Gremlin-1 mRNA expression in public RNA sequencing datasets of MoMF stimulated with LPS. Interestingly, Gremlin-1 mRNA was downregulated in MoMF treated with a combination of LPS and IFNγ, although in over-representation tests, this combination treatment led to a similar inflammatory regulation compared to LPS alone. Still, surprisingly, we could not reproduce these findings in our own *in vitro* culture system of primary human MoMF. Neither LPS, nor LPS plus IFNγ or IL4 had any appreciable effect on Gremlin-1 mRNA expression in differentiated macrophages. This may have arisen due to differences in monocyte isolation (adherence of PBMCs to plastic *vs* CD14 magnetic sorting) and monocyte-to-macrophage differentiation protocols, e.g. duration of treatment with M-CSF might have contributed to heterogeneous results. In addition, the type of cell donor might have had an impact, with healthy volunteers used in the literature, whereas we used blood from patients with haemochromatosis, who tend to be older and may have underlying significant liver disease. Eventually, in light of negative findings on liver inflammation in response to Gremlin-1 in the previous chapter, we decided to discontinue the work on Gremlin-1 in macrophages.

In summary, in line with negative results from the previous chapter, we found no evidence of a role for Gremlin-1 in driving liver inflammation. Still, as evidence from the literature suggests that Gremlin-1 can shape endothelial cell and macrophage phenotypes, more in-depth research might reveal some role of Gremlin-1 in liver biology, maybe in more complex multi-cellular study systems such as organ-on-a-chip models or in different contexts than chronic inflammatory and fibrotic liver disease.

CHAPTER 6

LIVER FIBROSIS AND HEPATIC STELLATE CELL RNA SEQUENCING DATA IDENTIFY FSTL3 A POTENTIAL DRIVER OF LIVER DISEASE

6.1 Introduction

The main aim of this thesis was to study the effects of Gremlin-1 on liver fibrosis progression in MASH and its potential as a therapeutic target. As shown in the previous three chapters, we found no effect when targeting Gremlin-1 using neutralising antibodies, recombinant Gremlin-1 protein or lentiviral overexpression vectors. In light of the negative data on Gremlin-1, we next sought to identify other potential therapeutic targets related to the BMP signalling pathway.

Next generation sequencing technologies offer the opportunity to study large scale transcriptional changes in a variety of physiological and disease conditions [252]. Unlike classical gene expression technologies, such as RTqPCR, RNA sequencing detects all expressed gene transcripts and therefore is not limited to the study of predefined targets or pathways. It is now widely accepted that upon publication omics data (including RNA sequencing - transcriptomics) should be made available on public servers for others to re-analyse (e.g. gene expression omnibus (GEO) [225], ArrayExpress[227] or the European Nucleotide Archive [226]). Therefore, if sufficient publicly available data on the condition of interest exists, the analysis of such transcriptome datasets can serve as a screening tool to identify potential novel markers or therapeutic targets. Others have already applied this strategy to their work on MASLD and MASH, facilitating the identification of gene signatures of disease or markers of disease progression [302, 303]

In this chapter, by analysing publicly available RNA sequencing datasets from human liver disease and TGFβ-treated primary hepatic stellate cells (HSCs) we sought to identify potential HSC-derived drivers of liver fibrosis. Using this approach we identified the Activin A antagonist follistatin-like 3 (*FSTL3*) as commonly upregulated in human liver fibrosis of different aetiologies and in HSCs treated with TGFβ. Subsequently, by employing siRNA knockdown of *FSTL3* in cell culture models of HSC activation and hepatocellular steatosis, we validated a potential role of *FSTL3* in the activation of HSCs and hepatocellular lipid accumulation.

6.2 Results

6.2.1 Liver fibrosis transcriptome data

As a first step, we aimed to study transcriptional changes with increasing stages of fibrosis across a spectrum of different aetiologies of chronic liver diseases. Searching public data repositories, we identified four datasets, comprising data from a total of 330 patients with either MASLD/MASH or viral hepatitis (Table 6.1). Unfortunately, no data from alcohol-related, autoimmune or cholestatic liver disease fulfilling our search criteria were available. Two of the datasets were generated using bulk RNA sequencing (GSE130970 and E-MTAB-6863) and the other two using Affymetrix gene expression microarrays (GSE48452 and GSE84844). Patients in the MASLD/MASH studies were slightly older and much more likely to be female than patients in the chronic viral hepatitis datasets (Table 6.1). The number of patients with advanced stages of fibrosis, i.e. fibrosis stage 3 or 4, was highly variable across datasets, ranging from 5.4 to 42 percent.

Table 6.1: Overview of human liver fibrosis transcriptome datasets

Accession	**disease**	**platform**	**patients (n)**	**age (mean±SD)**	**% female**	**% F3/4**
GSE48452 [304]	MASH	Affymetrix 1.1 ST Array	73	46±12	79.6	5.4
GSE130970 [305]	MASH	Illumina HiSeq 2500	78	50±12	61.5	20.5
GSE84844 [306]	HBV	Affymetrix U133 Plus 2.0 Array	124	43±12	29.0	22.6
E-MTAB-6863 [307]	HCV	Illumina NextSeq 500	55	44±11	29.1	42

Abbreviations: HBV/HCV - hepatitis B/C virus, MASH - metabolic dysfunction-associated steatohepatitis

Next, we performed differential gene expression analysis by ordinal regression for each dataset separately. The stage of fibrosis served as the dependent ordinal variable and the variance-stabilized expression values for each gene as the independent variable. The regression model was adjusted for sex as a potential confounder. Figure 6.1 summarises the differential gene expression results and overlap between the datasets in an upset plot. Overall, overlap between datasets was very low, with only 69 genes being up- and 4 genes being down-regulated in all four studies and most genes were not shared across different datasets.

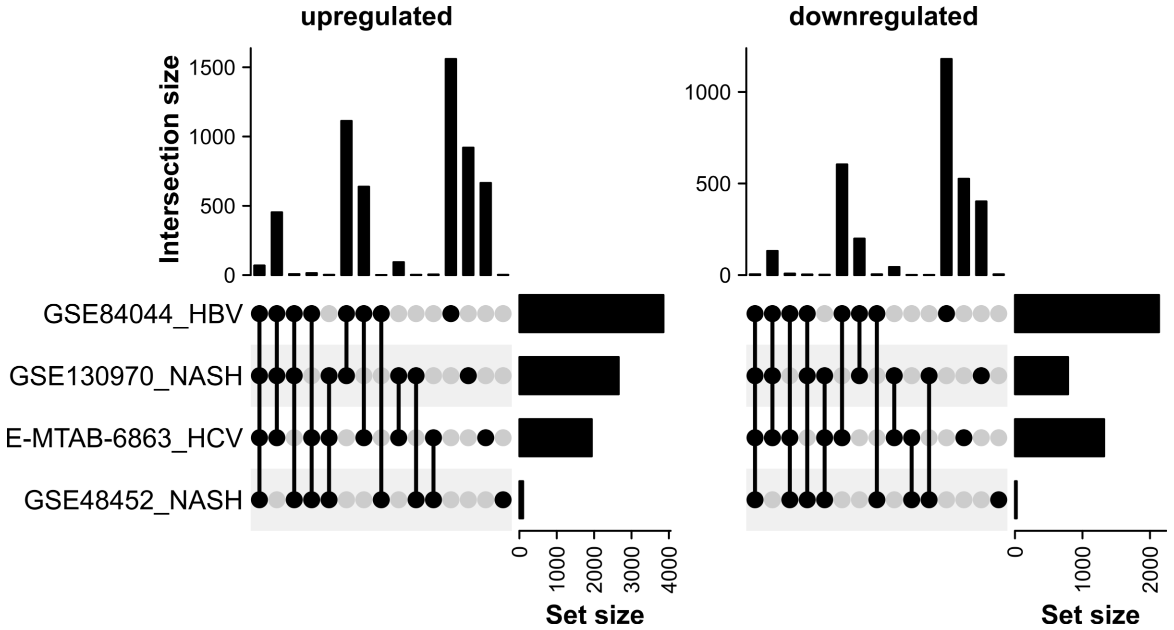

Figure 6.1: Upset plots for differentially expressed genes in human liver fibrosis datasets. Upregulated genes are given on the left and downregulated genes on the right-hand panel. The horizontal bar plots on the right side of each panel represent the total number of up- or downregulated genes per dataset and the vertical bar plot on the top gives the size of the overlap between different combinations of datasets, with the combinations being indicated by black connected lines in the bottom half of the plot.

Figure 6.2 visualises the batch-corrected and row-centred gene expression values for the 73 overlapping genes in a heatmap. Overall, based on gene expression, the clustering of patients was in good accordance with the stage of fibrosis and no major batch effects were visible between the datasets.

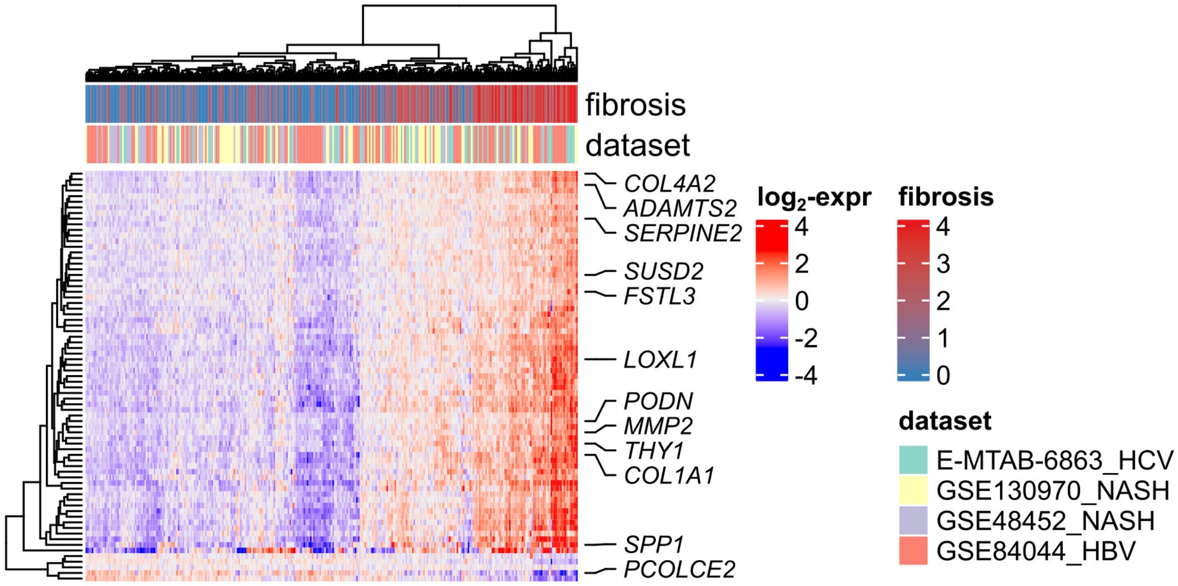

Figure 6.2: Heatmap of common differentially expressed genes in human liver fibrosis. The heatmap gives colour-coded, variance-stabilised and row-centred gene expression values on the $\log_2$ scale, where rows represent genes and columns represent individual patients. Stage of fibrosis and dataset identities are indicated in the top annotation and some exemplary genes are marked as row annotations.

Figure 6.3 visualises results from gene set over-representation tests on up- and downregulated genes with liver fibrosis. Upregulated genes were enriched for gene sets relating to synthesis and organisation of the extracellular matrix, wound healing response and tissue regeneration, as well as response to TGFβ. Only 14 gene sets were enriched for downregulated genes, all containing one gene only. Downregulated gene sets mostly related to amino acid and protein metabolism.

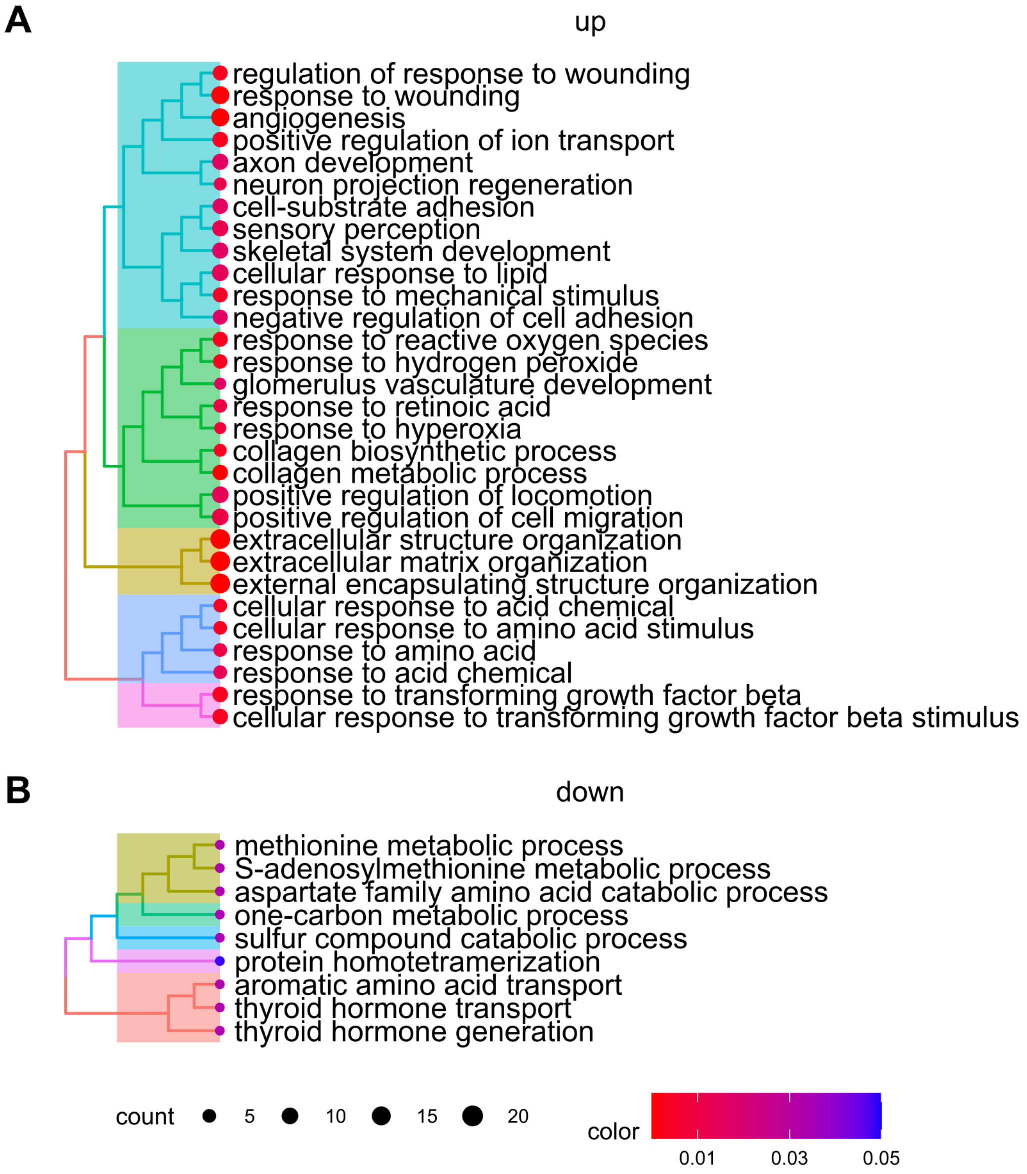

Figure 6.3: Treeplot showing over-representation analysis results from liver fibrosis datasets. The top 30 **(A)** Up- and top 14 **(B)** downregulated gene sets with increasing stages of liver fibrosis. Gene sets were clustered by similarity and the cluster dendrogram is shown on the left. The dot size indicates the number of genes per gene set and colour indicates the adjusted p-value in over-representation analysis.

6.2.2 Hepatic stellate cell transcriptome data

Hepatic stellate cells are the main fibrogenic cell-type in the liver and therefore, we aimed to identify those genes that are regulated not only in fibrotic livers but also upon activation of stellate cells. We identified five bulk RNA sequencing datasets of HSCs treated with TGFβ1, which are given in Table 6.2. All studies used commercially sourced HSCs from ScienCell, with the exception of GSE117329, which did not disclose the source of cells used. The TGFβ1 doses ranged from 2.5 ng/mL to 10 ng/mL, and again, were not given for dataset GSE117329. Cells were generally serum-starved and then treated with TGFβ1 for the indicated length of time.

Table 6.2: Overview of human hepatic stellate cell transcriptome datasets

Accession	**cell source**	**platform**	**treatment**	**dose**	**timepoints**
GSE117329	*NA*	Illumina HiSeq 4000	TGFβ1	*NA*	24h, 48h, 72h
GSE119047 [308]	ScienCell	Illumina HiSeq 2500	TGFβ1	2.5 ng/mL	48h
GSE119606 [309]	ScienCell	Illumina HiSeq 3000	TGFβ1	10ng/mL	48h
GSE127964 [310]	ScienCell	Illumina HiSeq 2500	TGFβ1	5ng/mL	24h
GSE128940 [311]	ScienCell	Illumina NextSeq 500	TGFβ1	5ng/mL	24h

Abbreviations: TGFβ1 - transforming growth factor beta 1

Differential gene expression analysis was performed using the Wald test implemented in the `DESeq2` package and Figure 6.4 gives an overview of the number of differentially up- and downregulated genes per dataset and the overlap between different datasets, independent of dose and duration of TGFβ1-treatment. Overall, 288 up- and 225 downregulated genes were shared between at least four out of five datasets.

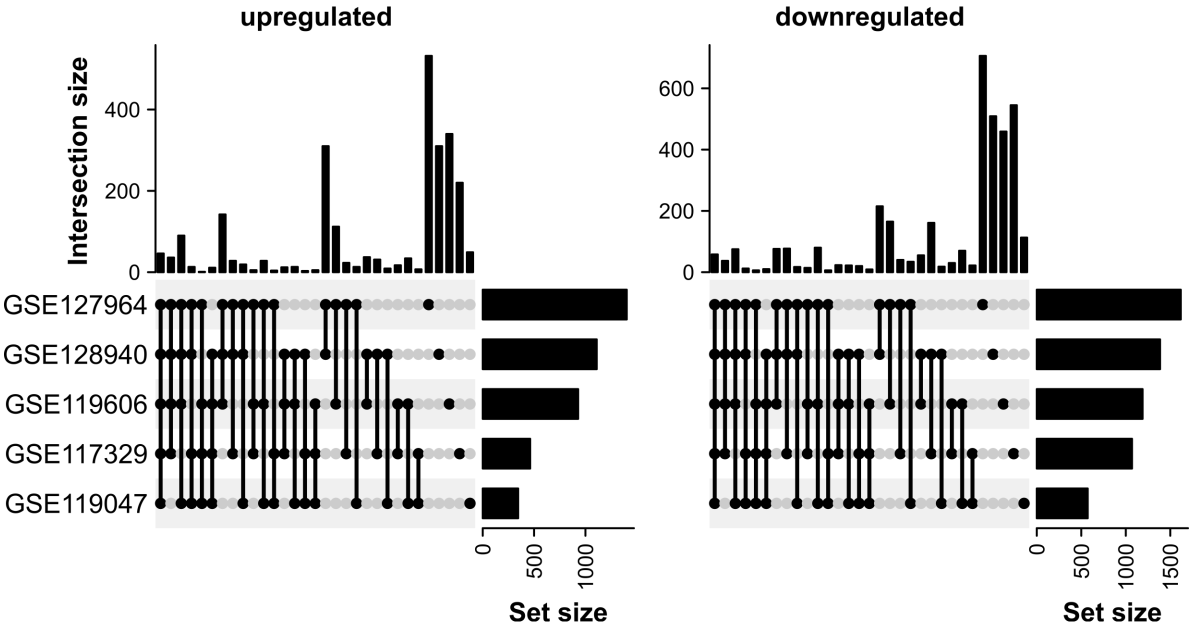

Figure 6.4: Upset plots for differentially expressed genes in hepatic stellate cell datasets. Upregulated genes are given on the left and downregulated genes on the right-hand panel. The horizontal bar plots on the right side of each panel represent the total number of up- or downregulated genes per dataset and the vertical bar plot on the top gives the size of the overlap between different combinations of datasets, with the combinations being indicated by black connected lines in the bottom half of the plot.

Figure 6.5 shows a heatmap visualising the row-centred gene expression values for the overlapping genes, adjusted for batch effects across datasets. The experiments, given in the rows, clustered well according to their treatment with TGFβ1 or control.

Figure 6.6 illustrates results from over-representation analysis on up- and downregulated genes in HHSC datasets. Interestingly, upregulated gene sets mostly related to cell differentiation, cell growth, protein metabolism and endoplasmic reticulum stress, while wound regulation processes were only weakly upregulated. Downregulated gene sets mostly related to immune processes, proliferative pathways, cell migration and regulation of MAPK and TGFβ signalling pathways as well as organisation of the extracellular matrix.

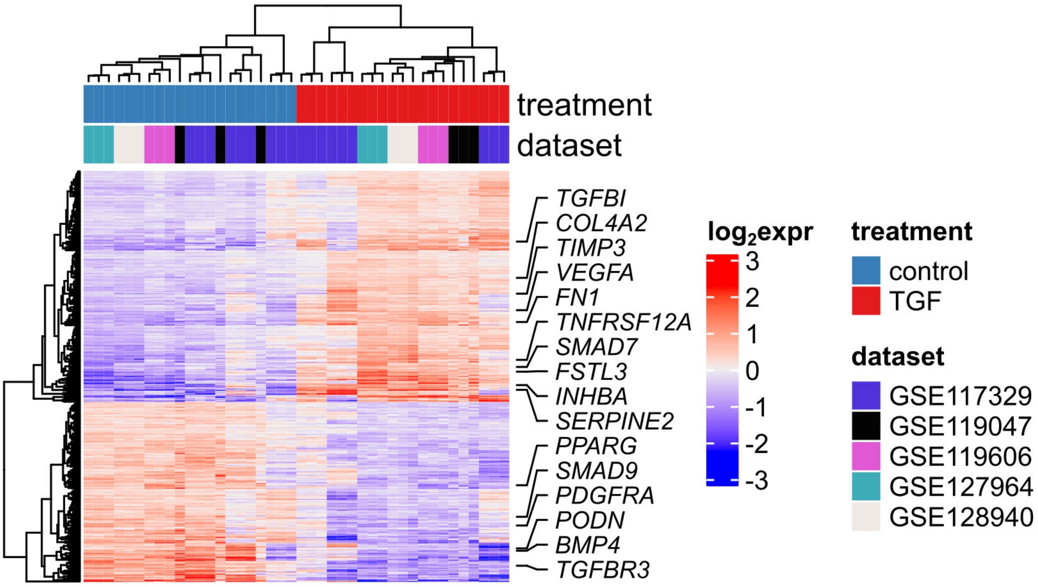

Figure 6.5: Heatmap of common differentially expressed genes in hepatic stellate cells. The heatmap gives colour-coded, variance-stabilised and row-centred gene expression values on the $\log_2$ scale, where rows represent genes and columns represent individual experiments. Treatment conditions and dataset identities are indicated in the top annotation and some exemplary genes are marked as row annotations.

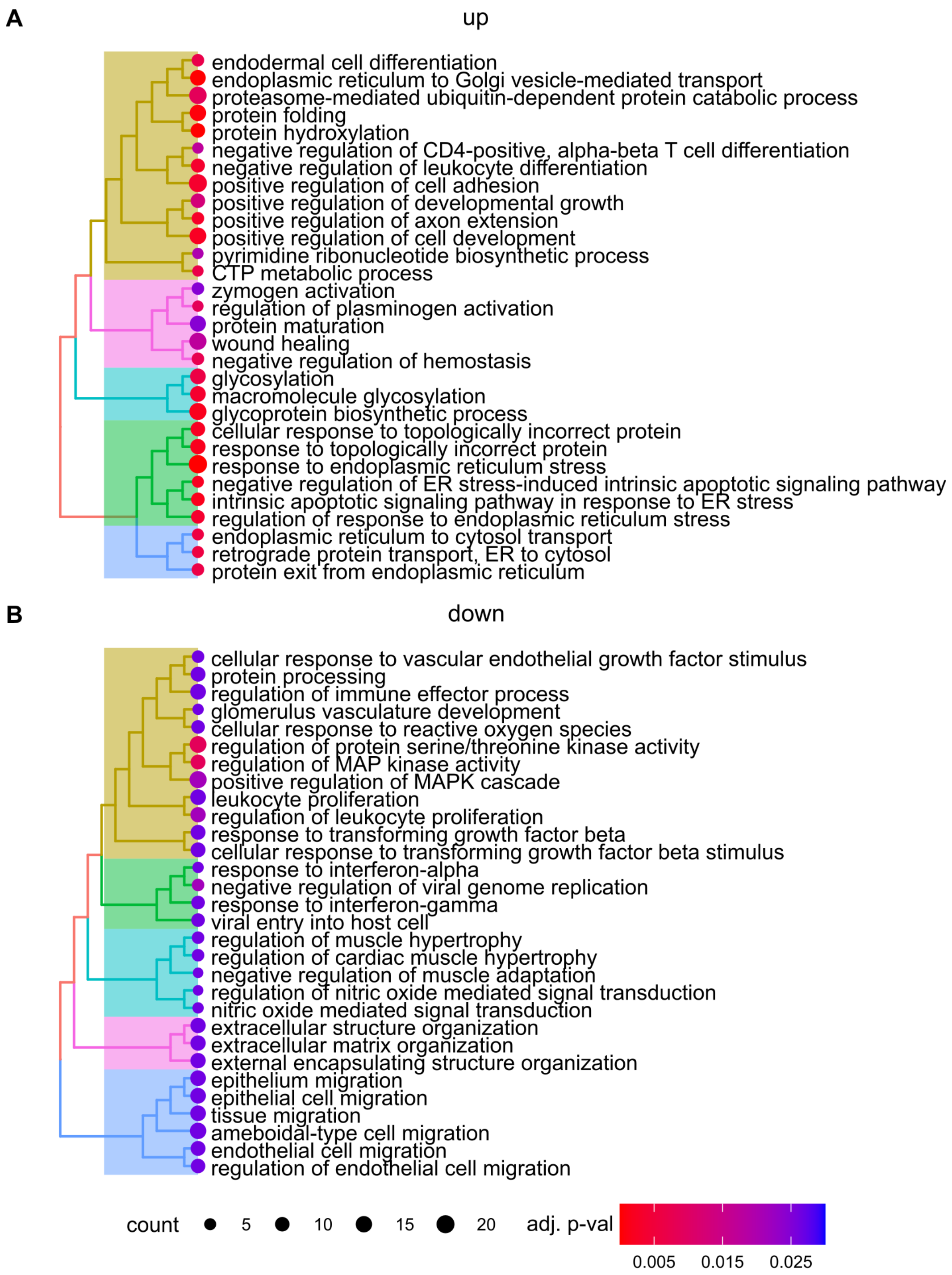

Figure 6.6: Treeplot showing over-representation analysis results from HHSC datasets. Top 30 **A.** Up- and **B.** downregulated gene sets with TGFβ-stimulation. Gene sets were clustered by similarity and the cluster dendrogram is shown on the left. The dot size indicates the number of genes per gene set and colour indicates the adjusted p-value in over-representation analysis.

Figure 6.7 visualises the overlap of up- and downregulated genes shared between human MASH fibrosis and primary human hepatic stellate cell (HHSC) activation. Overall, overlap was small. Only ten upregulated gene transcripts were shared (Figure 6.7A), while there was no overlap in downregulated genes (Figure 6.7B). Gene symbols for overlapping genes are given below the two Venn diagrams. Among these were genes coding for known matrix proteins (*COL4A2*, *COL5A1*, *FBLN5*, *LTBP2*), matrix receptors (*ITGBL1*), a sodium-channel usually expressed on neurons (*NALCN*), the glycolytic enzyme *PFKP*, a serine proteinase inhibitor (*SERPINE1*) and *UNC5B* which codes for a netrin-1 receptor associated with cell growth and apoptotic processes. Interestingly, one of the genes corresponds to follistatin-like 3 (*FSTL3*) which, alongside Gremlin-1, belongs to the group of BMP- and TGFβ-protein antagonists.

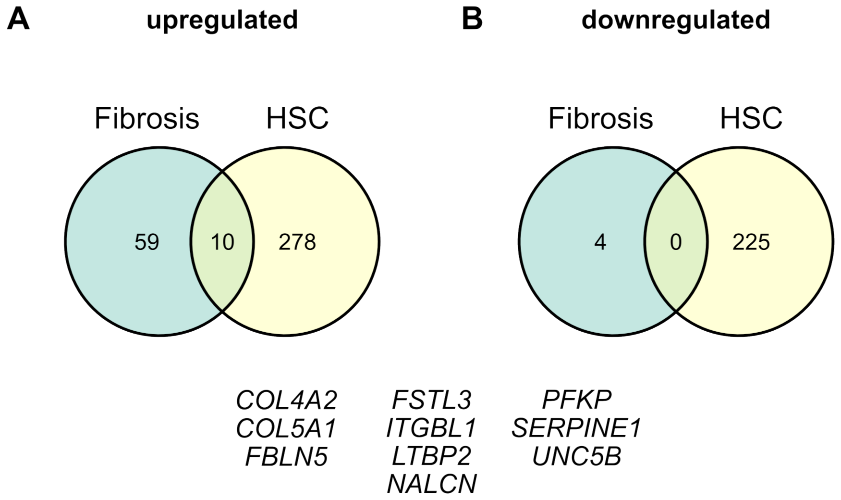

Figure 6.7: Venn diagrams showing overlap between up- (**A**) and downregulated (**B**) differentially expressed genes from human liver fibrosis datasets and primary HSC data. Gene symbols at the bottom give the names of all overlapping genes.

6.2.3 Increased *FSTL3* in liver cirrhosis and in activated fibrogenic cells and hepatocytes

After identification of *FSTL3* as a consistently regulated target gene in MASH fibrosis and in the activation of hepatic stellate cells, we wanted to verify these expression changes in our own study systems and include other liver disease pathologies. RTqPCR on human explant livers showed consistently 3.12 to 3.52-fold increased expression of *FSTL3* in MASH, alcohol-related liver disease (ArLD), primary biliary cholangitis (PBC) and primary sclerosing cholangitis (PSC) when compared to donor livers (all $p < 0.001$, Figure 6.8).

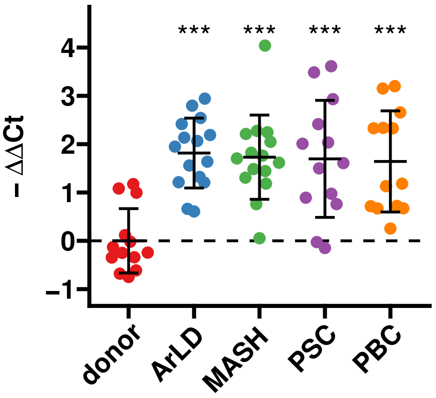

Figure 6.8: *FSTL3* gene expression by RTqPCR in tissue lysates from human liver cirrhosis compared to donor liver. Data are given as individual data points (each representing a different patient sample measured in duplicate) and mean -ΔΔCt ± SD, relative to donor liver and normalised to the expression of *SRSF4*, *HPRT1*, and *ERCC3*. ArLD ($p = 1.1 \times 10^{-5}$), MASH ($p = 2.0 \times 10^{-5}$), PBC ($p = 9.9 \times 10^{-5}$) and PSC ($p = 4.2 \times 10^{-5}$). n = 13 - 15 per group. ***$p < 0.001$ compared to donor using One-Way ANOVA with post-hoc Dunnett test.
Abbreviations: ArLD - alcohol-related liver disease, MASH - metabolic dysfunction-associated steatohepatitis, PBC - primary biliary cholangitis, PSC - primary sclerosing cholangitis.

Consistent with the upregulation of *FSTL3* in TGFβ1-treated primary hepatic stellate cells in public RNA sequencing data, we found a 2.9-fold and 3.8-fold upregulation of *FSTL3* in LX-2 in response to 100 ng/mL Activin-A and 50 U/mL TGFβ1 treatment, respectively (Figure 6.9A, $p = 0.016$ and $p = 0.00064$, respectively). Similarly, *INHBA* mRNA, the gene coding for Activin A which is the main target of *FSTL3*, was significantly upregulated with Activin A and TGFβ1 treatment (1.5- and 2.3-fold, Figure 6.9B, $p = 0.008$ and $p = 0.00056$, respectively).

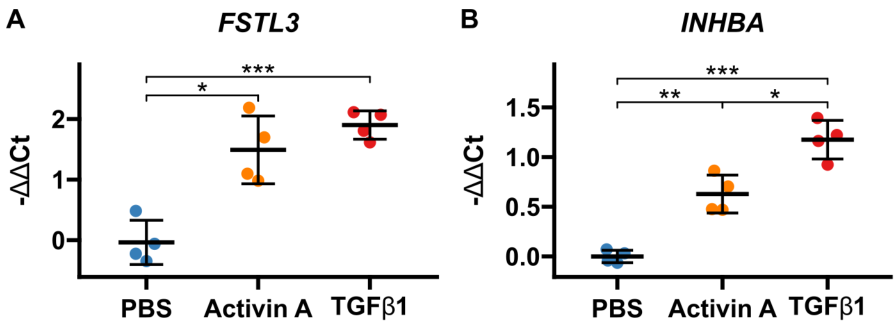

Figure 6.9: RTqPCR results for *FSTL3* (A) and *INHBA* (B) expression in LX-2 cells upon activation with Activin A or TGFβ1. LX-2 cells were treated with 100 ng/mL Activin A or 50 U/mL TGFβ1 for 24 h.
All data are given as individual data points (each representing an independent experiment measured in duplicate) and mean±SD for -ΔΔ Ct relative to PBS control and normalised to the expression of *SRSF4*, n = 4 per group.
Abbreviations: FSTL3 - follistatin-like 3, INHBA - inhibin β_A chain, PBS - phosphate-buffered saline, TGFβ1 - transforming growth factor beta 1.
$p < 0.05$, **$p < 0.01$, ***$p < 0.001$ using One-Way ANOVA with post-hoc Dunnett T3 test

FSTL3 has previously been implicated in hepatocellular steatosis, and therefore, in addition to studying fibrotic effects in LX-2 cells, we measured expression changes in the hepatocyte cell line HepG2 in response to fatty acid and Activin A treatment. Treatment of HepG2 cells with 100 ng/mL Activin A led to a significant 22.8-fold upregulation of *FSTL3* expression ($p = 3.14 \times 10^{-10}$, Figure 6.10). Supplementation of media with 0.6 mM BSA-conjugated fatty acids, consisting of palmitic acid:oleic acid (PA/OA) at a 1:2 ratio, also led to a slight nominal 1.35-fold increase in *FSTL3* expression in the Activin A-treated cells only, but this difference was not significant (*p* = 0.09, Figure 6.10). Unlike in the LX-2 cells, *INHBA* was not detectable under any condition.

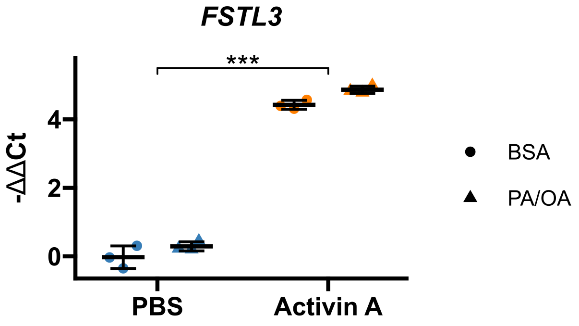

Figure 6.10: RTqPCR results for *FSTL3* expression in HepG2 cells. Cells were treated with 100 ng/mL Activin A or a 0.6 M of 1:2 palmitic acid/oleic acid (PA/OA) for 24 h.
Data are given as individual data points (each representing an independent experiment measured in duplicate) and mean±SD for -ΔΔ Ct relative to PBS+BSA control and normalised to the expression of *SRSF4*, n = 3 per group.
Abbreviations: BSA - bovine serum albumin, FSTL3 - follistatin-like 3, PBS - phosphate-buffered saline, PA/OA - palmitic/oleic acid.
***p* < 0.001 for Activin A *vs* PBS using Two-Way ANOVA with interaction effect and post-hoc Tukey HSD test.

6.2.4 Establishing *FSTL3* knockdown in LX-2 and HepG2

Having established that *FSTL3* is significantly regulated in LX-2 and HepG2 cells in response to either Activin A or TGFβ1 treatment, we sought to modulate *FSTL3* expression to determine its biological function in the context of liver steatosis and fibrosis. We tested four different siRNAs targeted at *FSTL3* (named *FSTL3* siRNA 5, 6, 8 and 9) and compared a range of concentrations to negative control siRNA

(Figure 6.11A). To achieve a biologically meaningful response, we aimed for a minimum 70 % reduction of *FSTL3* mRNA expression following siRNA transfection. The majority of the siRNA knockdown experiments were performed by Kavitha Kirubendran and Alex Reeves as part of their Bachelor dissertation projects, jointly supervised by Dr Chris Weston and the author of this thesis.

In a first screening, cells were harvested at 24 hours after transfection. In LX-2 cells, *FSTL3* siRNA 5 induced a more than 75 % reduction in *FSTL3* expression, while the other siRNAs achieved about 50-60 % reduction (Figure 6.11A, left panel). Similarly in HepG2 cells, *FSTL3* siRNA 5, but also *FSTL3* siRNA 9 led to reduction in *FSTL3* expression by 70 % to 75 %, respectively, while the other two siRNAs achieved only a 50 % reduction (Figure 6.11A, right panel). The responses had a slight dose-dependent effect with maximum effects seen from 2.5-5.0 nM concentrations upwards without any visible effects on cell viability.

Based on these results, siRNAs 5 and 9 at 5 nM concentration were selected for further testing. The efficacy of siRNA-induced knockdown can be highly time-dependent and thus we performed a time-course experiment, harvesting cells at 24, 48 and 72 hours after transfection. Negative control siRNA and no siRNA controls were run in parallel as reference. Both siRNA 5 and 9 were highly effective at knocking down *FSTL3* expression in LX-2 cells, achieving a up to 81 and 86 % reduction, respectively, with the maximum effect at 48 and 72 h (Figure 6.11B, left panel). In HepG2 cells, siRNA 5 was more effective at reducing *FSTL3* expression, achieving up to 87 % after 24h, while siRNA 9 exceeded 70 % knockdown by 72 h with only 62 to 45 % reduction at earlier time points (Figure 6.11B, right panel). Based on these results, *FSTL3* siRNA 5 at 5 nM concentration and an overall incubation time of 48 h after transfection were chosen for all subsequent experiments.

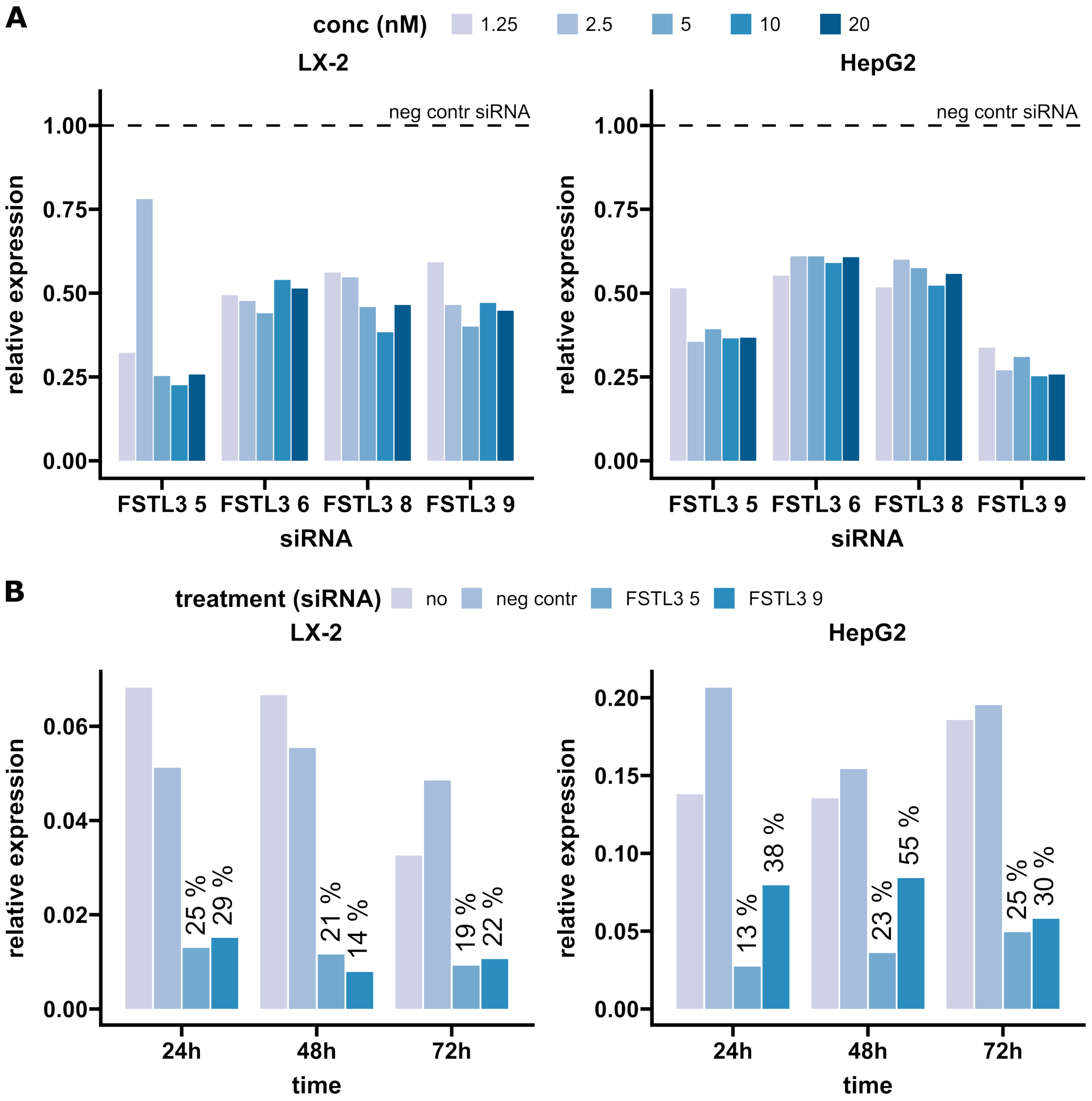

Figure 6.11: RTqPCR results for testing *FSTL3* siRNA knockdown in LX-2 and HepG2 cells. A. Bar diagram showing expression values for *FSTL3* on the linear scale relative to negative control siRNA (dashed line) for four different siRNAs at concentrations ranging from 1.25 nM to 20 nM for LX-2 (left) and HepG2 cells (right). **B.** Bar diagram showing expression values for *FSTL3* relative to SRSF4 on the linear scale for selected siRNAs at 5 nM concentration for LX-2 (left) and HepG2 cells (right). All bars represent n = 1, each representing an independent experiment measured in duplicate, and statistical testing was therefore omitted.

6.2.5 Knockdown of *FSTL3* modulates fibrogenic gene expression in LX-2

As shown in Figure 6.2, *FSTL3* strongly associated with the stage of fibrosis in datasets of human MASLD and MASH. We also found a prominent regulation of *FSTL3* in hepatic stellate cells with TGFβ-stimulation and therefore we sought to investigate whether *FSTL3* has a role in the activation of those cells. For this purpose, we used LX-2 cells as a model of hepatic stellate cells and treated these with TGFβ1 with or without prior *FSTL3* siRNA knockdown. Consistent with results shown in Figure 6.9, TGFβ1 treatment significantly upregulated the expression of *FSTL3* ($p = 2.85 \times 10^{-5}$, Figure 6.12A), while *FSTL3* siRNA knockdown effectively and significantly reduced *FSTL3* expression in both PBS control and TGFβ1 treated cells ($p = 1.57 \times 10^{-3}$ and $p = 4.35 \times 10^{-3}$, respectively). As expected, TGFβ1 treatment also upregulated the expression of the fibrogenic marker genes *COL1A1*, *ACTA2* and *TIMP1* ($p = 1.2 \times 10^{-12}$, $p = 1.05 \times 10^{-11}$, and $p = 2.67 \times 10^{-5}$, respectively, Figure 6.12B). Strikingly, knockdown of *FSTL3* resulted in 1.22-fold increased expression of *COL1A1* and 1.65-fold increased expression of *TIMP1*, and a 0.32-fold decreased expression of *ACTA2* in PBS controls ($p = 0.018$, $p = 5.9 \times 10^{-5}$ and $p = 7.3 \times 10^{-8}$, respectively, Figure 6.12B). For *ACTA2* and *TIMP1*, this effect was also present after TGFβ1 treatment (0.35-fold, $p = 1.6 \times 10^{-7}$ and 1.72-fold, $p = 5.7 \times 10^{-5}$, respectively) while *FSTL3* knockdown did not modulate *COL1A1* expression in response to TGFβ1 ($p = 0.328$, Figure 6.12B).

TGFβ1 treatment did not affect the expression of the proliferation marker gene *MKI67* ($p = 0.694$), whereas *FSTL3* knockdown significantly increased *MKI67* expression in both PBS and TGFβ1 treated cells ($p = 0.01$ and $p = 0.024$, respectively, Figure 6.12C).

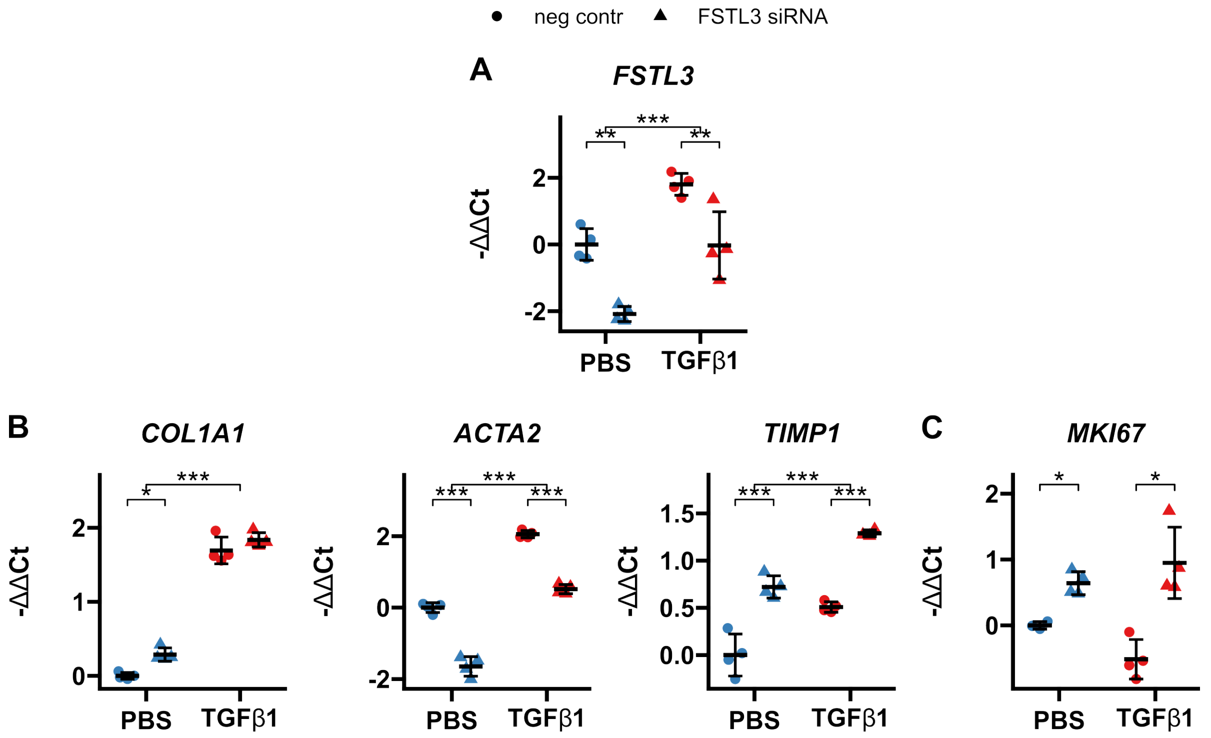

Figure 6.12: Gene expression changes in LX-2 cells in response to TGFβ1 treatment and *FSTL3* siRNA knockdown. Cells were transfected with 5 nM negative control (circles) or *FSTL3* (triangles) siRNA and incubated for 24 h before being treated with 50 U/mL TGFβ1 or PBS control. Cells were harvested 24 h after TGFβ1 treatment. Data are given as individual data points (each representing an independent experiment measured in duplicate) and mean±SD for -ΔΔ Ct relative to PBS+negative control siRNA and normalised to the expression of *SRSF4*.

Abbreviations: ACTA2 - alpha smooth muscle actin, COL1A1 - collagen type I alpha 1, FSTL3 - follistatin-like 3, MKI67 - antigen Kiel 67, PBS - phosphate-buffered saline, TGFβ1 - transforming growth factor beta 1, TIMP1 - tissue inhibitor of metalloproteinases 1.

$p < 0.05$, **$p < 0.01$, ***$p < 0.001$ using wo-Way ANOVA with post-hoc Tukey HSD or Dunnett T3 test.

6.2.6 Knockdown of *FSTL3* modulates lipogenic gene expression in HepG2

FSTL3 has previously been implicated in hepatic steatosis [196, 203, 204], and therefore we wanted to investigate whether knockdown of *FSTL3* influences gene expression related to lipid metabolism in the human hepatocyte cell line HepG2.

HepG2 cells were transfected with either 5 nM negative control or *FSTL3* siRNA 5, and after 24 hours were treated with 100 ng/mL Activin A or PBS control for another 24 hours. As shown before (see Figure 6.10), Activin A led to a strong and significant increase in *FSTL3* expression ($p = 1.25 \times 10^{-13}$) and *FSTL3* knockdown effectively reduced *FSTL3* expression both in PBS control and Activin A treated cells ($p = 6.59 \times 10^{-10}$ and $p = 7.2 \times 10^{-9}$, respectively, Figure 6.13A).

While Activin A treatment led to a non-significant reduction in *PPARA* expression ($p = 0.0621$) and a significantly increased expression of *PPARG* ($p = 9 \times 10^{-9}$), *FSTL3* knockdown did not significantly affect the expression of these genes in the absence or presence of Activin A ($p > 0.05$, Figure 6.13B). Similarly for the *de novo* lipogenic gene *FASN*, Activin A significantly increased its expression ($p = 0.014$) while *FSTL3* knockdown only led to a slight and non-significant increase in PBS control treated cells ($p = 0.173$, Figure 6.13C), the latter not being observed for Activin A-treated cells. We next looked at genes involved in fatty acid uptake (*CD36*), mitochondrial translocation (*CPT1A*) and β-oxidation (*ACADM* and *ACADL*). All genes were significantly upregulated by Activin A treatment and the expression of *CD36*, *CPT1A* and *ACADM* was further increased by *FSTL3* knockdown in PBS treated cells ($p = 0.021$, $p = 1.49 \times 10^{-3}$ and $p = 0.012$, respectively). Furthermore, *FSTL3* knockdown further increased the expression of *CPT1A* in Activin A treated cells ($p = 1.89\text{x}10^{-3}$), while knockdown did not modulate expression of the other genes with Activin A treatment ($p > 0.05$, Figure 6.13)

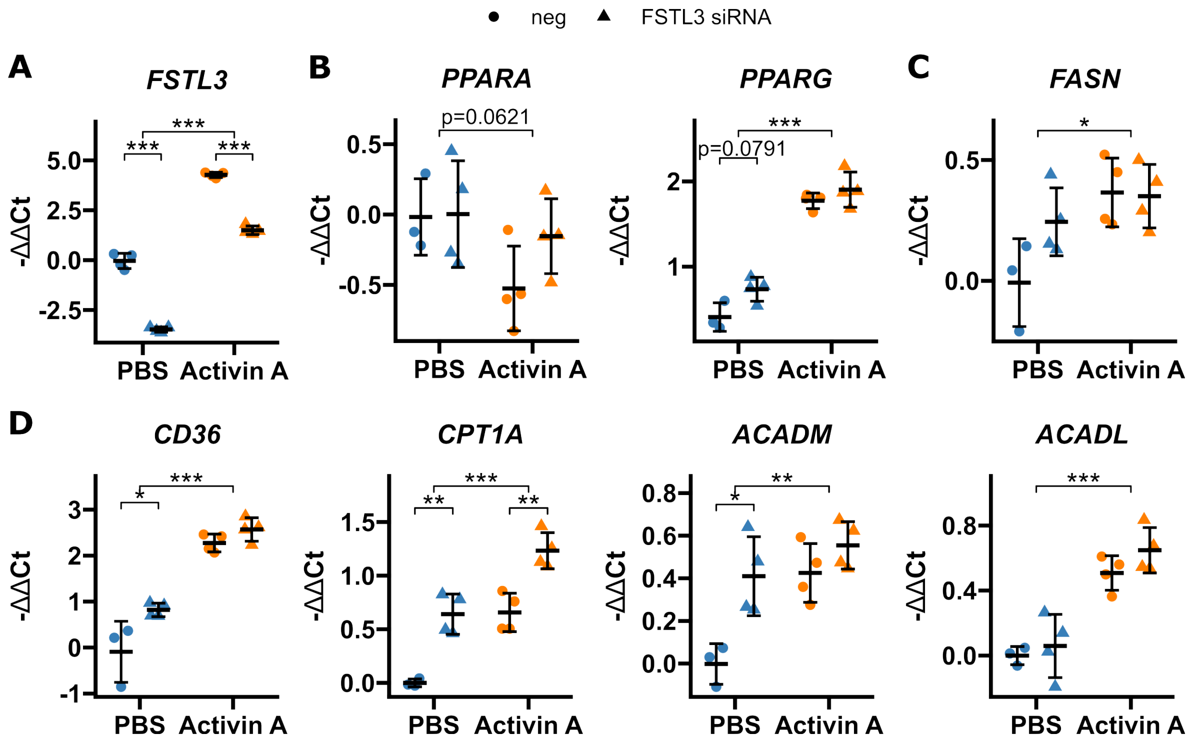

Figure 6.13: Gene expression changes in HepG2 cells in response to Activin A treatment and *FSTL3* siRNA knockdown. Cells were transfected with 5 nM negative control or *FSTL3* siRNA and incubated for 24 h before being treated with 100 nM Activin A or PBS control. Cells were harvested 24 h after Activin A treatment. **A.** *FSTL3* expression. **B.** *PPARA* and *PPARG* expression, representing important nuclear receptors regulating hepatocellular lipid metabolism. **C.** Gene expression of the *de novo* lipogenic enzyme *FASN*. **D.** Key lipid catabolic genes involved in fatty acid uptake (*CD36*), mitochondrial translocation (*CPT1A*) and β-oxidation (*ACADM* and *ACADL*).
Data are given as individual data points (each representing an independent experiment measured in duplicate) and mean±SD for -ΔΔ Ct relative to PBS+negative control siRNA and normalised to the expression of *SRSF4*.
Abbreviations: ACADM/L - acyl-CoA dehydogenase medium/long chain, CPT1 - carnithine palmitoyl transferase 1, FASN - fatty acid synthase, FSTL3 - follistatin-like 3, PBS - phosphate-buffered saline, PPARA/G - peroxisome proliferator-activated receptor alpha/gamma.
$p < 0.05$, **$p < 0.01$, ***$p < 0.001$ using Two-Way ANOVA with post-hoc Tukey-HSD test.

Activin A has previously been implicated in the differential regulation of proliferation and apoptosis in different cell types, including hepatocytes. Therefore, we assessed gene expression changes of the proliferation marker *MKI67*, and the two apoptosis markers *BAX* and *BCL-2* in HepG2 cells in response to knockdown and Activin A treatment. Activin A effectively downregulated *MKI67* and upregulated *BCL-2* mRNA expression while expression of *BAX* was unaffected ($p = 1.09\text{x}10^{-6}$, $p = 2.77\text{x}10^{-4}$ and $p = 0.995$, respectively, Figure 6.14). Knockdown of *FSTL3* led to a further numerical but non-significant decrease of *MKI67* and increase of *BCL2* in Activin-treated cells only, while *BAX* expression again remained unaffected ($p = 0.063$, $p = 0.40$ and $p = 0.885$, respectively, Figure 6.14).

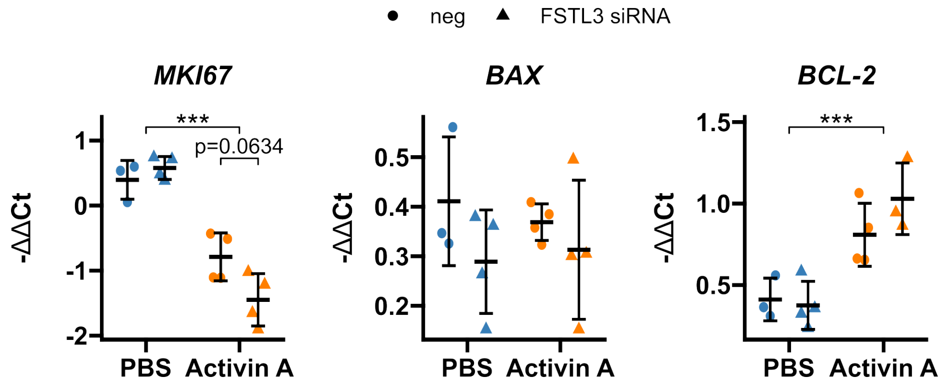

Figure 6.14: Gene expression changes related to cell proliferation (*MKI67*) and apoptosis (*BAX* and *BCL-2*) in response to Activin A treatment and *FSTL3* siRNA knockdown in HepG2 cells. Cells were transfected with 5 nM negative control or *FSTL3* siRNA and incubated for 24 h before being treated with 100 nM Activin A or PBS control for 24 h. Cells were harvested 24 h after Activin A treatment.

Data are given as individual data points (each representing an independent experiment measured in duplicate) and mean±SD for -ΔΔCt relative to PBS+negative control siRNA and normalised to the expression of *SRSF4*.

Abbreviations: BAX - bcl-2-like protein 4, BCL-2 - BCL2 apoptosis regulator, FSTL3 - follistatin-like 3, PBS - phosphate-buffered saline.

$p < 0.05$, **$p < 0.01$, ***$p < 0.001$ using Two-Way ANOVA with post-hoc Tukey-HSD test.

6.2.7 Hepatocellular lipid uptake in response to *FSTL3* knockdown

Having observed significant regulation of lipogenic gene expression in HepG2 with Activin A treatment and *FSTL3* knockdown, we wanted to check how these changes affected cellular lipid uptake. For this purpose, we performed *FSTL3* knockdown and Activin A treatment as before, followed by treatment with a palmitic acid (PA)/oleic acid (OA) 1:2 mixture. In order to visualise lipid uptake over time, LipidTox DeepRed stain was added, and phase gradient and fluorescence images were recorded over time on a Zeiss Celldiscoverer 7 high-content imaging platform.

As can be seen in Figure 6.15, DeepRed fluorescence positive areas corresponded well to visible intracellular droplets on phase gradient images. We also calculated and quantified the Gaussian curvature of the phase gradient images as described in the methods (Appendix A.6), in order to identify ellipsoid 'lipid-containing' structures as an alternative method to fluorescence quantification. There was a good correlation between the Gaussian curvature representation of lipid and the signal detected from LipidTox DeepRed fluorescence.

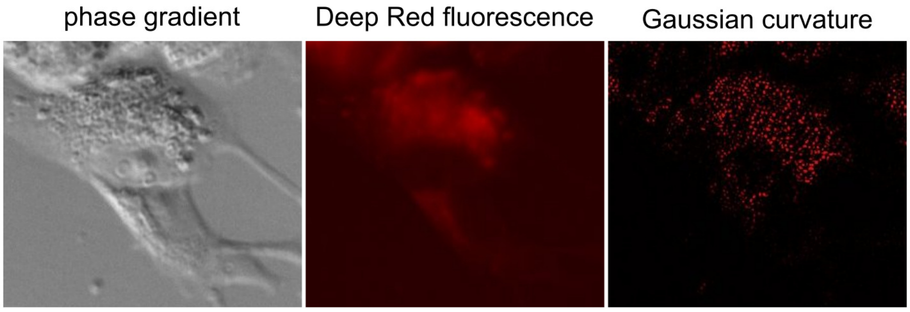

Figure 6.15: Validation of microscopy lipid uptake assays. The figure shows representative images for phase gradient, Deep Red fluorescence (lipid) and Gaussian curvature calculated from the phase gradient information.

Figure 6.16 shows results for quantification of lipid uptake using the mean fluorescence of the LipidTox DeepRed dye over a 24h period. In PBS-treated cells transfected with negative control siRNA, mean fluorescence intensity increased initially and then plateaued from around the 10 hours time-point (Figure 6.16A). In *FSTL3* knockdown cells, however, we observed only a slight initial increase, followed by a fall in fluorescence intensity (Figure 6.16B). Activin A-treated cells displayed a different behaviour with higher initial fluorescence intensity that rapidly declined over time. This effect occurred earlier in *FSTL3* knockdown cells (Figure 6.16D) compared to negative control siRNA-transfected cells (Figure 6.16C). To compare different treatment conditions, we calculated the area under the curve (AUC) of the fluorescence intensity over time. Fluorescence intensity was higher in PBS- compared to Activin-A treated cells ($p = 7x10^{-4}$) and lower in *FSTL3* siRNA compared to negative control siRNA transfected cells ($p = 7x10^{-4}$, Figure 6.16F). When considering interaction effects, however, *FSTL3* siRNA only had a significant effect in PBS-treated and not in Activin A-treated cells ($p = 5.2x10^{-10}$ and $p = 0.57$, respectively, Figure 6.16F).

A different response was observed using Gaussian curvature for the identification of ellipsoid structures corresponding to intracellular lipid droplets (Figure 6.17). In contrast to the fluorescence signal, we observed a steady increase of Gaussian-positive area over the time course of the experiment. The percentage of Gaussian positive area was numerically higher in Activin A- compared to PBS-treated cells and in negative control compared to *FSTL3* siRNA-transfected cells (Figure 6.17E) but these differences were not significant ($p = 0.32$ and $p = 0.13$, respectively, for AUC, Figure 6.17F), possibly owing to the higher spread of data points.

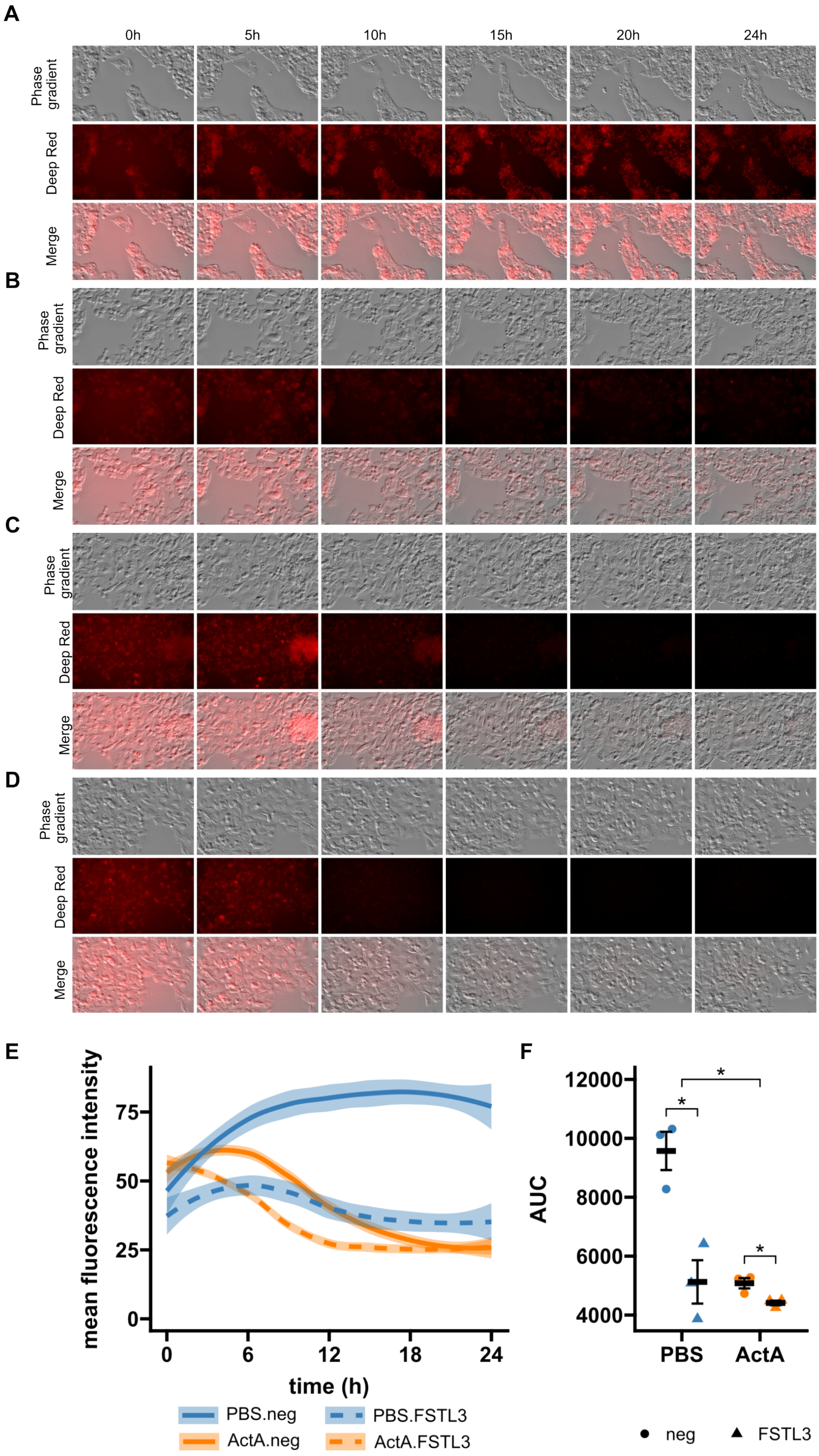

Figure 6.16: *caption see next page*

Figure 6.16 *(previous page)*: Results of lipid uptake assays using DeepRed fluorescence. Panels A-D give representative phase gradient, DeepRed fluorescence and merged images over time for different treatment conditions. **A.** PBS + negative control siRNA, **B.** PBS + *FSTL3* siRNA, **C.** Activin A + negative control siRNA and **D.** Activin A + *FSTL3* siRNA. **E.** Quantification of imaging. Shown is the mean fluorescence of the cell-containing area over time. Data are given as mean±SEM. **F.** Area under the curve (AUC) calculated from results shown in E. Data are given as single data points (each representing an independent experiment performed in technical duplicate) and mean±SEM.
Abbreviations: ActA - activin A, FSTL3 - follistatin-like 3, PBS - phosphate-buffered saline.
*$p < 0.05$ using repeated measures Two-Way ANOVA and post-hoc two-sided Tukey test with Bonferroni-Holm correction for pre-selected comparisons.

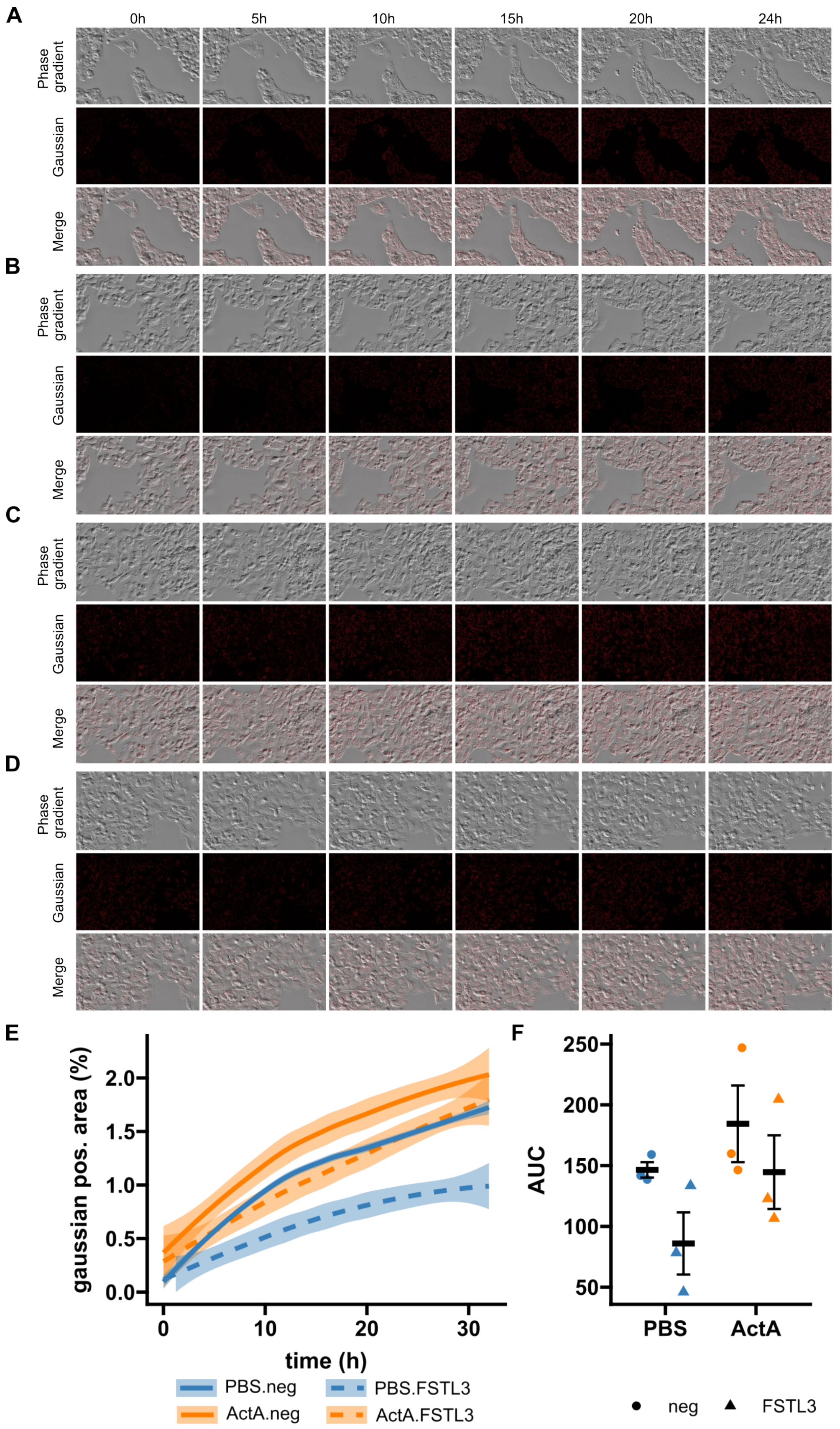

Figure 6.17: *caption see next page*

Figure 6.17 ***(previous page)*****: Results of lipid uptake assays using the Gaussian curvature.** Panels A-D give representative phase gradient, filtered positive values of the Gaussian curvature and merged images over time for different treatment conditions. **A.** PBS + negative control siRNA, **B.** PBS + *FSTL3* siRNA, **C.** Activin A + negative control siRNA and **D.** Activin A + *FSTL3* siRNA. **E.** Quantification of imaging. Shown is the positive area based on Gaussian curvature in percent of the cell-containing area over time. Data are given as mean±SEM. **F.** Area under the curve (AUC) calculated from results shown in E. Data are given as single data points (each representing an independent experiment performed in technical duplicate) and mean±SEM.
Abbreviations: ActA - activin A, FSTL3 - follistatin-like 3, PBS - phosphate-buffered saline.

6.3 Discussion

The lack of pharmacological options for most chronic liver disease aetiologies calls for the need to better our understanding of underlying mechanisms in order to identify potential novel targets. In the previous chapters we showed that Gremlin-1 is not a suitable target for treating liver fibrosis in MASH. Therefore, we employed screening of publicly available bulk RNA sequencing datasets from human liver fibrosis and primary HHSCs to identify therapeutic targets related to the BMP signalling pathway. We identified *FSTL3* as a highly regulated transcript in liver fibrosis which warrants further assessment of its therapeutic potential.

Transcriptional changes with increasing stages of liver fibrosis were related to TGFβ-signalling, collagen production, extracellular matrix organisation and wound healing, which are well characterised components in the progression of chronic liver disease (see Chapter 1), and pathway analyses revealed changes related to cell adhesion and amino acid metabolism. Downregulated pathways corresponded to amino acid metabolism, particularly sulfur amino acids, which have previously been implicated in dampening stellate cell activation and fibrosis [312], and methionine-deficient dietary animal models are often used to induce a MASH phenotype with severe fibrosis [313]. However, only four genes were downregulated across all datasets and therefore downregulated pathways need to be interpreted with caution. Notably, we found very little overlap between datasets, largely driven by the GSE48422 MASH dataset, which showed very little transcriptional regulation with increasing stages of fibrosis. When looking at the characteristics of the datasets, the reason likely lies in the small proportion of patients with advanced stages of fibrosis in this dataset. Relaxing the criteria would have resulted in a higher number of commonly regulated genes, but as we were looking for highly conserved responses in liver fibrosis and HSC activation, we deliberately chose to apply very stringent criteria.

Similarly in HSC RNA sequencing datasets, the overlap between differentially expressed genes across datasets was quite low and most genes were only commonly regulated in one or two datasets. This result was somewhat surprising as the general characteristics of experimental conditions were quite similar, which highlights the heterogeneity of results obtained from *in vitro* experiments performed at different institutions. Furthermore, although primary HSC were mainly sourced from the same vendor, different organ donors for cell isolation probably further impacted on the heterogeneity of results. Still, we found a relatively high number of commonly up- and downregulated genes across datasets. Enriched pathways were in line with what can be expected from the literature. Regulation of cell differentiation, adhesion and extracellular matrix organisation are with no doubt hallmarks of HSC activation [71]. Surprisingly, gene sets relating to cell proliferation and migration were downregulated, which likely reflects the differential effects of different HSC-activators, where TGFβ1 more prominently induces extracellular matrix production and can induce apoptosis whereas platelet-derived growth factor (PDGF) more notably regulates cell proliferation and migration [71], highlighting that HSC activation cannot be fully recapitulated *in vitro*. Also surprising was the downregulation of TGFβ-signalling and MAPK activity, which might be related to negative feedback mechanisms, including receptor internalisation and upregulation of inhibitory Smad proteins triggered by activation of the TGFβ pathway [94]. Most prominently regulated with TGFβ-treatment however, were genes relating to protein folding end endoplasmic reticulum (ER) stress, which is a highly conserved sensor of cellular stress [314], in response unfolded proteins in particular, that is involved in a number of diseases including cancer, type 2 diabetes, the metabolic syndrome and MASH [72, 315]. Increased ER stress is linked to the activation of HSCs [316, 317], and thereby directly plays an active role in liver fibrogenesis [71]. We can therefore conclude that both liver fibrosis and HSC datasets adequately reflect the condition of interest and are suited to identify common signatures in liver fibrosis and HSC activation.

The aim of this chapter was to identify potential novel players in HSC activation and the progression of liver fibrosis. So far, transcriptional regulation in the analysed datasets recapitulated pathways and mechanisms already described in the literature. When looking at the commonly regulated genes in liver fibrosis progression and HSC activation, some were also well known to be regulated in liver fibrosis. COL4A2 and COL5A2 are less well studied collagens that are upregulated in liver fibrosis and correlate with disease progression and hepatocarcinogenesis [318, 319]. Fibulin-2 (FBLN2) is a marker protein of portal fibroblasts [320] while integrin subunit beta-like 1 (ITGBL1) and latent transforming growth factor binding protein 2 (LTBP2) are proteins involved in the maturation and signalling of TGFβ1 and thereby have a role in organ fibrosis [94, 321], and Serpin E1 (SERPINE1, or plasminogen activator inhibitor 1, PAI1) which is a well-known proteinase inhibitor involved in tissue fibrosis [322] and has a potential role in dimethylnitrosamine-induced liver fibrosis and biliary fibrosis [323, 324]. Some other commonly regulated genes have however not been studied in the context of liver fibrosis yet, including (i) *NALCN* which codes for a non-selective sodium leak channel mainly involved in neurotransmission [325] and in one report has been identified as a potential regulator in malignant transformation [326], (ii) Phosphofructokinase 1 isoform P (*PFKP*) which is a rate-limiting glycolytic enzyme that has not been studied in liver fibrosis but has been implicated in hepatocarcinogenesis [327], and (iii) Uncoordinated-5 homolog B receptor (*UNC5B*) which is best known for its function in neuronal guidance [328] but has also been implicated in liver steatosis and inflammation [329, 330].

Another of the few commonly regulated genes with liver fibrosis and HSC activation was *FSTL3*, a known soluble antagonist of TGFβ-family members, including Activin A and myostatin, and is notable for its role in energy metabolism, bone formation, stem cell differentiation and cancer metastasis [192]. In line with our results from bulk liver RNA sequencing, we found increased *FSTL3* mRNA in human liver cirrhotic tissue of different aetiologies when compared to donor livers. A previous report found increased *FSTL3* expression in human MASLD and MASH livers but - possibly due to the low number of studied subjects - no correlation with the stage of fibrosis [202]. Using the LX-2 cell line we could also reproduce our findings of increased *FSTL3* expression in TGFβ1-treated HSCs. Additionally, *FSTL3* was upregulated in response to Activin A. To our knowledge we are the first to describe a regulation of *FSTL3* in HSCs, and data on the expression of *FSTL3* in extrahepatic (myo-)fibroblasts are also not available.

Using siRNA-mediated knockdown we were able to consistently knock down *FSTL3* mRNA in LX-2 cells in order to study the role of FSTL3 on HSC activation. Interestingly, we found a dichotomous response to *FSTL3* knockdown with upregulation of *COL1A1* and *TIMP1* and a profound downregulation of ACTA2, coding for α-smooth muscle actin. This implies that FSTL3 might differentially regulate the matrix-producing and contractile phenotype of HSCs. Interestingly, myostatin - a target of FSTL3-inhibitory activity [331] - promotes matrix production in the mesenchymal stem cell line C3H 10T1/2 without inducing a myofibroblast phenotype [332] and induces fibrotic responses in LX-2 cells [333], which provides a potential mechanisms for differential regulation of the HSC phenotype. However, there are few data available supporting a role of FSTL3 in matrix-producing cells. In cardiac hypertrophy, cardiomyocytes upregulate FSTL3 [199] and cardiomyocyte-derived FSTL3 promotes fibroblast activation *in vitro* [200]. Furthermore, *FSTL3* knockdown significantly increased *MKI67* expression in LX-2 cells, which suggests an inhibitory effect of *FSTL3* on HSC proliferation. By contrast, others have found increased proliferative activity in cardiac fibroblasts stimulated with FSTL3 [200] and more detailed studies, including functional assays, involving primary HSCs are needed to pin down the effects of FSTL3 on HSC proliferation. Another member of the follistatin-like group of proteins, FSTL1, with similar activity against TGFβ-family proteins, has been implicated in liver fibrosis. Similar to *FSTL3* it is upregulated in LX-2 cells in response to TGFβ1 and treatment with a neutralising antibody led to reduced fibrosis in CCl_4-induced murine fibrosis [205]. A more recent report also found that in liver fibrosis FSTL1 is highly expressed in myeloid cells and targeted myeloid knockout reduces necroinflammatory activity and fibrosis in different models of chronic liver injury [206]. Furthermore, FSTL3 in the context of fibrosis is best known for its inhibitory activity on activins [334], including Activin A which is involved in hepatic fibrotic processes in several ways: Activin A elicits similar downstream signalling pathways as TGFβ1, and thereby can activate HSCs and extrahepatic stellate cells directly [207, 208]. Furthermore, HSC-derived Activin A promotes an inflammatory phenotype in hepatic monocyte-derived macrophages, and thereby indirectly promotes HSC activation [209], although recent studies found decreased hepatic *ACTA2* expression upon Activin A overexpression in mice [335]. Interestingly, browsing the online 'Liver disease app' for *FSTL1* and *FSTL3* [336] reveals distinct expression patterns with higher regulation of *FSTL1* in acute liver disease models, whereas *FSTL3* is predominantly regulated in chronic conditions. Taken together, our findings point to a role of FSTL3 in regulating HSC activation and liver fibrosis. Studies on primary cells and *in vivo* models of liver fibrosis, e.g. using conditional lineage-specific knockout of *FSTL3*, e.g. by generating $Fstl3^{fl/fl}$ *LratCre+/-* mice, will be needed to define its exact role and dissect the underlying mechanisms.

Existing evidence from *in vivo* mouse studies using knockout or overexpression of *FSTL3* imply a potential role for hepatocellular steatosis [196, 203, 204]. Therefore, we also studied the effects on hepatocellular lipid accumulation *in vitro*. We found that *FSTL3* was upregulated in HepG2 cells in response to Activin A and - similar to findings in LX-2 cells - we were able to consistently knock down *FSTL3* mRNA by more than 70 percent. As expected, *FSTL3* knockdown regulated the gene expression of key lipogenic proteins. Knockdown non-significantly increased gene expression of the *de novo* lipogenic enzyme *FASN* and significantly increased the expression of *CD36*, *CPT1A* and *ACADM*, key transporters and enzymes of cellular lipid uptake and β-oxidation [337]. Furthermore, it non-significantly increased the expression of *PPARG*, which serves as a key regulator of glucose and lipid metabolism [338], and the lipogenic enzyme *FASN*, a major driver of MASH [339]. Figure 6.18 gives an overview of gene expression changes relating to fatty acid metabolism induced by *FSTL3* knockdown. These findings are in line with existing evidence that knockout of *FSTL3* in mice leads to liver steatosis [196, 203] and upregulation of genes involved in hepatic gluconeogenesis [196] and *de novo* lipogenic enzymes [203]. Conversely, overexpression of *FSTL3* reduces liver fat content [204]. The changes observed with *FSTL3* knockdown generally followed the same pattern as that of Activin A treatment, which also upregulated lipogenic gene expression. This suggests that the effects of *FSTL3* knockdown may be mediated by dis-inhibition of Activin A effects. This idea was further supported by our findings of decreased *MKI67* and increased *BCL-2* expression in response to Activin A treatment, which was non-significantly enhanced by *FSTL3* knockdown and was in line with the known function of Activin A as an inductor of hepatocellular apoptosis [340] and inhibitor of hepatocellular proliferation [341, 342].

In order to validate our qPCR findings regarding hepatocellular lipid metabolism on the functional level, we performed lipid uptake assays on HepG2 treated with a mix of palmitic and oleic acid. We then assessed lipid uptake using live cell imaging of LipidTOX DeepRed staining and by calculating and quantifying the Gaussian curvature as a measure of ellipsoid structures.

The mean fluorescence intensity of the LipidTOX dye showed a quite unexpected behaviour. In PBS-control cells we observed a steady increase that levelled after approximately 8-10 hours of incubation, whereas in Activin A-treated or *FSTL3* siRNA-treated cells, we observed a rapid decline in fluorescence intensity, contrasting the increase of lipid droplets which could be visualised upon light microscopy.

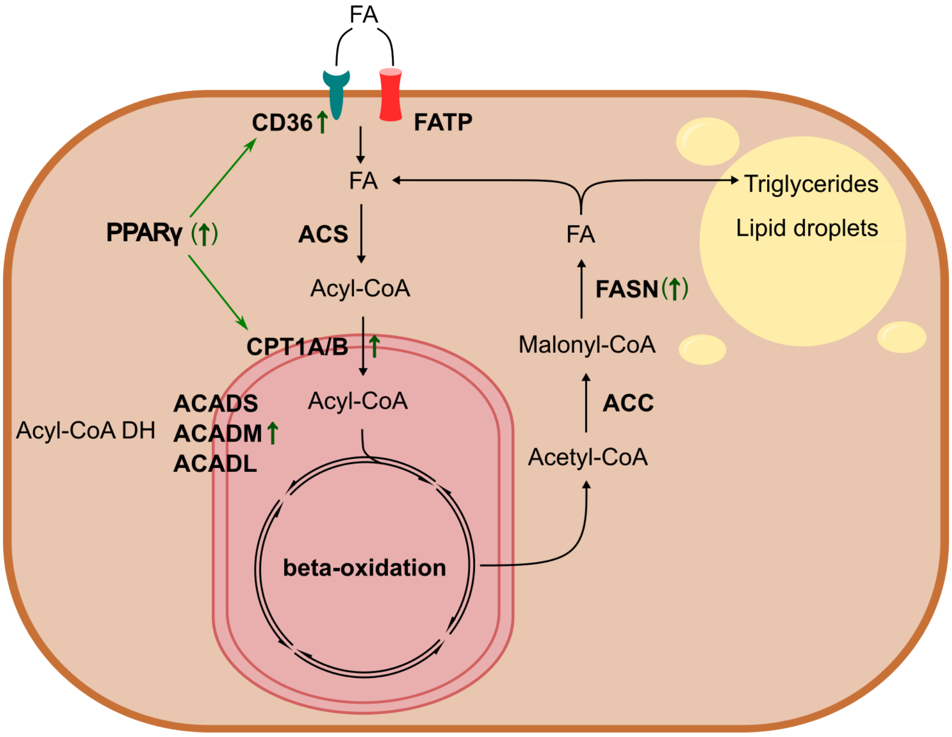

Figure 6.18: Overview of *FSTL3* knockdown effects on lipid metabolism. Very simplified schematic of major proteins and enzymes involved hepatocellular lipid uptake, fatty acid catabolism and *de novo* lipogenesis. Genes positively regulated by *FSTL3* knockdown are indicated by a green arrow. Non-significant regulation is indicated by parenthesis.
ACADS, ACADM, ACADL - Acyl-CoA Dehydrogenase Short/Medium/Long Chain; ACC - Acetyl-CoA Carboxylase; ACS - Acyl-CoA Synthetase; DH - Dehydrogenase; FASN - Fatty Acid Synthase; FA - Fatty Acid; FATP - FA Transport Protein; PPARγ - Peroxisome Proliferator-Activated Receptor γ

Unfortunately, the chemistry of the LipidTox dye is not declared by the vendor and therefore, we can only speculate on reasons for this behaviour. Given the effects of Activin A and *FSTL3* knockdown on the gene expression of genes involved in β-oxidation, it is possible that the LipidTox dye, was metabolised more quickly in Activin A-treated or *FSTL3* siRNA-treated cells. Therefore, although the LipidTox assay probably does not adequately reflect lipid uptake into the cells, it might hint at a functionally increased lipid catabolism upon these treatments which warrants further investigation.

The Gaussian curvature, defined as the product of the principal curvature for each point in space, can be utilised to detect ellipsoid, blob-like structures in images [343]. Our measurements based on Gaussian curvature aligned more clearly with observations of increased lipid droplet abundance over time compared to LipidTox fluorescence. In all treatment groups we observed a steady increase in the Gaussian curvature-positive area and this tended to be higher in Activin-treated cells. Surprisingly, Gaussian curvature area was lower in cells treated with *FSTL3* siRNA, as based on our qPCR results we would have expected a further increase of lipid droplet abundance. However, lipid metabolism is complex and the net accumulation of lipids depends on *de novo* lipogenesis, lipid uptake, excretion and lipid catabolic processes. Therefore, additional methods (e.g. Seahorse assays, Agilent Biotechnology) of assessing cellular lipid metabolism are necessary to define the exact role of FSTL3 in hepatocellular lipid metabolism. On a technical note, we feel that the Gaussian curvature measurements developed here are more reflective of the abundance of cellular lipid droplets and can be used to assess dynamic changes in cellular lipid uptake over time, and validation experiments are ongoing at our institute. Overall, our findings still support the notion that FSTL3 is involved in regulating liver fat content and may be involved in the pathogenesis of steatotic liver disease.

In summary, we fulfilled our goal of identifying a potential novel player in liver fibrosis by comparing transcriptional changes in human liver fibrosis and TGFβ-induced HSC activation. We here provide first evidence that the Activin A and myostatin inhibitor FSTL3 is involved in HSC activation and add evidence for a regulation of hepatocellular lipid metabolism. Future research will need to define its exact role in the context of liver disease and whether it can be leveraged as a therapeutic target.

CHAPTER 7

CONCLUSIONS AND OUTLOOK

7.1 Summary and discussion

Hepatic fibrogenesis as the common consequence of chronic liver injury is a complex process involving all hepatic cell types as well as extrahepatic signals. Through disruption of the sinusoidal microarchitecture and replacement of functionally active liver tissue, liver fibrosis leads to cirrhosis of the liver and predisposes to the development of hepatocellular carcinoma (HCC). Consequently, liver fibrosis is the predominant risk factor for hepatic outcomes in patients with chronic liver disease. Despite an increasing understanding of the mechanisms underlying liver fibrosis, currently no specifically licensed treatment options are available, calling for the need to explore novel pathways for drug development.

Bone morphogenetic proteins (BMPs) are involved in a plethora of cellular processes and have been implicated in hepatic fibrogenesis through their pro-inflammatory effects on hepatic sinusoidal endothelial cells (HSECs) and anti-fibrotic effects on matrix-producing hepatic stellate cells (HSCs). Gremlin-1 as a BMP antagonist has been implicated in hepatic fibrosis, promoting HSC activation and driving hepatocellular senescence. However, to date the therapeutic potential of Gremlin-1 blockade has not been investigated.

Therefore, we hypothesised that Gremlin-1 is upregulated in metabolic dysfunction-associated steatohepatitis (MASH) fibrosis and promotes hepatic fibrogenic pathways in chronic liver disease. Furthermore, we hypothesised that blocking Gremlin-1 ameliorates the inflammatory and fibrotic response in animal and human models of liver fibrosis.

7.1.1 Increased Gremlin-1 expression across liver disease aetiologies and stages of disease

We first aimed to assess the expression of Gremlin-1 across different stages of liver fibrosis and identify the predominant cell type expressing Gremlin-1.

In line with existing evidence from human MASH and rodent models of liver fibrosis [89, 180, 187], we found increased Gremlin-1 mRNA expression in human liver biopsies from patients with MASH fibrosis. Interestingly, we found strikingly increased Gremlin-1 mRNA expression levels in liver tissue from end-stage alcohol-related liver disease (ArLD), primary biliary cholangitis (PBC) and primary sclerosing cholangitis (PSC) patients undergoing liver transplantation, which corroborates findings of increased Gremlin-1 in livers from rodent bile-duct ligation, *Mdr2* knockout and CCl_4 models of liver fibrosis [89, 187]. However, in our hands, when we explored Gremlin-1 expression in rodent models of MASH, we only found consistent expression and upregulation of *GREM1* mRNA in the rat CDAA-HFD model, which prompted us to use this model for subsequent *in vivo* animal studies on Gremlin-1. To what extent Gremlin-1 expression patterns and functions differ between species across different organs is currently unknown and warrants further investigation. Furthermore, the substantial increase in *GREM1* expression in end-stage liver disease compared to the small changes observed in MASH fibrosis by RNA sequencing and *in situ* hybridisation (ISH), points towards a specific regulation of Gremlin-1 in end-stage liver disease. While we did not follow up on this, validation of our RTqPCR findings by other methods, such as ISH or assessing tissue protein levels in end-stage liver disease samples may shed more light on the expression pattern of Gremlin-1 in end-stage and decompensated liver disease.

The literature suggests that in the liver Gremlin-1 is mainly expressed by activated HSCs and portal fibroblasts [89, 189]. Interestingly, using RNAscope ISH co-staining on human liver biopsies, we found co-localisation of *GREM1* mRNA with *THY1* and *COL3A1*, the former being markers of portal fibroblasts not generally considered to be expressed at high levels in HSCs [243, 244]. This was corroborated by analyses of publicly available scRNA-seq datasets, where - despite overall very low expression levels - *GREM1* was highest in smooth muscle cells and portal fibroblasts, and very low in quiescent or activated HSCs, partly contradicting the existing literature. However, given the sparsity of scRNA-seq data in general and low abundance of *GREM1* expression, these findings need to be interpreted with caution. Still, we found high levels in all cultured hepatic fibrogenic cell types and an upregulation with transforming growth factor beta (TGFβ)1 stimulation, which conforms with the concept of increased Gremlin-1 production with fibrogenic cell activation. Therefore, more sensitive methods for quantifying Gremlin-1 expression in freshly isolated pure cell isolates would be necessary to define whether it is expressed in hepatic stellate cells *in vivo* at relevant levels. Furthermore, fibrogenic cells were grown in monolayer culture on plastic dishes, which leads to spontaneous activation of HSCs and LX-2 cells and higher expression levels of fibrogenic transcripts [344]. Thus, growing LX-2 cells and HSCs in 2D cell culture might have altered BMP and Gremlin-1 expression and 3D cultures likely would have yielded different results. Overall, our findings suggest that Gremlin-1 may be a marker of portal fibroblasts, and future studies may address its potential use as a biomarker of disease activity in cholestatic liver diseases and biliary fibrosis.

One of the main findings of this report was that we found no detectable levels of Gremlin-1 protein in the circulation, both in human MASH fibrosis and in our rat CDAA-HFD model. Providing a plausible explanation of why Gremlin-1 may not enter the blood stream in detectable quantities, we found avid binding of Gremlin-1 to heparan sulfate, which also resulted in the formation of higher order complexes, in agreement with the literature [165]. However, we cannot finally disprove that Gremlin-1 is entering systemic circulation, although the increase in Gremlin-1 protein in response to anti-Gremlin-1 treatment makes us confident that our assays were able to pick up even small quantities of Gremlin-1 protein. Furthermore, Gremlin-1 could theoretically be complexed with another yet unidentified protein, preventing detection using current approaches, but we think this is unlikely. Therefore, we feel that the possibility of Gremlin-1 being absent from circulation needs to be considered when interpreting Gremlin-1 biology and studying clinical correlations.

7.1.2 Gremlin-1 as a therapeutic target in liver fibrosis

Next, we sought to characterise the effects of Gremlin-1 and anti-Gremlin-1 treatment on liver fibrosis using human *in vitro* and *ex vivo* and rat *in vivo* models of HSC activation and liver fibrosis.

When using lentiviral vectors for overexpression of Gremlin-1 in LX-2 cells and primary human hepatic stellate cell (HHSC) we found subtle but distinct changes in gene expression mainly relating to BMP-related pathways. This was however not reflected in the corresponding RNA sequencing data, possibly due to the low abundance of target transcripts, for which the 3´-RNA sequencing protocol lacks sensitivity. Overall, we found no convincing effects of anti-Gremlin-1 treatment on liver fibrosis or inflammation *in vivo* or on fibrogenic gene expression *ex vivo* or *in vitro*, despite convincing evidence of target engagement. Possible reasons for the absence of an effect lie in the low abundance of Gremlin-1 in the liver and a possible redundancy of Gremlin-1 signalling, as well as negative feedback loops, which might result from compensatory increased BMP signalling in response to Gremlin-1, as seen following overexpression in LX-2 cells. In addition, we found that *in vivo*, Gremlin-1 was primarily expressed in portal fibroblasts, a cell type that may have a more important role in biliary fibrosis and possibly in the ductular reaction in more advanced and decompensated liver disease [89, 243, 244]. Therefore, it may be worth studying the role of Gremlin-1 and therapeutic neutralisation thereof in conditions other than metabolic dysfunction-associated steatotic liver disease (MASLD) and MASH. Not least, the work on antibody development and validation provided by Novo Nordisk highlights the importance to acknowledge potential heparin-binding properties when developing therapeutic antibodies, as immune complex deposition might occur with heparin-binding antibodies and could result in inflammatory responses.

Furthermore, we aimed to study the role of Gremlin-1 in hepatic sinusoidal endothelial cell activation, leukocyte recruitment and in the differentiation of monocyte-derived macrophages.

In summary, we found no effect of Gremlin-1 on HSEC adhesion molecule expression or leukocyte adhesion in flow-based adhesion assays, both by using either recombinant human protein or lentiviral overexpression of Gremlin-1. This came as a surprise since Gremlin-1 acts directly on vascular endothelial growth factor receptor 2 (VEGFR2) and BMPs which have an established role in endothelial cell function and activation, including leukocyte recruitment [144, 277]. Because these negative results might have been caused by the low complexity of HSEC monolayer cell culture, we used platelet supernatants to deliver Gremlin-1 protein in a more complex and biologically relevant manner which should also provide other co-factors necessary for Gremlin-1 action, including BMPs [280]. Indeed, corroborating existing evidence, we found increased Gremlin-1 protein levels in supernatants from activated platelets [181]. Treatment of HSEC with these supernatants did however not translate into significant changes in leukocyte recruitment in flow-based adhesion assays. Previous research from our group found increased leukocyte recruitment when incubating HSEC with platelets directly instead of using platelet supernatants [78], and therefore it might be worth repeating flow-based adhesion experiments using similar treatment conditions.

Existing literature provided some evidence for increased expression of Gremlin-1 in monocyte-derived macrophages and a role for shaping macrophage phenotypes [181]. In a first step, we therefore analysed existing bulk RNA sequencing datasets for changes in Gremlin-1 expression in response to different stimulations. In agreement with existing evidence that Gremlin-1 is upregulated upon inflammatory stimulation of macrophages [279], we found increased *GREM1* mRNA in macrophages differentiated in the presence of lipopolysaccharide (LPS). We were, however, not able to replicate these findings of increased *GREM1* expression when using PBMC-derived macrophages. Taken together with our findings that anti-Gremlin-1 treatment elicited no inflammation-related responses in our rat CDAA-HFD model or human PCLS, we decided not to follow up on the potential effects of Gremlin-1 on hepatic macrophages.

7.1.3 Follistatin-like 3 as a potential novel driver of liver disease

In light of the mostly negative data on Gremlin-1 we subsequently aimed to identify common transcriptional signatures in activated HSCs and human liver fibrosis in order to identify and validate potential alternative therapeutic targets relating to BMP signalling.

Using this approach, we identified *FSTL3* as a highly upregulated transcript in TGFβ1-mediated HSC activation and human liver fibrosis of different aetiologies. *FSTL3* is mainly involved in regulating glucose and lipid metabolism, skeletal muscle mass and bone formation, while it has also been implicated in haematopoietic stem cell differentiation and placenta development [192]. Aside from one report on fibrogenic properties of FSTL3 in cardiomyopathy [200], FSTL3 has not been linked to fibrosis.

In our studies *FSTL3* was upregulated in LX-2 cells in response to TGFβ1 and Activin A, and using siRNA-mediated knockdown of *FSTL3*, we were able to show a potential involvement of FSTL3 in HSC activation. *FSTL3* knockdown resulted in increased *COL1A1* and *TIMP1* mRNA, while downregulating *ACTA2* mRNA, which suggest an antifibrotic role of FSTL3 while potentially promoting a contractile phenotype. In addition, *FSTL3* knockdown upregulated *MKI67* mRNA in LX-2 cells and thus FSTL3 might be involved in reducing HSC proliferative activity, which is in contrast to its pro-proliferative effects described for cardiac fibroblasts [200] and cancer cells [345, 346].

There is strong evidence for a role of FSTL3 in liver steatosis. *FSTL3* knockdown in mice leads to liver steatosis and upregulation of gluconeogenesis and *de novo* lipogenesis [196, 203] while overexpression results in reduced liver fat content and lipogenic gene expression [204]. When we performed siRNA mediated knockdown of *FSTL3* on the hepatoma cell line HepG2, we observed increased lipogenic gene expression and an upregulation of genes involved in fatty acid uptake and medium chain fatty acid oxidation, which suggests that FSTL3 exerts its anti-steatotic actions by directly acting on hepatocytes. These data strongly suggest that enhanced hepatic FSTL3 levels could reduce steatosis and inhibit fibrosis progression. More work is needed to understand the pathways that control the expression of FSTL3 and how this may be translated to improved clinical outcomes.

7.2 Limitations and outlook

In this project, we focused on the effects of hepatic Gremlin-1 on liver fibrosis. We found very low hepatic Gremlin-1 expression in rat and human MASH fibrosis that was also restricted to *THY1/COL3A1*$^+$ portal fibroblasts, which raises the question of disease relevance. However, our investigations were limited to studying mRNA levels, and even low expression could result in high protein abundance over time. Unfortunately, available Gremlin-1 antibodies for immunohistochemistry were found to be unreliable (personal communication Novo Nordisk), which limits investigations into the spatial distribution and abundance of hepatic Gremlin-1 protein. In human MASH, dysfunctional and hypertrophic adipose tissue plays a central role in disease pathogenesis [260], which is not adequately reflected in our rat choline-deficient, L-amino acid defined, 1% cholesterol, high-fat diet (CDAA-HFD) model of MASH fibrosis or in precision-cut liver slices (PCLS). Gremlin-1 is increased in adipose tissue of subjects with type 2 diabetes and involved in driving adipose tissue dysfunction [238] and therefore, targeting of adipose tissue Gremlin-1 represents an alternative therapeutic strategy and might be studied by applying neutralising antibodies in diet-induced obesity models capturing the metabolic component of disease, such as Western Diet or the High-Fat, High-Fructose Diet [347].

We found increased Gremlin-1 expression across different aetiologies of chronic liver disease, including cholestatic liver diseases PBC and PSC. In biliary fibrosis, portal fibroblasts play a more prominent role than in chronic hepatocellular injury such as seen in ArLD or MASH [89, 243, 244]. Evidence suggests a higher expression of Gremlin-1 in portal fibroblasts compared to activated HSCs [89], which is supported by our findings of a predominant expression in *THY1* and *COL3A1* positive periportal cells. Therefore, future studies should investigate whether Gremlin-1 can be utilised as a therapeutic target in biliary fibrosis.

Notably, we found consistently reduced cell contraction in LX-2 cells overexpressing Gremlin-1, an observation contrary to what we would have expected under the hypothesis that Gremlin-1 drives HSC activation. BMPs are capable of regulating cell contractility. This has been shown for cardiomyoctes, where BMP2 stimulates contractility through activation of phospho inositide-3 kinase activation [348] and BMP4 promotes cardiomyocyte differentiation and contractility through inhibition of fibroblast growth factor (FGF) signalling in embryogenic development [349]. However, BMP7 promotes cell migration through modulation of myosin light chain activity and actin reorganisation [350], which could also impact on cell contractility, and another study demonstrated that Gremlin-1 promotes fibrogenic activation and cell contractility in cancer-associated fibroblasts [351]. Our results from RNA sequencing did not reveal any regulation in pathways relating to cell contractility and unfortunately limitations in cell numbers did not allow for replication of our results in primary HHSC. Still, we feel that the inhibitory effects of Gremlin-1 overexpression on LX-2 contraction warrant further investigation, e.g. by using calcium imaging and characterising subsequent cytoskeletal changes.

Our findings of absent Gremlin-1 protein from circulation and its high-affinity heparin-binding properties have important implications for interpreting the biology and clinical importance of Gremlin-1, as discussed above. However, proving absence of a protein from the circulation is inherently challenging and despite the extensive additional testing performed by Novo Nordisk, including mass spectrometry on plasma samples undergoing Gremlin-1 pull-down, we cannot finally rule out the presence of Gremlin-1 protein in circulation. In addition, others found Gremlin-1 in exosomes released from hepatic cancer-associated fibroblasts [352], and such alternative mechanisms of protein transport might still enable organ crosstalk through Gremlin-1.

An increasing body of evidence supports a role for Gremlin-1 in carcinogenesis [240]. One study reported increased Gremlin-1 expression in hepatocellular carcinoma [353] and a more recent report suggested that Gremlin-1 produced by cancer-associated fibroblasts in HCC might promote hepatocarcinogenesis [352]. Further research is needed to define the role of Gremlin-1 in HCC and evaluate Gremlin-1 as a therapeutic target in cancer.

Although our findings of increased *FSTL3* with increasing stages of liver fibrosis and in HHSC activation are highly suggestive for an involvement in hepatic fibrogenesis, our investigations into FSTL3 were solely based on cell culture models using immortalised cell lines. While cell lines are a suitable screening tool and can be used to test specific cellular responses, their translatability into the clinical setting is clearly limited. Therefore, our findings need to be replicated in primary animal and human *in vitro* models and eventually, the role of FSTL3 will need to be defined *in vivo*. Conditional *FSTL3* knockout mice could be generated using the available floxed *Fstl3*$^{f/f}$ mouse strain [354], which could be crossed with *Lrat-Cre* mice to generate HSC-specific knockout animals [82]. In addition, Activin A has been described to promote inflammatory phenotypes in hepatic macrophages [209] and FSTL3 could therefore have a role in liver inflammation by shaping macrophage function, which has not been explored in this thesis. Finally, when thinking about targeting FSTL3, its diverse functions need to be taken into account. Of relevance for chronic liver disease in particular are its role in regulating muscle mass [354] and its role in carcinogenesis [192], with sarcopenia and hepatocarcinogenesis often complicating the clinical course of chronic liver disease [355]. When developing therapeutic compounds targeting FSTL3 in chronic liver disease, it therefore needs to be ensured that they do not augment sarcopenic or cancerogenic pathways.

7.3 Conclusions

In conclusion, this work demonstrates that, although Gremlin-1 is regulated in liver fibrosis of different aetiologies including MASH, it likely does not represent a suitable or priority therapeutic target. The potential reasons include low hepatic expression, primary expression in portal fibroblasts that may not be of immediate relevance to MASH disease progression, avid heparin binding resulting in the absence from circulation and a potential high redundancy in the TGFβ/BMP signalling pathway, compensating for removal of Gremlin-1 protein from the system. At the same time, our findings may prompt investigations into Gremlin-1 as a (bio-)marker for portal fibroblasts and its role biliary fibrosis and end-stage liver disease.

FSTL3 on the other hand is highly regulated in liver fibrosis and manipulating FSTL3 activity *in vitro* showed effects on hepatocellular lipid metabolism in HepG2 cells and on the fibrogenic response in the HSCs model cell line LX-2 and therefore warrants further investigation as a therapeutic target.

APPENDIX

A.1 Methods

Table A.1: Taqman™ assays

Target	Assay ID
ACADL	Hs00155630_m1
ACADM	Hs00936584_m1
ACTA2	Hs01879841_s1
ACTB	Hs01060665_g1
AFTPH	Hs00214281_m1
BAX	Hs00180269_m1
BCL-2	Hs00608023_m1
BMP2	Hs00154192_m1
BMP4	Hs00370078_m1
BMP7	Hs00233476_m1
BMPR1A	Hs04980288_g1
BMPR1B	Hs01010965_m1
BMPR2	Hs00176148_m1
CCL2	Hs00234140_m1
CD36	Hs00354519_m1
COL1A1	Hs00164004_m1
CPT1A	Hs00912671_m1
CTCF	Hs00902016_m1
ERCC3	Hs01554457_m1
FASN	Hs01005622_m1
FSTL3	Hs00610505_m1
GAPDH	Hs02786624_g1

Table A.1 Continued

Target	Assay ID
GREM1	Hs01879841_s1
GUSB	Hs00939627_m1
HPRT1	Hs02800695_m1
ICAM1	Hs00164932_m1
ID1	Hs00357821_g1
ID2	Hs00747379_m1
INHBA	Hs01081598_m1
INHBB	Hs00173582_m1
LOX	Hs00942483_m1
LOXL1	Hs00935937_m1
MKI67	Hs04260396_g1
PPARA	Hs00947536_m1
PPARG	Hs01115513_m1
SMAD1	Hs00195432_m1
SMAD2	Hs00998187_m1
SMAD3	Hs00969210_m1
SMAD4	Hs00929647_m1
SMAD5	Hs00195437_m1
SMAD6	Hs00178579_m1
SMAD7	Hs00998193_m1
SMAD9	Hs00931723_m1
SRSF4	Hs00194538_m1
TIMP1	Hs01092512_g1
VCAM1	Hs01003372_m1

Table A.2: Custom primers for SYBR® Green PCR

Target	**Primer**	**Sequence**
GAPDH	GAPDH_116bp_fw	5’ - CTC TGC TCC TCC TGT TCG AC - 3’
	GAPDH_116bp_rv	5’ - CAA TAC GAC CAA ATC CGT TGA C - 3’
GFP	GFP_109bp_fw	5’ - GCT ACC CCG ACC ACA TGA AG - 3’
	GFP_109bp_rv	5’ - CGG GTC TTG TAG TTG CCG T - 3’
GREM1	GREM1_109bp_fw	5’ - GAG CCC TGC TTC TCC TCT TG - 3’
	GREM1_109bp_rv	5’ - TCT GAG TCA TTG TGC TGG GC - 3’

A.2 RNA sequencing GREM1 overexpression

A.2.1 Top differentially expressed genes

Table A.3: Significant DEG in GREM1 overexpressing LX-2

log2FoldChange	pvalue	padj	gene
3.22	2.2E-33	2.53E-29	*DPY19L1*
8.66	5.13E-23	2.95E-19	*NAPA*
-12.12	2.03E-16	7.79E-13	*MRPL22*
2.09	2.85E-14	8.2E-11	*UAP1*
3.46	1.61E-13	3.69E-10	*TBX2*
-2.31	4.16E-13	7.98E-10	*YWHAB*
-10.74	2.01E-12	3.31E-09	*EBNA1BP2*
-10.33	1.45E-11	2.08E-08	*TEDC2*
10.18	3.55E-11	4.5E-08	*FZD3*
10.27	3.91E-11	4.5E-08	*SMARCC1*
6.54	9.24E-11	9.67E-08	*NUDT16*
7.30	2.1E-08	2.01E-05	*TCEAL4*
-3.25	5.19E-08	4.6E-05	*LRRC23*
3.28	6.34E-08	5.21E-05	*ENSG00000237352*
8.99	7.2E-08	5.52E-05	*PRORP*
-3.36	1.24E-07	8.93E-05	*SPATA13*
-6.05	2.35E-07	0.000159	*ADNP*
8.90	3.49E-07	0.000208	*POLR2J2*
-3.48	3.62E-07	0.000208	*FAM86EP*
2.59	3.58E-07	0.000208	*ZNF432*
-6.96	1.07E-06	0.000587	*L3MBTL2*
-8.33	2.36E-06	0.001235	*MTERF2*
22.45	2.7E-06	0.001352	*CLASP1*
-8.29	3.14E-06	0.001506	*MKLN1*
8.36	3.54E-06	0.001632	*ENSG00000218890*
2.13	4.93E-06	0.00218	*DAP*
8.01	1.15E-05	0.004919	*LOC102724159*
3.61	1.31E-05	0.005208	*PGA4*
-6.45	1.29E-05	0.005208	*ENSG00000278966*
1.39	1.37E-05	0.005248	*PRELID1*

Table A.3 Continued

log2FoldChange	**pvalue**	**padj**	**gene**
2.86	1.6E-05	0.005933	*RPS16*
1.65	3.83E-05	0.013783	*MEGF8*
3.71	5.67E-05	0.019199	*GDNF*
1.59	5.66E-05	0.019199	*ANKRD13D*
3.86	7.24E-05	0.023805	*EIF2S3*
7.65	7.78E-05	0.024872	*CRY1*
7.61	9.08E-05	0.028231	*CC2D2A*
-7.85	0.0001	0.030311	*VPS36*
4.86	0.000111	0.032845	*UBA2*
2.95	0.000121	0.034184	*KDM4B*
7.58	0.000122	0.034184	*NUDT8*
-7.59	0.000125	0.034232	*ABAT*
-7.53	0.00013	0.034701	*POGLUT2*
5.31	0.000142	0.037141	*TMEM183A*
2.28	0.000146	0.037417	*C19orf54*
2.21	0.000164	0.041048	*ARMCX4*
-6.88	0.000183	0.044761	*LCA5*
-7.86	0.000204	0.048928	*RPL22*

Table A.4: Significant DEGs in GREM1 overexpressing HHSC

log2FoldChange	**pvalue**	**padj**	**gene**
10.69	1.07E-46	1E-42	*CALM2*
3.71	1.06E-12	4.97E-09	*GREM1*
-4.82	5.62E-12	1.76E-08	*PDXDC2P*
10.11	1.03E-09	2.41E-06	*RAB18*
3.03	5.67E-09	1.07E-05	*ZNRD2*
-9.72	1.19E-08	1.86E-05	*RAB4A*
-9.40	1.46E-07	0.000196	*YWHAH*
24.55	2.87E-07	0.000338	*SOD1*
-9.13	3.59E-07	0.000375	*POP1*
5.59	4.59E-07	0.000393	*PRKD3*
3.62	4.51E-07	0.000393	*U2AF1*
23.85	6.2E-07	0.000486	*LRPAP1*

Table A.4 Continued

log2FoldChange	pvalue	padj	gene
-8.71	1.03E-06	0.000693	*NDUFS1*
-23.42	9.9E-07	0.000693	*MFSD1*
23.19	1.26E-06	0.000792	*ATXN10*
-8.29	4.81E-06	0.002827	*POLA1*
8.14	6.12E-06	0.003384	*USP30*
-2.83	9.04E-06	0.004722	*MEGF8*
2.90	1.4E-05	0.00694	*PDXDC1*
-4.61	1.63E-05	0.007654	*ABCF1*
-6.40	1.92E-05	0.00859	*PTCH1*
4.81	2.11E-05	0.009016	*NAF1*
5.39	2.6E-05	0.010624	*RPS16*
5.47	5.68E-05	0.022262	*ATP5F1E*
-3.48	7.43E-05	0.027957	*NCAPD3*
7.47	0.000124	0.044809	*GATAD2B*
6.03	0.000139	0.048399	*PRDM5*

A.3 Anti-Gremlin-1 treatment in rat CDAA-HFD

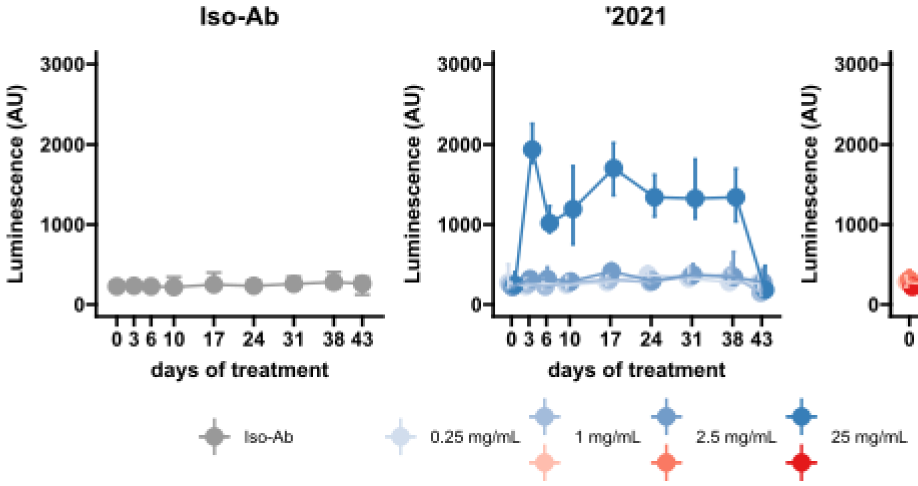

Figure A.1: Target engagement studies in the rat CDA-HFD model. Peripheral bloods samples were taken before first antibody injection and at different timepoints during treatment, as indicated on the x-axes. Plots show signal intensity for Gremlin-1 protein in plasma by alphaLISA. All data are given as median and IQR.

Table A.5: CDAA-HFD study: Results for all antibody concentrations

	chow	Iso-Ab	2021:HD				0361:ND		
			25 mg/kg	2.5 mg/kg	1 mg/kg	0.25 mg/kg	25 mg/kg	2.5 mg/kg	1 mg/kg
body weight (g)	639±20	459±45	443±36	438±36	442±28	447±42	473±33	453±41	446±47
ALT (U/mL)	72±12	197±88	170±69	247±209	155±47	194±66	149±28	170±34	191±71
AST (U/mL)	283±195	572±108	534±141	551±101	522±82	607±103	558±89	518±157	587±114
relative liver weight (%)	2.77±0.11	5.7±0.79	5.72±0.97	5.79±1.12	6.03±0.86	5.45±0.82	5.24±0.84	5.58±1.01	5.48±0.82
steatosis (% area)	0.85±0.23	19.7±2.53	17.77±3.41	18.46±3.36	18.36±3.46	16.76±3.01	17.78±2.35	19.25±2.66	18.12±3.54
PSR (% area)	1.12±0.31	5.26±1.61	7.11±2.54	5.58±2.82	6±2.83	5.78±2.62	4.71±1.03	5.54±2.36	6±2.59
CD45 (% area)	1.26±0.67	4.89±2.07	4.7±1.01	4.03±1.14	5.87±2.68	7.18±2.8	4.17±1.35	5.81±3.76	4.74±2.07
Collagen 1 (% area)	2.59±1.47	10.9±2.6	13.62±3.14	13.15±6.51	13.37±4.44	14.35±6.42	10.49±2.68	11.32±4.14	12.62±4.46
aSMA (% area)	0.83±0.16	13.15±3.16	13.75±2.41	11.82±2.42	14±2.67	13.56±3.14	12.25±2.68	12.84±2.05	13.43±2.88
CD68 (% area)	3.79±0.5	14.45±2.37	15.16±2.11	14.81±3.35	14.69±2.72	15.73±3.27	13.34±2.4	14.14±2.91	14.49±2.51
CD11b (% area)	0.07±0.04	0.68±0.53	0.84±0.71	0.54±0.42	0.91±0.57	0.96±0.89	0.67±0.5	0.9±0.89	0.75±0.59

Table A.6: CDAA-HFD study: qPCR results for all antibody concentrations

	chow	Iso-Ab	2021:HD				0361:ND		
			25 mg/kg	2.5 mg/kg	1 mg/kg	0.25 mg/kg	25 mg/kg	2.5 mg/kg	1 mg/kg
Col1a1	0.00±1.13	6.97±0.78	6.95±0.71	6.82±0.63	7.12±0.95	7.39±0.57	7.09±0.69	7.03±0.73	6.97±0.78
Col3a1	0.00±0.72	3.63±0.68	3.40±0.48	3.58±0.54	3.81±0.58	3.97±0.39	3.77±0.37	3.75±0.52	3.79±0.80
Grem1	0.00±0.51	3.33±0.55	3.37±0.37	3.28±0.36	3.66±0.64	3.75±0.46	3.49±0.39	3.47±0.35	3.42±0.35
Mki67	0.00±0.52	4.53±0.54	4.59±0.46	4.54±0.69	4.83±0.71	4.59±0.57	4.79±0.54	4.55±0.60	4.27±0.61
Tgfb1	0.00±1.14	4.12±1.32	4.44±0.62	4.24±0.83	4.02±2.17	4.57±0.53	4.08±1.11	4.35±0.65	4.50±0.64
Timp1	0.00±0.25	4.35±0.36	4.50±0.36	4.36±0.51	4.50±0.61	4.47±0.29	4.30±0.40	4.26±0.35	4.35±0.40
Tnf	0.00±1.22	2.96±1.13	3.52±1.09	3.10±0.78	3.55±0.99	3.82±1.11	3.54±0.77	3.46±0.95	3.61±0.91

A.4 ImageJ code for scratch wound analysis

```
/*
* Macro template to process multiple images in a folder
*/
//Creates an GUI input for choosing input and output directories, file suffix and
//whether batch-processing mode should be used
#@ File (label = ”Input directory”, style = ”directory”) input
#@ File (label = ”Output directory”, style = ”directory”) output
#@ String(value=”This macro will save processed images and a results file in csv format into the specified output directory.”, visibility=”MESSAGE”) output_info1;
#@ String(value=”When choosing ’Subfolder’ in the following dialog, the folder structure of the input directory will be mirrored in the output.”, visibility=”MESSAGE”) output_info2;
#@ String (label = ”File suffix”, value = ”.jpg”) suffix
#@ Boolean (label = ”Do not show images”, value = ”TRUE”) batch
#@ String(value=”Untick this box when you want to see the processed images”, visibility=”MESSAGE”) batch_hint;

mode = newArray(”Folder”, ”Subfolder”);
{        Dialog.create(”Choose running mode”);
         Dialog.addMessage(”Choose the mode for running scratch-wound analysis”);
         Dialog.addChoice(”Mode”, mode, ”Subfolder”);
         Dialog.addMessage(”’Folder’ scans for images only in the specifically selected folder but not in any subdirectories.”);
```

```
        Dialog.addMessage(”’Subfolder’ scans for images in all subdirectories of the specified folder but not in the folder itself.”);
        Dialog.show();

        mode = Dialog.getChoice();
}

//Pre−set of variables. So far, these parameters have worked reasonably well for pictures taken by the CelliQ (1x1 grid).
var filter_radius = 30; //filter radius for variance filtering
var threshold = 10;     //threshold on variance filtered image
var sat_pix = 0.001; //fraction of saturated pixels in image
var min_area = 10; //minimum area in px^2 that gets detected
var fract_area = 0.3; //area fraction of largest area
var number_areas = 2; //number of areas above fract_area∗max_area that gets measured
var scale = 0.7; //scale in µm/pixel

//Creates a GUI to input/change parameters
{   Dialog.create(”Wound healing size options”);
        Dialog.addNumber(”Variance window radius”, filter_radius);
        Dialog.addSlider(”Threshold value”, 0, 255,  threshold);
        Dialog.addNumber(”Fraction of saturated pixels”, sat_pix);
        Dialog.addCheckbox(”Gaussion blur”, true);
        Dialog.addNumber(”Minimal area size”, min_area);
        Dialog.addNumber(”Fraction of largest area to be detected”, fract_area);
```

```
        Dialog.addNumber(”Max number of areas to be measured”, number_areas
            );
        Dialog.addNumber(”Scale in µm/pixel”, scale);
        Dialog.show();

        filter_radius = Dialog.getNumber();
        threshold = Dialog.getNumber();
        sat_pix = Dialog.getNumber();
        gauss_blur = Dialog.getCheckbox();
        min_area = Dialog.getNumber();
        fract_area = Dialog.getNumber();
        number_areas = Dialog.getNumber();
        scale = Dialog.getNumber();
}

if (gauss_blur == true){
        Dialog.create(”Gaussian blur options”);
        Dialog.addNumber(”Radius [pixels]”, 5);
        Dialog.show();

        gauss_rad = Dialog.getNumber();
}

setBatchMode(batch);

if (mode == ”Subfolder”){
        processSubFolder(input);

```

```
    saveAs("Results", output+"/Results.csv");

    // function to scan input folder to find files with correct suffix.
    //This will not search or process files in subdirectories.
    function processSubFolder(input) {
        list = getFileList(input);
        list = Array.sort(list);
        run("Clear Results");
        for (i = 0; i < list.length; i++) {
            if(File.isDirectory(input + File.separator + list[i]))
            File.makeDirectory(output + File.separator + list[i]);
            folder = list[i];
            list_2 = getFileList(input + File.separator + list[i]);
            list_2 = Array.sort(list_2);
            for (j = 0; j < list_2.length; j++){
                if(endsWith(list_2[j], suffix))
                processFile(input+"/"+folder, output+"/"+folder, list_2[j]);
                updateResults();
            }
        }
    }
}

if (mode == "Folder"){
```

```
    processFolder(input);

    saveAs(”Results”, output+”/Results.csv”);

    // function to scan input folder to find files with correct suffix.
    //This will not search or process files in subdirectories.
    function processFolder(input) {
        list = getFileList(input);
        run(”Clear Results”);
        for (i = 0; i < list.length; i++) {
            if(endsWith(list[i], suffix))
            processFile(input, output, list[i]);
            updateResults();
        }
    }
}

function processFile(input, output, file) {

    open(input+”/”+file);

    {
        run(”Select None”);
        snapshot();
        setupUndo();
        run(”Options...”, ” black”);
        run(”Duplicate...”, ”duplicate”);
        setForegroundColor(0, 0, 0);
```

```
setBackgroundColor(255, 255, 255);
roiManager(”reset”);
roiManager(”Associate”, ”true”);
if (gauss_blur == true){
        run(”Gaussian Blur...”, ”sigma=”+gauss_rad);
}
run(”8-bit”);

if (isOpen(”ROI Manager”))
{
        selectWindow(”ROI Manager”);
        run(”Select None”);
        run(”Close”);
}

run(”Set Scale...”, ”distance=1 known=”+scale+” unit=µm global”);
getPixelSize(unit, pw, ph);

run(”Enhance Contrast...”, ”saturated=”+sat_pix+” normalize”);
run(”Variance...”, ”radius=”+filter_radius+” stack”);
setThreshold(0, threshold);
run(”Convert to Mask”, ”black”);
run(”Fill Holes”);
run(”Select All”);

```

```
        run(”Analyze Particles...”, ”size=”+min_area+”-Infinity
            circularity=0.00-1.00 show=Nothing add stack”);
        run(”Revert”);
        close();

        roiManager(”Show None”);

        if (roiManager(”count”)>=1)
        {
            if (roiManager(”count”)>1)
            {
                area_large = newArray(roiManager(”count”));
                for (i = 0; i<(roiManager(”count”)); i++)
                {
                    roiManager(”select”, i)
                    getStatistics(area_large[i], mean,
                        min, max, std, histogram);
                }

                largest = 0;
                for (i = 0; i<(roiManager(”count”)); i++)
                {
                    if (area_large[i]>largest)
                    {
                        largest = area_large[i];
                        large = i;
                    }
                }
```

```
cut_off = largest*fract_area;

selectAreas = newArray(0);
selectROIs = newArray(0);
for (i = 0; i<(roiManager(”count”)); i++)
if (area_large[i] > cut_off)
{
        selectAreas = Array.concat(
            selectAreas, area_large[i]);
        selectROIs = Array.concat(
            selectROIs, i);
}

//this set of operations sorts the ROIs
    according to size and selects only the
    top n ones
Array.sort(selectAreas, selectROIs);
Array.reverse(selectAreas);
Array.reverse(selectROIs);
selectAreas = Array.trim(selectAreas,
    number_areas);
selectROIs = Array.trim(selectROIs,
    number_areas);

if (selectROIs.length > 1)
{
        roiManager(”select”, selectROIs);
        roiManager(”Combine”);
```

```
                }

                else
                {
                    roiManager(”select”, large);
                }
            }

            else if (roiManager(”count”)==1)
            {
                roiManager(”select”, 0);
            }

            reset();
            setupUndo();
            roiManager(”Set Color”, ”cyan”);

            Roi.getContainedPoints(xpoints, ypoints);

            run(”Set Measurements...”, ”redirect=None decimal=3”);
            getStatistics(area, mean, min, max, std, histogram);
            height_total=getHeight()*pw;
            width_total=getWidth()*pw;
            total_area=(height_total*width_total);
            area_fraction=(area/total_area)*100;
            avg_width = (area/height_total);
```

```

        n1=getValue(”results.count”);
        title_image=getTitle();
        folder = File.getName(input);
        setResult(”Folder”, n1, folder);
        setResult(”File”, n1, title_image);
        setResult(”Area ”+unit+”^2”, n1, area);
        setResult(”Area %”, n1, area_fraction);
        setResult(”Width ”+unit, n1, avg_width);
        setTool(”rectangle”);

        //Add an outline to the image that gets saved in the output directory
        setForegroundColor(255, 255, 255);
        run(”Line Width...”, ”line=5”);
        run(”Draw”, ”slice”);
        run(”Select None”);
        run(”Scale...”, ”x=0.25 y=0.25 width=348 height=260 interpolation=Bilinear average create”);
        save(output+”/”+file);
        close();
    }
    else
    {
        n1=getValue(”results.count”);
        title_image=getTitle();
        folder = File.getName(input);
        setResult(”Folder”, n1, folder);
```

```
            setResult(”File”, n1, title_image);
            setResult(”Area ”+unit+”^2”, n1, 0);
            setResult(”Area %”, n1, 0);
            setResult(”Width ”+unit, n1, 0);
            setTool(”rectangle”);
            run(”Select None”);
            run(”Scale...”, ”x=0.25 y=0.25 width=348 height=260, interpolation=Bilinear average create”);
            save(output+”/”+file);
            close();
        }
    }
}
```

A.5 ImageJ script for fluorescence measurement

```
#@ String (visibility=MESSAGE, value=”Please set the radius for background substraction”) msg1
#@ Integer(label = ”radius”, min=0, max=100, value=10) radius2
#@ String (visibility=MESSAGE, value=”Please set the fluorescence threshold”) msg2
#@ Integer (label = ”threshold”, min=0, max = 65535, value = 100) threshold2
#@ String(value = ”set output directory to save results as comma separated file”, visibility = ”MESSAGE”) output_info
#@ File(label = ”Output directory”, style = ”directory”) output

title = getTitle();
selectImage(title);

slices = nSlices

selectImage(title);
run(”32-bit”);

saveSettings;
setOption(”Stack position”, true);
if (!Stack.isHyperstack) {
    getVoxelSize(width, height, depth, unit);
    for (n=1; n<=nSlices; n++) {
        setSlice(n);
        run(”Measure”);
```

```
	}
	if (unit!=”pixels”) {
		depths = newArray(Table.size);
		for (i=0; i<Table.size; i++)
		depths[i] = i*depth;
		Table.setColumn(unit, depths);
		Table.update;
	}
	restoreSettings;
	exit;
}
run(”Set Scale...”, ”distance=0 known=0 unit=pixel”);
Stack.getDimensions(w, h, channels, slices, frames);
Stack.getPosition(ch, sl, fr);
Dialog.create(”Measure Hyperstack”);
Dialog.addCheckbox(”Channels (”+channels+”)”, true);
Dialog.addCheckbox(”Slices (”+slices+”)”, true);
Dialog.addCheckbox(”Frames (”+frames+”)”, true);
choices = newArray(”czt(default)”, ”ctz”, ”zct”, ”ztc”, ”tcz”, ”tzc”);
Dialog.addChoice(”Order:”, choices, choices[0]);
Dialog.show();
state1 = Dialog.getCheckbox();
state2 = Dialog.getCheckbox();
state3 = Dialog.getCheckbox();
order = Dialog.getChoice();

if(state1) {startCh = 1; endCh = channels;}
else {startCh = ch; endCh = ch;}
```

```
if(state2) {startSl = 1; endSl = slices;}
else {startSl = sl; endSl = sl;}
if(state3) {startFr = 1; endFr = frames;}
else {startFr = fr; endFr = fr;}

run(”Clear Results”);

run(”Set Measurements...”, ”area mean standard modal min integrated median stack display redirect=None decimal=3”);

for (y=startSl; y<=endSl; y++){
        Stack.setSlice(y);
        for (u=startFr; u<=endFr; u++) {
                Stack.setFrame(u);
                Stack.setChannel(2);
                run(”Select All”);
                run(”Variance...”, ”radius=20 slice”);
                setThreshold(90000.6076, 6774397.0000);
                run(”Create Selection”);
                run(”Create Selection”);
                getStatistics(area);
                area_total = (getHeight() * getWidth());
                area_cells = area;
                area_cells_percent = area/area_total*100;

                run(”Set Measurements...”, ”area mean median area_fraction limit display redirect=None decimal=3”);
```

```
                Stack.setChannel(1)
                getStatistics(mean);
                mean_fluorescence = mean;
                run(”Subtract Background...”, ”rolling=10 slice”);
                setThreshold(threshold2, 65535);
                run(”Create Selection”);
                getStatistics(area);
                area_fluorescence = area;
                area_fluorescence_percent = area/area_cells*100;
                n1=getValue(”results.count”);
                setResult(”File”, n1, title);
                setResult(”Slice”, n1, y);
                setResult(”Frame”, n1, u);
                setResult(”total area”, n1, area_total);
                setResult(”cell area”, n1, area_cells);
                setResult(”cell area percent”, n1, area_cells_percent);
                setResult(”mean fluorescence”, n1, mean_fluorescence);
                setResult(”fluorescence area”, n1, area_fluorescence);
                setResult(”fluorescence area percent”, n1,
                    area_fluorescence_percent);
                updateResults();

        }
}

saveAs(”Results”, output+”/Results_fluorescence.csv”);
```

A.6 ImageJ script for gaussian curvature measurement

```
#@ String (visibility=MESSAGE, value=”Please select the gaussian smoothing scale”) msg
#@ Double (label=”smoothing scale”, min=0, max=1000, value=1, stepSize=0.1, style=”format:#.#”) smoothing
#@ Integer (label = ”threshold”, min=-1e30, max = 1e30, value = 100000) threshold
#@ String(value = ”set output directory to save results as comma separated file”, visibility = ”MESSAGE”) output_info
#@ File(label = ”Output directory”, style = ”directory”) output

title = getTitle();
selectImage(title);

slices = nSlices

selectImage(title);
run(”FeatureJ Hessian”, ”largest smallest smoothing=”+smoothing);
imageCalculator(”Multiply create stack”, title + ” largest Hessian eigenvalues”, title + ” smallest Hessian eigenvalues”);

selectWindow(title + ” largest Hessian eigenvalues”);
close();
selectWindow(title + ” smallest Hessian eigenvalues”);
close();

selectWindow(title);
```

```
run(”32−bit”);

run(”Interleave”, ”stack_1=[” + title + ”] stack_2=[Result of ” + title + ”
     largest Hessian eigenvalues]”);

run(”Stack to Hyperstack...”, ”order=xyczt(default) channels=2 slices=1
    frames=”+slices+” display=Grayscale”);

selectWindow(”Combined Stacks”)
rename(title + ” hyperstack”)

selectWindow(”Combined Stacks”)
rename(title + ” hyperstack”)

selectWindow(title)
close();

saveSettings;
setOption(”Stack position”, true);
if (!Stack.isHyperstack) {
        getVoxelSize(width, height, depth, unit);
        for (n=1; n<=nSlices; n++) {
                setSlice(n);
                run(”Measure”);
        }
        if (unit!=”pixels”) {
                depths = newArray(Table.size);
                for (i=0; i<Table.size; i++)
```

```
        depths[i] = i*depth;
        Table.setColumn(unit, depths);
        Table.update;
    }
    restoreSettings;
    exit;
}
Stack.getDimensions(w, h, channels, slices, frames);
Stack.getPosition(ch, sl, fr);
Dialog.create(”Measure Hyperstack”);
Dialog.addCheckbox(”Channels (”+channels+”)”, true);
Dialog.addCheckbox(”Slices (”+slices+”)”, true);
Dialog.addCheckbox(”Frames (”+frames+”)”, true);
choices = newArray(”czt(default)”, ”ctz”, ”zct”, ”ztc”, ”tcz”, ”tzc”);
Dialog.addChoice(”Order:”, choices, choices[0]);
Dialog.show();
state1 = Dialog.getCheckbox();
state2 = Dialog.getCheckbox();
state3 = Dialog.getCheckbox();
order = Dialog.getChoice();

if(state1) {startCh = 1; endCh = channels;}
else {startCh = ch; endCh = ch;}
if(state2) {startSl = 1; endSl = slices;}
else {startSl = sl; endSl = sl;}
if(state3) {startFr = 1; endFr = frames;}
else {startFr = fr; endFr = fr;}

```

```
run(”Clear Results”);

run(”Set Measurements...”, ”area mean standard modal min integrated median stack display redirect=None decimal=3”);

for (u=startFr; u<=endFr; u++) {
        Stack.setFrame(u);
        Stack.setChannel(1)
        run(”Select All”);
        run(”Variance...”, ”radius=20 slice”);
        setThreshold(90000.6076, 6774397.0000);
        run(”Create Selection”);
        getStatistics(area);
        area_total = (getHeight() * getWidth());
        area_cells = area;
        area_cells_percent = area/area_total*100;

        run(”Set Measurements...”, ”area mean median area_fraction limit display redirect=None decimal=3”);
        Stack.setChannel(2);
        setThreshold(threshold, 1000000000000000000000000000000.0000);
        run(”Create Selection”);
        getStatistics(area);
        area_gauss = area;
        area_gauss_percent = area/area_cells*100;
        n1=getValue(”results.count”);
        setResult(”File”, n1, title);
        setResult(”Frame”, n1, u);
```

```
        setResult(”total area”, n1, area_total);
        setResult(”cell area”, n1, area_cells);
        setResult(”cell area percent”, n1, area_cells_percent);
        setResult(”lipid area”, n1, area_gauss);
        setResult(”lipid area percent”, n1, area_gauss_percent);
        updateResults();
}



saveAs(”Results”, output+”/Results.csv”);
```

REFERENCES

1. Horn, P. & Newsome, P. N. Emerging Therapeutic Targets for NASH: Key Innovations at the Preclinical Level. *Expert Opinion on Therapeutic Targets* **24,** 175–186. doi:`10.1080/14728222.2020.1728742` (Mar. 2020).
2. Horn, P. & Tacke, F. in *Komplikationen Der Leberzirrhose* (Springer).
3. Horn, P. & Newsome, P. in *Metabolic Fatty Liver Disease - 1st Edition* (Elsevier Inc., Mar. 2024).
4. Renato, P. *et al.* in *Textbook of Hepatology* 89–128 (John Wiley & Sons, Ltd, 2007). doi:`10.1002/9780470691861.ch2b`.
5. Mao, S. A., Glorioso, J. M. & Nyberg, S. L. Liver Regeneration. *Translational Research* **163,** 352–362. doi:`10.1016/j.trsl.2014.01.005` (Apr. 2014).
6. Ginès, P. *et al.* Liver Cirrhosis. *The Lancet* **398,** 1359–1376. doi:`10.1016/S0140-6736(21)01374-X` (Oct. 2021).
7. Mokdad, A. A. *et al.* Liver Cirrhosis Mortality in 187 Countries between 1980 and 2010: A Systematic Analysis. *BMC Medicine* **12,** 145. doi:`10.1186/s12916-014-0145-y` (Sept. 2014).
8. Sepanlou, S. G. *et al.* The Global, Regional, and National Burden of Cirrhosis by Cause in 195 Countries and Territories, 1990–2017: A Systematic Analysis for the Global Burden of Disease Study 2017. *The Lancet Gastroenterology & Hepatology* **5,** 245–266. doi:`10.1016/S2468-1253(19)30349-8` (Mar. 2020).
9. Bentham, J. *et al.* Worldwide Trends in Body-Mass Index, Underweight, Overweight, and Obesity from 1975 to 2016: A Pooled Analysis of 2416 Population-Based Measurement Studies in 128˙9 Million Children, Adolescents, and Adults. *The Lancet* **390,** 2627–2642. doi:`10.1016/S0140-6736(17)32129-3` (2017).
10. O'Neill, S. & O'Driscoll, L. Metabolic Syndrome: A Closer Look at the Growing Epidemic and Its Associated Pathologies. *Obesity Reviews* **16,** 1–12. doi:`10.1111/obr.12229` (2015).
11. Kotronen, A., Westerbacka, J., Bergholm, R., Pietiläinen, K. H. & Yki-Järvinen, H. Liver Fat in the Metabolic Syndrome. *Journal of Clinical Endocrinology and Metabolism* **92,** 3490–3497. doi:`10.1210/jc.2007-0482` (2007).
12. Younossi, Z. M. *et al.* Global Epidemiology of Nonalcoholic Fatty Liver Disease—Meta-analytic Assessment of Prevalence, Incidence, and Outcomes. *Hepatology* **64,** 73–84. doi:`10.1002/hep.28431` (2016).

13. Rinella, M. E. *et al.* A Multisociety Delphi Consensus Statement on New Fatty Liver Disease Nomenclature. *Journal of Hepatology.* doi:`10.1016/j.jhep.2023.06.003`. (Nov. 20, 2023) (June 2023).
14. Wong, R. J. *et al.* Nonalcoholic Steatohepatitis Is the Second Leading Etiology of Liver Disease among Adults Awaiting Liver Transplantation in the United States. *Gastroenterology* **148,** 547–555. doi:`10.1053/j.gastro.2014.11.039` (2015).
15. Dyson, J. *et al.* Hepatocellular Cancer: The Impact of Obesity, Type 2 Diabetes and a Multidisciplinary Team. *Journal of Hepatology* **60,** 110–117. doi:`10.1016/j.jhep.2013.08.011` (Jan. 2014).
16. Marchesini, G. *et al.* EASL-EASD-EASO Clinical Practice Guidelines for the Management of Non-Alcoholic Fatty Liver Disease. *Journal of Hepatology* **64,** 1388–1402. doi:`10.1016/j.jhep.2015.11.004` (2016).
17. Chalasani, N. *et al.* The Diagnosis and Management of Nonalcoholic Fatty Liver Disease: Practice Guidance from the American Association for the Study of Liver Diseases. *Hepatology* **67,** 328–357. doi:`10.1002/hep.29367` (2018).
18. Machado, M. V. & Cortez-Pinto, H. Non-Invasive Diagnosis of Non-Alcoholic Fatty Liver Disease. A Critical Appraisal. *Journal of Hepatology* **58,** 1007–1019. doi:`10.1016/j.jhep.2012.11.021` (May 2013).
19. Taylor, R. S. *et al.* Association between Fibrosis Stage and Outcomes of Patients with Nonalcoholic Fatty Liver Disease: A Systematic Review and Meta-Analysis. *Gastroenterology* **158,** 1611–1625.e12. doi:`10.1053/j.gastro.2020.01.043` (Feb. 2020).
20. Sanyal, A. J. *et al.* Prospective Study of Outcomes in Adults with Nonalcoholic Fatty Liver Disease. *New England Journal of Medicine* **385,** 1559–1569. doi:`10.1056/NEJMoa2029349` (Oct. 2021).
21. Sterling, R. K. *et al.* Development of a Simple Noninvasive Index to Predict Significant Fibrosis in Patients with HIV/HCV Coinfection. *Hepatology* **43,** 1317–1325. doi:`10.1002/hep.21178` (2006).
22. Angulo, P. *et al.* The NAFLD Fibrosis Score: A Noninvasive System That Identifies Liver Fibrosis in Patients with NAFLD. *Hepatology* **45,** 846–854. doi:`10.1002/hep.21496` (2007).
23. Vilar-Gomez, E. & Chalasani, N. Non-Invasive Assessment of Non-Alcoholic Fatty Liver Disease: Clinical Prediction Rules and Blood-Based Biomarkers. *Journal of Hepatology* **68,** 305–315. doi:`10.1016/j.jhep.2017.11.013` (2018).
24. Berzigotti, A. *et al.* EASL Clinical Practice Guidelines on Non-Invasive Tests for Evaluation of Liver Disease Severity and Prognosis – 2021 Update. *Journal of Hepatology* **75,** 659–689. doi:`10.1016/j.jhep.2021.05.025` (Sept. 2021).
25. Boursier, J. *et al.* Non-Invasive Tests Accurately Stratify Patients with NAFLD Based on Their Risk of Liver-Related Events. *Journal of Hepatology* **76,** 1013–1020. doi:`10.1016/j.jhep.2021.12.031` (May 2022).

26. Srivastava, A. *et al.* Prospective Evaluation of a Primary Care Referral Pathway for Patients with Non-Alcoholic Fatty Liver Disease. *Journal of Hepatology* **71,** 371–378. doi:`10.1016/j.jhep.2019.03.033` (Aug. 2019).
27. Harrison, S. A. *et al.* Selonsertib for Patients with Bridging Fibrosis or Compensated Cirrhosis Due to NASH: Results from Randomized Phase III STELLAR Trials. *Journal of Hepatology* **73.** doi:`10.1016/j.jhep.2020.02.027` (Mar. 2020).
28. Newsome, P. N. *et al.* FibroScan-AST (FAST) Score for the Non-Invasive Identification of Patients with Non-Alcoholic Steatohepatitis with Significant Activity and Fibrosis: A Prospective Derivation and Global Validation Study. *The Lancet. Gastroenterology & Hepatology* **5,** 362–373. doi:`10.1016/S2468-1253(19)30383-8` (Apr. 2020).
29. Kleiner, D. E. *et al.* Design and Validation of a Histological Scoring System for Nonalcoholic Fatty Liver Disease. *Hepatology* **41,** 1313–1321. doi:`10.1002/hep.20701` (2005).
30. Nalbantoglu, Ilk. & Brunt, E. M. Role of Liver Biopsy in Nonalcoholic Fatty Liver Disease. *World Journal of Gastroenterology : WJG* **20,** 9026–9037. doi:`10.3748/wjg.v20.i27.9026` (July 2014).
31. Promrat, K. *et al.* Randomized Controlled Trial Testing the Effects of Weight Loss on Nonalcoholic Steatohepatitis. *Hepatology* **51,** 121–129. doi:`10.1002/hep.23276` (2010).
32. Petersen, K. F. *et al.* Reversal of Nonalcoholic Hepatic Steatosis, Hepatic Insulin Resistance, and Hyperglycemia by Moderate Weight Reduction in Patients With Type 2 Diabetes. *Diabetes* **54,** 603–608. doi:`10.2337/diabetes.54.3.603` (Mar. 2005).
33. Lassailly, G. *et al.* Bariatric Surgery Provides Long-term Resolution of Nonalcoholic Steatohepatitis and Regression of Fibrosis. *Gastroenterology* **159,** 1290–1301.e5. doi:`10.1053/j.gastro.2020.06.006` (Oct. 2020).
34. Aminian, A. *et al.* Association of Bariatric Surgery With Major Adverse Liver and Cardiovascular Outcomes in Patients With Biopsy-Proven Nonalcoholic Steatohepatitis. *JAMA* **326,** 2031–2042. doi:`10.1001/jama.2021.19569` (Nov. 2021).
35. Bazerbachi, F. *et al.* Intragastric Balloon Placement Induces Significant Metabolic and Histologic Improvement in Patients With Nonalcoholic Steatohepatitis. *Clinical Gastroenterology and Hepatology: The Official Clinical Practice Journal of the American Gastroenterological Association* **19,** 146–154.e4. doi:`10.1016/j.cgh.2020.04.068` (Jan. 2021).
36. Adams, L. A., Anstee, Q. M., Tilg, H. & Targher, G. Non-Alcoholic Fatty Liver Disease and Its Relationship with Cardiovascular Disease and Other Extrahepatic Diseases. *Gut* **66,** 1138–1153. doi:`10.1136/gutjnl-2017-313884` (June 2017).

37. Armstrong, M. J. *et al.* Liraglutide Safety and Efficacy in Patients with Non-Alcoholic Steatohepatitis (LEAN): A Multicentre, Double-Blind, Randomised, Placebo-Controlled Phase 2 Study. *Lancet (London, England)* **387,** 679–690. doi:`10.1016/S0140-6736(15)00803-X` (Feb. 2016).
38. Newsome, P. N. *et al.* A Placebo-Controlled Trial of Subcutaneous Semaglutide in Nonalcoholic Steatohepatitis. *The New England Journal of Medicine* **384,** 1113–1124. doi:`10.1056/NEJMoa2028395` (Mar. 2021).
39. Eriksson, J. W. *et al.* Effects of Dapagliflozin and N-3 Carboxylic Acids on Non-Alcoholic Fatty Liver Disease in People with Type 2 Diabetes: A Double-Blind Randomised Placebo-Controlled Study. *Diabetologia* **61,** 1923–1934. doi:`10.1007/s00125-018-4675-2` (Sept. 2018).
40. Cusi, K. *et al.* Effect of Canagliflozin Treatment on Hepatic Triglyceride Content and Glucose Metabolism in Patients with Type 2 Diabetes. *Diabetes, Obesity & Metabolism* **21,** 812–821. doi:`10.1111/dom.13584` (Apr. 2019).
41. Kahl, S. *et al.* Empagliflozin Effectively Lowers Liver Fat Content in Well-Controlled Type 2 Diabetes: A Randomized, Double-Blind, Phase 4, Placebo-Controlled Trial. *Diabetes Care* **43,** 298–305. doi:`10.2337/dc19-0641` (Feb. 2020).
42. Belfort, R. *et al.* A Placebo-Controlled Trial of Pioglitazone in Subjects with Nonalcoholic Steatohepatitis. *The New England Journal of Medicine* **355,** 2297–2307. doi:`10.1056/NEJMoa060326` (Nov. 2006).
43. Sanyal, A. J. *et al.* Pioglitazone, Vitamin E, or Placebo for Nonalcoholic Steatohepatitis. *The New England Journal of Medicine* **362,** 1675–1685. doi:`10.1056/NEJMoa0907929` (May 2010).
44. Cusi, K. *et al.* Long-Term Pioglitazone Treatment for Patients With Nonalcoholic Steatohepatitis and Prediabetes or Type 2 Diabetes Mellitus: A Randomized Trial. *Annals of Internal Medicine* **165,** 305–315. doi:`10.7326/M15-1774` (Sept. 2016).
45. Vilar-Gomez, E. *et al.* Type 2 Diabetes and Metformin Use Associate With Outcomes of Patients With Nonalcoholic Steatohepatitis-Related, Child-Pugh A Cirrhosis. *Clinical Gastroenterology and Hepatology: The Official Clinical Practice Journal of the American Gastroenterological Association* **19,** 136–145.e6. doi:`10.1016/j.cgh.2020.04.083` (Jan. 2021).
46. Zelber-Sagi, S. *et al.* A Double-Blind Randomized Placebo-Controlled Trial of Orlistat for the Treatment of Nonalcoholic Fatty Liver Disease. *Clinical Gastroenterology and Hepatology: The Official Clinical Practice Journal of the American Gastroenterological Association* **4,** 639–644. doi:`10.1016/j.cgh.2006.02.004` (May 2006).
47. Wang, H. *et al.* Efficacy of Orlistat in Non-Alcoholic Fatty Liver Disease: A Systematic Review and Meta-Analysis. *Biomedical Reports* **9,** 90–96. doi:`10.3892/br.2018.1100` (July 2018).
48. Ye, J. *et al.* Effect of Orlistat on Liver Fat Content in Patients with Nonalcoholic Fatty Liver Disease with Obesity: Assessment Using Magnetic

Resonance Imaging-Derived Proton Density Fat Fraction. *Therapeutic Advances in Gastroenterology* **12.** doi:`10.1177/1756284819879047` (2019).

49. Vadarlis, A. *et al.* Systematic Review with Meta-Analysis: The Effect of Vitamin E Supplementation in Adult Patients with Non-Alcoholic Fatty Liver Disease. *Journal of Gastroenterology and Hepatology* **36,** 311–319. doi:`10.1111/jgh.15221` (Feb. 2021).
50. Sinakos, E., Liava, C. & Loomba, R. Emerging Advances in the Pharmacologic Treatment of Nonalcoholic Steatohepatitis and Related Cirrhosis. *Annals of Gastroenterology* **35,** 213–225. doi:`10.20524/aog.2022.0704` (2022).
51. Harrison, S. A. *et al.* A Phase 3, Randomized, Controlled Trial of Resmetirom in NASH with Liver Fibrosis. *New England Journal of Medicine* **390,** 497–509. doi:`10.1056/NEJMoa2309000`. (Mar. 4, 2024) (Feb. 2024).
52. Hammerich, L. & Tacke, F. Hepatic Inflammatory Responses in Liver Fibrosis. *Nature Reviews Gastroenterology & Hepatology,* 1–14. doi:`10.1038/s41575-023-00807-x` (July 2023).
53. Marra, F. & Svegliati-Baroni, G. Lipotoxicity and the Gut-Liver Axis in NASH Pathogenesis. *Journal of Hepatology* **68,** 280–295. doi:`10.1016/j.jhep.2017.11.014` (2018).
54. De Muynck, K., Vanderborght, B., Van Vlierberghe, H. & Devisscher, L. The Gut–Liver Axis in Chronic Liver Disease: A Macrophage Perspective. *Cells* **10,** 2959. doi:`10.3390/cells10112959` (Nov. 2021).
55. Schuppan, D., Ruehl, M., Somasundaram, R. & Hahn, E. G. Matrix as a Modulator of Hepatic Fibrogenesis. *Seminars in Liver Disease* **21,** 351–372. doi:`10.1055/s-2001-17556` (2001).
56. Semela, D. & Shah, V. H. in *Textbook of Hepatology* 29–35 (John Wiley & Sons, Ltd, 2007). doi:`10.1002/9780470691861.ch1d`.
57. Jaeschke, H. in *Textbook of Hepatology* 36–42 (John Wiley & Sons, Ltd, 2007). doi:`10.1002/9780470691861.ch1e`.
58. Pinzani, M. in *Textbook of Hepatology* 43–51 (John Wiley & Sons, Ltd, 2007). doi:`10.1002/9780470691861.ch1f`.
59. Xie, G. *et al.* Cross-Talk between Notch and Hedgehog Regulates Hepatic Stellate Cell Fate. *Hepatology (Baltimore, Md.)* **58,** 1801–1813. doi:`10.1002/hep.26511` (Nov. 2013).
60. Chen, L., Brenner, D. A. & Kisseleva, T. Combatting Fibrosis: Exosome-Based Therapies in the Regression of Liver Fibrosis. *Hepatology Communications* **3,** 180–192. doi:`10.1002/hep4.1290` (Feb. 2019).
61. Mederacke, I. *et al.* The Purinergic P2Y14 Receptor Links Hepatocyte Death to Hepatic Stellate Cell Activation and Fibrogenesis in the Liver. *Science Translational Medicine* **14,** eabe5795. doi:`10.1126/scitranslmed.abe5795` (Apr. 2022).

62. An, P. *et al.* Hepatocyte Mitochondria-Derived Danger Signals Directly Activate Hepatic Stellate Cells and Drive Progression of Liver Fibrosis. *Nature Communications* **11,** 2362. doi:`10.1038/s41467-020-16092-0` (May 2020).
63. Kao, Y.-H. *et al.* High-Mobility Group Box 1 Protein Activates Hepatic Stellate Cells in Vitro. *Transplantation Proceedings* **40,** 2704–2705. doi:`10.1016/j.transproceed.2008.07.055` (Oct. 2008).
64. Poisson, J. *et al.* Liver Sinusoidal Endothelial Cells: Physiology and Role in Liver Diseases. *Journal of Hepatology* **66,** 212–227. doi:`10.1016/j.jhep.2016.07.009` (2017).
65. Ding, B.-S. *et al.* Divergent Angiocrine Signals from Vascular Niche Balance Liver Regeneration and Fibrosis. *Nature* **505,** 97–102. doi:`10.1038/nature12681` (Jan. 2014).
66. Tacke, F. Targeting Hepatic Macrophages to Treat Liver Diseases. *Journal of Hepatology* **66,** 1300–1312. doi:`10.1016/j.jhep.2017.02.026` (2017).
67. Gordon, S. & Plüddemann, A. Tissue Macrophages: Heterogeneity and Functions. *BMC Biology* **15,** 53. doi:`10.1186/s12915-017-0392-4` (June 2017).
68. Guillot, A. & Tacke, F. Liver Macrophages: Old Dogmas and New Insights. *Hepatology Communications* **3,** 730–743. doi:`10.1002/hep4.1356` (Apr. 2019).
69. Krenkel, O. & Tacke, F. Liver Macrophages in Tissue Homeostasis and Disease. *Nature Reviews Immunology* **17,** 306–321. doi:`10.1038/nri.2017.11` (2017).
70. Ramachandran, P. *et al.* Resolving the Fibrotic Niche of Human Liver Cirrhosis at Single-Cell Level. *Nature* **575,** 512–518. doi:`10.1038/s41586-019-1631-3` (2019).
71. Tsuchida, T. & Friedman, S. L. Mechanisms of Hepatic Stellate Cell Activation. *Nature reviews gastroenterology and hepatology* **14,** 397–411. doi:`10.1038/nrgastro.2017.38` (July 2017).
72. Wang, Q. *et al.* Role of XBP1 in Regulating the Progression of Non-Alcoholic Steatohepatitis. *Journal of Hepatology* **77,** 312–325. doi:`10.1016/j.jhep.2022.02.031` (Aug. 2022).
73. Ramirez-Pedraza, M. & Fernández, M. Interplay Between Macrophages and Angiogenesis: A Double-Edged Sword in Liver Disease. *Frontiers in Immunology* **10** (2019).
74. Ibidapo-Obe, O. & Bruns, T. Tissue-Resident and Innate-like T Cells in Patients with Advanced Chronic Liver Disease. *JHEP Reports.* doi:`10.1016/j.jhepr.2023.100812` (June 2023).
75. Kirschbaum, M. *et al.* Transient von Willebrand Factor-Mediated Platelet Influx Stimulates Liver Regeneration after Partial Hepatectomy in Mice. *Liver International* **37,** 1731–1737. doi:`10.1111/liv.13386` (2017).
76. Nakano, Y. *et al.* Platelet Dynamics in the Early Phase of Postischemic Liver in Vivo. *Journal of Surgical Research* **149,** 192–198. doi:`10.1016/j.jss.2007.09.016` (2008).

77. Takahashi, K., Murata, S. & Ohkohchi, N. Novel Therapy for Liver Regeneration by Increasing the Number of Platelets. *Surgery Today* **43,** 1081–1087. doi:`10.1007/s00595-012-0418-z` (2013).
78. Lalor, P. F., Herbert, J., Bicknell, R. & Adams, D. H. Hepatic Sinusoidal Endothelium Avidly Binds Platelets in an Integrin-Dependent Manner, Leading to Platelet and Endothelial Activation and Leukocyte Recruitment. *American Journal of Physiology - Gastrointestinal and Liver Physiology* **304,** G469–78. doi:`10.1152/ajpgi.00407.2012` (2013).
79. Malehmir, M. *et al.* Platelet GPIbα Is a Mediator and Potential Interventional Target for NASH and Subsequent Liver Cancer. *Nature Medicine* **25,** 641–655. doi:`10.1038/s41591-019-0379-5` (2019).
80. Aryal, B. *et al.* Therapeutic Implication of Platelets in Liver Regeneration –Hopes and Hues. *Expert Review of Gastroenterology and Hepatology* **12,** 1219–1228. doi:`10.1080/17474124.2018.1533813` (2018).
81. Chauhan, A., Adams, D. H., Watson, S. P. & Lalor, P. F. Platelets: No Longer Bystanders in Liver Disease. *Hepatology* **64,** 1774–1784. doi:`10.1002/hep.28526` (2016).
82. Mederacke, I. *et al.* Fate Tracing Reveals Hepatic Stellate Cells as Dominant Contributors to Liver Fibrosis Independent of Its Aetiology. *Nature Communications* **4,** 2823. doi:`10.1038/ncomms3823` (Nov. 2013).
83. Iredale, J. P. Models of Liver Fibrosis: Exploring the Dynamic Nature of Inflammation and Repair in a Solid Organ. *JOURNAL OF CLINICAL INVESTIGATION* **117,** 539–548. doi:`10.1172/JCI30542` (Mar. 2007).
84. Carter, J. K. & Friedman, S. L. Hepatic Stellate Cell-Immune Interactions in NASH. *Frontiers in Endocrinology* **13** (2022).
85. Krenkel, O., Hundertmark, J., Ritz, T. P., Weiskirchen, R. & Tacke, F. Single Cell RNA Sequencing Identifies Subsets of Hepatic Stellate Cells and Myofibroblasts in Liver Fibrosis. *Cells* **8,** E503. doi:`10.3390/cells8050503` (May 2019).
86. Dobie, R. *et al.* Single-Cell Transcriptomics Uncovers Zonation of Function in the Mesenchyme during Liver Fibrosis. *Cell Reports* **29,** 1832–1847.e8. doi:`10.1016/j.celrep.2019.10.024` (2019).
87. Filliol, A. *et al.* Opposing Roles of Hepatic Stellate Cell Subpopulations in Hepatocarcinogenesis. *Nature* **610,** 356–365. doi:`10.1038/s41586-022-05289-6` (Oct. 2022).
88. Kisseleva, T. *et al.* Myofibroblasts Revert to an Inactive Phenotype during Regression of Liver Fibrosis. *Proceedings of the National Academy of Sciences of the United States of America* **109,** 9448–9453. doi:`10.1073/pnas.1201840109` (June 2012).
89. Iwaisako, K. *et al.* Origin of Myofibroblasts in the Fibrotic Liver in Mice. *Proceedings of the National Academy of Sciences of the United States of America* **111,** E3297–305. doi:`10.1073/pnas.1400062111` (2014).

90. Lei, L. *et al.* Portal Fibroblasts with Mesenchymal Stem Cell Features Form a Reservoir of Proliferative Myofibroblasts in Liver Fibrosis. *Hepatology* **76,** 1360. doi:`10.1002/hep.32456` (Nov. 2022).
91. Kisseleva, T. & Brenner, D. Molecular and Cellular Mechanisms of Liver Fibrosis and Its Regression. *Nature Reviews Gastroenterology & Hepatology* **18,** 151–166. doi:`10.1038/s41575-020-00372-7` (Mar. 2021).
92. Hellerbrand, C., Stefanovic, B., Giordano, F., Burchardt, E. R. & Brenner, D. A. The Role of TGFβ1 in Initiating Hepatic Stellate Cell Activation in Vivo. *Journal of Hepatology* **30,** 77–87. doi:`10.1016/S0168-8278(99)80010-5` (Jan. 1999).
93. Breitkopf, K., Godoy, P., Ciuclan, L., Singer, M. V. & Dooley, S. TGF-β/Smad Signaling in the Injured Liver. *Zeitschrift für Gastroenterologie* **44,** 57–66. doi:`10.1055/s-2005-858989` (Jan. 2006).
94. Moustakas, A. & Heldin, C.-H. The Regulation of TGFβ Signal Transduction. *Development* **136,** 3699–3714. doi:`10.1242/dev.030338` (Nov. 2009).
95. Dewidar, B., Meyer, C., Dooley, S. & Meindl-Beinker, a. N. TGF-β in Hepatic Stellate Cell Activation and Liver Fibrogenesis—Updated 2019. *Cells* **8,** 1419. doi:`10.3390/cells8111419` (Nov. 2019).
96. Huang, Y. *et al.* Bevacizumab Attenuates Hepatic Fibrosis in Rats by Inhibiting Activation of Hepatic Stellate Cells. *PLOS ONE* **8,** e73492. doi:`10.1371/journal.pone.0073492` (Aug. 2013).
97. Kesar, V. & Odin, J. A. Toll-like Receptors and Liver Disease. *Liver International* **34,** 184–196. doi:`10.1111/liv.12315` (2014).
98. Devaraj, E., Perumal, E., Subramaniyan, R. & Mustapha, N. Liver Fibrosis: Extracellular Vesicles Mediated Intercellular Communication in Perisinusoidal Space. *Hepatology* **76,** 275. doi:`10.1002/hep.32239` (July 2022).
99. Tall, A. R. & Yvan-Charvet, L. Cholesterol, Inflammation and Innate Immunity. *Nature reviews. Immunology* **15,** 104–116. doi:`10.1038/nri3793` (Feb. 2015).
100. Hou, W. & Syn, W.-K. Role of Metabolism in Hepatic Stellate Cell Activation and Fibrogenesis. *Frontiers in Cell and Developmental Biology* **6** (2018).
101. Pu, S. *et al.* Roles of Nuclear Receptors in Hepatic Stellate Cells. *Expert Review of Gastroenterology & Hepatology* **15,** 879–890. doi:`10.1080/17474124.2021.1949288` (Aug. 2021).
102. Tacke, F. & Trautwein, C. Mechanisms of Liver Fibrosis Resolution. *Journal of Hepatology* **63,** 1038–1039. doi:`10.1016/j.jhep.2015.03.039` (Oct. 2015).
103. Radaeva, S. *et al.* Natural Killer Cells Ameliorate Liver Fibrosis by Killing Activated Stellate Cells in NKG2D-Dependent and Tumor Necrosis Factor–Related Apoptosis-Inducing Ligand–Dependent Manners. *Gastroenterology* **130,** 435–452. doi:`10.1053/j.gastro.2005.10.055` (Feb. 2006).
104. Hammerich, L. *et al.* Chemokine Receptor CCR6-dependent Accumulation of $\Gamma\delta$ T Cells in Injured Liver Restricts Hepatic Inflammation and Fibrosis. *Hepatology* **59,** 630–642. doi:`10.1002/hep.26697` (2014).

105. Koda, Y. *et al.* CD8+ Tissue-Resident Memory T Cells Promote Liver Fibrosis Resolution by Inducing Apoptosis of Hepatic Stellate Cells. *Nature Communications* **12,** 4474. doi:`10.1038/s41467-021-24734-0` (July 2021).
106. Iredale, J. P. *et al.* Mechanisms of Spontaneous Resolution of Rat Liver Fibrosis. Hepatic Stellate Cell Apoptosis and Reduced Hepatic Expression of Metalloproteinase Inhibitors. *Journal of Clinical Investigation* **102,** 538–549. doi:`10.1172/JCI1018` (Aug. 1998).
107. Murphy, F. R. *et al.* Inhibition of Apoptosis of Activated Hepatic Stellate Cells by Tissue Inhibitor of Metalloproteinase-1 Is Mediated via Effects on Matrix Metalloproteinase Inhibition: IMPLICATIONS FOR REVERSIBILITY OF LIVER FIBROSIS *. *Journal of Biological Chemistry* **277,** 11069–11076. doi:`10.1074/jbc.M111490200` (Mar. 2002).
108. Krizhanovsky, V. *et al.* Senescence of Activated Stellate Cells Limits Liver Fibrosis. *Cell* **134,** 657–667. doi:`10.1016/j.cell.2008.06.049` (Aug. 2008).
109. Campisi, J. & d'Adda di Fagagna, F. Cellular Senescence: When Bad Things Happen to Good Cells. *Nature Reviews Molecular Cell Biology* **8,** 729–740. doi:`10.1038/nrm2233` (Sept. 2007).
110. Schnabl, B., Purbeck, C. A., Choi, Y. H., Hagedorn, C. H. & Brenner, D. Replicative Senescence of Activated Human Hepatic Stellate Cells Is Accompanied by a Pronounced Inflammatory but Less Fibrogenic Phenotype. *Hepatology* **37,** 653–664. doi:`10.1053/jhep.2003.50097` (2003).
111. Ramachandran, P. *et al.* Differential Ly-6C Expression Identifies the Recruited Macrophage Phenotype, Which Orchestrates the Regression of Murine Liver Fibrosis. *Proceedings of the National Academy of Sciences* **109,** E3186–E3195. doi:`10.1073/pnas.1119964109` (Nov. 2012).
112. Uchinami, H., Seki, E., Brenner, D. A. & D'Armiento, J. Loss of MMP 13 Attenuates Murine Hepatic Injury and Fibrosis during Cholestasis. *Hepatology* **44,** 420–429. doi:`10.1002/hep.21268` (2006).
113. Fallowfield, J. A. *et al.* Scar-Associated Macrophages Are a Major Source of Hepatic Matrix Metalloproteinase-13 and Facilitate the Resolution of Murine Hepatic Fibrosis. *Journal of Immunology (Baltimore, Md.: 1950)* **178,** 5288–5295. doi:`10.4049/jimmunol.178.8.5288` (Apr. 2007).
114. Roeb, E. Matrix Metalloproteinases and Liver Fibrosis (Translational Aspects). *Matrix Biology. SI : Fibrosis – Mechanisms and Translational Aspects* **68–69,** 463–473. doi:`10.1016/j.matbio.2017.12.012` (Aug. 2018).
115. Wan, J. *et al.* M2 Kupffer Cells Promote M1 Kupffer Cell Apoptosis: A Protective Mechanism against Alcoholic and Nonalcoholic Fatty Liver Disease. *Hepatology* **59,** 130–142. doi:`10.1002/hep.26607` (2014).
116. Tacke, F., Puengel, T., Loomba, R. & Friedman, S. L. An Integrated View of Anti-Inflammatory and Antifibrotic Targets for the Treatment of NASH. *Journal of Hepatology* **79,** 552–566. doi:`10.1016/j.jhep.2023.03.038` (Aug. 2023).

117. Anstee, Q. M. *et al.* Cenicriviroc Lacked Efficacy to Treat Liver Fibrosis in Nonalcoholic Steatohepatitis: AURORA Phase III Randomized Study. *Clinical Gastroenterology and Hepatology.* doi:`10.1016/j.cgh.2023.04.003` (Apr. 2023).
118. Lefere, S. *et al.* Differential Effects of Selective- and Pan-PPAR Agonists on Experimental Steatohepatitis and Hepatic Macrophages73. *Journal of Hepatology* **73,** 757–770. doi:`10.1016/j.jhep.2020.04.025` (Oct. 2020).
119. Gao, B. & Bataller, R. Alcoholic Liver Disease: Pathogenesis and New Therapeutic Targets. *Gastroenterology* **141,** 1572–1585. doi:`10.1053/j.gastro.2011.09.002` (Nov. 2011).
120. Iannacone, M., Andreata, F. & Guidotti, L. G. Immunological Insights in the Treatment of Chronic Hepatitis B. *Current Opinion in Immunology* **77,** 102207. doi:`10.1016/j.coi.2022.102207` (Aug. 2022).
121. Liberal, R., de Boer, Y. S. & Heneghan, M. A. Established and Novel Therapeutic Options for Autoimmune Hepatitis. *The Lancet Gastroenterology & Hepatology* **6,** 315–326. doi:`10.1016/S2468-1253(20)30328-9` (Apr. 2021).
122. Gressner, A. M. & Weiskirchen, R. The Tightrope of Therapeutic Suppression of Active Transforming Growth Factor-β: High Enough to Fall Deeply? *Journal of Hepatology* **39,** 856–859. doi:`10.1016/S0168-8278(03)00432-X` (Nov. 2003).
123. Rahman, S. R. *et al.* Integrins as a Drug Target in Liver Fibrosis. *Liver International* **42,** 507–521. doi:`10.1111/liv.15157` (2022).
124. Dwyer, B. J., Macmillan, M. T., Brennan, P. N. & Forbes, S. J. Cell Therapy for Advanced Liver Diseases: Repair or Rebuild. *Journal of Hepatology* **74,** 185–199. doi:`10.1016/j.jhep.2020.09.014` (Jan. 2021).
125. Rider, C. C. & Mulloy, B. Bone Morphogenetic Protein and Growth Differentiation Factor Cytokine Families and Their Protein Antagonists. *Biochemical Journal* **429,** 1–12. doi:`10.1042/BJ20100305` (June 2010).
126. Little, S. C. & Mullins, M. C. Bone Morphogenetic Protein Heterodimers Assemble Heteromeric Type I Receptor Complexes to Pattern the Dorsoventral Axis. *Nature Cell Biology* **11,** 637–643. doi:`10.1038/ncb1870` (May 2009).
127. Rosen, V. *et al.* Purification and Molecular Cloning of a Novel Group of Bmps and Localization of Bmp Mrna in Developing Bone. *Connective Tissue Research* **20,** 313–319. doi:`10.3109/03008208909023902` (1989).
128. Bier, E. & De Robertis, E. M. BMP Gradients: A Paradigm for Morphogen-Mediated Developmental Patterning. *Science* **348,** aaa5838. doi:`10.1126/science.aaa5838` (2015).
129. Hogan, B. L. Bone Morphogenetic Proteins in Development. *Current Opinion in Genetics & Development* **6,** 432–438. doi:`10.1016/S0959-437X(96)80064-5` (Aug. 1996).
130. Wagner, D. O. *et al.* BMPs: From Bone to Body Morphogenetic Proteins. *Science Signaling* **3,** mr1. doi:`10.1126/scisignal.3107mr1` (Feb. 2010).

131. Conidi, A. *et al.* Few Smad Proteins and Many Smad-interacting Proteins Yield Multiple Functions and Action Modes in TGFβ/BMP Signaling in Vivo. *Cytokine & Growth Factor Reviews. Cytokine Research in Belgium* **22,** 287–300. doi:`10.1016/j.cytogfr.2011.11.006` (Oct. 2011).
132. Holtzhausen, A. *et al.* Novel Bone Morphogenetic Protein Signaling through Smad2 and Smad3 to Regulate Cancer Progression and Development. *The FASEB Journal* **28,** 1248–1267. doi:`10.1096/fj.13-239178` (2014).
133. Herrera, B., Addante, A. & Sánchez, A. BMP Signalling at the Crossroad of Liver Fibrosis and Regeneration. *International Journal of Molecular Sciences* **19.** doi:`10.3390/ijms19010039` (2018).
134. Herrera, B., Sanchez, A. & Fabregat, I. BMPS and Liver: More Questions than Answers. *Current Pharmaceutical Design* **18,** 4114–4125. doi:`10.2174/138161212802430503`. (Mar. 11, 2024) (Sept. 2012).
135. Guilliams, M. *et al.* Spatial Proteogenomics Reveals Distinct and Evolutionarily Conserved Hepatic Macrophage Niches. *Cell* **185,** 379–396.e38. doi:`10.1016/j.cell.2021.12.018` (Jan. 2022).
136. Kinoshita, K. *et al.* Adenovirus-Mediated Expression of BMP-7 Suppresses the Development of Liver Fibrosis in Rats. *Gut* **56,** 706–714. doi:`10.1136/gut.2006.092460` (2007).
137. Muñoz-Félix, J. M., González-Núñez, M., Martínez-Salgado, C. & López-Novoa, J. M. TGF-β/BMP Proteins as Therapeutic Targets in Renal Fibrosis. Where Have We Arrived after 25 Years of Trials and Tribulations? *Pharmacology and Therapeutics* **156,** 44–58. doi:`10.1016/j.pharmthera.2015.10.003` (2015).
138. Morrell, N. W. *et al.* Targeting BMP Signalling in Cardiovascular Disease and Anaemia. *Nature Reviews Cardiology* **13,** 106–120. doi:`10.1038/nrcardio.2015.156` (2016).
139. Do, N. *et al.* BMP4 Is a Novel Paracrine Inhibitor of Liver Regeneration. *American Journal of Physiology - Gastrointestinal and Liver Physiology* **303,** G1220–7. doi:`10.1152/ajpgi.00105.2012` (2012).
140. Breitkopf-Heinlein, K. *et al.* BMP-9 Interferes with Liver Regeneration and Promotes Liver Fibrosis. *Gut* **66,** 939–954. doi:`10.1136/gutjnl-2016-313314` (2017).
141. Sugimoto, H. *et al.* BMP-7 Functions as a Novel Hormone to Facilitate Liver Regeneration. *The FASEB Journal* **21,** 256–264. doi:`10.1096/fj.06-6837com` (2007).
142. Choi, T. Y. *et al.* Bone Morphogenetic Protein Signaling Governs Biliary-Driven Liver Regeneration in Zebrafish through Tbx2b and Id2a. *Hepatology* **66,** 1616–1630. doi:`10.1002/hep.29309` (2017).
143. Olsavszky, V. *et al.* GATA4 and LMO3 Balance Angiocrine Signaling and Autocrine Inflammatory Activation by BMP2 in Liver Sinusoidal Endothelial Cells. *Gene* **627,** 491–499. doi:`10.1016/j.gene.2017.06.051` (2017).

144. Helbing, T. *et al.* BMP Activity Controlled by BMPER Regulates the Proinflammatory Phenotype of Endothelium. *Blood* **118,** 5040–5049. doi:`10.1182/blood-2011-03-339762` (Nov. 2011).
145. Csiszar, A., Labinskyy, N., Jo, H., Ballabh, P. & Ungvari, Z. Differential Proinflammatory and Prooxidant Effects of Bone Morphogenetic Protein-4 in Coronary and Pulmonary Arterial Endothelial Cells. *American Journal of Physiology - Heart and Circulatory Physiology* **295,** H569–H577. doi:`10.1152/ajpheart.00180.2008` (Aug. 2008).
146. Arnold, L. *et al.* Endothelial BMP4 Promotes Leukocyte Rolling and Adhesion and Is Elevated in Patients after Survived Out-of-Hospital Cardiac Arrest. *Inflammation* **43,** 2379–2391. doi:`10.1007/s10753-020-01307-9` (Dec. 2020).
147. Ribera, J. *et al.* A Small Population of Liver Endothelial Cells Undergoes Endothelial-Tomesenchymal Transition in Response to Chronic Liver Injury. *American Journal of Physiology - Gastrointestinal and Liver Physiology* **313,** G492–G504. doi:`10.1152/ajpgi.00428.2016` (2017).
148. Desroches-Castan, A. *et al.* Bone Morphogenetic Protein 9 Is a Paracrine Factor Controlling Liver Sinusoidal Endothelial Cell Fenestration and Protecting against Hepatic Fibrosis. *Hepatology* **70,** 1392–1408. doi:`10.1002/hep.30655` (2019).
149. Wang, C. Y. *et al.* Ablation of Hepatocyte Smad1, Smad5, and Smad8 Causes Severe Tissue Iron Loading and Liver Fibrosis in Mice. *Hepatology* **70,** 1986–2002. doi:`10.1002/hep.30780` (2019).
150. Tacke, F. *et al.* Bone Morphogenetic Protein 7 Is Elevated in Patients with Chronic Liver Disease and Exerts Fibrogenic Effects on Human Hepatic Stellate Cells. *Digestive Diseases and Sciences* **52,** 3404–3415. doi:`10.1007/s10620-007-9758-8` (Dec. 2007).
151. Yang, T. *et al.* Bone Morphogenetic Protein 7 Suppresses the Progression of Hepatic Fibrosis and Regulates the Expression of Gremlin and Transforming Growth Factor B1. *Molecular Medicine Reports* **6,** 246–252. doi:`10.3892/mmr.2012.892` (2012).
152. Wang, L. P. *et al.* BMP-7 Attenuates Liver Fibrosis via Regulation of Epidermal Growth Factor Receptor. *International Journal of Clinical and Experimental Pathology* **7,** 3537–3547 (2014).
153. Fan, J. *et al.* Bone Morphogenetic Protein 4 Mediates Bile Duct Ligation Induced Liver Fibrosis through Activation of Smad1 and ERK1/2 in Rat Hepatic Stellate Cells. *Journal of Cellular Physiology* **207,** 499–505. doi:`10.1002/jcp.20593` (2006).
154. Arndt, S. *et al.* Enhanced Expression of BMP6 Inhibits Hepatic Fibrosis in Non-Alcoholic Fatty Liver Disease. *Gut* **64,** 973–981. doi:`10.1136/gutjnl-2014-306968` (2015).
155. Zakin, L. & Robertis, E. M. D. Extracellular Regulation of BMP Signaling. *Current Biology* **20,** R89–R92. doi:`10.1016/j.cub.2009.11.021` (Feb. 2010).

156. Samad, T. A. *et al.* DRAGON, a Bone Morphogenetic Protein Co-receptor *. *Journal of Biological Chemistry* **280,** 14122–14129. doi:`10.1074/jbc.M410034200` (Apr. 2005).
157. Sieber, C., Kopf, J., Hiepen, C. & Knaus, P. Recent Advances in BMP Receptor Signaling. *Cytokine & Growth Factor Reviews. Bone Morphogenetic Proteins, Stem Cells and Regenerative Medicine* **20,** 343–355. doi:`10.1016/j.cytogfr.2009.10.007` (Oct. 2009).
158. Onichtchouk, D. *et al.* Silencing of TGF-beta Signalling by the Pseudoreceptor BAMBI. *Nature* **401,** 480–485. doi:`10.1038/46794` (Sept. 1999).
159. Hsu, D. R., Economides, A. N., Wang, X., Eimon, P. M. & Harland, R. M. The Xenopus Dorsalizing Factor Gremlin Identifies a Novel Family of Secreted Proteins That Antagonize BMP Activities. *Molecular Cell* **1,** 673–683. doi:`10.1016/S1097-2765(00)80067-2` (1998).
160. Vitt, U. A., Hsu, S. Y. & Hsueh, A. J. Evolution and Classification of Cystine Knot-Containing Hormones and Related Extracellular Signaling Molecules. *Molecular Endocrinology* **15,** 681–694. doi:`10.1210/mend.15.5.0639` (2001).
161. Topol, L. Z. *et al.* Biosynthesis, Post-Translation Modification, and Functional Characterization of Drm/Gremlin. *Journal of Biological Chemistry* **275,** 8785–8793. doi:`10.1074/jbc.275.12.8785` (2000).
162. Grillo, E. *et al.* Monomeric Gremlin Is a Novel Vascular Endothelial Growth Factor Receptor-2 Antagonist. *Oncotarget* **7,** 35353–35368. doi:`10.18632/oncotarget.9286` (2016).
163. Mitola, S. *et al.* Gremlin Is a Novel Agonist of the Major Proangiogenic Receptor VEGFR2. *Blood* **116,** 3677–3680. doi:`10.1182/blood-2010-06-291930` (2010).
164. Mueller, K. A. *et al.* Gremlin-1 Identifies Fibrosis and Predicts Adverse Outcome in Patients with Heart Failure Undergoing Endomyocardial Biopsy. *Journal of Cardiac Failure* **19,** 678–684. doi:`10.1016/j.cardfail.2013.09.001`. PMID: `24125106` (Oct. 2013).
165. Chiodelli, P. *et al.* Heparan Sulfate Proteoglycans Mediate the Angiogenic Activity of the Vascular Endothelial Growth Factor Receptor-2 Agonist Gremlin. *Arteriosclerosis, Thrombosis, and Vascular Biology* **31,** e116–27. doi:`10.1161/ATVBAHA.111.235184`. PMID: `21921258` (Dec. 2011).
166. Tatsinkam, A., Mulloy, B. & Rider, C. C. Mapping the Heparin-Binding Site of the BMP Antagonist Gremlin by Site-Directed Mutagenesis Based on Predictive Modelling. *Biochemical Journal* **470,** 53–64. doi:`10.1042/BJ20150228` (2015).
167. Kišonaite, M., Wang, X. & Hyvönen, M. Structure of Gremlin-1 and Analysis of Its Interaction with BMP-2. *Biochemical Journal* **473,** 1593–1604. doi:`10.1042/BCJ20160254` (2016).
168. Tatsinkam, A. J. *et al.* The Binding of the Bone Morphogenetic Protein Antagonist Gremlin to Kidney Heparan Sulfate: Such Binding Is Not Essential for BMP Antagonism. *International Journal of Biochemistry and Cell Biology* **83,** 39–46. doi:`10.1016/j.biocel.2016.12.006` (2017).

169. Müller, I. I. *et al.* Protective Role of Gremlin-1 in Myocardial Function. *European Journal of Clinical Investigation.* doi:`10.1111/eci.13539` (2021).
170. Chen, S. *et al.* Grem1 Accelerates Nucleus Pulposus Cell Apoptosis and Intervertebral Disc Degeneration by Inhibiting TGF-β-mediated Smad2/3 Phosphorylation. *Experimental & Molecular Medicine* **54,** 518–530. doi:`10.1038/s12276-022-00753-9` (Apr. 2022).
171. Chan, T.-C. *et al.* The Autocrine Glycosylated-GREM1 Interacts with TGFB1 to Suppress TGFβ/BMP/SMAD-mediated EMT Partially by Inhibiting MYL9 Transactivation in Urinary Carcinoma. *Cellular Oncology.* doi:`10.1007/s13402-023-00788-8` (Mar. 2023).
172. Gustafson, B. *et al.* BMP4 and BMP Antagonists Regulate Human White and Beige Adipogenesis. *Diabetes* **64,** 1670–1681. doi:`10.2337/db14-1127` (May 2015).
173. Church, R. H. *et al.* Gremlin1 Plays a Key Role in Kidney Development and Renal Fibrosis. *American Journal of Physiology - Renal Physiology* **312,** F1141–F1157. doi:`10.1152/ajprenal.00344.2016` (2017).
174. Rowan, S. C. *et al.* Gremlin 1 Depletion in Vivo Causes Severe Enteropathy and Bone Marrow Failure. *The Journal of Pathology* **251,** 117–122. doi:`10.1002/path.5450` (Apr. 2020).
175. Stabile, H. *et al.* Bone Morphogenic Protein Antagonist Drm/Gremlin Is a Novel Proangiogenic Factor. *Blood* **109,** 1834–1840. doi:`10.1182/blood-2006-06-032276` (Mar. 2007).
176. Zhang, Y. *et al.* Gremlin-1 Is a Key Regulator of Endothelial-to-Mesenchymal Transition in Human Pulmonary Artery Endothelial Cells. *Experimental Cell Research* **390.** doi:`10.1016/j.yexcr.2020.111941`. PMID: `32145252` (May 2020).
177. Chen, M. H. *et al.* Expression of Gremlin 1 Correlates with Increased Angiogenesis and Progression-Free Survival in Patients with Pancreatic Neuroendocrine Tumors. *Journal of Gastroenterology* **48,** 101–108. doi:`10.1007/s00535-012-0614-z` (Jan. 2013).
178. Hoggard, N., Cruickshank, M., Moar, K. M., Bashir, S. & Mayer, C. D. Using Gene Expression to Predict Differences in the Secretome of Human Omental vs. Subcutaneous Adipose Tissue. *Obesity* **20,** 1158–1167. doi:`10.1038/oby.2012.14` (2012).
179. Hammarstedt, A., Gogg, S., Hedjazifar, S., Nerstedt, A. & Smith, U. Impaired Adipogenesis and Dysfunctional Adipose Tissue in Human Hypertrophic Obesity. *Physiological Reviews* **98,** 1911–1941. doi:`10.1152/physrev.00034.2017` (2018).
180. Hedjazifar, S. *et al.* The Novel Adipokine Gremlin 1 Antagonizes Insulin Action and Is Increased in Type 2 Diabetes and NAFLD/NASH. *Diabetes* **69,** 331–341. doi:`10.2337/db19-0701` (Mar. 2020).

181. Chatterjee, M. *et al.* Platelets as a Novel Source of Gremlin-1: Implications for Thromboinflammation. *Thrombosis and Haemostasis* **117,** 311–324. doi:`10.1160/TH16-08-0665` (2017).
182. Müller, I. I. *et al.* Impact of Counterbalance between Macrophage Migration Inhibitory Factor and Its Inhibitor Gremlin-1 in Patients with Coronary Artery Disease. *Atherosclerosis* **237,** 426–432. doi:`10.1016/j.atherosclerosis.2014.09.010` (Dec. 2014).
183. Müller, K. A. *et al.* High Plasma Levels of Gremlin-1 and Macrophage Migration Inhibitory Factor, but Not Their Ratio, Indicate an Increased Risk for Acute Coronary Syndrome in Patients with Type 2 Diabetes Mellitus. *Clinical Cardiology* **39,** 201–206. doi:`10.1002/clc.22509` (2016).
184. Koli, K. *et al.* Bone Morphogenetic Protein-4 Inhibitor Gremlin Is Overexpressed in Idiopathic Pulmonary Fibrosis. *American Journal of Pathology* **169,** 61–71. doi:`10.2353/ajpath.2006.051263` (July 2006).
185. Staloch, D. *et al.* Gremlin Is a Key Pro-Fibrogenic Factor in Chronic Pancreatitis. *Journal of Molecular Medicine* **93,** 1085–1093. doi:`10.1007/s00109-015-1308-9` (2015).
186. Yang, Y. *et al.* Targeting Gremlin 1 Prevents Intestinal Fibrosis Progression by Inhibiting the Fatty Acid Oxidation of Fibroblast Cells. *Frontiers in Pharmacology* **12.** doi:`10.3389/fphar.2021.663774` (Apr. 2021).
187. Boers, W. *et al.* Transcriptional Profiling Reveals Novel Markers of Liver Fibrogenesis: Gremlin and Insulin-like Growth Factor-Binding Proteins. *Journal of Biological Chemistry* **281,** 16289–16295. doi:`10.1074/jbc.M600711200` (2006).
188. Zhang, Y. Q. *et al.* Gremlin1 Accelerates Hepatic Stellate Cell Activation through Upregulation of TGF-Beta Expression. *DNA and Cell Biology* **36,** 603–610. doi:`10.1089/dna.2017.3707`. PMID: 28467108 (July 2017).
189. Ogawa, T. *et al.* Identification of Vitamin A-free Cells in a Stellate Cell-Enriched Fraction of Normal Rat Liver as Myofibroblasts. *Histochemistry and Cell Biology* **127,** 161–174. doi:`10.1007/s00418-006-0237-7` (2007).
190. Zeng, X. Y. *et al.* Suppression of Hepatic Stellate Cell Activation through Downregulation of Gremlin1 Expression by the miR-23b/27b Cluster. *Oncotarget* **7,** 86198–86210. doi:`10.18632/oncotarget.13365` (Dec. 2016).
191. Baboota, R. K. *et al.* BMP4 and Gremlin 1 Regulate Hepatic Cell Senescence during Clinical Progression of NAFLD/NASH. *Nature Metabolism* **4,** 1007–1021. doi:`10.1038/s42255-022-00620-x` (Aug. 2022).
192. Tian, S. *et al.* Roles of Follistatin-like Protein 3 in Human Non-Tumor Pathophysiologies and Cancers. *Frontiers in Cell and Developmental Biology* **10** (2022).
193. Hayette, S. *et al.* FLRG (Follistatin-Related Gene), a New Target of Chromosomal Rearrangement in Malignant Blood Disorders. *Oncogene* **16,** 2949–2954. doi:`10.1038/sj.onc.1201807` (June 1998).

194. Tortoriello, D. V., Sidis, Y., Holtzman, D. A., Holmes, W. E. & Schneyer, A. L. Human Follistatin-Related Protein: A Structural Homologue of Follistatin with Nuclear Localization. *Endocrinology* **142,** 3426–3434. doi:`10.1210/endo.142.8.8319` (Aug. 2001).
195. Tsuchida, K. *et al.* Identification and Characterization of a Novel Follistatin-like Protein as a Binding Protein for the TGF-β Family. *Journal of Biological Chemistry* **275,** 40788–40796. doi:`10.1074/jbc.M006114200` (Dec. 2000).
196. Mukherjee, A. *et al.* FSTL3 Deletion Reveals Roles for TGF-beta Family Ligands in Glucose and Fat Homeostasis in Adults. *Proceedings of the National Academy of Sciences of the United States of America* **104,** 1348–1353. doi:`10.1073/pnas.0607966104` (Jan. 2007).
197. Bartholin, L. *et al.* FLRG, a New ADAM12-associated Protein, Modulates Osteoclast Differentiation. *Biology of the Cell* **97,** 577–588. doi:`10.1042/BC20040506` (2005).
198. Robling, A. G. *et al.* Mechanical Stimulation of Bone in Vivo Reduces Osteocyte Expression of Sost/Sclerostin. *Journal of Biological Chemistry* **283,** 5866–5875. doi:`10.1074/jbc.M705092200` (Feb. 2008).
199. Shimano, M. *et al.* Cardiac Myocyte-Specific Ablation of Follistatin-like 3 Attenuates Stress-Induced Myocardial Hypertrophy. *The Journal of Biological Chemistry* **286,** 9840–9848. doi:`10.1074/jbc.M110.197079` (Mar. 2011).
200. Panse, K. D. *et al.* Follistatin-like 3 Mediates Paracrine Fibroblast Activation by Cardiomyocytes. *Journal of Cardiovascular Translational Research* **5,** 814–826. doi:`10.1007/s12265-012-9400-9` (Dec. 2012).
201. Runhua, M., Qiang, J., Yunqing, S., Wenjun, D. & Chunsheng, W. FSTL3 Induces Lipid Accumulation and Inflammatory Response in Macrophages and Associates With Atherosclerosis. *Journal of Cardiovascular Pharmacology* **74,** 566. doi:`10.1097/FJC.0000000000000742` (Dec. 2019).
202. Polyzos, S. A. *et al.* Targeted Analysis of Three Hormonal Systems Identifies Molecules Associated with the Presence and Severity of NAFLD. *The Journal of Clinical Endocrinology and Metabolism* **105,** dgz172. doi:`10.1210/clinem/dgz172` (Mar. 2020).
203. Ungerleider, N. A., Bonomi, L. M., Brown, M. L. & Schneyer, A. L. Increased Activin Bioavailability Enhances Hepatic Insulin Sensitivity While Inducing Hepatic Steatosis in Male Mice. *Endocrinology* **154,** 2025–2033. doi:`10.1210/en.2012-1844` (June 2013).
204. Brandt, C. *et al.* Over-Expression of Follistatin-like 3 Attenuates Fat Accumulation and Improves Insulin Sensitivity in Mice. *Metabolism: Clinical and Experimental* **64,** 283–295. doi:`10.1016/j.metabol.2014.10.007` (Feb. 2015).
205. Xu, X.-Y. *et al.* Targeting Follistatin like 1 Ameliorates Liver Fibrosis Induced by Carbon Tetrachloride through TGF-β1-miR29a in Mice. *Cell communication and signaling: CCS* **18,** 151. doi:`10.1186/s12964-020-00610-0` (Sept. 2020).

206. Rao, J. *et al.* FSTL1 Promotes Liver Fibrosis by Reprogramming Macrophage Function through Modulating the Intracellular Function of PKM2. *Gut,* gutjnl–2021–325150. doi:`10.1136/gutjnl-2021-325150` (Feb. 2022).
207. Ohnishi, N. *et al.* Activin A Is an Autocrine Activator of Rat Pancreatic Stellate Cells: Potential Therapeutic Role of Follistatin for Pancreatic Fibrosis. *Gut* **52,** 1487–1493. doi:`10.1136/gut.52.10.1487` (Oct. 2003).
208. Wada, W., Kuwano, H., Hasegawa, Y. & Kojima, I. The Dependence of Transforming Growth Factor-β-Induced Collagen Production on Autocrine Factor Activin A in Hepatic Stellate Cells. *Endocrinology* **145,** 2753–2759. doi:`10.1210/en.2003-1663` (June 2004).
209. Kiagiadaki, F. *et al.* Activin-A Causes Hepatic Stellate Cell Activation via the Induction of TNFα and TGFβ in Kupffer Cells. *Biochimica et Biophysica Acta (BBA) - Molecular Basis of Disease* **1864,** 891–899. doi:`10.1016/j.bbadis.2017.12.031` (Mar. 2018).
210. Yoong, K. F., McNab, G., Hübscher, S. G. & Adams, D. H. Vascular Adhesion Protein-1 and ICAM-1 Support the Adhesion of Tumor-Infiltrating Lymphocytes to Tumor Endothelium in Human Hepatocellular Carcinoma. *The Journal of Immunology* **160,** 3978–3988 (Apr. 1998).
211. Harris, R. & Ukaejiofo, E. O. Tissue Typing Using a Routine One-Step Lymphocyte Separation Procedure. *British Journal of Haematology* **18,** 229–236. doi:`10.1111/j.1365-2141.1970.tb01436.x` (1970).
212. Cazenave, J. P. *et al.* Preparation of Washed Platelet Suspensions from Human and Rodent Blood. *Methods in molecular biology (Clifton, N.J.)* **272,** 13–28. doi:`10.1385/1-59259-782-3:013`. PMID: `15226531` (2004).
213. Paish, H. L. *et al.* A Bioreactor Technology for Modeling Fibrosis in Human and Rodent Precision-Cut Liver Slices. *Hepatology* **70,** 1377–1391. doi:`10.1002/hep.30651` (2019).
214. Tiscornia, G., Singer, O. & Verma, I. M. Production and Purification of Lentiviral Vectors. *Nature Protocols* **1,** 241–245. doi:`10.1038/nprot.2006.37` (June 2006).
215. Shetty, S., Weston, C. J., Adams, D. H. & Lalor, P. F. A Flow Adhesion Assay to Study Leucocyte Recruitment to Human Hepatic Sinusoidal Endothelium under Conditions of Shear Stress. *Journal of Visualized Experiments.* doi:`10.3791/51330` (Mar. 2014).
216. Tickle, J. *The Role of Vascular Adhesion Protein (VAP)-1 during Inflammatory Liver Disease* PhD thesis (University of Birmingham, 2018).
217. Bell, E, Ivarsson, B & Merrill, C. Production of a Tissue-like Structure by Contraction of Collagen Lattices by Human Fibroblasts of Different Proliferative Potential in Vitro. | PNAS. *Proceedings of the National Academy of Sciences of the United States of America* **76,** 1274–1278. doi:`10.1073/pnas.76.3.1274` (Mar. 1979).
218. Lampugnani, M. G. in *Adhesion Protein Protocols* (eds Dejana, E. & Corada, M.) 177–182 (Humana Press, Totowa, NJ, 1999). doi:`10.1385/1-59259-258-9:177`.

219. Suarez-Arnedo, A. *et al.* An Image J Plugin for the High Throughput Image Analysis of in Vitro Scratch Wound Healing Assays. *PLoS ONE* **15.** doi:`10.1371/journal.pone.0232565` (July 2020).
220. Horn, P. *et al. Evaluation of Gremlin-1 as a Therapeutic Target in Metabolic Dysfunction-Associated Steatohepatitis* Jan. 2024. doi:`10.1101/2024.01.03.574043`. (Mar. 6, 2024).
221. Ritz, C., Baty, F., Streibig, J. C. & Gerhard, D. Dose-Response Analysis Using R. *PLOS ONE* **10,** e0146021. doi:`10.1371/journal.pone.0146021` (Dec. 2015).
222. Livak, K. J. & Schmittgen, T. D. Analysis of Relative Gene Expression Data Using Real-Time Quantitative PCR and the 2-$\Delta\Delta$CT Method. *Methods* **25,** 402–408. doi:`10.1006/meth.2001.1262` (Dec. 2001).
223. Andersen, C. L., Jensen, J. L. & Ørntoft, T. F. Normalization of Real-Time Quantitative Reverse Transcription-PCR Data: A Model-Based Variance Estimation Approach to Identify Genes Suited for Normalization, Applied to Bladder and Colon Cancer Data Sets. *Cancer Research* **64,** 5245–5250. doi:`10.1158/0008-5472.CAN-04-0496` (Aug. 2004).
224. Vandesompele, J. *et al.* Accurate Normalization of Real-Time Quantitative RT-PCR Data by Geometric Averaging of Multiple Internal Control Genes. *Genome biology* **3,** research0034.1–research0034.11. doi:`10.1186/gb-2002-3-7-research0034` (2002).
225. Barrett, T. *et al.* NCBI GEO: Archive for Functional Genomics Data Sets - Update. *Nucleic Acids Research* **41,** D991–D995. doi:`10.1093/nar/gks1193` (Jan. 2013).
226. Harrison, P. W. *et al.* The European Nucleotide Archive in 2020. *Nucleic Acids Research* **49,** D82–D85. doi:`10.1093/nar/gkaa1028` (Jan. 2021).
227. Athar, A. *et al.* ArrayExpress Update - From Bulk to Single-Cell Expression Data. *Nucleic Acids Research* **47,** D711–D715. doi:`10.1093/nar/gky964` (Jan. 2019).
228. Afgan, E. *et al.* The Galaxy Platform for Accessible, Reproducible and Collaborative Biomedical Analyses: 2016 Update. *Nucleic acids research* **44,** W3–W10. doi:`10.1093/nar/gkw343` (July 2016).
229. Chen, S., Zhou, Y., Chen, Y. & Gu, J. *Fastp: An Ultra-Fast All-in-One FASTQ Preprocessor* in *Bioinformatics* **34** (Oxford University Press, Sept. 2018), i884–i890. doi:`10.1093/bioinformatics/bty560`.
230. Patro, R., Duggal, G., Love, M. I., Irizarry, R. A. & Kingsford, C. Salmon Provides Fast and Bias-Aware Quantification of Transcript Expression. *Nature Methods* **14,** 417–419. doi:`10.1038/nmeth.4197` (Mar. 2017).
231. Soneson, C., Love, M. I. & Robinson, M. D. Differential Analyses for RNA-seq: Transcript-level Estimates Improve Gene-Level Inferences [Version 2; Referees: 2 Approved]. *F1000Research* **4,** 1521. doi:`10.12688/F1000RESEARCH.7563.2` (Feb. 2016).
232. Love, M. I., Huber, W. & Anders, S. Moderated Estimation of Fold Change and Dispersion for RNA-seq Data with DESeq2. *Genome Biology* **15,** 550. doi:`10.1186/s13059-014-0550-8` (Dec. 2014).

233. *Liver Cell Atlas* https://www.livercellatlas.org/umap-humanAll.php. (June 19, 2023).
234. Lun, A. T., McCarthy, D. J. & Marioni, J. C. A Step-by-Step Workflow for Low-Level Analysis of Single-Cell RNA-seq Data with Bioconductor. *F1000Research* **5.** doi:`10.12688/f1000research.9501.2` (2016).
235. McGinnis, C. S., Murrow, L. M. & Gartner, Z. J. DoubletFinder: Doublet Detection in Single-Cell RNA Sequencing Data Using Artificial Nearest Neighbors. *Cell Systems* **8,** 329–337.e4. doi:`10.1016/j.cels.2019.03.003` (Apr. 2019).
236. Hao, Y. *et al.* Integrated Analysis of Multimodal Single-Cell Data. *Cell* **184,** 3573–3587.e29. doi:`10.1016/j.cell.2021.04.048` (June 2021).
237. Kim, M. *et al.* Gremlin-1 Induces BMP-independent Tumor Cell Proliferation, Migration, and Invasion. *PLoS ONE* **7,** e35100. doi:`10.1371/journal.pone.0035100` (Apr. 2012).
238. Grillo, E. *et al.* Role of Gremlin-1 in the Pathophysiology of the Adipose Tissues. *Cytokine & Growth Factor Reviews* **69,** 51–60. doi:`10.1016/j.cytogfr.2022.09.004` (Feb. 2023).
239. Duffy, L. *et al.* Bone Morphogenetic Protein Antagonist Gremlin-1 Increases Myofibroblast Transition in Dermal Fibroblasts: Implications for Systemic Sclerosis. *Frontiers in Cell and Developmental Biology* **9.** doi:`10.3389/fcell.2021.681061` (2021).
240. Elemam, N. M., Malek, A. I., Mahmoud, E. E., El-Huneidi, W. & Talaat, I. M. Insights into the Role of Gremlin-1, a Bone Morphogenic Protein Antagonist, in Cancer Initiation and Progression. *Biomedicines* **10,** 301. doi:`10.3390/biomedicines10020301` (Feb. 2022).
241. Yovchev, M. I., Zhang, J., Neufeld, D. S., Grozdanov, P. N. & Dabeva, M. D. Thymus Cell Antigen-1-Expressing Cells in the Oval Cell Compartment. *Hepatology* **50,** 601–611. doi:`10.1002/hep.23012` (2009).
242. Liu, D. *et al.* Identification and Characterization of Mesenchymal-Epithelial Progenitor-Like Cells in Normal and Injured Rat Liver. *The American Journal of Pathology* **185,** 110–128. doi:`10.1016/j.ajpath.2014.08.029` (Jan. 2015).
243. Katsumata, L. W., Miyajima, A. & Itoh, T. Portal Fibroblasts Marked by the Surface Antigen Thy1 Contribute to Fibrosis in Mouse Models of Cholestatic Liver Injury. *Hepatology Communications* **1,** 198–214. doi:`10.1002/hep4.1023` (May 2017).
244. Nishio, T. *et al.* Activated Hepatic Stellate Cells and Portal Fibroblasts Contribute to Cholestatic Liver Fibrosis in MDR2 Knockout Mice. *Journal of Hepatology* **71,** 573–585. doi:`10.1016/j.jhep.2019.04.012` (Sept. 2019).
245. Isabel, Z. *et al.* Isolation, Characterization and Culture of Thy1-positive Cells from Fetal Rat Livers. *World Journal of Gastroenterology : WJG* **12,** 3841–3847. doi:`10.3748/wjg.v12.i24.3841` (June 2006).

246. *Tissue Cell Type - COL3A1 - The Human Protein Atlas* https://www.proteinatlas.org/ENSG00000168542-COL3A1/tissue+cell+type. (July 11, 2023).
247. Engelmann, C., Clària, J., Szabo, G., Bosch, J. & Bernardi, M. Pathophysiology of Decompensated Cirrhosis: Portal Hypertension, Circulatory Dysfunction, Inflammation, Metabolism and Mitochondrial Dysfunction. *Journal of Hepatology. New Concepts and Perspectives in Decompensated Cirrhosis* **75,** S49–S66. doi:`10.1016/j.jhep.2021.01.002`. (Mar. 11, 2024) (July 2021).
248. Ginès, P. *et al.* Liver Cirrhosis. *The Lancet* **398,** 1359–1376. doi:`10.1016/S0140-6736(21)01374-X`. (Mar. 11, 2024) (Oct. 2021).
249. Sato, K. *et al.* Ductular Reaction in Liver Diseases: Pathological Mechanisms and Translational Significances. *Hepatology* **69,** 420. doi:`10.1002/hep.30150`. (Mar. 4, 2024) (Jan. 2019).
250. Orlando, C., Pinzani, P. & Pazzagli, M. Developments in Quantitative PCR. **36,** 255–269. doi:`10.1515/CCLM.1998.045` (May 1998).
251. Wang, S. *et al.* Up-Regulation of BMP-2 Antagonizes TGF-β1/ROCK-enhanced Cardiac Fibrotic Signalling through Activation of Smurf1/Smad6 Complex. *Journal of Cellular and Molecular Medicine* **16,** 2301–2310. doi:`10.1111/j.1582-4934.2012.01538.x` (Oct. 2012).
252. Wang, Z., Gerstein, M. & Snyder, M. RNA-Seq: A Revolutionary Tool for Transcriptomics. *Nature reviews. Genetics* **10,** 57–63. doi:`10.1038/nrg2484` (Jan. 2009).
253. Sims, D., Sudbery, I., Ilott, N. E., Heger, A. & Ponting, C. P. Sequencing Depth and Coverage: Key Considerations in Genomic Analyses. *Nature Reviews Genetics* **15,** 121–132. doi:`10.1038/nrg3642` (Feb. 2014).
254. Papalexi, E. & Satija, R. Single-Cell RNA Sequencing to Explore Immune Cell Heterogeneity. *Nature Reviews Immunology* **18,** 35–45. doi:`10.1038/nri.2017.76` (Jan. 2018).
255. Corchete, L. A. *et al.* Systematic Comparison and Assessment of RNA-seq Procedures for Gene Expression Quantitative Analysis. *Scientific Reports* **10,** 19737. doi:`10.1038/s41598-020-76881-x` (Nov. 2020).
256. O'Reilly, S. Gremlin: A Complex Molecule Regulating Wound Healing and Fibrosis. *Cellular and Molecular Life Sciences* **78,** 7917–7923. doi:`10.1007/s00018-021-03964-x` (Dec. 2021).
257. Al Ojaimi, Y. *et al.* Therapeutic Antibodies – Natural and Pathological Barriers and Strategies to Overcome Them. *Pharmacology & Therapeutics* **233,** 108022. doi:`10.1016/j.pharmthera.2021.108022` (May 2022).
258. Nishio, T. *et al.* The Role of Mesothelin in Activation of Portal Fibroblasts in Cholestatic Liver Injury. *Biology* **11,** 1589. doi:`10.3390/biology11111589` (Nov. 2022).
259. Yang, W. *et al.* Single-Cell Transcriptomic Analysis Reveals a Hepatic Stellate Cell-Activation Roadmap and Myofibroblast Origin During Liver Fibrosis in Mice.

Hepatology (Baltimore, Md.) **74,** 2774–2790. doi:`10.1002/hep.31987` (Nov. 2021).

260. Gastaldelli, A. & Cusi, K. From NASH to Diabetes and from Diabetes to NASH: Mechanisms and Treatment Options. *JHEP Reports* **1,** 312–328. doi:`10.1016/j.jhepr.2019.07.002` (Oct. 2019).
261. Tilg, H. & Moschen, A. R. Adipocytokines: Mediators Linking Adipose Tissue, Inflammation and Immunity. *Nature Reviews Immunology* **6,** 772–783. doi:`10.1038/nri1937` (Oct. 2006).
262. Yang, W. *et al.* Single-cell Transcriptomic Analysis Reveals a Hepatic Stellate Cell-activation Roadmap and Myofibroblast Origin during Liver Fibrosis. *Hepatology* **74,** 2774–2790. doi:`10.1002/hep.31987` (June 2021).
263. Suriguga, S. *et al.* Distinct Responses between Healthy and Cirrhotic Human Livers upon Lipopolysaccharide Challenge: Possible Implications for Acute-on-Chronic Liver Failure. *American Journal of Physiology-Gastrointestinal and Liver Physiology* **323,** G114–G125. doi:`10.1152/ajpgi.00243.2021` (Aug. 2022).
264. Chen, W. *et al.* Lysyl Oxidase (LOX) Family Members: Rationale and Their Potential as Therapeutic Targets for Liver Fibrosis. *Hepatology* **72,** 729–741. doi:`10.1002/hep.31236` (2020).
265. Sethi, A., Wordinger, R. J. & Clark, A. F. Gremlin Utilizes Canonical and Non-Canonical TGFβ Signaling to Induce Lysyl Oxidase (LOX) Genes in Human Trabecular Meshwork Cells. *Experimental Eye Research* **113,** 117–127. doi:`10.1016/j.exer.2013.05.011` (2013).
266. Liu, F. *et al.* A Human Mad Protein Acting as a BMP-regulated Transcriptional Activator. *Nature* **381,** 620–623. doi:`10.1038/381620a0` (June 1996).
267. Imamura, T. *et al.* Smad6 Inhibits Signalling by the TGF-β Superfamily. *Nature* **389,** 622–626. doi:`10.1038/39355` (Oct. 1997).
268. Afrakhte, M. *et al.* Induction of Inhibitory Smad6 and Smad7 mRNA by TGF-β Family Members. *Biochemical and Biophysical Research Communications* **249,** 505–511. doi:`10.1006/bbrc.1998.9170` (Aug. 1998).
269. Bloise, E. *et al.* Activin A in Mammalian Physiology. *Physiological Reviews* **99,** 739–780. doi:`10.1152/physrev.00002.2018` (Jan. 2019).
270. Meunier, H, Rivier, C, Evans, R. M. & Vale, W. Gonadal and Extragonadal Expression of Inhibin Alpha, Beta A, and Beta B Subunits in Various Tissues Predicts Diverse Functions. *Proceedings of the National Academy of Sciences* **85,** 247–251. doi:`10.1073/pnas.85.1.247` (Jan. 1988).
271. Tuuri, T., Erämaa, M., Hildén, K. & Ritvos, O. The Tissue Distribution of Activin Beta A- and Beta B-subunit and Follistatin Messenger Ribonucleic Acids Suggests Multiple Sites of Action for the Activin-Follistatin System during Human Development. *The Journal of Clinical Endocrinology and Metabolism* **78,** 1521–1524. doi:`10.1210/jcem.78.6.8200957` (June 1994).

272. Frost, K. *et al.* Inhibin/Activin Expression in Human and Rodent Liver: Subunits α and βB as New Players in Human Hepatocellular Carcinoma? *British Journal of Cancer* **104,** 1303–1312. doi:`10.1038/bjc.2011.53` (Apr. 2011).
273. Zhu, A., Ibrahim, J. G. & Love, M. I. Heavy-Tailed Prior Distributions for Sequence Count Data: Removing the Noise and Preserving Large Differences. *Bioinformatics* **35,** 2084–2092. doi:`10.1093/bioinformatics/bty895`. (Mar. 11, 2024) (June 2019).
274. Shahidi, R. K. *et al.* Adult Mice Are Unresponsive to AAV8-Gremlin1 Gene Therapy Targeting the Liver. *PLOS ONE* **16,** e0247300. doi:`10.1371/journal.pone.0247300` (Feb. 2021).
275. Rider, C. C. & Mulloy, B. Heparin, Heparan Sulphate and the TGF- Cytokine Superfamily. *Molecules* **22.** doi:`10.3390/molecules22050713` (2017).
276. McNamee, N., Daly, R., Crown, J. & O'Driscoll, L. A Method of Separating Extracellular Vesicles from Blood Shows Potential Clinical Translation, and Reveals Extracellular Vesicle Cargo Gremlin-1 as a Diagnostic Biomarker. *Translational Oncology* **15,** 101274. doi:`10.1016/j.tranon.2021.101274` (Jan. 2022).
277. Corsini, M. *et al.* Cyclic Adenosine Monophosphate-Response Element-Binding Protein Mediates the Proangiogenic or Proinflammatory Activity of Gremlin. *Arteriosclerosis, Thrombosis, and Vascular Biology* **34,** 136–145. doi:`10.1161/ATVBAHA.113.302517`. PMID: `24233491` (Jan. 2014).
278. Müller, I. I. *et al.* Gremlin-1 Inhibits Macrophage Migration Inhibitory Factor-Dependent Monocyte Function and Survival. *International Journal of Cardiology* **176,** 923–929. doi:`10.1016/j.ijcard.2014.08.051` (Oct. 2014).
279. Müller, I. *et al.* Gremlin-1 Is an Inhibitor of Macrophage Migration Inhibitory Factor and Attenuates Atherosclerotic Plaque Growth in ApoE-/- Mice. *Journal of Biological Chemistry* **288,** 31635–31645. doi:`10.1074/jbc.M113.477745` (2013).
280. Kalén, A., Wahlström, O., Linder, C. H. & Magnusson, P. The Content of Bone Morphogenetic Proteins in Platelets Varies Greatly between Different Platelet Donors. *Biochemical and Biophysical Research Communications* **375,** 261–264. doi:`10.1016/j.bbrc.2008.08.014`. PMID: `18706392` (Oct. 2008).
281. Wahlström, O., Linder, C., Kalén, A. & Magnusson, P. Acidic Preparations of Platelet Concentrates Release Bone Morphogenetic Protein-2. *Acta Orthopaedica* **79,** 433–437. doi:`10.1080/17453670710015364`. PMID: `18626808` (June 2008).
282. Vinholt, P. J., Hvas, A.-M. & Nybo, M. An Overview of Platelet Indices and Methods for Evaluating Platelet Function in Thrombocytopenic Patients. *European Journal of Haematology* **92,** 367–376. doi:`10.1111/ejh.12262` (2014).
283. Kang, J. H. *et al.* Cell-Penetrating Peptides Selectively Targeting SMAD3 Inhibit Profibrotic TGF-β Signaling. *Journal of Clinical Investigation* **127,** 2541–2554. doi:`10.1172/JCI88696` (June 2017).

284. *GEO Accession Viewer* https://www.ncbi.nlm.nih.gov/geo/query/acc.cgi?acc=GSE100382. (July 20, 2023).
285. Gupta, S. *et al.* Novel Combination BMP7 and HGF Gene Therapy Instigates Selective Myofibroblast Apoptosis and Reduces Corneal Haze in Vivo. *Investigative Ophthalmology and Visual Science* **59,** 1045–1057. doi:`10.1167/iovs.17-23308` (Feb. 2018).
286. Managò, A. *et al.* Extracellular Nicotinate Phosphoribosyltransferase Binds Toll like Receptor 4 and Mediates Inflammation. *Nature Communications* **10,** 4116. doi:`10.1038/s41467-019-12055-2` (Sept. 2019).
287. Jayme, T. S. *et al.* Human Interleukin-4–Treated Regulatory Macrophages Promote Epithelial Wound Healing and Reduce Colitis in a Mouse Model. *Science Advances* **6,** eaba4376. doi:`10.1126/sciadv.aba4376` (June 2020).
288. Gurvich, O. L. *et al.* Transcriptomics Uncovers Substantial Variability Associated with Alterations in Manufacturing Processes of Macrophage Cell Therapy Products. *Scientific Reports* **10,** 14049. doi:`10.1038/s41598-020-70967-2` (Aug. 2020).
289. Vishnyakova, P. *et al.* The Response of Two Polar Monocyte Subsets to Inflammation. *Biomedicine & Pharmacotherapy* **139,** 111614. doi:`10.1016/j.biopha.2021.111614` (July 2021).
290. Seki, E. & Schwabe, R. F. Hepatic Inflammation and Fibrosis: Functional Links and Key Pathways. *Hepatology* **61,** 1066. doi:`10.1002/hep.27332` (Feb. 2015).
291. de Jesus, D. S. *et al.* Nox1/Ref-1-mediated Activation of CREB Promotes Gremlin1-driven Endothelial Cell Proliferation and Migration. *Redox Biology* **22,** 101138. doi:`10.1016/j.redox.2019.101138` (Apr. 2019).
292. Lavoz, C. *et al.* Gremlin Regulates Renal Inflammation via the Vascular Endothelial Growth Factor Receptor 2 Pathway. *Journal of Pathology* **236,** 407–420. doi:`10.1002/path.4537` (Aug. 2015).
293. Zuo, W. H. *et al.* Promotive Effects of Bone Morphogenetic Protein 2 on Angiogenesis in Hepatocarcinoma via Multiple Signal Pathways. *Scientific Reports* **6.** doi:`10.1038/srep37499` (Nov. 2016).
294. Sato, A. Y. S., Bub, G. L. & Campos, A. H. BMP-2 and -4 Produced by Vascular Smooth Muscle Cells from Atherosclerotic Lesions Induce Monocyte Chemotaxis through Direct BMPRII Activation. *Atherosclerosis* **235,** 45–55. doi:`10.1016/j.atherosclerosis.2014.03.030` (July 2014).
295. Dutton, L. R., O'Neill, C. L., Medina, R. J. & Brazil, D. P. No Evidence of Gremlin1-mediated Activation of VEGFR2 Signaling in Endothelial Cells. *The Journal of Biological Chemistry* **294,** 18041–18045. doi:`10.1074/jbc.AC119.010148` (Nov. 2019).
296. Davì, G. & Patrono, C. Platelet Activation and Atherothrombosis. *New England Journal of Medicine* **357,** 2482–2494. doi:`10.1056/NEJMra071014` (Dec. 2007).

297. Brass, L. F., Newman, D. K., Wannermacher, K. M., Zhu, L. & Stalker, T. J. in *Platelets (Third Edition)* (ed Michelson, A. D.) 367–398 (Academic Press, Jan. 2013). doi:`10.1016/B978-0-12-387837-3.00019-5`.
298. Golebiewska, E. M. & Poole, A. W. Platelet Secretion: From Haemostasis to Wound Healing and Beyond. *Blood Reviews* **29,** 153–162. doi:`10.1016/j.blre.2014.10.003` (May 2015).
299. Mthunzi, L., Knaus, U. & McLoughlin, P. Macrophages Increase the Bone Morphogenetic Protein Antagonist Gremlin-1 in Response to Hypoxia. *AMERICAN JOURNAL OF RESPIRATORY AND CRITICAL CARE MEDICINE* **197** (2018).
300. Rocher, C. & Singla, D. K. SMAD-PI3K-Akt-mTOR Pathway Mediates BMP-7 Polarization of Monocytes into M2 Macrophages. *PLOS ONE* **8,** e84009. doi:`10.1371/journal.pone.0084009` (Dec. 2013).
301. Martínez, V. G. *et al.* BMP4 Induces M2 Macrophage Polarization and Favors Tumor Progression in Bladder Cancer. *Clinical Cancer Research* **23,** 7388–7399. doi:`10.1158/1078-0432.CCR-17-1004` (Nov. 2017).
302. Ryaboshapkina, M. & Hammar, M. Human Hepatic Gene Expression Signature of Non-Alcoholic Fatty Liver Disease Progression, a Meta-Analysis. *Scientific Reports* **7,** 12361. doi:`10.1038/s41598-017-10930-w` (Sept. 2017).
303. Hasin-Brumshtein, Y., Sakaram, S., Khatri, P., He, Y. D. & Sweeney, T. E. A Robust Gene Expression Signature for NASH in Liver Expression Data. *Scientific Reports* **12,** 2571. doi:`10.1038/s41598-022-06512-0` (Feb. 2022).
304. Ahrens, M. *et al.* DNA Methylation Analysis in Nonalcoholic Fatty Liver Disease Suggests Distinct Disease-Specific and Remodeling Signatures after Bariatric Surgery. *Cell Metabolism* **18,** 296–302. doi:`10.1016/j.cmet.2013.07.004` (Aug. 2013).
305. Hoang, S. A. *et al.* Gene Expression Predicts Histological Severity and Reveals Distinct Molecular Profiles of Nonalcoholic Fatty Liver Disease. *Scientific Reports* **9,** 12541. doi:`10.1038/s41598-019-48746-5` (Aug. 2019).
306. Tasaki, S. *et al.* Multiomic Disease Signatures Converge to Cytotoxic CD8 T Cells in Primary Sjögren's Syndrome. *Annals of the Rheumatic Diseases* **76,** 1458–1466. doi:`10.1136/annrheumdis-2016-210788` (Aug. 2017).
307. Ramnath, D. *et al.* Hepatic Expression Profiling Identifies Steatosis-Independent and Steatosis-Driven Advanced Fibrosis Genes. *JCI Insight* **3.** doi:`10.1172/jci.insight.120274` (July 2018).
308. Fabre, T. *et al.* Type 3 Cytokines IL-17A and IL-22 Drive TGF-β–Dependent Liver Fibrosis. *Science Immunology* **3,** eaar7754. doi:`10.1126/sciimmunol.aar7754` (Oct. 2018).
309. Martin-Mateos, R. *et al.* Enhancer of Zeste Homologue 2 Inhibition Attenuates TGF-β Dependent Hepatic Stellate Cell Activation and Liver Fibrosis. *Cellular and Molecular Gastroenterology and Hepatology* **7,** 197–209. doi:`10.1016/j.jcmgh.2018.09.005` (Jan. 2019).

310. Wang, Y. *et al.* P300 Acetyltransferase Is a Cytoplasm-to-Nucleus Shuttle for SMAD2/3 and TAZ Nuclear Transport in Transforming Growth Factor β–Stimulated Hepatic Stellate Cells. *Hepatology* **70,** 1409–1423. doi:`10.1002/hep.30668` (Oct. 2019).
311. Widjaja, A. A. *et al.* Inhibiting Interleukin 11 Signaling Reduces Hepatocyte Death and Liver Fibrosis, Inflammation, and Steatosis in Mouse Models of Nonalcoholic Steatohepatitis. *Gastroenterology* **157,** 777–792.e14. doi:`10.1053/j.gastro.2019.05.002` (Sept. 2019).
312. Matsui, H. *et al.* Sulfur-Containing Amino Acids Attenuate the Development of Liver Fibrosis in Rats through down-Regulation of Stellate Cell Activation. *Journal of Hepatology* **40,** 917–925. doi:`10.1016/j.jhep.2004.02.011` (June 2004).
313. Itagaki, H., Shimizu, K., Morikawa, S., Ogawa, K. & Ezaki, T. Morphological and Functional Characterization of Non-Alcoholic Fatty Liver Disease Induced by a Methionine-Choline-Deficient Diet in C57BL/6 Mice. *International Journal of Clinical and Experimental Pathology* **6,** 2683–2696 (Nov. 2013).
314. Lebeaupin, C. *et al.* Endoplasmic Reticulum Stress Signalling and the Pathogenesis of Non-Alcoholic Fatty Liver Disease. *Journal of Hepatology* **69,** 927–947. doi:`10.1016/j.jhep.2018.06.008` (Oct. 2018).
315. Grootjans, J., Kaser, A., Kaufman, R. J. & Blumberg, R. S. The Unfolded Protein Response in Immunity and Inflammation. *Nature reviews. Immunology* **16,** 469–484. doi:`10.1038/nri.2016.62` (Aug. 2016).
316. Hernández-Gea, V. *et al.* Endoplasmic Reticulum Stress Induces Fibrogenic Activity in Hepatic Stellate Cells through Autophagy. *Journal of Hepatology* **59,** 98–104. doi:`10.1016/j.jhep.2013.02.016` (July 2013).
317. Koo, J. H., Lee, H. J., Kim, W. & Kim, S. G. Endoplasmic Reticulum Stress in Hepatic Stellate Cells Promotes Liver Fibrosis via PERK-Mediated Degradation of HNRNPA1 and Up-regulation of SMAD2. *Gastroenterology* **150,** 181–193.e8. doi:`10.1053/j.gastro.2015.09.039` (Jan. 2016).
318. Chen, W. *et al.* Multitranscriptome Analyses Reveal Prioritized Genes Specifically Associated with Liver Fibrosis Progression Independent of Etiology. *American Journal of Physiology-Gastrointestinal and Liver Physiology* **316,** G744–G754. doi:`10.1152/ajpgi.00339.2018` (June 2019).
319. Liu, Z. *et al.* Causal Relationships between NAFLD, T2D and Obesity Have Implications for Disease Subphenotyping. *Journal of Hepatology* **0.** doi:`10.1016/j.jhep.2020.03.006` (Mar. 2020).
320. Koyama, Y. *et al.* Mesothelin/Mucin 16 Signaling in Activated Portal Fibroblasts Regulates Cholestatic Liver Fibrosis. *The Journal of Clinical Investigation* **127,** 1254–1270. doi:`10.1172/JCI88845` (Apr. 2017).
321. Wang, L. *et al.* Intrahepatic Angiogenesis Increases Portal Hypertension in Hepatitis B Patients with Cirrhosis. *Hepatology Research* **47,** E94–E103. doi:`10.1111/hepr.12732` (Mar. 2017).

322. Ghosh, A. K. & Vaughan, D. E. PAI-1 in Tissue Fibrosis. *Journal of Cellular Physiology* **227,** 493–507. doi:`10.1002/jcp.22783` (2012).
323. Wang, H., Zhang, Y. & Heuckeroth, R. O. PAI-1 Deficiency Reduces Liver Fibrosis after Bile Duct Ligation in Mice through Activation of tPA. *FEBS Letters* **581,** 3098–3104. doi:`10.1016/j.febslet.2007.05.049` (2007).
324. Hu, P.-F. *et al.* Adenovirus-Mediated Transfer of siRNA against PAI-1 mRNA Ameliorates Hepatic Fibrosis in Rats. *Journal of Hepatology* **51,** 102–113. doi:`10.1016/j.jhep.2009.02.025` (July 2009).
325. Cochet-Bissuel, M., Lory, P. & Monteil, A. The Sodium Leak Channel, NALCN, in Health and Disease. *Frontiers in Cellular Neuroscience* **8** (2014).
326. Chen, H.-Q. *et al.* Gene Expression Network Regulated by DNA Methylation and microRNA during Microcystin-Leucine Arginine Induced Malignant Transformation in Human Hepatocyte L02 Cells. *Toxicology Letters* **289,** 42–53. doi:`10.1016/j.toxlet.2018.03.003` (June 2018).
327. Park, Y.-Y. *et al.* TARDBP Regulates Glycolysis in Hepatocellular Carcinoma by Regulating PFKP through miR-520. *Hepatology (Baltimore, Md.)* **58,** 182–191. doi:`10.1002/hep.26310` (July 2013).
328. Klagsbrun, M. & Eichmann, A. A Role for Axon Guidance Receptors and Ligands in Blood Vessel Development and Tumor Angiogenesis. *Cytokine & Growth Factor Reviews* **16,** 535–548. doi:`10.1016/j.cytogfr.2005.05.002` (Aug. 2005).
329. König, K. *et al.* The Uncoordinated-5 Homolog B Receptor Affects Hepatic Ischemia Reperfusion Injury. *PLOS ONE* **7,** e41085. doi:`10.1371/journal.pone.0041085` (July 2012).
330. Choi, S. W. *et al.* Netrin-1 Attenuates Hepatic Steatosis via UNC5b/PPARγ-mediated Suppression of Inflammation and ER Stress. *Life Sciences* **311,** 121149. doi:`10.1016/j.lfs.2022.121149` (Dec. 2022).
331. Hill, J. J. *et al.* The Myostatin Propeptide and the Follistatin-related Gene Are Inhibitory Binding Proteins of Myostatin in Normal Serum *. *Journal of Biological Chemistry* **277,** 40735–40741. doi:`10.1074/jbc.M206379200` (Oct. 2002).
332. Artaza, J. N. *et al.* Myostatin Promotes a Fibrotic Phenotypic Switch in Multipotent C3H 10T1/2 Cells without Affecting Their Differentiation into Myofibroblasts. *Journal of Endocrinology* **196,** 235–249. doi:`10.1677/JOE-07-0408` (Feb. 2008).
333. Delogu, W. *et al.* Myostatin Regulates the Fibrogenic Phenotype of Hepatic Stellate Cells via C-Jun N-terminal Kinase Activation. *Digestive and Liver Disease* **51,** 1400–1408. doi:`10.1016/j.dld.2019.03.002` (Oct. 2019).
334. Schneyer, A., Schoen, A., Quigg, A. & Sidis, Y. Differential Binding and Neutralization of Activins A and B by Follistatin and Follistatin Like-3 (FSTL-3/FSRP/FLRG). *Endocrinology* **144,** 1671–1674. doi:`10.1210/en.2002-0203` (May 2003).

335. Liu, H. *et al.* Beneficial Effects of Moderate Hepatic Activin A Expression on Metabolic Pathways, Inflammation, and Atherosclerosis. *Arteriosclerosis, Thrombosis, and Vascular Biology* **43,** 330–349. doi:`10.1161/ATVBAHA.122.318138` (Feb. 2023).
336. *Liver Disease App* https://saezlab.shinyapps.io/liverdiseaseatlas/. Sept. 2023.
337. Houten, S. M., Violante, S., Ventura, F. V. & Wanders, R. J. The Biochemistry and Physiology of Mitochondrial Fatty Acid β-Oxidation and Its Genetic Disorders. *Annual Review of Physiology* **78,** 23–44. doi:`10.1146/annurev-physiol-021115-105045` (2016).
338. Tontonoz, P. & Spiegelman, B. M. Fat and Beyond: The Diverse Biology of PPARγ. *Annual Review of Biochemistry* **77,** 289–312. doi:`10.1146/annurev.biochem.77.061307.091829` (2008).
339. O'Farrell, M. *et al.* FASN Inhibition Targets Multiple Drivers of NASH by Reducing Steatosis, Inflammation and Fibrosis in Preclinical Models. *Scientific Reports* **12,** 15661. doi:`10.1038/s41598-022-19459-z` (Sept. 2022).
340. Hully, J. R. *et al.* Induction of Apoptosis in the Murine Liver with Recombinant Human Activin a. *Hepatology* **20,** 854–862. doi:`10.1002/hep.1840200413` (1994).
341. Ichikawa, T. *et al.* Transforming Growth Factor β and Activin Tonically Inhibit DNA Synthesis in the Rat Liver. *Hepatology* **34,** 918–925. doi:`10.1053/jhep.2001.29132` (2001).
342. Chen, L. *et al.* Activin A Induces Growth Arrest through a SMAD- Dependent Pathway in Hepatic Progenitor Cells. *Cell Communication and Signaling* **12,** 18. doi:`10.1186/1478-811X-12-18` (Mar. 2014).
343. Marsh, B. P., Chada, N., Sanganna Gari, R. R., Sigdel, K. P. & King, G. M. The Hessian Blob Algorithm: Precise Particle Detection in Atomic Force Microscopy Imagery. *Scientific Reports* **8,** 978. doi:`10.1038/s41598-018-19379-x` (Jan. 2018).
344. Brovold, M., Keller, D. & Soker, S. Differential Fibrotic Phenotypes of Hepatic Stellate Cells within 3D Liver Organoids. *Biotechnology and bioengineering* **117,** 2516–2526. doi:`10.1002/bit.27379`. (Sept. 13, 2023) (Aug. 2020).
345. Gao, L., Chen, X., Wang, Y. & Zhang, J. <p>Up-Regulation of FSTL3, Regulated by lncRNA DSCAM-AS1/miR-122-5p Axis, Promotes Proliferation and Migration of Non-Small Cell Lung Cancer Cells</P>. *OncoTargets and Therapy* **13,** 2725–2738. doi:`10.2147/OTT.S236359` (Apr. 2020).
346. Li, J., Shen, J., Qin, L., Lu, D. & Ding, E. LBX2-AS1 Activates FSTL3 by Binding to Transcription Factor RARα to Foster Proliferation, Migration, and Invasion of Thyroid Cancer. *Frontiers in Genetics* **12** (2021).
347. Delire, B., Starkel, P. & Leclercq, I. Animal Models for Fibrotic Liver Diseases: What We Have, What We Need, and What Is under Development. *JOURNAL OF CLINICAL AND TRANSLATIONAL HEPATOLOGY* **3,** 53–66. doi:`10.14218/JCTH.2014.00035` (Jan. 2015).

348. Ghosh-Choudhury, N., Abboud, S. L., Chandrasekar, B. & Ghosh Choudhury, G. BMP-2 Regulates Cardiomyocyte Contractility in a Phosphatidylinositol 3 Kinase-Dependent Manner. *FEBS Letters* **544,** 181–184. doi:`10.1016/S0014-5793(03)00507-6` (2003).
349. Tirosh-Finkel, L. *et al.* BMP-mediated Inhibition of FGF Signaling Promotes Cardiomyocyte Differentiation of Anterior Heart Field Progenitors. *Development* **137,** 2989–3000. doi:`10.1242/dev.051649` (Sept. 2010).
350. Konstantinidis, G., Moustakas, A. & Stournaras, C. Regulation of Myosin Light Chain Function by BMP Signaling Controls Actin Cytoskeleton Remodeling. *Cellular Physiology and Biochemistry* **28,** 1031–1044. doi:`10.1159/000335790` (Dec. 2011).
351. Ren, J. *et al.* Cancer-Associated Fibroblast-Derived Gremlin 1 Promotes Breast Cancer Progression. *Breast Cancer Research* **21,** 1–19. doi:`10.1186/s13058-019-1194-0` (Sept. 2019).
352. Qin, W. *et al.* CAF-derived Exosomes Transmitted Gremlin-1 Promotes Cancer Progression and Decreases the Sensitivity of Hepatoma Cells to Sorafenib. *Molecular Carcinogenesis* **61,** 764–775. doi:`10.1002/mc.23416` (2022).
353. Wang, L. *et al.* Decreased BMP-7 and p-Smad1/5/8 Expression, and Increased Levels of Gremlin in Hepatocellular Carcinoma. *Oncology Letters* **16,** 2113–2118. doi:`10.3892/ol.2018.8918` (2018).
354. Lee, S.-J. *et al.* Regulation of Muscle Mass by Follistatin and Activins. *Molecular Endocrinology* **24,** 1998–2008. doi:`10.1210/me.2010-0127` (Oct. 2010).
355. Dasarathy, S. & Merli, M. Sarcopenia from Mechanism to Diagnosis and Treatment in Liver Disease. *Journal of Hepatology* **65,** 1232–1244. doi:`10.1016/j.jhep.2016.07.040` (Dec. 2016).